CORA Cork Open Research Archive
Cartlann Taighde Oscailte Chorcaí

Title	Toward single-growth monolithically integrated electro-absorption modulated lasers
Authors	Mulcahy, Jack
Publication date	2023
Original Citation	Mulcahy, J. 2023. Toward single-growth monolithically integrated electro-absorption modulated lasers. PhD Thesis, University College Cork.
Type of publication	Doctoral thesis
Rights	© 2023, Jack Mulcahy. - https://creativecommons.org/licenses/by/4.0/
Download date	2026-10-31 11:48:48
Item downloaded from	https://hdl.handle.net/10468/15979

UCC
University College Cork, Ireland
Coláiste na hOllscoile Corcaigh

Toward Single-Growth Monolithically Integrated Electro-Absorption Modulated Lasers

Jack Mulcahy
PhD
114458482

NATIONAL UNIVERSITY OF IRELAND, CORK

School of Physics

Thesis submitted for the degree of Doctor of Philosophy

July 2023

Head of School: Prof. Paul Callanan

Supervisors: Prof. Frank Peters
Mr. Brian Corbett

Research supported by Science Foundation Ireland & Rockley Photonics

Contents

List of Figures iv
List of Tables xi
Abbreviations xii
Acknowledgements xiv
Abstract xv

1 Introduction **1**
1.1 A Brief History of LASERs 1
1.2 Motivation 4
1.3 Photonic Integration 6
1.4 Regrowth-free Monolithic Integration 7
1.4.1 Selective Area Growth (SAG) 7
1.4.2 Quantum Well Intermixing (QWI) 8
1.5 Project Outline 9

2 Background **11**
2.1 The Principle of Laser Operation 11
2.1.1 Absorption 12
2.1.2 Spontaneous Emission 12
2.1.3 Stimulated Emission 13
2.2 Absorption and Emission Rates 13
2.2.1 Absorption and Amplification of Light in a Medium . . . 15
2.3 Fabry-Pérot Cavities 17
2.3.1 Non-Linear Gain in Quantum Well Structures 18
2.4 Absorption in Quantum Well Materials 20
2.5 Quantum Well Offsetting 24

3 Epitaxial Refinement **31**
3.1 Quantum Well Structure Effects on Lasers 31
3.2 Quantum Well Structure Effects on EAMs 35
3.2.1 Simulations using Harold-EAM Software 35
3.2.2 Simulations using Lateral Software 37
3.3 Experimental Verification 39
3.4 DC Processing 40
3.4.1 Ridge-etch Lithography 41
3.4.2 Deep-etch Lithography 44
3.4.3 Oxide-opening Lithography 45
3.4.4 Metal-Liftoff Lithography 47
3.5 Laser Characterisation 50
3.6 Absorption Characterisation 54
3.7 Epitaxial Verdict 56

4 Laser Design, Simulation & Characterisation **58**
4.1 Fabry-Pérot Lasers 60
4.2 Slotted Fabry-Pérot Lasers 64

4.2.1 Tuning . . . 67
4.2.2 Single Section Slotted Fabry-Pérot Laser Testing . . . 68
4.2.3 Two Section Slotted Fabry-Pérot Laser Testing . . . 70
4.3 Dual-mirror Slotted Fabry-Pérot Lasers . . . 75
4.3.1 Dual-mirror Slotted Fabry-Pérot Testing . . . 76
4.3.2 Dual-mirror Slotted Fabry-Pérots as Externally Modulated Laser Sources . . . 81
4.4 Pitted Fabry-Pérot Lasers . . . 83
4.4.1 Single Section Pitted Fabry-Pérot Laser Testing . . . 86
4.4.2 Two Section Pitted Fabry-Pérot Laser Testing . . . 88
4.5 Grouped Pitted Fabry-Pérot Lasers . . . 91
4.5.1 Grouped Pitted Fabry-Pérot Laser Testing . . . 93
4.6 The Inverse Scattering Method . . . 96
4.6.1 Inverse Scattering Device Testing . . . 99
4.7 Ring Lasers . . . 101
4.8 Snail Lasers . . . 105
4.8.1 Snail Laser Testing . . . 106
4.9 Laser Verdict . . . 109

5 EAM Design, Fabrication & Characterisation 111
5.1 Direct Modulation . . . 111
5.2 External Modulation . . . 114
5.3 Lumped Element EAMs . . . 114
5.3.1 Bandwidth and equivalent circuit . . . 117
5.3.2 Parasitic impedances . . . 118
5.3.3 Traditional RF Contacts . . . 119
5.3.4 Contact Pillar Isolation . . . 120
5.4 Device Design . . . 121
5.5 High-Speed Processing . . . 122
5.5.1 Ridge-etch Lithography . . . 122
5.5.2 Substrate Isolation-etch Lithography . . . 124
5.5.3 Lower N-Metal Lithography and BCB Planarisation . . . 126
5.5.4 BCB Patterning Lithography . . . 128
5.5.5 P-metal Window-Opening Lithography . . . 129
5.5.6 P-metal Deposition Lithography . . . 130
5.5.7 Full N-metal Deposition Lithography . . . 131
5.5.8 Contact Layer Etch Lithography . . . 132
5.6 Equivalent Circuit Modelling . . . 134
5.7 Contact Pad Optimisation . . . 135
5.8 Metal Bridge Optimisation . . . 137
5.9 EAM Measurements . . . 140

6 EML Design, Fabrication & Characterisation 144
6.1 EML Device Design . . . 146
6.2 EML Processing . . . 147
6.2.1 Electrical Isolation Techniques . . . 147
6.2.2 Ridge-etch Lithography . . . 150

6.3 Device Outputs 153
6.4 Fabrication Issues 155
6.5 Proposed Fabrication Modifications 157

7 Conclusions & Future Work **158**
7.1 Future Work 160
7.1.1 Micro-Transfer Printing 160
7.1.2 Iron Doping 162
7.1.3 Quantum Well Intermixed EAMs 164

References **1**

List of Figures

1.1 Internet traffic growth in recent years from CISCO VNI Global Traffic Forecast 5

2.1 Three basic processes of interaction of radiation with a two-level atomic system 11
2.2 Propagation of radiation along the z direction 15
2.3 Fabry-Pérot Resonator consisting of a gain medium between two reflectors 17
2.4 Quantum well number vs threshold current 20
2.5 Schematic of the quantum confined stark effect (QCSE) 21
2.6 Simulation of a quantum well with barrier bandgap at $1.1\,\mathrm{eV}$ and the well bandgap at $0.9\,\mathrm{eV}$ 22
2.7 A MQW material highlighting the intrinsic transit distance, s_t, the MQW transit distance, s_{MQW}, and the distances the holes and electrons must travel, s_h and s_e respectively. 26
2.8 Eqn. 2.44 with varying γ_{off} and s_t 29
2.9 Eqn. 2.46 with varying s_{mqw} and s_t in an optimal γ_{off} configuration. 30

3.1 Previously used custom EAM epitaxy 32
3.2 The Harold software was used to generate simulated epitaxies for QW laser structures with varying QW width and number . . 32
3.3 The FP lasers with varying epitaxies can then be analysed in terms of their slope efficiency; SE, and threshold current; I_{th} . 33
3.4 Characteristics of a $300\,\mu\mathrm{m}$ FP laser with varying QW structure . 35
3.5 Simulated Harold absorption for an epitaxy with 6QW of width $7\,\mathrm{nm}$ 35
3.6 Simulated Harold EAM absorption for an epitaxy with 6QW of varying width 36
3.7 Simulated Harold EAM absorption for an epitaxy with a varying number of $9\,\mathrm{nm}$ quantum wells 37
3.8 Simulated Lateral EAM absorption of bound states for an epitaxy QW of varying width 38
3.9 Peak EAM ER/IL for an epitaxy with QW of varying width . . . 39
3.10 A view of some of the overlayed lithographic mask layers used to fabricate FP lasers designed in PICDraw. This picture shows waveguides of widths 2.5 and 3 μm. Waveguides of widths 2.5-5 μm were fabricated. The lower image shows a zoomed in portion of the 2.5 μm waveguide 40
3.11 A view of shallow and deep waveguides 41
3.12 A schematic view of the etch endpoint detection system 42
3.13 Process flow for the first lithographic step 43
3.14 A view of the waveguides for the second step of the lithography 44
3.15 Process flow for the second lithographic step 45
3.16 A view of the waveguides for the third step of the lithography . 46

3.17 Process flow for the third lithographic step 46
3.18 A view of the waveguides for the fourth step of the lithography 47
3.19 Transfer Length Measurement (TLM) 48
3.20 Process flow for the fourth lithographic step 49
3.21 SEM images of the completed DC Fabrication 50
3.22 Experimental setup used for collecting LIV measurements . . . 51
3.23 Experimental setup used for collecting material absorption measurements 55
3.24 Close up view of the photodiode structure used for absorption measurements in Fig.3.23 55
3.25 Absorption results for PD test measurements 56

4.1 The commercially produced IQE epitaxial material designed for $1550\,\mathrm{nm}$ emission. 59
4.2 Scattering matrices represent the transformation from input to output of a system 60
4.3 Transfer matrices represent the transformation from left to right in a system 61
4.4 The reflectivity versus wavelength for an $600\ \mu m$ Fabry-Pérot etalon. 62
4.5 The lasing modes for a $600\,\mu\mathrm{m}$ Fabry-Pérot with an arbitrary gain profile centred on $1550\,\mathrm{nm}$ 63
4.6 Schematic of a waveguide with a single slot 64
4.7 Transmission of a $1000\,\mu\mathrm{m}$ cavity (blue), reflectivity of a slotted mirror with a $150\,\mu\mathrm{m}$ separation (red), and the combined resonance (green). 66
4.8 The reflectivity of Fig. 4.7 with gain as in Eqn. 4.9 66
4.9 The reflectivity versus wavelength for changing refractive index of the waveguide between slot 67
4.10 The reflectivity versus wavelength for changing slot separations. The number of slots was fixed at 8 and the slot width was $1\mu m$ 68
4.11 A view of the lithographic mask design for the single section SFP. The numbers in the metal layer represent the separation between slots which are highlighted in red. The slot width is $1\,\mu\mathrm{m}$ 68
4.12 Experimental measurements of an FP laser with slots etched into the gain section 69
4.13 A comparison of the experimentally measured spectra of a 1000 μm device with 3 slots placed $250\ \mu m$ apart (blue) and the corresponding simulated power output (red) showing a good match for a separation of $250\ \mu m$ with $n = 3.22$. 69
4.14 The number of slots in a $1000\,\mu\mathrm{m}$ device v.s. the measured threshold current and slope efficiency 70
4.15 A view of the lithographic mask design for the two section SFP with six slots spaced $108\,\mu\mathrm{m}$ apart and a gain length of $800\,\mu\mathrm{m}$. 70

4.16 An experimentally measured LI of the dual slot Fabry-Pérot Laser with varying left (L) and right (R) mirror currents. Each colour represents a different bias current on the mirror section from $10\,\mathrm{mA}$ (red) to $60\,\mathrm{mA}$ (purple). 71
4.17 An experimental measurement of a two section slotted device comparing section currents and the resultant wavelength. . . . 71
4.18 An experimental measurement of a two section slotted device comparing section currents and the resultant SMSR. 71
4.19 SFP behaviour while the mirror section was at a fixed 30mA . . 72
4.20 Wavelength vs SMSR for each collected spectrum of the SFP . . 73
4.21 Experimental vs simulated output of a the SFP with a slot separation of $108\,\mu m$ 74
4.22 Dual-mirror slotted Fabry-Pérot reflectivity. 75
4.23 Simulated available lasing modes of Fig. 4.22 76
4.24 A view of the lithographic mask design for the three section SFPs. The gain section had length $800\,\mu\mathrm{m}$. The two surrounding mirror sections have 6 slots each. M1 had a slot separation of $36\,\mu\mathrm{m}$. M2 had a slot separation of $74\,\mu\mathrm{m}$. 76
4.25 An experimentally measured LI of the dual-mirror slotted Fabry-Pérot Laser with varying left (L) and right (R) mirror currents. . 77
4.26 A selection of experimentally measured spectra with $\sim 5\,\mathrm{nm}$ gaps showcasing some of the available lasing wavelengths 77
4.27 Wavelength vs SMSR for each collected spectrum of the DSFP. . 78
4.28 Experimental measurements of the DSFP device with M_1 at fixed currents. M_2 was varied from $20\,\mathrm{mA}$-$200\,\mathrm{mA}$ with a step size of $10\,\mathrm{mA}$. The gain section was varied from $20\,\mathrm{mA}$-$300\,\mathrm{mA}$ with a step size of $10\,\mathrm{mA}$. 78
4.29 Colour plot measurements of the DSFP device with M_1 at fixed currents. 79
4.30 Wavelength spread of the device showing $> 40\,\mathrm{nm}$ $50\,\mathrm{GHz}$ spacing achieved. Spectra are normalised to $0\,\mathrm{dB}$ to accommodate for variations on power due to optical fibre drift during automated measurements. 80
4.31 A schematic view of the DSFP integrated monolithically with an electro-absorption modulator. 81
4.32 With the DSFP set to specific wavelengths the light was injected into a monolithically integrated EAM and the voltage across the EAM was varied. The normalised result of the change in power is presented for various tuned wavelengths set via varying the current across the three DSFP sections. 82
4.33 A SEM image of a waveguide with multiple pits etched, each with a diameter of $1\,\mu\mathrm{m}$ 83
4.34 Transmission of a $1000\,\mu\mathrm{m}$ cavity (blue), reflectivity of a pitted mirror with a $34\,\mu\mathrm{m}$ separation (red), and the combined resonance (green). 84
4.35 The reflectivity of Fig. 4.34 with gain as in Eqn. 4.9 84

4.36 The reflectivity versus wavelength for changing pit separations. This simulation used 10 pits each with a diameter of $1\,\mu\mathrm{m}$ to cause a 3% reflection. 85
4.37 A view of the lithographic mask design for the single section PFP. P6 is a device with 6 pits equally dispersed throughout the cavity. P10 is a device with 10 pits equally dispersed throughout the cavity. 86
4.38 Experimental measurements of an FP laser with pits (PFP) etched into the gain section 86
4.39 A comparison of the experimentally measured spectra of a 1000 μm device with 16 pits placed 62.5 μm apart (blue) and the corresponding simulated reflectivity values (red) showing a good match for a separation of 62.5 μm with $n = 3.22$. 87
4.40 The number of pits in a 1000 μm device v.s. the measured threshold current and slope efficiency 87
4.41 A view of the lithographic mask design for the two section PFP with six pits spaced $34\,\mu\mathrm{m}$ apart and a gain length of $800\,\mu\mathrm{m}$. . . 88
4.42 An experimentally measured LI of the pitted Fabry-Pérot Laser with varying mirror currents. Each colour represents a different bias current on the mirror section from $10\,\mathrm{mA}$ (red) to $60\,\mathrm{mA}$ (purple). 88
4.43 An experimental measurement of a PFP with six pits spaced $34\,\mu\mathrm{m}$ apart and a gain length of $800\,\mu\mathrm{m}$ comparing section currents and the resultant wavelength. 89
4.44 An experimental measurement of a two section pitted device comparing section currents and the resultant SMSR. 89
4.45 Wavelength vs SMSR for each collected spectrum of the PFP. . . 90
4.46 Experimental vs simulated output of a the PFP with a slot separation of $34\,\mu\mathrm{m}$ 91
4.47 Resonance of a $1200\,\mu\mathrm{m}$ cavity with grouped pits with an outer separation of $108\,\mu\mathrm{m}$ (red) and an inner separation $12\,\mu\mathrm{m}$ (blue). The combined resonance is shown in green 92
4.48 The reflectivity of Fig. 4.47 with gain as in Eqn. 4.9 92
4.49 A view of the lithographic mask design for the grouped PFP showing a zoomed in view of the inner pit groupings. The outer pit separation was $108\,\mu\mathrm{m}$. The inner pit separation was $12\,\mu\mathrm{m}$. 93
4.50 An experimentally measured LI of the grouped pitted Fabry-Pérot Laser with varying mirror currents. Each colour represents a different bias current on the mirror section from $10\,\mathrm{mA}$ (red) to $60\,\mathrm{mA}$ (purple). 93
4.51 An experimental measurement of the grouped pitted device comparing section currents and the resultant wavelength. 94
4.52 An experimental measurement of the grouped pitted device comparing section currents and the resultant SMSR. 94
4.53 Wavelength vs SMSR for each collected spectrum of the SFP. . . 94

4.54 Experimental vs simulated output of a the GPFP (blue) with an outer pit separation of $108\,\mu\mathrm{m}$ (red) and an inner pit separation of $12\,\mu\mathrm{m}$ (green) 95
4.55 Index perturbations along a cavity form subcavities, $P(\theta)$ and subfacets, T. The cavity has varying refractive index regions shown in purple (n_1) with no perturbation, and and pink (n_2) with perturbation. 97
4.56 Distribution of 15 perturbations along a $1000\,\mu\mathrm{m}$ cavity to minimise the threshold gain at $1570\,\mathrm{nm}$. Here, the 0 position of the cavity is taken to be the center. The right facet is at 0.5. 98
4.57 A view of the lithographic mask design for the inverse scattering design device. A zoomed in view shows the scattered distribution of the pits. 99
4.58 LI curve of an inverse scattering device with 15 perturbations targetting $1570\,\mathrm{nm}$. 99
4.59 Peak wavelength (blue) and SMSR (red) of a $1570\,\mathrm{nm}$ inverse scattering device vs a changing current across the laser. 100
4.60 Peak wavelength (blue) and SMSR (red) of a $1550\,\mathrm{nm}$ inverse scattering device vs a changing current across the laser. 101
4.61 A schematic of a ring resonator with a half-wave coupler 101
4.62 U bend FP laser radii vs corresponding threshold current. In the inset is a schematic representation of the U bend FP with curve radius highlighted. 102
4.63 A simulated ring transmission spectrum 103
4.64 Coupled Ring and Fabry-Pérot resonance spectrum. 104
4.65 A schematic of a snail laser with a directional coupler. L_T is the length of the tail section. L_R is the remainder of the ring until it re-couples back into itself from point A to B. 105
4.66 CCW and CW modes of a snail laser, as well as their coupled modes 106
4.67 LI curve of a snail laser, device 4 from Table 4.1. 107
4.68 Peak wavelength (blue) and SMSR (red) of device 4 vs a changing current across the ring. 107
4.69 Experimentally measured spectra of device 4 at $I = 175mA$ (red) and the beat resonance of two ring cavities of length $775\,\mu\mathrm{m}$ and $899\,\mu\mathrm{m}$. 108

5.1 Electronic schematic diagram of lumped element EAM with A load resistor (R_l) in parallel terminating the electrical signal. . 115
5.2 An equivalent circuit diagram of an EAM driven by a biased RF source 117
5.3 How f_{3dB} is affected by changing capacitance and $R_l + 2R_j$ . . 118
5.4 On the left is a DC device with GSG contacts planar to the waveguide on an n-doped substrate. On the right is a modified contact scheme designed to minimise the influence of the signal pad's capacitance. 121

5.5 EAM model and SEM image 122
5.6 A view of the ridge definitions for the high speed fabrication process shown in red. Here we define the waveguide and the planar contact pillars. 123
5.7 Process flow for the first lithographic step at the cross section shown in the dashed line in Fig. 5.6. 124
5.8 A view of the isolation etch definitions for the high speed fabrication process shown in blue. 124
5.9 Process flow for the second lithographic step at the cross section shown in the dashed line in Fig. 5.8 125
5.10 A view of the n-metal definitions for the high speed fabrication process shown in light green. 126
5.11 Process flow for the third lithographic step 127
5.12 A view of the BCB patterning definitions for the high speed fabrication process show in orange. 128
5.13 Process flow for the fourth lithographic step 128
5.14 A view of the oxide opening patterning definitions for the high speed fabrication process shown in cyan. Dielectric is removed here to provide an opening for metal contacts to the waveguide. 129
5.15 Process flow for the fifth lithographic step 129
5.16 A view of the P metal deposition definitions for the high speed fabrication process shown in purple. 130
5.17 Process flow for the sixth lithographic step 131
5.18 A view of the n metal deposition definitions for the high speed fabrication process shown in grey. 131
5.19 Process flow for the seventh lithographic step 132
5.20 A view of the contact layer etch definitions for the high speed fabrication process 132
5.21 Process flow for the eighth lithographic step 133
5.22 EAM equivalent circuit 134
5.23 Pad test structure 135
5.24 Experimental measurements from the pad test device. 136
5.25 EAM test structure and the resultant change in capacitance . . . 136
5.26 EAM structure with varying isolation 137
5.27 EAM bridge test structure 137
5.28 Experimental measurements from the bridge test device. 138
5.29 EAM bridge test structure with varying bridge width 139
5.30 Impedance and resistance with varying bridge width 139
5.31 A simulated magnitude of a single S_{21} measurement based off experimental S_{11} data taken from an EAM with length of $50\,\mu\mathrm{m}$. The simulation is made for an impedance match of $50\,\Omega$ (black) and $25\,\Omega$ (red). 141
5.32 EAM f_{3dB} measurements for varying lengths 142

6.1 A schematic of the test structure used for electrical isolation measurement and optical loss measurements. 147

6.2 The resistance vs isolation width for various isolation styles. . . 148
6.3 The fractional optical loss versus isolation width for various isolation styles. 149
6.4 A view of the ridge definitions for the EML process shown in red and the deep etch shown in blue. 150
6.5 Process flow for the shallow and deep waveguide definitions . . 152
6.6 The LI curve for the SFP laser at varying mirror currents. 153
6.7 Experimental data versus simulated outputs for the SFP laser. . 154
6.8 The IV curves for different devices fabricated in the high speed EML process. 155
6.9 Changes in BCB planarisation for different fabrications processes 156
6.10 The current oxide opening lithography shown in pink and the proposed new oxide opening shown in dark blue. 157

7.1 Transfer Printing Process 161
7.2 Contact pillar electrical isolation regimes. 162
7.3 Iron doping test structure and IV. 163
7.4 FP emission spectra for non QWI and QWI FP lasers. The QWI laser underwent rapid thermal annealing to $675\,^{\circ}\mathrm{C}$ for 2 minutes. 165

List of Tables

3.1 Results extracted from simulated $300\,\mu\mathrm{m}$ FP laser with varying quantum well structure 34
3.2 A selection of some of the experimental results obtained when testing FP lasers on 6QW with width $7\,\mathrm{nm}$ 52
3.3 A selection of some of the experimental results obtained when testing FP lasers on 6QW with width $9\,\mathrm{nm}$ 52
3.4 A selection of some of the experimental results obtained when testing FP lasers on 8QW with width $7\,\mathrm{nm}$ 53
3.5 A comparison of $2.5\,\mu\mathrm{m}$ wide, $300\,\mu\mathrm{m}$ long FP lasers based on simulated and experimental data 54

4.1 Experimental Measurements of varying snail designs 106
4.2 A summary of the characterisation of the various laser designs. 109

6.1 The fractional optical loss of different slot styles with widths $1\,\mu\mathrm{m}$. 150

7.1 Iron doping test structure results. 164

Abbreviations

EM	Electromagnetic
QW	Quantum Well
VCSEL	Vertical Cavity Surface Emitting Laser
QCL	Quantum Cascade Laser
HBT	Heterojunction Bipolar Transistor
MQW	Multi-Quantum Well
SAG	Selective Area Growth
QWI	Quantum Well Intermixing
DFB	Distributed Feedback Laser
DBR	Distributed Bragg Reflector
QCSE	Quantum Confined Stark Effect
ER	Extinction Ratio
IL	Insertion Loss
TE	Transverse Electric
TM	Transverse Magnetic
PiN	Positive-Intrinsic-Negative
GS	Ground-Signal
GSG	Ground-Signal-Ground
PECVD	Plasma-Enhanced Chemical Vapour Deposition
TLM	Transfer Length Measurement
TLS	Tunable Laser Source
PIC	Photonic Integrated Circuit
FP	Fabry Perot
SM	Slotted Mirror
SFP	Slotted Fabry Perot
DSFP	Dual-mirror Slotted Fabry Perot
PM	Pitted Mirror
PFP	Pitted Fabry Perot
GPFP	Grouped Pitted Fabry Perot
SRL	Semiconductor Ring Laser
EAM	Electro-absorption Modulator
EML	Externally Modulated Laser
FCB	Flip-Chip Bonding
MTP	Micro-Transfer Printing

"Watch for that moment - and when it comes, do not hesitate to leap. It is only when you fall that you learn whether you can fly."

Acknowledgements

PhDs are tricky things. Before I started my own I thought they were purely the domain of the brilliant masterminds of the world and far beyond my reach, and if I had been alone in doing it then it still would be. Thankfully I had a lot of help along the way.

Firstly, I would like to thank my supervisor, Professor Frank Peters. He has given professional advice and life advice both of which I am grateful for in equal measure. I'd also like to thank the entire Peters family for welcoming me to their home on multiple occasions for board games I would've never seen, and Cork's greatest cookies.

I also want to thank the members of the Integrated Photonics Group, both past and present. Alison, Ludovic, Mohamad, Xing, Shengtai, Zhengkai, Maryam, John, Shane, Kevin, Joyce, Hui, Hua. Each and every one of you has supplied advice, teachings, friendship, and support for the entirety of this journey and for that I am forever grateful.

I extend my heartfelt thanks to my family, friends and loved ones for their love, support, and understanding during the ups and downs of my PhD journey. Their unwavering belief in me and encouragement kept me from changing my name and fleeing the country. Each of you was willing to hear me either joyfully praise or dreadfully bemoan said ups and downs in this journey. Thanks for listening, and if wasn't interesting I hope it was at least entertaining.

I would like to acknowledge the staff and colleagues at Tyndall for their support and assistance, and IPIC for providing me with access to resources and facilities that were crucial for my research.

Once again, I express my deep gratitude to everyone who has contributed to my PhD journey. Thank you all.

Jack

Abstract

Every year the demand for bandwidth is growing exponentially due to the emergence of data-intensive services such as high-definition video streaming, cloud-based computing, and machine-to-machine communication. This rapid expansion is primarily driven by the extensive deployment of fibre-based optical communication networks. Consequently, there is an increasing need for photonic components to meet the requirements of these networks, which are expanding both in geographical coverage and terminal density.

To satisfy this demand, the photonics industry must enhance its production capabilities and adopt more efficient fabrication processes. A crucial aspect of streamlining fabrication involves eliminating slow and costly processes. In photonics fabrication, epitaxial regrowth and advanced lithography steps are typically time-consuming and expensive, making them prime targets for process optimisation. Moreover, the integrated electronics approach provides valuable insights by enabling the monolithic integration of multiple photonic components fabricated simultaneously. This integration technique allows for the creation of highly complex circuits while reducing overall fabrication complexity.

This research focuses on a key component at the heart of photonic circuits: the tunable single-mode laser. The aim is to contribute to the development of components that can be fabricated without the need for regrowth or advanced lithography. Additionally, the study emphasises the importance of monolithic integration, specifically with electro-absorption modulators (EAMs). By integrating EAMs with tunable lasers, the resulting devices can offer enhanced functionality and performance, leading to more efficient and compact photonic systems. The issue at hand, however is the varied epitaxial requirements of lasers and EAMs, which provides a noted barrier to a monolithic, regrowth-free integration process.

This thesis aims to advance the development of single-growth monolithically integrated externally modulated lasers (EMLs) based on electro-absorption modulators (EAMs). The design of quantum well structures is explored, revealing the significance of introducing an imbalance in the position of the quantum wells to optimise the transit times of carriers in EAMs, thus maximising the bandwidth. Simulation studies on epitaxial structures led to the identification of an optimal material that balances the performance of

lasers and EAMs, providing an ideal platform for EML fabrication.

Different laser designs are investigated, including slotted Fabry Pérot lasers and snails, with a focus on achieving a redshifted single-mode laser. Simulation models are developed to predict laser reflectivity and spectral output, which were verified through fabrication and testing. The optimal laser design for integrated EMLs was determined through critical evaluation with a laser being produced with $> 40\,\mathrm{dB}$ SMSR and a tuning range of $60\,\mathrm{nm}$.

A high-speed process for fabricating EAMs is developed, featuring optimised lithographic mask layers for the isolation of contact pads and metal bridges to reduce parasitic capacitance. The resulting EAMs exhibited a predicted bandwidth of approximately $80\,\mathrm{GHz}$.

Drawing upon the knowledge gained from laser and EAM simulation, fabrication, and characterisation, a new high-speed process for EMLs is devised. The o-band lasers and EAMs were designed based on optimal principles determined in previous chapters. The fabricated single-mode lasers were successfully matched to simulated models. Further analysis identified potential avenues for improving future EML fabrication yields.

In summary, this thesis provides valuable insights and tools for the creation of single-growth monolithically integrated electro-absorption modulated lasers. The journey spans from material design to device outputs, with the aim of enabling readers to replicate and enhance the development of EMLs.

I, Jack Mulcahy, certify that this thesis is my own work and I have not obtained a degree in this university or elsewhere on the basis of the work submitted in this thesis.

Jack Mulcahy

Chapter 1

Introduction

In this thesis we seek to focus on the creation of a single growth monolithically integrated electro-absorption modulated laser. Lasers, with their remarkable properties and diverse applications, have risen to become vitally important in today's world. Their coherent and focused beams of light have revolutionised numerous fields, from technology and medicine to communication and manufacturing. The precision and intensity of lasers enable cutting-edge research, high-speed data transmission, and efficient manufacturing processes. In medicine, lasers have become indispensable tools for surgical procedures [1], vision correction, and even cancer treatment [2]. Lasers play a pivotal role in telecommunications, allowing for rapid and reliable transmission of information over long distances [3]. Their versatility and ability to manipulate light have opened up endless possibilities, making lasers an integral part of modern society and a driving force behind technological advancements.

1.1 A Brief History of LASERs

The essential phenomenon involved in the operation of the laser is stimulated emission. Einstein came up with the idea for this technique in 1917 [4]. Bose's work gave a solid framework for understanding the nature of photons and the statistics that the particles obeyed [5].

Several researchers looked into the possibilities of creating semiconductor lasers, including Aigrain [6, 7], Basov et al. [8, 9], Boyle and Thomas [10, 11], and Pankove [12]. Lax considered the transition across quantified Landau

levels [13]. Direct band-gap semiconductors were determined to be a necessary requirement to produce the desired effect, according to research done across the world [14, 15].

Townes and coworkers developed the maser (Microwave Amplication by Stimulated Emission of Radiation) as the first device to use stimulated emission of electromagnetic (EM) radiation [16, 17]. It has since been discovered that von Neumann demonstrated laser action in a p-n junction in an unpublished note [18]. Townes and Schawlow proposed an optical maser in 1958 [19]. Soon after, Javan et al. [20] and Maiman [21] announced gas lasers and solid-state (ruby) lasers, respectively.

Bernard and Duraffourg's key study [22] emphasised the importance of high injection to produce stimulated emission. Finally, in 1962, four groups reported laser emission from a forward-biased p-n junction employing various material combinations, virtually simultaneously [23–26].

Early homojunction p-n junction lasers were unable to operate continuously at temperatures at or above room temperature. Kroemer highlighted the benefits of employing heterostructures to increase the performance of diode lasers in 1963 [27]. The group lead by Alferov researched a similar concept and made significant advancements in the structure's evolution [28, 29].

Hayashi and Panish made great strides in the construction of the first continuous-wave (CW) room-temperature diode lasers [30] using a junction between two different semiconductor materials to produce a "built-in potential" that aided in optical confinement and waveguiding. The ability to successfully manufacture such junction lasers was previously constrained by defects in the semiconductor materials, which could result in the laser failing or functioning only intermittently. By utilising a novel production method that decreased the amount of material flaws, the researchers were able to develop a small, dependable laser that was able to run constantly at room temperature. All of these efforts resulted in diode lasers being mass-produced in large quantities and their performance being improved in terms of power output, efficiency, and modulation bandwidth, with new materials constantly being researched to expand the operating wavelength range.

Semiconductor heterojunctions can be thought of as a simple example of how a device's band structure can be manipulated. Esaki and Tsu proposed the concept of the superlattice, which was a crucial concept in band structure

engineering [31]. Kazarinov and Suris proposed a unipolar laser incorporating transitions between quantised energy levels around the same time, though the structure that used this concept arrived much later [32]. Soon after the Esaki and Tsu publications, two papers dealing with energy quantisation in heterostructures, Dingle et al. [33] and Chang et al. [34], appeared in the literature. After those, the term quantum well (QW) was coined.

Dingle and Henry presented a QW laser in their patent application [35]. Van der Ziel et al. [36] revealed the first optically pumped QW laser, followed by Dupuis et al. [37] with the first electrically pumped QW laser. Iga introduced the vertical-cavity surface-emitting laser (VCSEL) and began substantial research on it almost at the same time [38]. Jewell et al. created and reported VCSEL arrays [39], and Coldren et al. [40] and Chang-Hasnain et al. [41] made enhancements to the original concept.

Further quantisation in a QW structure yields quantum-wire (QWR) and quantum-box/dot (QB/QD) structures, and Arakawa and Sakaki showed the advantages of employing such structures in lasers [42]. In 1994, a paper was published detailing the successful design and implementation of QD lasers [43].

Faist et al. first described unipolar laser action including transitions between subbands in a QW in 1994, more than two decades after Kazarinov and Suris proposed it [44]. This laser, known as a quantum cascade laser (QCL), was then demonstrated by a variety of researchers for various wavelengths and materials systems. In 1996, Nakamura published a paper on blue-green lasers made from nitride-based materials and alloys [45, 46]. Since their discovery, these lasers have vastly improved. Bhattacharyya et al. presented the notion of tunnel injection in QW lasers in the same year, and the benefits were demonstrated [47].

Evans et al. announced the first QCL functioning in the so-called terahertz range in 2002 ($\lambda = 6\mu m$), and room-temperature operation with high power was obtained by them [48, 49]. A group lead by Feng and Holonyak disclosed a new type of laser called a transistor laser in 2004 [50], essentially a heterojunction bipolar transistor (HBT), with stimulated emission from the QWs in the base producing light while also acting as an amplifier for electrical signals, similar to a regular transistor.

The development of semiconductor lasers has always sparked interest in lasers

on the silicon platform that would benefit from silicon's bank of previously established research. Because silicon is an indirect band gap semiconductor, it cannot be used as an efficient light emitter. A silicon-based light emitter and other photonic devices combined with electronic circuits on the same Si platform would offer a variety of benefits. Many workers have worked for nearly four decades to make this long-held ambition a reality. Finally, in 2005, Rong et al. presented the Raman laser, which was hailed as a breakthrough [51]. Later, it was discovered that tensile strain applied to Ge, another indirect-gap group IV semiconductor, can cause an indirect-to-direct band crossover. Liu et al. disclosed an optically pumped Ge laser produced on Si in 2010, while Liu et al. presented an electrically pumped version in 2012 [52, 53].

The research undertaken in the field of laser physics has led to a plethora of benefits across various disciplines, from allowing a better understanding of photon behaviour to a revolution in advanced communication systems and high-speed data transfer. In communications in particular, the field of photonics seeks to merge its benefits with the pre-established electronic structures therein to facilitate the growing need. As businesses and organisations store and analyse more data in the cloud, data centres continue to expand in size. Data centre networks have correspondingly greater demands as computation increases. Compared to copper cables, optical cables can support more lane bandwidth across longer transmission distances. Lane bandwidth is the capacity or data rate of individual lanes within a multi-lane optical communication system. Non-integrated methods, such as vertical-cavity surface-emitting lasers, can be used for optical transceivers on multi-mode optical fibre networks for short-reach distances and up to $40\,\mathrm{Gbps}$ data transfer rates [54]. Photonic integrated circuits are essential for enabling high-performance, low-cost optical transceivers beyond this range and bandwidth which motivates research towards low-cost photonics-based solutions.

1.2 Motivation

In recent years the growth of the internet has been explosive as shown in Fig. 1.1 [55], as its role in our daily lives increases in prevalence due to the burgeoning popularity of social media sites, video streaming services, and online gaming. With each subsequent year the consumption of data grows

resulting in an ever intensifying need for more efficient and more robust data communications. Optical communications has thus been called on to satisfy these demands, being essential in the development of fast communication networks.

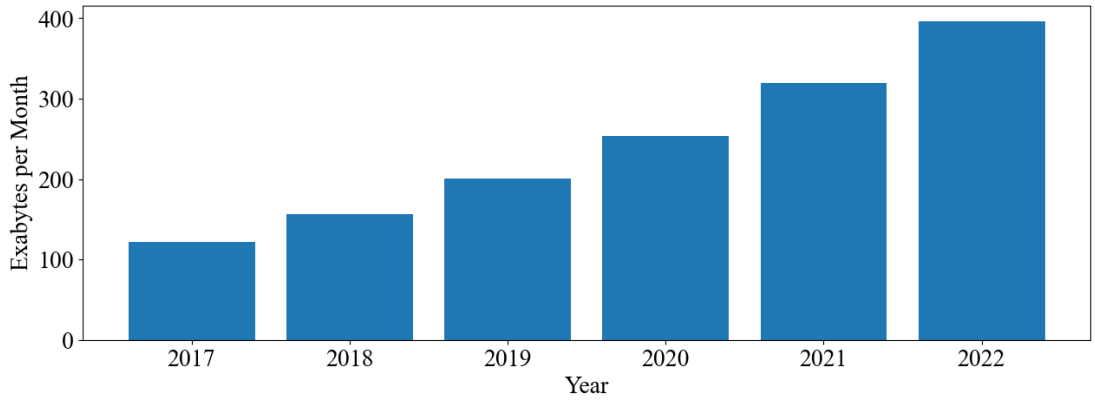

Figure 1.1: Internet traffic growth in recent years from CISCO VNI Global Traffic Forecast

While most devices connect wirelessly to local relays, those relays require wired connections in order to provide satisfying data transmission rates to all users of the service. Such speeds necessitate the use of optical fibre communications which serve to guide modulated light from transmitter to receiver. In transmission intense areas such as data centres, where much of this information is stored and processed, the modulation of this light must be accomplished at a very high speed in order to handle the processing of the myriad of wireless user data which passes through the centre every second. These centres typically use multi-mode fibre in conjunction with $850\,\mathrm{nm}$ sources, which may take the form of a laser or an LED for lowered cost.

Multi-mode fibre however presents the issue of modal dispersion, which can cause it to be unsuitable for larger networks. Sources emitting at 1.3μm are commonly used in systems that require low chromatic dispersion due to minimum optical fibre dispersion at this wavelength. The benefits of optical communication have inspired many of these centres to switch to all optical networks to meet the ever increasing demands of massive data transportation. Thus, the demand for the creation of faster, more efficient optical communication devices is ever-growing, resulting in a call for a better photonic integration of optical components.

1.3 Photonic Integration

Components required to build a photonic integrated circuit are monolithically integrated on the same substrate. The primary drawbacks of this strategy are fabrication complexity and epitaxial performance. Different components such as lasers and EAMs have different epitaxial requirements in regards to the optimum number and width of quantum wells, often requiring expensive epitaxial regrowth. Epitaxial regrowth is frequently used to determine regions on the wafer that will act as active and passive zones in order to achieve its goal of multi-functional devices on the same substrate. This initial growth must first be etched in a fabrication facility, and it must then be regrown as required so as to have more than one bandgap energy, E_g.

A buttjoint regrowth technique is a typical integration technique [56]. This includes the wafer growth, with the active region often forming first in the MQW region. Then, using conventional lithography, the wafer's passive portions are defined, processed, and etched. The passive zone is defined by the etched-away portions being grown back with bulk or quantum well semiconductor having a larger band gap. The materials' discontinuities will be subjected to strain and an index mismatch, which will produce optical reflections. The asymmetric vertical twin waveguide is a variation of this technique [57] and the dual quantum well process [58]. This approach uses vertical coupling to connect the upper and lower regions of the wafer in order to reduce optical feedback caused by significant changes in refractive index.

Each of these approaches involves growing part of the epitaxy, removing parts of it with an etch, and then growing new material on top to define new sections of the wafer with different optical properties. Because aluminium oxidises quickly when exposed to air, using it as a component in the alloys used in etch and regrowth processes can be challenging [59]. InGaAsP based MQWs have typically been used in integrated EAMs, as this allows for etch and re-growth processes without oxidation of the quantum wells [60]. Two more common approaches used to define the passive regions during growth will be discussed in the next section, namely Selective Area Growth (SAG) and Quantum Well Intermixing (QWI).

1.4 Regrowth-free Monolithic Integration

Early integrated photonic circuits included optical modulators with integrated single frequency lasers. When combining single frequency lasers with high speed modulators, distributed feedback (DFB) lasers and, more recently, distributed bragg reflector (DBR) lasers have been employed [61, 62]. Due to the fact that they require at least two epitaxial growth procedures, DBR lasers are costly and time-consuming to produce. Facetless lasers may now be created using ridge waveguides with controlled reflective slots added, eliminating the need for a grating development stage and providing a platform for other optical functionalities to be implemented [63].

One photonic integration business has previously established a platform using a laterally corrugated ridge forming a DFB laser [64]. The cost and complexity of semiconductor regrowth increases the number of fabrication stages required to complete a device. Eliminating regrowth would make the integrated photonics market more open by enabling a fabrication facility to grow the necessary epitaxy externally. Several methods are now in use to try and lessen the fabrication process' reliance on regrowth. While single growth monolithic integration is ideal, what is already available should be taken into consideration.

1.4.1 Selective Area Growth (SAG)

Through a method known as selective area growth (SAG), the growth rate of a semiconductor material can be altered at various locations on a semiconductor substrate. SAG is frequently used to specify areas with variously sized quantum wells. SiO_2 is deposited and patterned in areas close to where active region waveguides are to be positioned during the formation of InGaAsP quantum wells. As there is no epitaxy growth on the dielectric during MOVPE growth, there is a residual buildup of indium and gallium, leading to a larger concentration of these atoms. Due to the greater diffusion constant of indium, the indium concentration in these areas rises, redshifting the material.

It has also been shown for AlInGaAs [65] that the growth rate increases, widening quantum wells, reducing energy levels, and further red-shifting the material. Due to the fact that the structure is preserved at a single level, removing a significant discontinuity in the material compositions, and reducing reflections, selective area growth is currently attracting a lot of

interest in the field of monolithic integration [66]. In order to determine the layers beneath the MQW area, the technique normally requires one growth before the SAG growth.

After the growth, the SiO_2 still needs to be removed, which would be challenging because some material is still on top. Before the final p-doped cap layers are developed, a post-growth etch of these regions must be carried out due to the considerable increase in growth rate at the border of the SiO_2. The growth is still dependent on the fabrication facility due to the pre-growth processing of the SiO_2, which limits the ability to fabricate such devices outside of places having both a growth and fabrication facility.

1.4.2 Quantum Well Intermixing (QWI)

In the process known as quantum well intermixing (QWI), the atoms from quantum wells and the related barriers interdiffuse. The quantum well is deformed and loses definition as a result of this. This alters the quantised energy state and typically causes the band edge to shift to the blue. Although a red-shift of the observed energy transition has been seen [67], it is more common and simpler to blue-shift the material's band edge. Band-edge shift must be implemented selectively across the chip in single growth monolithic integration in order to distinguish between active and passive regions. There are several ways to put QWI into practice. Among them is the use of laser irradiation to achieve mixing by photoabsorption-induced disordering (PAID) [68].

Other techniques, like the implant-enhanced interdiffusion technique, demand the pricey insertion of ions [69]. For this procedure, a sacrificial InP layer is developed on top of the structure to safeguard the epitaxy surface during the implantation, and it is afterwards removed. By combining the device with a sacrificial cap layer when it is only partly grown, one can further improve the spatial resolution of the intermixing. The capping layers are then grown once this sacrificial layer has been removed [70]. As a result, this growth is not accomplished in a single step, further increasing the interdependence of the fabrication and growth facilities. The impurity free vacancy-enhanced disordering (IFVD) approach introduces vacancies post-growth, allowing them to flow across the lattice where adjacent atoms switch places, resulting in intermixing, during a subsequent heating phase commonly referred to as annealing. This is a desirable option since it avoids potential ion beam damage

and does not call for sacrificial layers. It has been shown to function on InP substrates with InGaAs cap layers [71] by adding a SiO_2 layer to encourage the out-diffusion of gallium, which results in the diffusion of vacancies during the annealling process.

SiO_2 is frequently utilised to encourage intermixing in quantum wells made of InGaAsP [72]. AlInGaAs-based quantum wells don't always exhibit the same behaviour, which could be explained by a distinct diffusion mechanism [73]. A SiN_x dielectric capping layer can be used to promote interdiffusion in AlInGaAs-based multiple quantum wells, according to recent work in the impurity-free vacancy technique [74–76]. Rapid thermal annealing (RTA) settings allow for the management of the intermixing's extent, and annealing at $700\,^{\circ}\mathrm{C}$ was seen to produce a photoluminescence (PL) wavelength blue shift as large as $110\,\mathrm{nm}$. However, when annealed with a SiO_2 capping layer under the same circumstances, the wavelength blue shift is constrained to less than $10\,\mathrm{nm}$. This technique is very easy to use and does not require expensive procedures like ion implantation, but more research is needed to reduce propagation loss, and it has not yet been successful in combining materials that contain carbon as a p-dopant, which is advantageous to EAM structures because it diffuses less than the commonly used p-dopant, zinc.

1.5 Project Outline

The aim of this project is to design a high speed, InP based, monolithically integrated externally modulated laser (EML) based on a single epitaxial growth. In order to construct this EML, two components are required, a single mode laser and an electro-absorption modulator (EAM).

In Chapter 2 we develop a basis for our material design principles, highlighting the physics and mathematics behind the emission and absorption in semiconductor materials.

For the ease of integration and in order to minimise the coupling losses between these two components a unique Multi-Quantum Well (MQW) epitaxy was designed for the fabrication of a monolithically integrated EML. The goal of this structure is to balance the MQW requirements of the laser, whose performance is optimal using a lower number of smaller quantum wells and the requirements of the EAM, whose performance is optimal using a higher number of wider quantum wells. The development of this material is explored

in Chapter 3.

The design of several single-mode tunable lasers were also simulated using both PICWAVE and self-made code based on transfer matrices in order to optimise laser design. For this aspect of the project, four main designs were researched; slotted Fabry Pérot lasers (SFPs), pitted Fabry Pérot lasers (PFPs), ring lasers, and snail lasers. The design, simulation and fabrication of these devices is detailed in Chapter 4. Redshifting was necessary for the laser design as the monolithic integration of the laser and the EAM onto the same material requires the laser emission to be sufficently redshifted so as to avoid the primary absorption peak of the EAM at $0\,\mathrm{V}$.

For the purposes of this project a high speed electro-absorption modulator was also developed. This included the creation of a specialised fabrication process. The design, optimisation, fabrication and characterisation of the lumped element electro-absorption modulator is detailed in Chapter 5. A significant focus is placed on the minimisation of the parasitic capacitance of the EAM electrical contact scheme so as to optimise the f_{3dB} of the lumped element EAM.

Finally, in Chapter 6, we combine our previous learnings, adopting the material designed in Chapter 3, the laser design principles developed in Chapter 4, and the high speed processing techniques and EAM designs created in Chapter 5.

Chapter 2

Background

2.1 The Principle of Laser Operation

The working principle of lasers is best understood by considering a hypothetical two-level atomic system and its interaction with EM waves. In this section, the interaction mechanisms and the conditions to be satisfied for the amplification of EM waves are described.

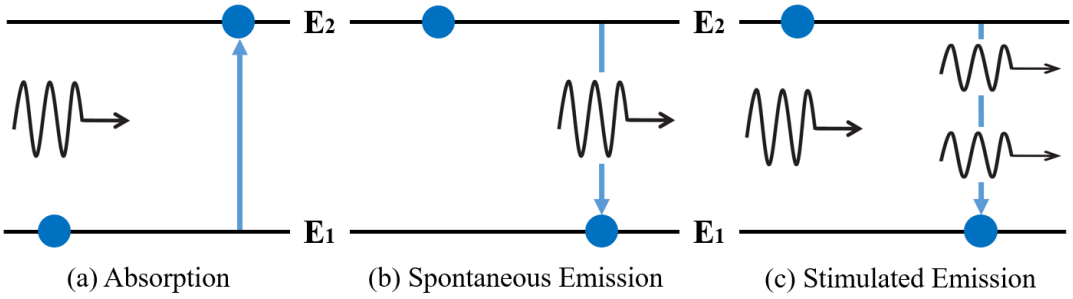

Figure 2.1: Three basic processes of interaction of radiation with a two-level atomic system: (a) absorption, (b) spontaneous emission, and (c) stimulated emission. In each of (a), (b), and (c), the left half represents the initial state of occupancy of a level, while the right half represents the state of occupancy after the process.

There are three basic processes through which EM radiation can interact with matter:

1. Spontaneous emission
2. Absorption
3. Stimulated Emission

These processes were first identified by Einstein in 1917. The processes are illustrated in Fig. 2.1 using a hypothetical atom having only two energy levels: E_1 (lower level) and E_2 (upper level). The respective population densities in these levels are N_1 and N_2. A collimated monochromatic beam of light with angular frequency $\omega = (E_2 - E_1)/\hbar$ may interact with the atoms in the following three ways.

2.1.1 Absorption

Under normal conditions, all materials absorb light. The absorption process is illustrated by Fig. 2.1(a), in which a photon of energy $\hbar\omega \geq (E_2 - E_1)$ is absorbed, transferring an electron from the lower level to the upper level. The left side of Fig. 2.1(a) represents the initial state of the atom, while the right side depicts the states after the transition. The intensity of the incident light is attenuated due to absorption, but the direction of propagation and polarisation of light remains unaltered. The rate of absorption is given by

$$\frac{dN_1(t)}{dt} = -B_{12}N_1\rho(\omega) = -\frac{dN_2(t)}{dt} \tag{2.1}$$

where:

- B_{12} is the Einstein B-coefficient for absorption
- ρ is the energy density of the incident photon flux
- N_1 and N_2 are the populations of 1, the lower band, and 2, the upper band, respectively

2.1.2 Spontaneous Emission

In this process, as shown in Fig. 2.1(b), an atom from the upper level jumps down spontaneously to the lower level, and a photon of energy $\hbar\omega = E_2 - E_1$ is emitted. The direction of propagation and polarisation of the emitted radiation is arbitrary. The corresponding rate equation is

$$\frac{dN_1(t)}{dt} = A_{21}N_2(t) = -\frac{dN_2(t)}{dt} \tag{2.2}$$

where A_{21} is called the Einstein A-coefficient and is related to the spontaneous emission lifetime by $\tau = (A_{21})^{-1}$.

2.1.3 Stimulated Emission

In this case, as illustrated in Fig. 2.1(c), the incident photon induces the atom to make a downward transition from the upper to the lower level. The energy is released in the form of a photon, which has the same frequency, phase, polarisation, and direction of propagation as the incident photon stimulating the transition. The corresponding rate equation is

$$\frac{dN_2(t)}{dt} = -B_{21}N_2(t)\rho(\omega) = -\frac{dN_1(t)}{dt} \tag{2.3}$$

where B_{21} is the Einstein B-coefficient for stimulated emission.

2.2 Absorption and Emission Rates

We may write the rates of spontaneous emission, stimulated emission, and absorption from Eqns 2.1 through 2.3 as

$$R_{spon} = A_{21}N_2 \qquad R_{stim} = B_{21}N_2\rho(\omega) \qquad R_{abs} = B_{12}N_1\rho(\omega) \tag{2.4}$$

In thermal equilibrium, atomic densities obey Boltzmann statistics, and accordingly

$$\frac{N_2}{N_1} = exp\left[-\left(\frac{E_2 - E_1}{k_BT}\right)\right] = exp\left(\frac{-\hbar\omega}{k_BT}\right) \tag{2.5}$$

where:

- k_B is the Boltzmann constant
- T is the absolute temperature

Under steady state, the rates for upward and downward transitions should be equal, leading to

$$A_{21}N_2 + B_{21}N_2\rho(\omega) = B_{12}N_1\rho(\omega) \tag{2.6}$$

Using Eqns 2.5 and 2.6

$$\begin{aligned}\rho(\omega) &= \frac{A_{21}N_2}{B_{12}N_1 - B_{21}N_2} \\ &= \frac{N_2}{N_1}\left[\frac{A_{21}}{B_{12} - B_{21}\frac{N_2}{N_1}}\right] \\ &= \frac{A_{21}}{B_{21}}\frac{1}{(B_{12}/B_{21})\exp(\hbar\omega/k_BT) - 1}\end{aligned} \tag{2.7}$$

In thermal equilibrium, the radiation spectral density must be identical with that for blackbody radiation, given by the Planck formula

$$\rho_{BB}(\omega) = \frac{2\hbar\omega^3}{\pi c^3}\frac{1}{\exp(\hbar\omega/k_BT) - 1} \tag{2.8}$$

With this comparison in mind we can determine that

$$A_{21} = B_{21}\frac{2\hbar\omega^3}{\pi c^3} \qquad and \qquad B_{12} = B_{21} \tag{2.9}$$

The ratio of stimulated to spontaneous emission rates is therefore

$$\frac{R_{stim}}{R_{spon}} = \left[\exp\left(\frac{\hbar\omega}{k_BT}\right) - 1\right]^{-1} \tag{2.10}$$

So for the telecommunications wavelengths used in this project, $\hbar\omega_{1550nm} \approx 0.8\,eV$ and $\hbar\omega_{1310nm} = 0.9464\,eV$ and at room temperature $k_BT = 25.7\,meV$. This results in a ratio from Eqn 2.10 of $1.27 \cdot 10^{-14}$ for $1550\,\mathrm{nm}$ and $3.6 \cdot 10^{-17}$ for $1310\,\mathrm{nm}$. These calculations show that for the wavelengths of interest for this project, spontaneous emission dominates over stimulated emission at room temperature.

Eqns 2.4 and 2.10 also shows that unless $N_2 >> N_1$ the rate of absorption will dominate that of stimulated emission. Thus in order to achieve lasing we require the system to operate away from thermal equilibrium in a condition referred to as population inversion. This is necessary for the operation of a laser.

It is worth noting that the discussion here assumed that the energy levels

noted here are sharp and exact. However, in reality, the energy levels are broadened due to a delayed phase caused by instantaneous changes in the field intensity which require relaxation oscillations to correct. The emitted radiation is no longer a singular wavelength but instead has a linewidth with a lineshape function, $L(\omega)$, whose shape may be Gaussian, Lorentzian, or a mixture of the two. The total number of stimulated emissions per unit volume considering this lineshape function may then be written as

$$W_{21} = N_2 \int B_{21}\rho(\omega)L(\omega)d\omega = N_2 \frac{\pi^2 c^3}{\hbar\tau_{sp} n_r^3} \int \frac{\rho(\omega)}{\omega^3} L(\omega)d\omega \tag{2.11}$$

2.2.1 Absorption and Amplification of Light in a Medium

Now we consider the propagation of this stimulated emission in a medium as shown in Fig 2.2 in which there are only two available energy levels as we have previously assumed. Here we have chosen z as the direction of propagation of the beam. For this we have two planes, P_1 and P_2 each with area, S which is perpendicular to the direction of the beam. P_2 is located at a distance of dz from P_1. Therefore we can write the number of stimulated emissions per unit time through this volume element Sdz is $W_{21}Sdz$ with each photon having energy $\hbar\omega$, thus the energy per unit time through the volume element is $\hbar\omega W_{21}Sdz$.

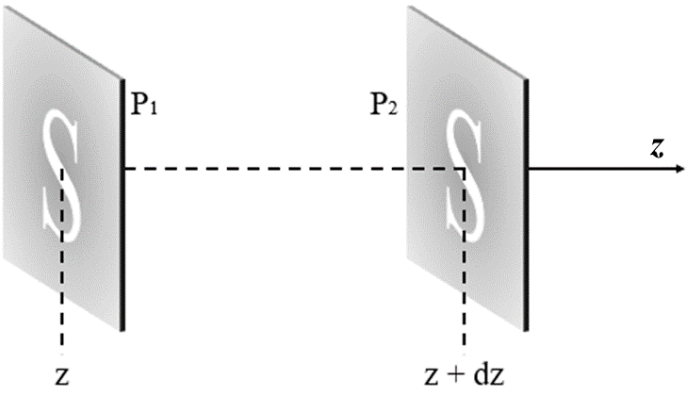

Figure 2.2: Propagation of radiation along the z direction

The intensity of light at P_1 and P_2 is $I_\omega(z)$ and $I_\omega(z+dz)$ respectively. Therefore the total energy exiting the volume Sdz is

$$\left[I_\omega(z+dz) - I_\omega(z)\right] S = \frac{\partial I_\omega}{\partial z} Sdz \tag{2.12}$$

Combining Eqn 2.12 with the energy relation described above we can describe the net energy per unit time from the volume element as

$$\frac{\partial I_\omega}{\partial z} S dz = -(W_{12} - W_{21})\hbar\omega S dz \tag{2.13}$$

So now using Eqn 2.11 to rewrite both W_{12} and W_{21} and considering a small frequency interval $d\omega$ we then have

$$\begin{aligned} \frac{\partial I_\omega}{\partial z} &= -(N_1 - N_2)\frac{\pi^2 c^3}{\tau_{sp} n_r^3} \int \frac{\rho(\omega) L(\omega)}{\omega^2} d\omega \\ &= -(N_1 - N_2)\frac{\pi^2 c^3 \rho(\omega) L(\omega)}{\tau_{sp} n_r^3 \omega^2} \end{aligned} \tag{2.14}$$

The energy density of light and the intensity of said light can be related by $I_\omega = (c/n_r)\rho(\omega)$ where c is the speed of light and n_r is he refractive index of the medium in question.

$$\frac{\partial I_\omega}{\partial z} = -(N_1 - N_2)\frac{\pi^2 c^2 L(\omega)}{\tau_{sp} n_r^2 \omega^2} I_\omega = -\alpha_\omega I_\omega \tag{2.15}$$

The derivative of this equation resulting in the equation reappearing recursively i.e $(\delta I_\omega / \delta z) \propto I_\omega$ implies that I_ω is an exponential function. Integrating Eqn 2.15 with the assumption the the population states N_1 and N_2 are independent of the intensity results in the expression

$$I_\omega(z) = I_\omega(0)\exp(-\alpha_\omega z) \tag{2.16}$$

where:

- $I_\omega(0)$ is the intensity at the surface of the medium
- α_ω is the absorption coefficient of the medium at the angular frequency ω

Without the population inversion previously mentioned $N_1 > N_2$, and thus there is always absorption of light travelling in the medium. However, looking at the definition presented for α_ω, we see that in the case that $N_2 > N_1$, the emission will be amplified rather than absorbed, allowing the stimulated emission to exceed the rate of absorption.

2.3 Fabry-Pérot Cavities

Up to this point we have covered one element of a classic Fabry-Pérot (FP) laser, a gain medium. However this alone is not enough to create a laser. In order to create a sustained oscillation we need a method of creating feedback. Fig. 2.3 shows an example of a FP laser wherein the reflective feedback is provided by a back mirror with 100% reflectively and a front mirror with 90% reflectively.

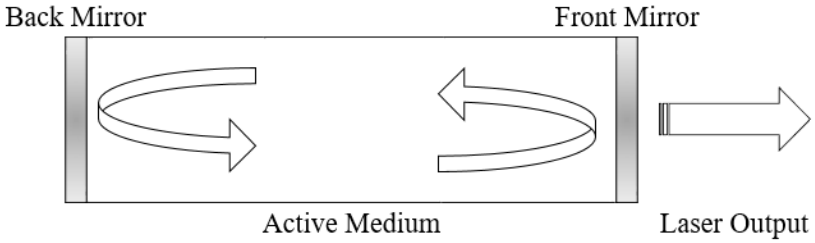

Figure 2.3: Fabry-Pérot Resonator consisting of a gain medium between two reflectors

These parallel mirrors form a resonant cavity which supports a selection of modes which satisfy a standing wave condition dependant on the length of the resonant cavity, L. These mirrors may be planar or curved. In theory the resonant modes of this cavity can span the entire EM spectrum however the gain medium in which resonance occurs has a well defined range of operation wherein positive gain is achieved. We consider the gain medium to have a gain coefficient, g, and an absorption coefficient, α. The reflectivity of mirrors forming the cavity can be denoted as R_1 and R_2 for the back and front respectively. With this in mind, we can write the intensity after one round trip of the cavity as,

$$I(2L) = I_0 R_1 R_2 \exp\left[(g - \alpha)2L\right] \tag{2.17}$$

When $g > \alpha$ amplification occurs. The oscillation is considered self sustained if $I(2L) = I_0$, and the minimum gain required for this is denoted as the threshold gain, g_{th}, which can be found through rearranging Eqn 2.17.

$$\begin{aligned} g_{th} &= \alpha + \frac{1}{2L} \ln\left(\frac{1}{R_1 R_2}\right) \\ &= \alpha_i + \alpha_m \end{aligned} \tag{2.18}$$

Here we separate the absorption, α into two parts. The intrinsic absorption, α_i and the mirror absorption, $\alpha_m = \frac{1}{2L} \ln\left(\frac{1}{R_1 R_2}\right)$.

2.3.1 Non-Linear Gain in Quantum Well Structures

It is important to design the laser structure to maximise the laser efficiency. To maximise this, we desire the least amount of current for a given output power. An analytical expression for gain vs carrier density is required for this. This relationship is non-linear [77]. To connect gain to injected carrier density, some writers [78] have utilised the three-parameter logarithmic formula:

$$g = g_{0s} \ln\left(\frac{n + n_s}{n_{tr} + n_s}\right) \tag{2.19}$$

where:

- g_{0s} is an empirical gain coefficient
- n_{tr} is the transparency carrier density
- n_s is the parameter used to make $\ln$ finite at $n = 0$ so that the gain will equal the absorption

Eqn 2.19 can then be further simplified as

$$g = g_0 \ln\left(\frac{n}{n_{tr}}\right) \qquad (g \geq 0) \tag{2.20}$$

Now we can rewrite our equation in terms of the threshold carrier density, n_{th} which occurs at the threshold gain, g_{th} as defined in Eqn 2.18.

$$\begin{aligned} n_{th} &= n_{tr} \exp \frac{g_{th}}{g_0} \\ &= n_{tr} \exp\left(\frac{\alpha_i + \alpha_m}{\Gamma g_0}\right) \end{aligned} \tag{2.21}$$

where Γ is the modal confinement factor. The modal confinement factor is the fraction of power of the mode which is confined within the active area of our material [79].

The threshold carrier density can then be related back to the threshold current via,

$$\frac{\eta_i I_{th}}{eV} = \frac{n_{th}}{\tau_r} = R_{sp} + R_{nr} + R_l = An + Bn^2 + Cn^3 \tag{2.22}$$

where τ_r is the total recombination time and η_i is the internal quantum efficiency. R_{nr} and A represents non-radiative recombination. R_{sp} and B represent spontaneous emission. R_l and C represent the leakage.

In general laser materials, at threshold the spontaneous emission is the dominant process and thus we can simplify the threshold current as $I_{th} \approx Bn_{th}^2 eV/\eta_i$ and rewrite Eqn 2.22 as

$$I_{th} \approx \frac{eVBn_{tr}^2}{\eta_i} \exp\left(\frac{2(\alpha_i + \alpha_m)}{\Gamma g_0}\right) \tag{2.23}$$

The above equation represents a singular quantum well. The addition of multiple quantum wells (MQWs) leads to an increase in the mode confinement factor by N_w, the number of quantum wells. The threshold current is now modified by multiplying both the volume and the confinement factor by N_w,

$$I_{th} \approx \frac{eN_w V_1 Bn_{tr}^2}{\eta_i} \exp\left(\frac{2(\alpha_i + \alpha_m)}{N_w \Gamma_1 g_0}\right) \tag{2.24}$$

The threshold current of a laser often serves as a benchmark for laser performance. By plotting the threshold current as a function of the number of quantum wells, $I_{th}(N_w)$ we can observe the impact the number of wells has on laser performance. Fig. 2.4 shows this plot with values taken for an InGaAsP laser from Coldren & Corzine [80]. The change in threshold current has been calculated for laser emission dominated by spontaneous emission and laser regimes where both spontaneous emission and leakage factors into the threshold current. For most laser materials spontaneous emission alone is the dominating factor. It becomes necessary to take leakage into account when dealing with long wavelength emission however.

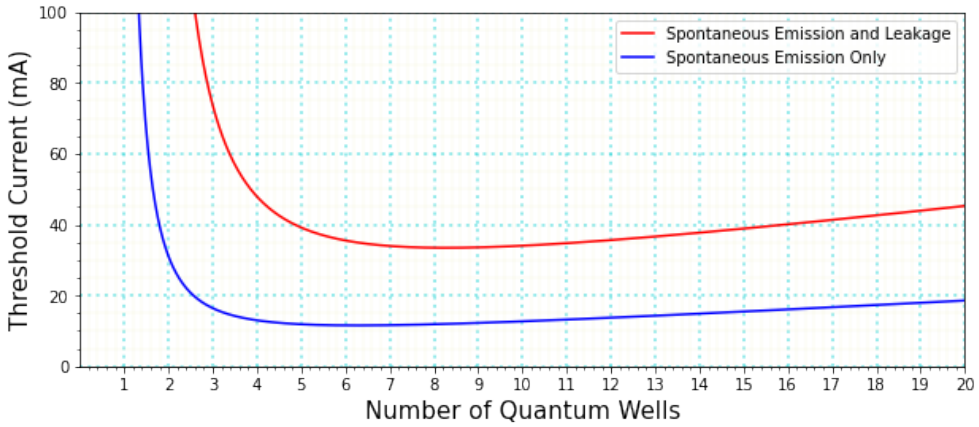

Figure 2.4: Quantum well number vs threshold current

Observation of the above figure shows that the equation possesses a minimum value, an optimum number of quantum wells for laser threshold where $\partial I_{th}/\partial N_w = 0$. Beyond this number of quantum wells, the threshold of the laser begins to degrade. This leads to the first major exploration of this project as we attempt to determine an suitable epitaxial structure which balances the quantum well requirements of a laser, as detailed in the equations above, and an electro-absorption modulator, whose needs we will now explore.

2.4 Absorption in Quantum Well Materials

Up to this point we have discussed how the increase in the number of quantum wells impacts the threshold performance of a laser; however the laser is only part of the desired product, the EML. For the modulator function we focus on the electro-absorption modulator, which, as its namesake dictates, relies on the absorption of incoming light in order to instigate on/off transmission. In the same way that our semiconductor material can create photons through the descent of an electron from the conduction band to the valence band, photons of an energy equal to or greater than the semiconductor band gap may also be absorbed. This process is shown in Fig. 2.1. The energy required to excite the electron from the valence band to the conduction band is known as the band gap energy, E_g.

As a result of this absorption, a positively charged hole appears in the valence band. A hole isn't a particle in and of itself, it's the location from which an electron was transported which has positive charge relative to the surrounding remaining electrons which were not promoted. There will be a Coulomb effect

between the electron and hole at low carrier densities and low temperatures, generating what is known as an exciton pair [81, 82].

In the absence of an external electric field, electrons and holes in a potential well can only occupy a finite set of energy states, allowing the potential well to absorb or emit only a discrete set of light frequencies. The electron states change to lower energies when an electric field is applied, while the hole states shift to higher energies. As a result, the quantum well's effective band-gap shrinks, causing the permissible absorbed and emitted frequencies to redshift. This process is shown in Fig. 2.5 which shows how the electrons and holes shift to opposing sides of the quantum well. This leads to a decrease in the overlap of the wavefunctions of the electrons and holes which leads to a decrease in recombination efficiency. This behaviour is known in QW materials as the Quantum Confined Stark Effect (QCSE) [83]

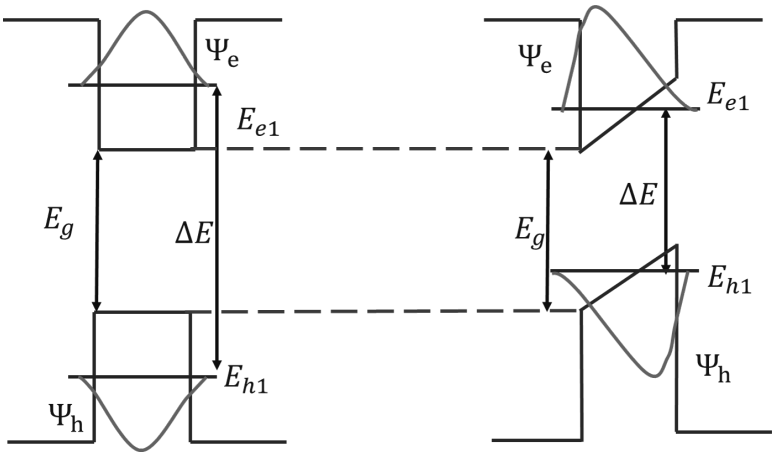

Figure 2.5: Schematic of the band line-up and confined states in a quantum well, with and without an electric field.

The QCSE is exclusive to quantum materials such as quantum wires, quantum dots, and quantum wells. A similar phenomenon appears in bulk semiconductors known as the Franz-Keldysh effect [84]. The spatial confinement of the electron and holes causes different electro-absorption effects in MQW materials compared to bulk semiconductors. Because of the spatial confinement, the Coulomb attraction between electrons and holes is substantially amplified. The excitons are more difficult to field-ionize because the electrons and holes take a long time to tunnel out of the quantum well. An exciton in a quantum well is confined in two dimensions and has energy,

$$E_{ex}^{2D} = -\frac{R_y}{\left(n-\frac{1}{2}\right)^2} = -\frac{m_r e^4}{2\hbar^2\left(4\pi\epsilon_g\right)\left(n-\frac{1}{2}\right)^2} \tag{2.25}$$

where R_y is known as the Rydberg energy [85].

The potential barrier in the quantum well confines the electrons and holes to discrete sets of energies which depend on the width and depth of the well. The electrons and holes are represented by wave-functions which describes the probability of the carrier being in a particular location. When a electron from the valence band is promoted to the conduction band, the minimum energy required is the bandgap energy, E_g, but as the energy levels in the conduction band which the promoted electron can occupy is discrete then the energies required for an electron to be promoted must also be discrete. Thus we denote the conduction band energies, E_c^n, where n is a natural number. E_c^1 is the ground state energy of the conduction band. The same rhetoric is true for the wavefunction states in the valence band.

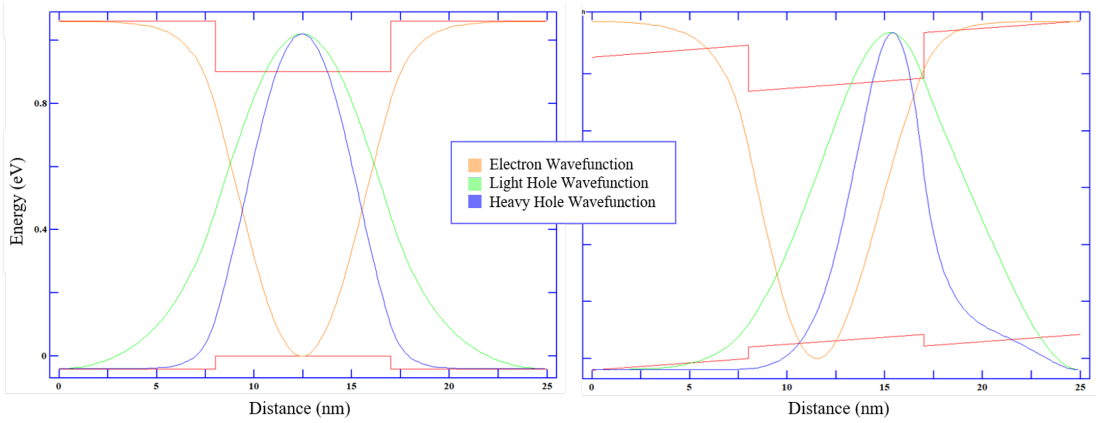

Figure 2.6: Simulation of a quantum well with barrier bandgap at $1.1\,\mathrm{eV}$ and the well bandgap at $0.9\,\mathrm{eV}$. On the left the electric field is $0\,\mathrm{kV/cm}$. On the right the field has been increased to $50\,\mathrm{kV/cm}$. The wavefunctions are noted to shift, decreasing the overlap between the wavefunction of the electron in the conduction band and the wavefunctions of the light and heavy holes in the valence band.

The photon energy required to create an electron hole pair for both the electron and hole in the ground state (E_c^1 and E_v^1 respectively) can therefore

be written as,

$$E_{cv}^{1}(\overrightarrow{F}) = E_g + E_c^{1}(\overrightarrow{F}) - E_v^{1}(\overrightarrow{F}) \tag{2.26}$$

where F represents the wavefunctions' dependence on the electric field applied as shown in Fig. 2.5.

The amount of light absorbed in a MQW material will be determined by a number of factors. The output power of a device of length L with a quantum interband absorption coefficient $\alpha(\lambda, F)$ in an electric field, F can be denoted as,

$$P(\lambda, F, L) = P_0 \exp\left(-\Gamma L(\alpha_0 + \alpha(\lambda, F))\right) \tag{2.27}$$

In MQW material, the absorption we are focusing happens within the quantum wells and thus we can define Γ as,

$$\Gamma = \frac{\iint_{MQW} |E_{WG}|^2 dxdy}{\iint_{WG} |E_{WG}|^2 dxdy} \tag{2.28}$$

Γ, physically, is the percentage of the propagating optical mode that interacts with the active absorbing region. The modulator will be cycled between two states in a standard on-off key modulation regime, allowing two distinct optical powers to pass through. The "on" state is one in which the maximum amount of light travels through the device, whereas the "off" state is one in which the bias has been applied and the light has been absorbed to reduce the power through the EAM. Changing the EAM's status from on to off is accomplished by switching the electric field from F_{on} to F_{off}. The extinction ratio of a modulator is defined as the ratio of optical power in its on (P_{on}) and off (P_{off}) states. It is generally stated on a dB scale.

$$ER = -10\log_{10}\left(\frac{P_{off}}{P_{on}}\right) = \frac{10}{\ln(10)}\Gamma L(\alpha_{off} - \alpha_{on}) \tag{2.29}$$

The insertion loss, η_{ins}, is the loss incurred by the modulator when it is turned on, when the electric field is not supplied. It is the loss due to absorption and other loss mechanisms in the case of the electro-absorption modulator.

$$\eta_{ins} = 10 \log_{10} \frac{P_{on}}{P_0} = \Gamma \alpha_{on} L \frac{10}{\ln(10)} \tag{2.30}$$

While the extinction ratio is an important modulator specification, its reliance on length makes it impossible to utilize as a fair figure of merit when considering different EAM materials. An increase or decrease in length directly increases or decreases the insertion loss proportionally. The extinction ratio and insertion loss ratio can be simplified to be independent of length however, which can be seen by combining Eqn 2.29 and Eqn 2.30

$$\begin{aligned} \frac{ER}{\eta_{ins}} &= \frac{10}{\ln(10)} \Gamma L (\alpha_{off} - \alpha_{on}) \cdot \left[\Gamma \alpha_{on} L \frac{10}{\ln(10)} \right]^{-1} \\ &= \frac{\alpha_{off} - \alpha_{on}}{\alpha_{on}} \end{aligned} \tag{2.31}$$

2.5 Quantum Well Offsetting

In terms of electrical behaviour, a reverse-biased lumped Electro-Absorption Modulator (EAM) can be characterised as a differential resistance (R_j) and a junction capacitance (C), which has an associated response time, $\tau_{RC} = RC$, where R is the impedance of the transmitter. From a materials perspective, the p-i-n structure of the EAM is similar to a parallel plate capacitor, where the capacitance (C) is determined by the permittivity of the material (ϵ), as well as the area overlap of the p- and n-doped regions (A) and the distance between them (d). By controlling the thickness of the intrinsic region, the distance (d) can be altered, which can affect the effective thickness and hence the capacitance (C).

$$C = \frac{\epsilon A}{d} \tag{2.32}$$

While the small signal bandwidth of the EAM is not dependent on the transit

time (τ_t) of the carriers due to the Quantum Confined Stark Effect (QCSE) being dependent on the electric field and not the carriers, the transit time can influence the dynamic extinction ratio and power handling capability of the device. This implies that the carrier transit time provides a limitation on the bandwidth of our device as we approach higher frequencies. Faster removal of the photogenerated carriers from the intrinsic region can reduce their impact on the electric field and minimise perturbations in the QCSE due to screening. Assuming negligible effects from electrical parasitics of the RF contacts and packaging, the EAM's $3\,\mathrm{dB}$ frequency (bandwidth) due to the capacitance can be calculated as

$$f_{RC} = \frac{1}{2\pi\tau_{RC}} \tag{2.33}$$

Thus the bandwidth of a photodiode can be denoted as

$$\frac{1}{f_{PD}^2} = \frac{1}{f_{RC}^2} + \frac{1}{f_t^2} \tag{2.34}$$

Where f_t represents the frequency limitation of the transit time of the carriers as described in [86] such that

$$f_t = \frac{0.55}{\tau_t} \tag{2.35}$$

In the context of discussing additional components that can be integrated into a photonic integrated circuit (PIC), high-speed photodetectors are an important consideration. These are essential for converting optical energy into electrical signals, which is required for optical measurement and transmission systems. Unlike EAMs, the performance of photodetectors is dependent on their ability to convert light into photocarriers and then extract those carriers, generating a photocurrent. Consequently, the bandwidth of the photodetector is determined by the transit time of the carriers (τ_t), and more specifically, the heavy holes due to their lower mobility. The bandwidth also depends on the electrical RC time of the device (τ_{RC}). Assuming τ_{RC} and τ_t are independent of each other, the total response time can be expressed as:

$$\tau = \sqrt{\tau_{RC}^2 + \frac{\tau_t^2}{11.942}} \tag{2.36}$$

The transit time of the photocarriers creates a ceiling for the maximum bandwidth of our modulation system. In order to optimise the material for single growth monolithic integration, it is necessary to minimise the sweep out time (τ_t) to enhance the power handling ability of the EAM and increase the bandwidth of monolithically integrated photodetectors. However, the mobilities of the carriers are limited by the alloys used to form the MQW and intrinsic regions, meaning that the respective drift velocities of the corresponding layers are fixed. Therefore, the most straightforward way to reduce the transit time is to reduce the intrinsic region thickness by doping closer to the MQW region, which shortens the distance that carriers need to travel before recombination. The MQW region still needs to remain intrinsic to preserve exciton absorption enhancement by eliminating ionisation through dopant diffusion. However, if the structure is treated as a parallel plate capacitor, decreasing the intrinsic thickness will increase the capacitance of the device, thereby increasing τ_{RC}.

The transit time τ_t is limited by the slowest carrier, which is generally the heavy hole due to its higher effective mass and lower mobility. By offsetting the MQW region within the intrinsic region, it is possible to compensate for the lower drift velocity of heavy holes while preserving the intrinsic region thickness so as not to influence the capacitance of the device.

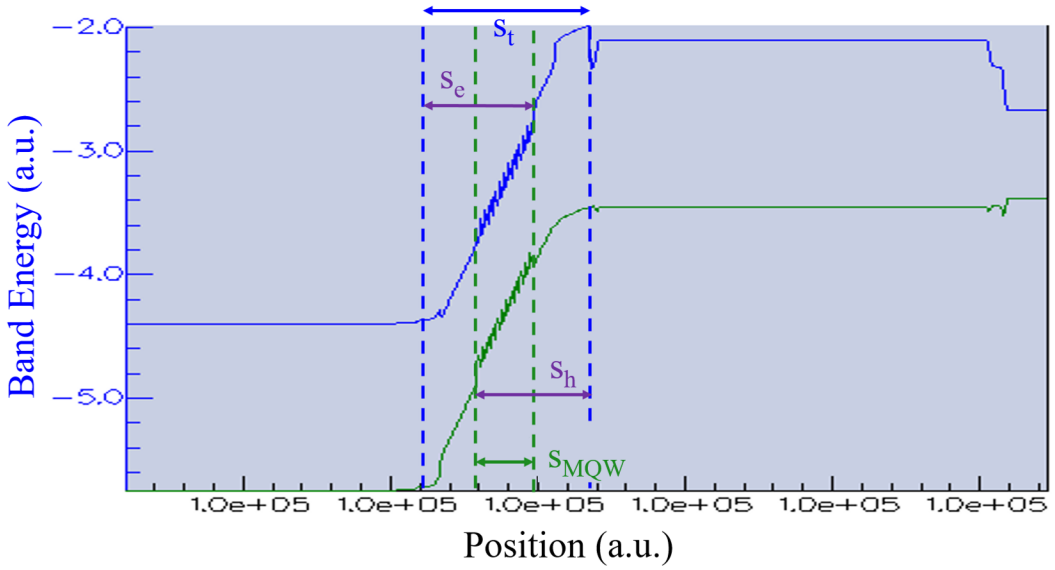

Figure 2.7: A MQW material highlighting the intrinsic transit distance, s_t, the MQW transit distance, s_{MQW}, and the distances the holes and electrons must travel, s_h and s_e respectively.

The distances can be defined as follows: s_e and s_h are the maximum distances that a photo-generated electron or hole, respectively, must travel, s_{MQW} is the thickness of the MQW region, and s_t is the overall thickness of the intrinsic region. These distances ae shown in Fig.2.7. The electron and the hole must each traverse a part of the intrinsic region and then across the length of the MQW region. Thus, these distances are related to each other by

$$s_t + s_{MQW} = s_e + s_h \tag{2.37}$$

Such is to say, the distance travelled by the electrons and holes is the length of the instrinsic region with an overlap in the MQW region. We can thus relate the transit time, τ_t, the distances, s, and the drift velocity, ν as

$$\tau_{t,i} = \frac{s_i}{\nu_i} = \frac{s_i}{\mu_i F} \tag{2.38}$$

where the transit occurs in a field, F, and the particle, i, in question has mobility, μ_i. The resultant intrinsic distance is the longest distance a photo-generated carrier must travel to exit the intrinsic region.

We can therefore introduce a spatial offset, γ_{off}, into the positioning of the MQW region to compensate for the varying transit times of the electron and heavy hole in order equalise the two transit times.

$$\gamma_{off} = \frac{s_e}{s_h} = \frac{\nu_e}{\nu_h} \tag{2.39}$$

The offset of the MQW region within the intrinsic region is determined by the ratio of the electron and heavy hole drift velocities. However, the drift velocity saturates at a large electric field required for the QCSE, which is not directly proportional to the electric field. Carrier pile up can also increase the overall transit time due to a localised reduction of the electric field. In this section, it is assumed that the electric field is strong enough to ensure that the carriers travel at their saturation drift velocity, although in reality, the electric field decays across the intrinsic region due to background doping.

We can now rewrite Eqn. 2.36 in terms of the response time and transit distance determined by the limiting carrier.

$$\tau = \sqrt{\left(\frac{R\epsilon A}{s_t}\right)^2 + \left(\frac{s_i}{\nu_i}\right)^2 \frac{1}{11.942}} \tag{2.40}$$

The offset of the multiple quantum well region within the intrinsic region can be defined using the ratio γ_{off}, s_h, and s_e. Therefore, the hole transit distance in the intrinsic region can be expressed in terms of s_t

$$s_h = \frac{s_t + s_{MQW}}{1 + \gamma_{off}} \tag{2.41}$$

The multiple quantum well region can be offset up to the point where it begins to enter the p-doped region. However, it is important to keep the MQW region intrinsic in order to maintain exciton absorption enhancement and preserve the electric field. Therefore, the offset is limited to a point where the hole transit time is equal to the time required to escape from the MQW region. At this point, the hole transit distance is equal to the thickness of the MQW region, $s_h = s_{MQW}$. This limits the value of γ_{off} to a maximum of s_t/s_{MQW}. Using Eqn. 2.41, the constrained hole transit time can be approximated as

$$\tau_{t,h} = \begin{cases} \frac{s_t + s_{MQW}}{(1+\gamma_{off})\nu_h} & \gamma_{off} < \frac{s_t}{s_{MQW}} \\ \frac{s_{MQW}}{\nu_h} & \gamma_{off} = \frac{s_t}{s_{MQW}} \end{cases} \tag{2.42}$$

When the offset is fixed according to the constraint on γ_{off}, two regimes are formed for $\gamma_{off} > 1$ as the intrinsic thickness is increased. When $s_t = s_{MQW}$ and $s_e = s_h$, increasing s_t will cause the transit time to be limited by the hole transit time according to the second condition of Eqn. 2.42. If s_t is sufficiently large so that the first condition is met, the hole transit distance will be given by Eqn. 2.41. If γ_{off} is greater than the condition given by Eqn. 2.39, but s_t is large enough such that

$$s_t > \frac{\nu_e s_{MQW}}{\nu_h} \tag{2.43}$$

then γ_{off} is greater than the condition given by Eqn. 2.39 but the intrinsic thickness s_t is large enough such that the constraint in Eqn. 2.42 is not met, then the system will be limited by the electron transit time since the MQW region has been offset too much. However, once s_t is sufficiently large such that the system can be under or over compensated while still meeting the first

condition of Eqn. 2.42, then the limiting carrier will be determined by the offset. The limiting transit time τ_t can then be approximated as

$$\tau_t = \begin{cases} \frac{s_t + s_{MQW}}{(1+\gamma_{off})\nu_h} & \gamma_{off} \leq \frac{\nu_e}{\nu_h} \\ \frac{\gamma_{off}(s_t + s_{MQW})}{(1+\gamma_{off})\nu_e} & \gamma_{off} > \frac{\nu_e}{\nu_h} \end{cases} \tag{2.44}$$

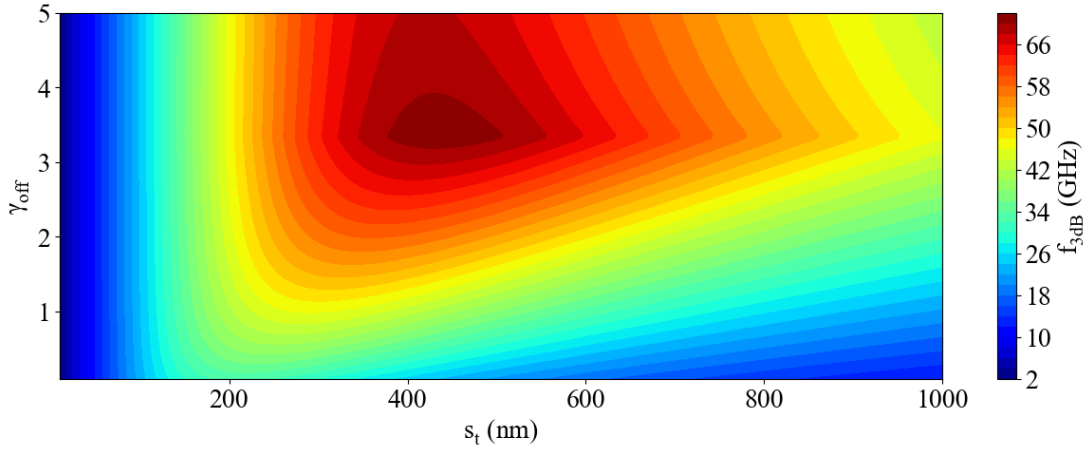

Figure 2.8: Eqn. 2.44 with varying γ_{off} and s_t for an EAM with $l = 50\mu m$, $w = 2.5\mu m$, and $s_{mqw} = 150nm$

Fig. 2.8 shows how the change in γ_{off} can rapidly change the bandwidth of the device. For small $s_t < 150nm$ there is no change caused by changing γ_{off}. This is due to γ_{off} being RC limited, still being dictated by Eqn. 2.40.

The optimal offset according to Eqn. 2.39 can be written as

$$\tau_t = \frac{s_t + s_{MQW}}{\nu_h + \nu_e} \tag{2.45}$$

Thus rewriting Eqn. 2.40 with this relationship we get

$$\tau = \sqrt{\left(\frac{R\epsilon A}{s_t}\right)^2 + \left(\frac{s_t + s_{MQW}}{\nu_h + \nu_e}\right)^2 \frac{1}{11.942}} \tag{2.46}$$

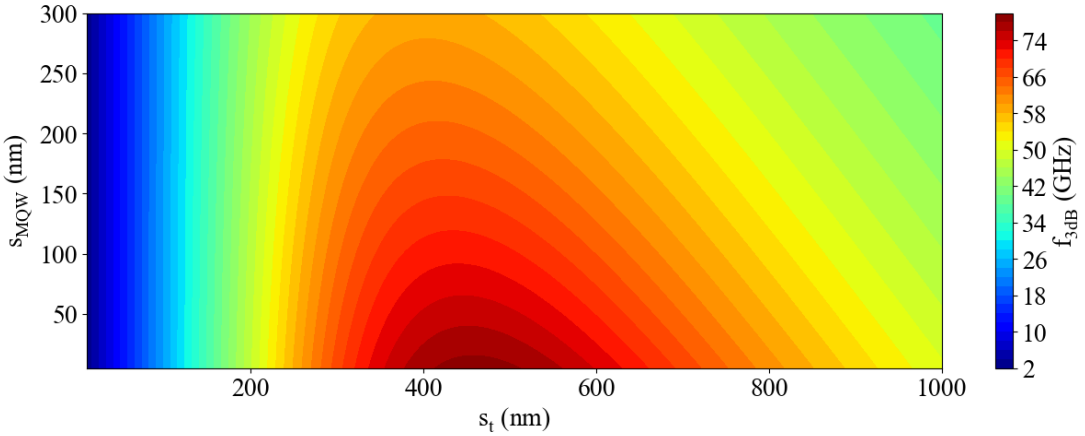

Figure 2.9: Eqn. 2.46 with varying s_{mqw} and s_t in an optimal γ_{off} configuration.

Fig. 2.9 shows how for the optimal configuration of γ_{off} there exists an optimal ratio between s_{mqw} and s_t which can also heavily influence the bandwidth of the device. In summary, the epitaxy must be carefully considered in order to prevent the bandwidth of our devices from becoming limited by the carrier transit times rather than the RC circuit limitations of the lumped element EAM.

Chapter 3

Epitaxial Refinement

As discussed in the previous chapter, the largest challenge in designing and making a monolithically integrated electro-absorption modulated laser stems from the fact that the quantum well requirements of a laser and an EAM are fundamentally antithetical to each other. A laser has a lower optimum number of quantum wells as shown in Fig.2.4 whereas an EAM benefits from an increased number of quantum wells in order to increase the level of absorption. To overcome this, we sought to create a material which balanced the requirements of both devices without sacrificing much functionality from either.

To this end, two simulation softwares were used, both part of the Photon Design™ package. Harold™ is a software used to simulate epitaxial structures with its own material database. PICwave™ is a software designed to simulate PIC components such as lasers, Mach–Zehnder modulators (MZMs) and waveguide couplers. Epitaxies designed in Harold can be imported into PICwave to simulate lasers based on the custom designed epitaxies.

3.1 Quantum Well Structure Effects on Lasers

To begin the simulation experiment we first began with importing a previously used custom designed EAM epitaxy which used 12 quantum wells each with a width of $9\,\mathrm{nm}$ as shown in Fig.3.1. This involved recreating the epitaxy using materials which were available from Harold's material database.

Layer	Mutlpl.	Material	Composition	Wavelength	Thickness	Doping	Notes
14		InGaAs	LM		120+30	1e19 CBr+Zn	
13		InGaAsP		1100	50	1.5e18 Zn	
12		InP	-	-	1340	1e18 Zn	Growth rate adjusted to match designed thickness
11		InGaAsP		1100	20	1e18 Zn	
10		AlInAs			60	1e17 to 1e18	
9		AlInAs		843	60	1e17 Zn	
8		AlInGaAs		968	79		
7	12x	AlInGaAs	CS:0.4	1033	7		Adjusted from A2927
6	12x	AlInGaAs	TS:0.42	1310	9		A2926
5		AlInGaAs	CS:0.4	1033	7		Adjusted from A2927
4		InGaAsP		1100	117		Growth interruption removed
3		InP	-	-	80	2e17 Si	
2		InP	-	-	70	5e17 Si	Growth rate adjusted to match designed thickness
1		InP	-	-	920	8e17 Si	
0	InP substrate (SI)						

Figure 3.1: Previously used custom EAM epitaxy

With the material recreated in Harold as shown in Fig.3.2, variations of the same material could be generated using the original material as a basis. The number of quantum wells was varied from 6-12 and the width of the quantum wells was varied from 7-9 nm. This resulted in the creation of 21 epitaxy design files.

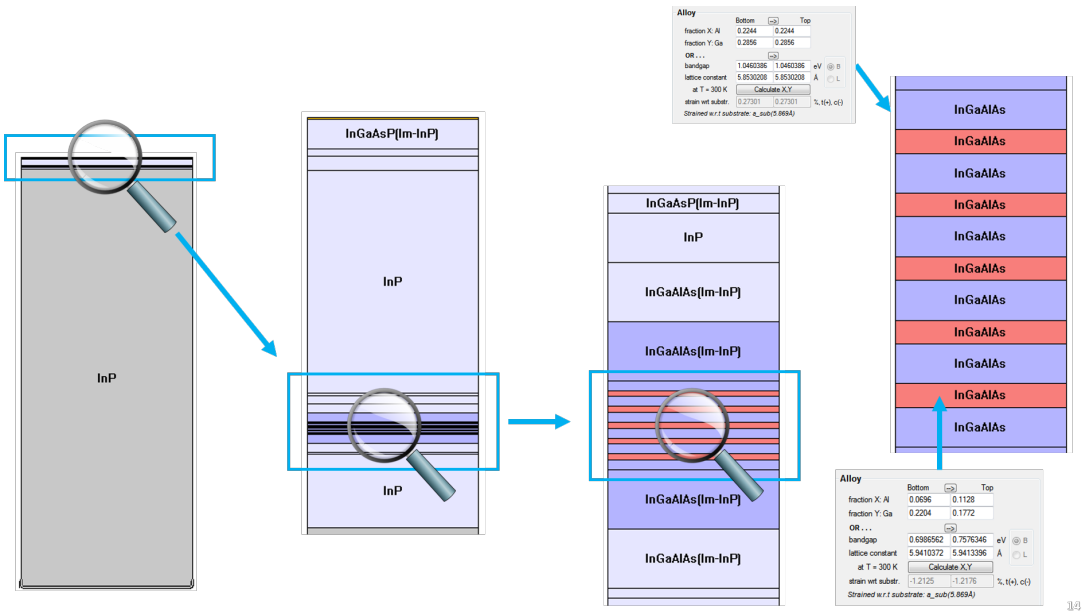

Figure 3.2: The Harold software was used to generate simulated epitaxies for QW laser structures with varying QW width and number

These epitaxy variations were imported into PICwave as shown in Fig.3.3. Within PICwave a simulated volume with a width of $7\,\mu\mathrm{m}$ and length $300\,\mu\mathrm{m}$ was generated. A waveguide was then defined with an artificial etch down to just above the quantum wells to form a $2.5\,\mu\mathrm{m}$ wide waveguide. The possible optical modes of this waveguide were then generated and a suitable confined mode was chosen as shown in Fig.3.3. With the waveguide and the mode defined, a FP etalon could be generated by adding two facets with 33% reflectivity to the ends of the waveguide. Monitors were placed on these facets to gauge the power and spectral output of the FP laser. With this setup in place the FP laser would receive a simulated supply of electrical current, and would begin to lase accordingly.

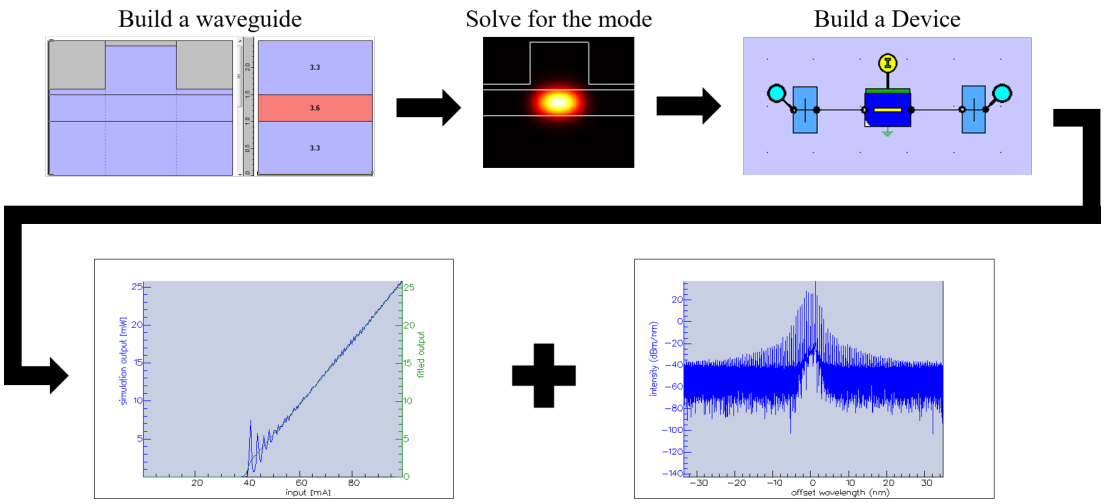

Figure 3.3: The FP lasers with varying epitaxies can then be analysed in terms of their slope efficiency; SE, and threshold current; I_{th}

With the method of how to create an FP laser based on an imported custom QW structure epitaxy, the threshold current (I_{th}) and the slope efficiency (SE) could be collected with varying quantum well width and number as shown in Table 3.1. The results of this investigation are shown in Fig.3.4. As seen in Fig.3.4(a) the increase in either the width or the number of the quantum wells leads to a linear increase in the threshold current of the laser. This aligns with Eqn.2.22 which tells us as that, the absorption in the cavity increases the threshold gain of the laser also linearly increases. This linear increase harshly increases the threshold current of the laser. A laser with 9 QWs with widths of $9\,\mathrm{nm}$ having more than double the threshold of an equivalent laser with 5 QWs with widths of $7\,\mathrm{nm}$.

The slope efficiency in Fig.3.4(b) shows a less linear behaviour. When the QW

width is $7\,\mathrm{nm}$ we can see that the slope efficiency of the laser begins to increase, reaching a maximal value at 6 quantum wells. This can be attributed to the gain of the laser increasing with additional quantum wells. Additional quantum wells degrade the laser's performance although it must be noted that the maximum difference in slope efficiency is only $0.05\,\mathrm{W/A}$

Table 3.1: Results extracted from simulated $300\,\mu\mathrm{m}$ FP laser with varying quantum well structure

QW Width (nm)	#QWs	I_{th} (mA)	dQE (W/A)	P@3*I_{th} (mW)
7	5	17.9886	0.296125	10.65374835
7	6	19.1602	0.324911	12.45071948
7	7	20.9141	0.318951	13.34114622
7	8	23.0243	0.313414	14.43227592
7	9	25.243	0.303491	15.32204663
7	10	27.4606	0.299771	16.46378305
7	11	29.732	0.294844	17.53260362
7	12	32.0751	0.291012	18.668478
8	5	19.3022	0.291973	11.27144248
8	6	20.7686	0.317764	13.19902682
8	7	23.0208	0.312288	14.37823918
8	8	25.4632	0.305741	15.57028846
8	9	28.1365	0.296806	16.70216404
8	10	30.7193	0.291836	17.92999527
8	11	33.3371	0.286622	19.11029255
8	12	35.991	0.281591	20.26948336
9	5	20.1841	0.32094	12.95577011
9	6	22.5572	0.313155	14.12779993
9	7	25.1427	0.305089	15.3415224
9	8	28.1537	0.294802	16.59953413
9	9	30.9935	0.289516	17.94622829
9	10	34.0483	0.283502	19.30552229
9	11	36.8872	0.279111	20.59124656
9	12	39.9528	0.274184	21.90883703

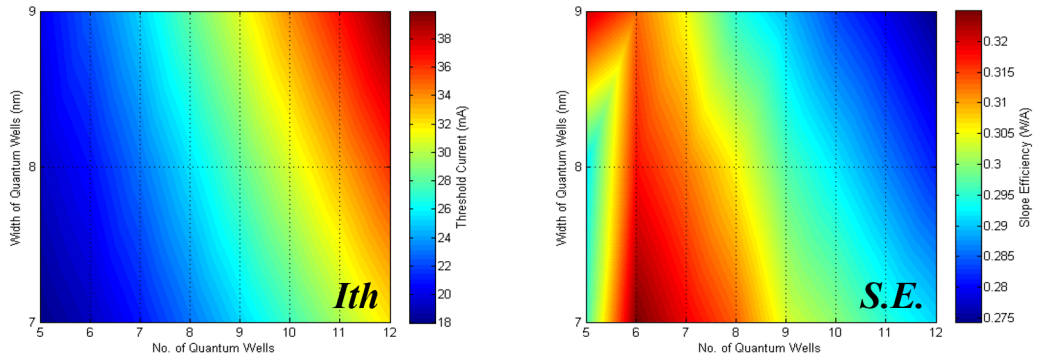

(a) Threshold current (I_{th}) of a $300\,\mu$m FP laser with varying QW structure

(b) Slope efficiency ($S.E.$) of a $300\,\mu$m FP laser with varying QW structure

Figure 3.4: Characteristics of a $300\,\mu$m FP laser with varying QW structure

3.2 Quantum Well Structure Effects on EAMs

3.2.1 Simulations using Harold-EAM Software

To create a balanced epitaxy which worked for both the laser and the EAM, the changing quantum well structure's effects on the EAM's performance was also investigated. The simulated epitaxy files created in Harold were also capable of being simulated as EAMs using Harold-EAM, as shown in Fig.3.5.

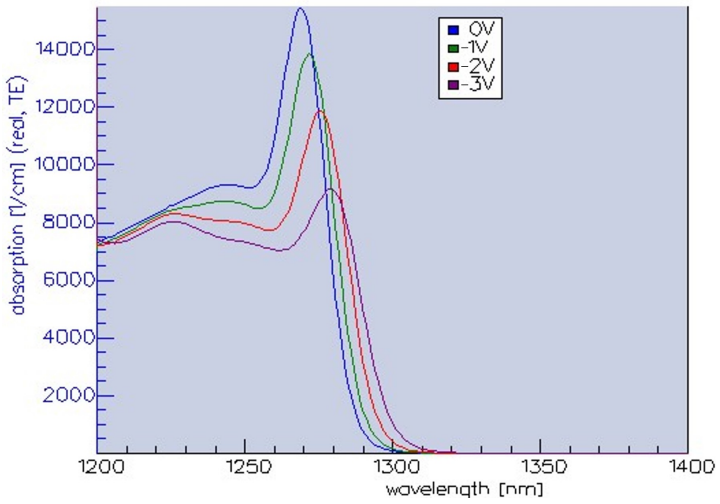

Figure 3.5: Simulated Harold absorption for an epitaxy with 6QW of width $7\,\mathrm{nm}$

This simulation works via a one-dimensional simulator which calculates the complex electrical permittivity and escape time of an epitaxial layer structure under a reverse bias. Harold-EAM consists of six solvers that run in sequence.

The Poisson solver, given the epitaxial layer structure, calculates the band edge spatial variation under a given bias. The result is then passed to a Schrödinger solver. This solver, given the band edges of the biased quantum well structure, calculates electron, light-hole and heavy-hole eigenvalues and eigenmodes. It takes into account the fact that in a biased structure the modes are quasi-confined, i.e. their eigenvalues are complex and their eigenmodes have radiating tails at the low-potential side of the biased structure.

The result is then passed to the exciton solver. Given the electron and hole eigenmodes, this solver calculates the energy levels of the exciton transition for each electron-hole pair. The result is finally passed to the electrical permittivity solver which, given the eigenvalues of the electrons and holes as well as the exciton transition energies, calculates the real and imaginary parts of the permittivity.

Using this the absorption of the varying quantum well structures designed could be compared in terms of EAM absorption per cm at an operating bias of $1\,\mathrm{V}$. The results of this calculation for a fixed quantum well number of 6 and varying quantum well width is shown in Fig.3.6. This result suggests that the optimum level of absorption of the quantum wells occurs at $9\,\mathrm{nm}$.

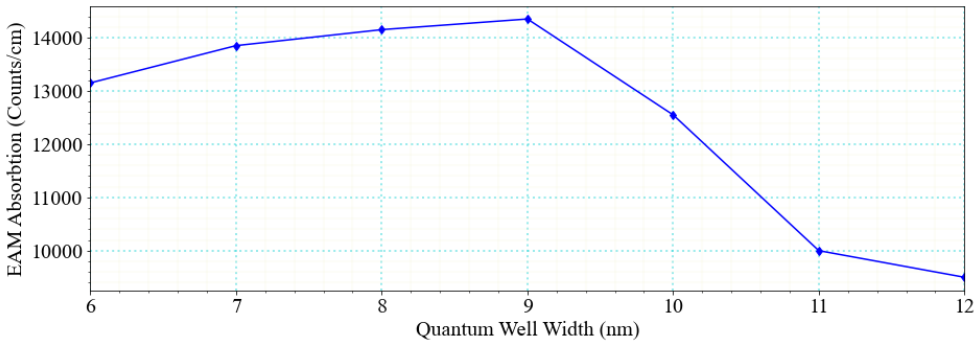

Figure 3.6: Simulated Harold EAM absorption for an epitaxy with 6QW of varying width

Using the results of Fig. 3.6 different EAMs were simulated with a varying number of quantum wells with width $9\,\mathrm{nm}$. The results of this simulated comparison are shown in Fig.3.7 and show a linear increase in the absorption as the number of quantum wells increases. This aligns with our description in Eqn.2.22 which stated that the modal confinement Γ scaled linearly with N quantum wells. In essence, this implies that any number of quantum wells are appropriate as any decrease in quantum well number can be compensated for by increasing the length of the EAM, resulting in the same overall effect.

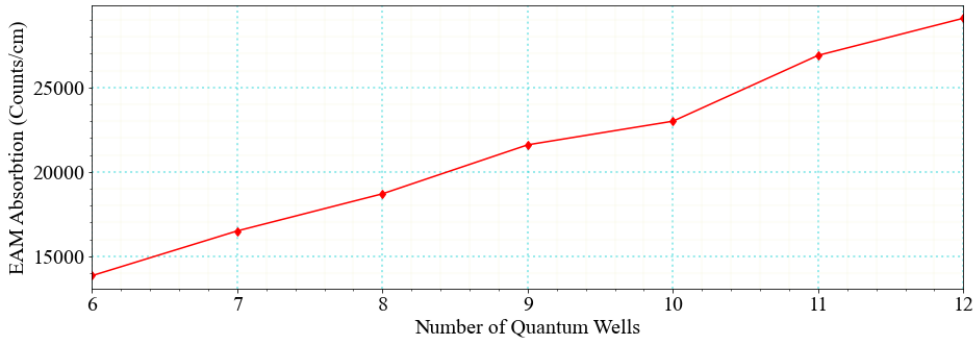

Figure 3.7: Simulated Harold EAM absorption for an epitaxy with a varying number of $9\,\mathrm{nm}$ quantum wells

The results of the Harold-EAM simulation are limited as the pure absorption of a quantum well does not constitute an adequate figure of merit of EAM performance as it does not consider the change in the insertion loss of the EAM. Harold-EAM is incapable of calculating loss and, as such, additional simulation software must be used in order to confirm the optimal quantum well structure capable of balancing the laser and EAM requirements of the material.

3.2.2 Simulations using Lateral Software

As mentioned in the previous chapter, a ratio of the extinction ratio (ER) versus the insertion loss (IL) of an EAM offers a unitless figure of merit by which to judge the performance of our EAMs. The number of quantum wells numerically increases both these factors and there is no noted change in the EAM performance when increasing or decreasing the number of quantum wells in a material. The width of the quantum wells however does not induce a linear change in the EAM performance and thus a simulated experiment is necessary in order to determine the optimum width of the EAM's quantum wells.

Lateral is a simulation software used to calculate the band-gap, absorption, index, extinction ratio, transmission and chirp for quantum well epitaxial structures at differing electrical biases across the material. Thus, by creating simulated epitaxies with varying quantum well width, similar to the ones generated in Harold-EAM, then the absorption spectra for varying biases of different quantum well widths can be obtained.

The power through an EAM, based on the length of the EAM, L, the

confinement factor of the optical mode, Γ, and the absorption spectrum, $\alpha(\lambda)$, can be written as

$$P(dB) = 10\log_{10}\left(e^{-\Gamma L\alpha(\lambda)}\right) = \left(\frac{-10\Gamma L}{\ln 10}\right)\alpha(\lambda) = F\alpha(\lambda) \tag{3.1}$$

By isolating the absorption spectra we can determine the factor F which, when multiplied by our absorption spectra which we can obtain directly from Lateral, will give us the power through the EAM at varying biases. This can then be used to calculate the extinction ratio of the device via

$$ER(V) = |P(V) - P(0V)| \tag{3.2}$$

Our figure of merit can also be calculated directly from the absorption spectra presented as

$$\frac{ER}{IL}(\lambda) = \frac{\alpha_V(\lambda) - \alpha_{0V}(\lambda)}{\alpha_{0V}(\lambda)} \tag{3.3}$$

This process was completed for quantum well structures of varying widths. The results of this simulated comparison can be seen in Fig.3.8 and Fig.3.9. The results of these figures suggest, similar to Fig.3.6 that the optimum width of the EAM varies quadratically. The optimum value from the lateral simulations is a QW width of $10\,\mathrm{nm}$ compared to the $9\,\mathrm{nm}$ peak absorption value noted from the Harold-EAM simulations.

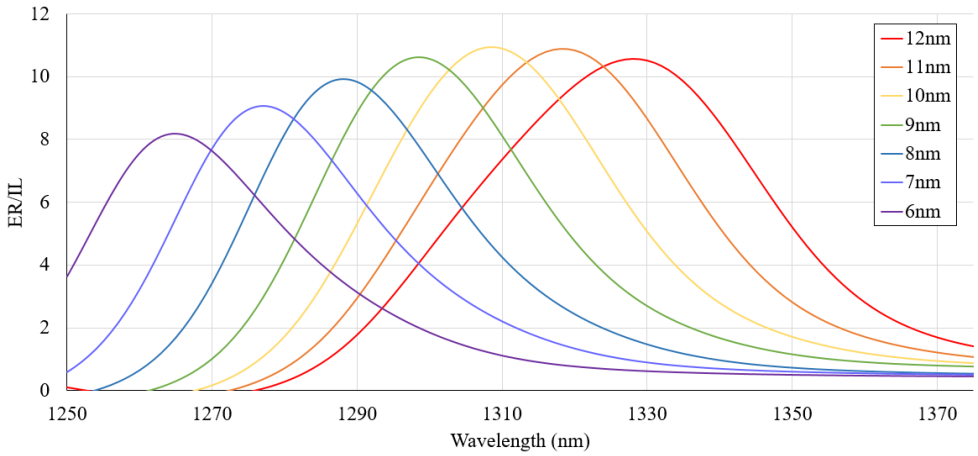

Figure 3.8: Simulated Lateral EAM absorption of bound states for an epitaxy QW of varying width

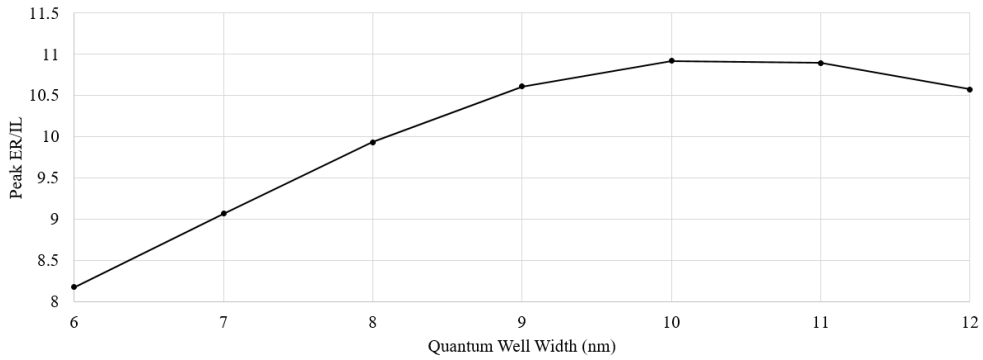

Figure 3.9: Peak EAM ER/IL for an epitaxy with QW of varying width

3.3 Experimental Verification

The results of the previous simulations show how the threshold current and slope efficiency of the laser degrades with an increase of the number of quantum wells or an increase of their width. The chosen figure of merit of the EAM, ER/IL, varies with quantum well width, with the maximum value occuring at $10\,\mathrm{nm}$. Thus the width of the quantum well need not exceed $10\,\mathrm{nm}$ as beyond this point there is no improvement to EAM performance. The number of quantum wells does not affect our chosen EAM figure of merit. However, increasing the number of quantum wells does degrade our laser performance. Overall, from our simulations we are presented with many suitable choices of quantum well structure which satisfy our desired EML specifications assuming our simulations are reflected accurately in later physical experiments. As such it was decided to verify our simulated findings by generating three different QW epitaxies and fabricating lasers from these materials in order to determine a suitable candidate material for further EML processing.

To accomplish this we used Fig.3.1 as a base, changing the strain from tensile to compressive to prevent the lasing of TM modes. The box experiment consisted of 3 material variants based on this design. The first had 6 quantum wells with width $7\,\mathrm{nm}$. This material would form the base of the comparison. The second material had 6 quantum wells of width $9\,\mathrm{nm}$ and would serve to show the effect of increasing quantum well width. The final epitaxy has 8 quantum wells of width $7\,\mathrm{nm}$ and would serve to show the effect of increasing the number of quantum wells when compared with our base material.

3.4 DC Processing

To verify the previous results a 4 layer lithographic mask was designed in order to fabricate FP lasers of varying length and widths. The four layers were

- Ridge-etch Layer - Used to define the waveguides in the semiconductor
- Deep-etch Layer - Used to define areas on the semiconductor that would be etched past the quantum wells
- Oxide-opening Layer - Used to open the passivation on the topside of the waveguides to allow for metal contact
- Metal-liftoff Layer - Used to deposit metal contact onto the waveguide openings and to create large contact pads for needle probing

The design of masks used for this project used software known as PICDraw, which allowed the numerical and computation design of masks through a C++ interface. A view of the lithographic mask layers is shown in Fig.3.10.

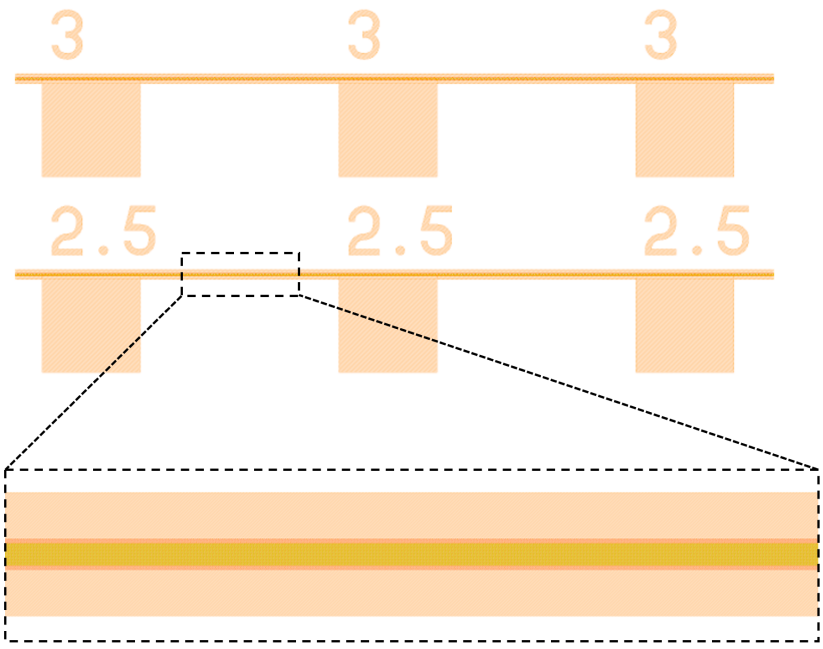

Figure 3.10: A view of some of the overlayed lithographic mask layers used to fabricate FP lasers designed in PICDraw. This picture shows waveguides of widths 2.5 and 3 μm. Waveguides of widths 2.5-5 μm were fabricated. The lower image shows a zoomed in portion of the 2.5 μm waveguide

3.4.1 Ridge-etch Lithography

The first step of our processing is to define our waveguides as shown in Fig.3.11(a). Here we will define our "shallow" waveguides, those which will be etched to just above the quantum wells, and our "deep" waveguides, those which will be etched below the quantum wells. For the purposes of this experiment the waveguides were designed with varying width ranging from $2.5\text{-}5\,\mu\mathrm{m}$. The optical mode is confined near the quantum wells, a depth to which the shallow etch does not penetrate. Shallow-etch waveguides confine the mode by creating an effective index difference between the area under the waveguide and the area which has been etched as shown in Fig.3.11(b). Deep-etched waveguides confine the mode through the index difference between the semiconductor ridge and the air as shown in Fig.3.11(c).

(a) A view of the waveguides for the first step of the lithography

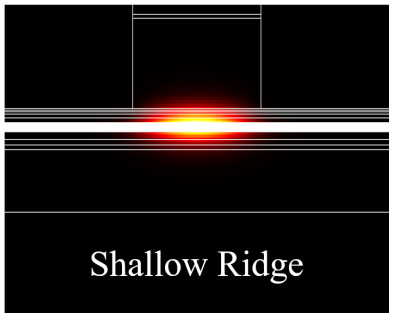

(b) The optical mode of the shallow-etched waveguide

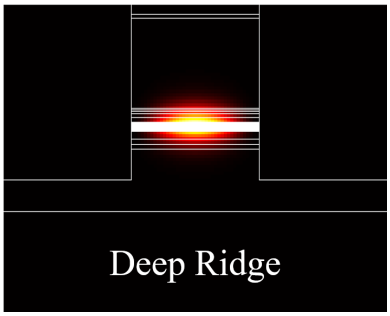

(c) The optical mode of the deep-etched waveguide

Figure 3.11: A view of shallow and deep waveguides

Beginning with a clean semiconductor surface as shown in Fig.3.13(a), a $300\,\mathrm{nm}$ layer of dielectric, silicon dioxide (SiO_2), is deposited via a Plasma Enhanced Chemical Vapour Deposition (PECVD) machine. This is used as a "hard mask", a covering which will protect the area of semiconductor which we do not wish to etch later. Next S1800 Microposit photoresist (PR) was used

to define the shapes of the ridges as a "soft mask", which defines the areas we do not want to etch from our hard mask. The PR used was positive, such is to say, it begins as insoluble polymer and upon light exposure of an appropriate wavelength, becomes soluble. HMDS was used as an adhesion promoter. Once developed the exposed resist is removed using a developer; MF319.

Following this step a plasma etch is used to etch away the areas of SiO_2 which are not protected by PR. Etch depth monitoring is done via laser interferometry monitoring. In this method a small laser spot, approximately $20\text{-}60\,\mu\mathrm{m}$ in diameter, is focused onto the surface of the material to be etched and the reflected light is measured. A special camera is mounted on top of the etch chamber so the laser can be focused on the area of the material to be etched. This camera also collects the reflected laser light to provide a measure of the laser reflectance. Metal etches typically provide different intensities of reflectance and thus the change in the measured feedback of the laser. Semiconductor layers are often transparent to the laser, causing ripples in the reflected intensity which can be counted to track the depth of the etch. The reflectance of multi-layer structures can be modelled using Oxford Instrument's Endpoint detection software to determine the correct etch depth based on the number of ripples measured from the laser feedback as shown in Fig.3.12.

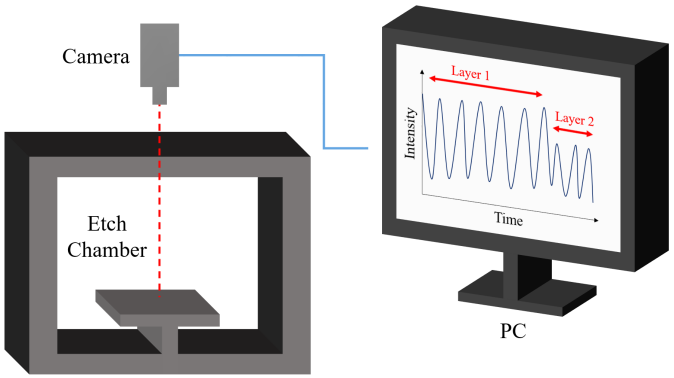

Figure 3.12: A schematic view of the etch endpoint detection system

Plasma etching involves RF-excitation of a selected gas mixture to create a plasma with the right reactive species to etch any un-masked areas on the wafer surface. For SiO_2 etching a mix of He, H_2, and C_4F_8 is used. The reactions form volatile by-products which are removed by vacuum pumping. Once this step is complete the remaining photoresist can be removed via a combination of oxygen plasma etching provided by a Asher Plasma Cleaner and Microposit Remover - 1165. Finally a layer of dielectric silicon nitride

(SiN) is deposited via PECVD to prepare for the next step; the deep-etch lithography.

Note here we have not begun our etch into the semiconductor material but rather we have only defined all our waveguides using SiO_2. This technique is used in order to have the etch defining both the shallow and deep waveguides completed collectively so as to minimise discontinuity between the different etches. This helps to improve the quality of our deep-etched waveguides as any discontinuities in the etch will impact the quality of the waveguide's sidewalls. This degradation would result in a larger loss in our deep-etched waveguides, increasing the threshold current of these devices.

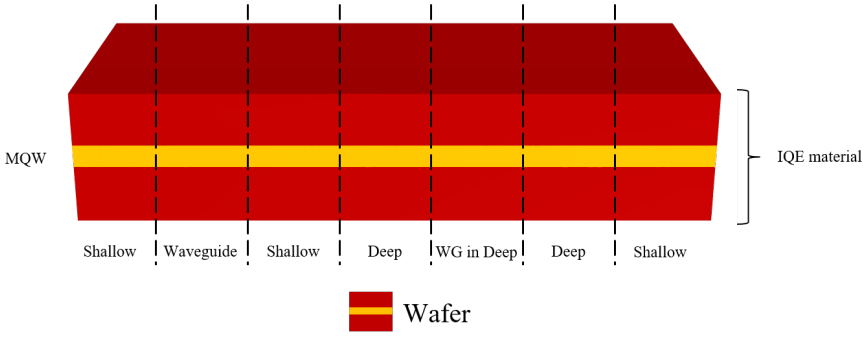

(a) Our starting semiconductor with dividers indicating where future lithographies will occur

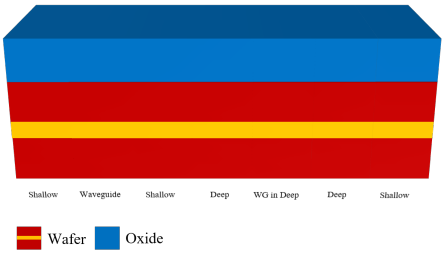

(b) A layer of passivation, SiO_2, is deposited

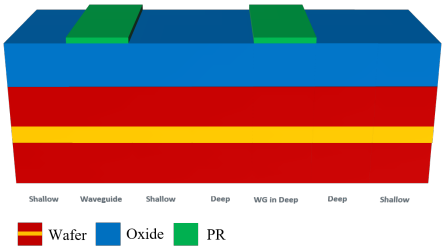

(c) PR is used to define the waveguides

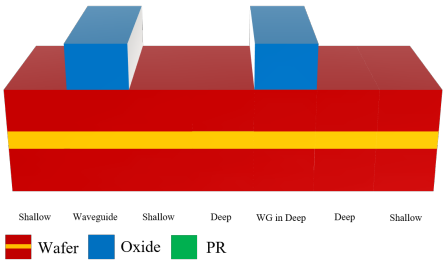

(d) With PR as a soft mask, the SiO_2 is etched to form a waveguide pattern

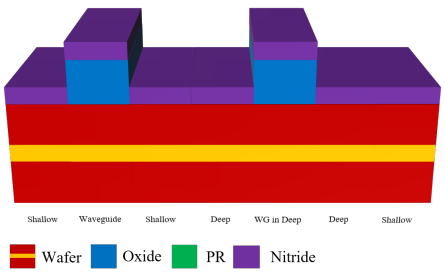

(e) SiN_x is deposited to prepare for the next step

Figure 3.13: Process flow for the first lithographic step

3.4.2 Deep-etch Lithography

The next step required is to identify the parts of the sample to be deep-etched, that is etched past the quantum wells and into the n substrate. An etch such as this has many uses. In general, deep-etched waveguides tend to experience more optical loss and more electrical isolation compared to their shallow-etched counterparts. The extra scattering loss is due to a higher modal confinement factor caused by the larger index difference between the semiconductor and the air, which now confines the mode, instead of the effective index confinement that occurs in shallow etched waveguides.

This deep etch also allows topside access to the n-doped material of our positive-intrinsic-negative (PIN) semiconductor material. This is useful for the creation of Ground-Signal (GS) or Ground-Signal-Ground (GSG) contacts commonly used in contacts for high speed devices.

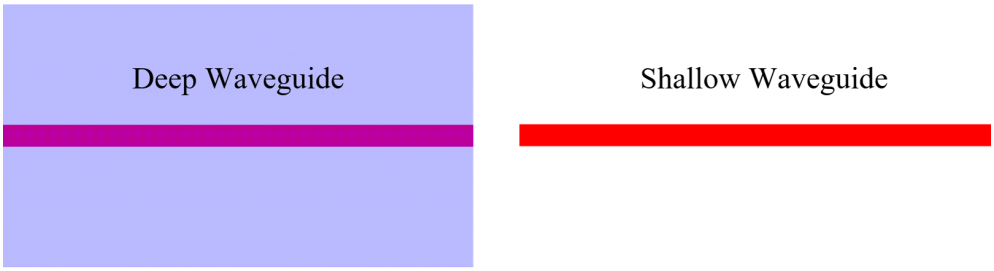

Figure 3.14: A view of the waveguides for the second step of the lithography

With the layer of SiN_x passivation deposited as a second hard mask, PR is deposited as before to form a soft mask for the patterning of the deep areas. Once the PR pattern is defined, plasma etching is used to expose the areas of the semiconductor to be deep-etched. SiN_x is etched using a mixture of SF_6, C_4F_8, H_2 and He. The semiconductor etch is completed using an inductively coupled plasma reactive ion etcher (ICP-RIE) using a mixture of Cl_2, CH_4, and H_2.

For this first step of the etch, the SiN_x acts as a hard mask but once the semiconductor is etched to just above the quantum wells the remaining SiN_x is removed revealing the secondary SiO_2 hard mask used to define our waveguides. The semiconductor etch now continues until the shallow waveguide etch reaches near the quantum wells and the deep waveguide etch reaches past the quantum wells down into the n-substrate of the material. At the end of this step the shallow-etched waveguide depth is approximately

$1.67\,\mu\mathrm{m}$ and the deep-etch depth is approximately $2.2\,\mu\mathrm{m}$

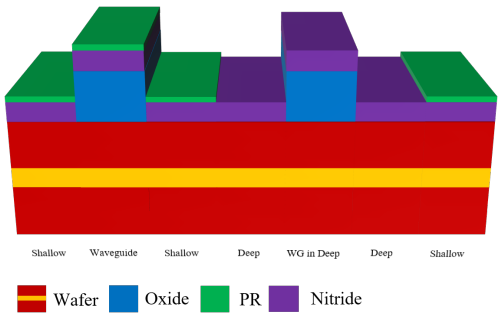

(a) PR is used to define the areas of the wafer to be deep-etched

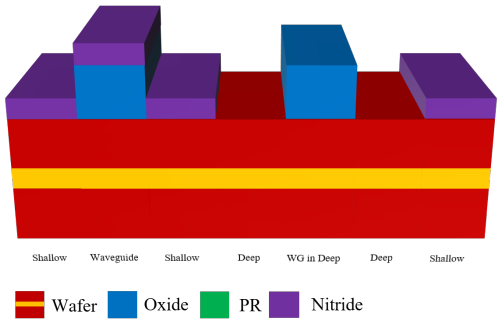

(b) Plasma etching is used to remove the SiN_x from the area to be deep-etched

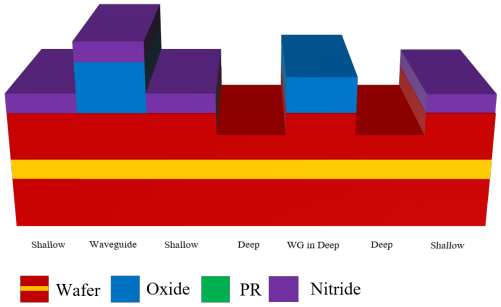

(c) The area of the semiconductor to be deep-etched is etched

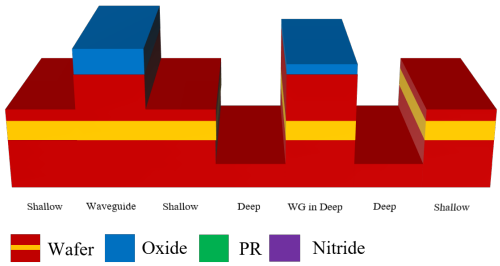

(d) Remaining SiN_x is removed and the semiconductor etches continues, defining the waveguides

Figure 3.15: Process flow for the second lithographic step

3.4.3 Oxide-opening Lithography

The next step involves opening up the passivation on our newly formed waveguides. Both shallow and deep waveguides are opened simultaneously. This stage, though it involves few steps, is the most critical and difficult. The alignment involves opening a fraction of the ridge up to electrical contact as shown in Fig.3.16. This requires high alignment accuracy in order to avoid opening the passivation on the sidewalls of the ridge, which would lead to a high leakage current or non functioning devices. The difficulty in alignment here is due to the relatively small feature size of the oxide opening, which is in general $1\,\mu\mathrm{m}$ smaller than the waveguide being opened. Precise development time is also a necessity as overdevelopment would increase the size of the opening, possibly compromising the passivation of the sidewalls, and underdevelopment could fail to open the contact at all, preventing electrical contact to the device.

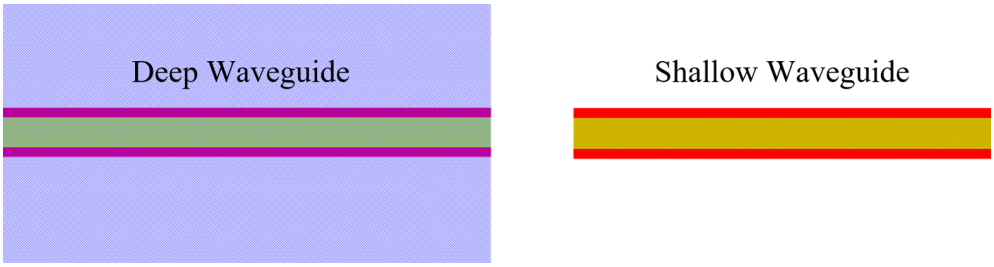

Figure 3.16: A view of the waveguides for the third step of the lithography

To begin, a fresh layer of SiO_2 passivation is deposited onto the surface of the sample via PECVD. The third lithographic step is then completed as in the previous steps, with careful attention being paid to the exposure time used and the subsequent development time of the sample in MF319. Subsequently the exposed oxide was then etched using plasma etching until the waveguide was seen to be exposed using the endpoint laser monitoring system. Unnecessary overetching was avoided here in order to prevent damage to the contact layer of the waveguides.

An alternate method of removing the passivation can be completed using chemical wet etching, instead of plasma or "dry" etching. In this method the exposed passivation is removed by dipping the sample into a buffered-oxide etchant, a mixture of nitric acid (HNO_3) and hydrofluoric acid (HF). Determining the etch rate for this method requires the use of a separate unpatterned sample, normally silicon due to its low cost, which has also been covered in SiO_2. Measurement of the blank "dummy" sample before and after a timed dip into the etchant determines the etch rate for the etchant solution. the benefit of wet etching is that it does not risk any damage to the contact layer of the material.

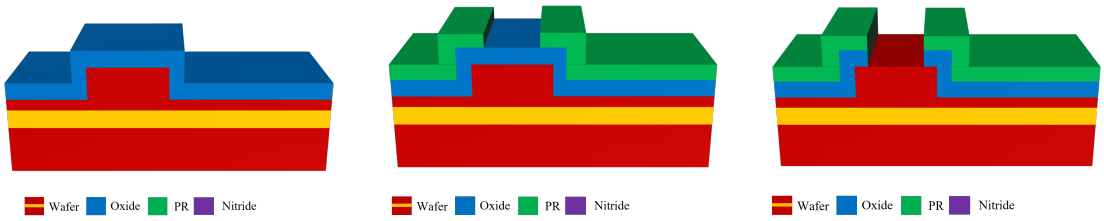

(a) The previous remaining oxide is removed and a fresh layer of passivation SiO_2 is deposited

(b) PR is deposited and patterned to expose areas of the passivation to be removed

(c) The exposed passivation is removed, exposing the contact layer of the waveguide

Figure 3.17: Process flow for the third lithographic step

3.4.4 Metal-Liftoff Lithography

The final lithographic stage of the process is used to define the areas of the mask where a p-contact metal is to be deposited as shown in Fig.3.18. The shallow and deep-etched waveguides are processed in the same way for this step. In this step we use a thick metal consisting of $25\,\mathrm{nm}$ of titanium which provides excellent adhesion, and $500\,\mathrm{nm}$ of gold. The metal covers the oxide opening to provide electrical contact to the waveguide's PIN junction to facilitate biasing. Additionally, the metal is used to form larger patterns which connect to the waveguide contacts in order to allow easier needle probing of the devices under test. Once deposited the contact resistance of the metal can be measured using the transfer length measurement (TLM) across various contacts of a set length.

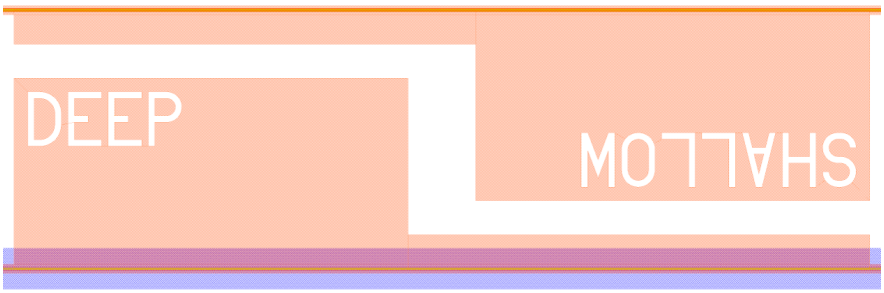

Figure 3.18: A view of the waveguides for the fourth step of the lithography

TLMs are a method of measuring the specific contact resistivity of a metal-semiconductor interface through the resistance measurement. For this method we use a series of rectangular metal contact pads separated by a variable length, d_i in Fig. 3.19. Probes are placed to measure the total resistance, R_{TOT} between each consecutive pad which produces the graph shown. The total resistance between each pad is formed by the resistance of the uncovered semiconductor between the contacts and by the area of the voltage drop in the two metal-semiconductor interfaces, one for each pad measured. R_S is the sheet resistance of the semiconductor substrate. Z is the width of the metal pads.

$$R_{TOT} = \frac{R_S d}{Z} + 2R_C \tag{3.4}$$

The contact resistance, R_C can thus be obtained from graphical analysis of the resistance measurements of the TLM structures as shown on the right of

Fig.3.19. The voltage drop underneath the contact pad occurs within the length $L_T = \sqrt{\frac{\rho_C}{R_S}}$; which is known as the transfer length, highlighted in green in the accompanying figure. The contact resistivity, ρ_C, can thereby be calculated using the contact resistance R_C obtained as in Fig. 3.19.

$$R_C \approx \frac{\rho_C}{Z L_T} = \frac{\sqrt{R_S \rho_C}}{Z} \tag{3.5}$$

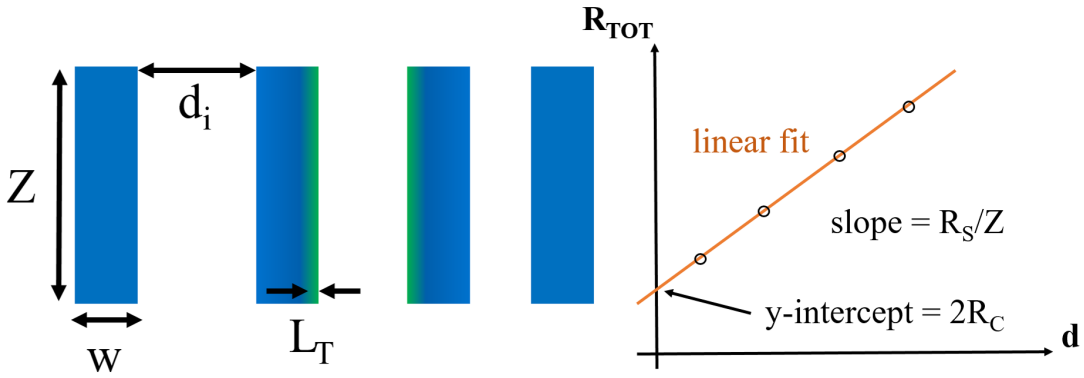

Figure 3.19: Transfer Length Measurement (TLM)

The definition of the metal contact lithography requires the deposition of two separate photoresist polymers in addition to the regular adhesion promoter HMDS. The first polymer is a polydimethylglutarimide (PGMI) known as Lift-off resist (LOR). LOR is insoluble in typical photoresist solvents, therefore, there is no intermixing between layers when baked at $\geq 150\,^{\circ}\mathrm{C}$. Following this, the previously used S1800 series PR is deposited on top and baked accordingly. The sample is exposed as before however this time the development time is significantly longer, $>$ 2 minutes, in order to create an undercut in the two resists used to facilitate the lift-off of the unwanted metal. The undercut can be visually inspected using a microscope to confirm the piece is suitable for metal deposition. Metal is deposited using a Temescal electron beam evaporator that is used to deposit thin films onto substrates. Evaporation is done under a high vacuum in a bell jar chamber and is achieved by heating the desired metal source with an electron beam. As the source material evaporates, it forms a thin film on the samples. A visualisation of this process is shown in Fig.3.20.

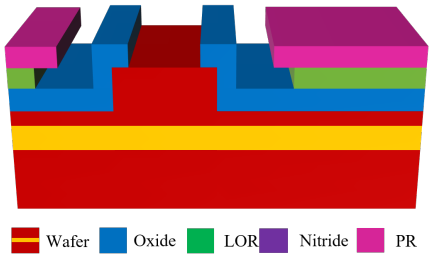

(a) Two layers of PR are used to create an undercut

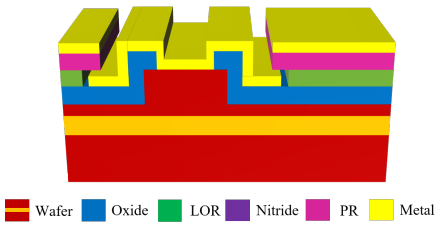

(b) The metal is evaporated onto the sample

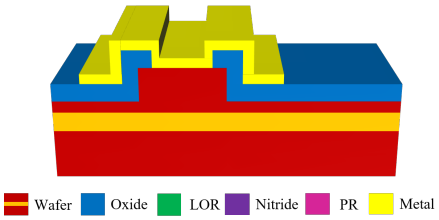

(c) The sample is left in 1165 to remove the PR and the metal attached to the PR

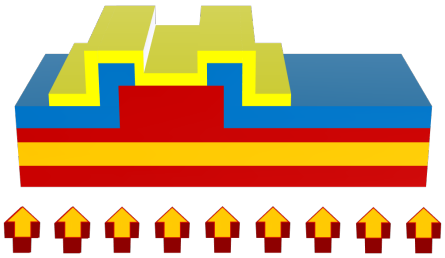

(d) The backside of the sample is thinned using a bubbling bromine-methanol solution

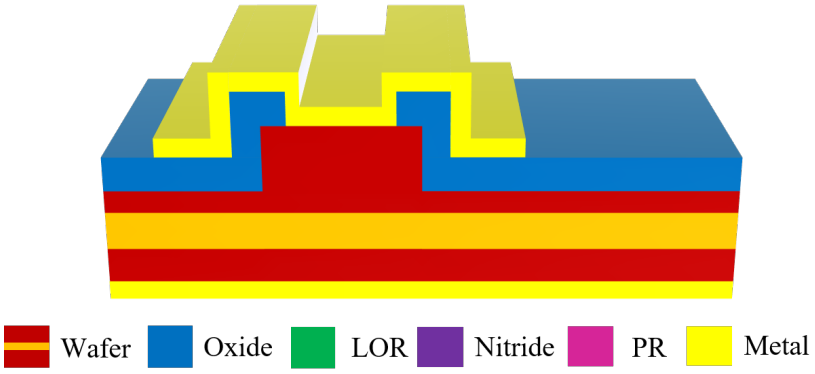

(e) N metal is deposited onto the backside and annealed

Figure 3.20: Process flow for the fourth lithographic step

Once the deposition is complete the sample is submerged in 1165, which dissolves the remaining PR, removing the metal from the unwanted areas. The topside of the sample is now complete. The final processing step is the chemical thinning of the sample's substrate in order to facilitate the cleaving of the sample into smaller devices. This removal of substrate involves mounting the sample onto a glass carrier using wax. The holder is then placed above a solution of bromine-methanol without the solution touching the sample. A bubbler then pumps nitrogen gas through the solution causing it to form a foam. The carrier rotates in place to provide even coverage. This foam etches the InP substrate leaving behind a highly polished substrate suitable for

metallisation. The sample is loaded again into the metal evaporator and a layer of n-metal, consisting of gold, titanium, germanium and nickel (Au:14 nm, Ge:14 nm, Au:14 nm, Ni:11 nm, Au:250 nm). Once the metal is evaporated the sample is removed from the carrier, gently cleaned with toluene to remove the wax, and then the backside metal is annealed in a furnace to improve electrical contact to the sample. When annealed in this way the backside metal can be seen to take on a rosy hue. SEM images of the fabricated samples can be seen in Fig.3.21.

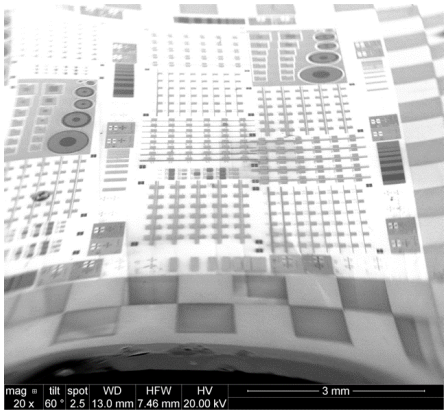

(a) An overview SEM image of the fabricated sample

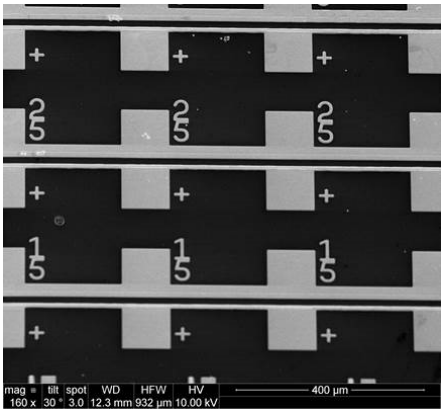

(b) A closer SEM image showing the waveguides coated in metal

Figure 3.21: SEM images of the completed DC Fabrication

Finally the sample can be cleaved into smaller FP chips. This involves using a diamond scribe blade to form an initial cut on the topside of the sample along the crystalline axis of the semiconductor. Pressure can then be applied to the backside of the piece to break the sample into a smaller chip along the crystalline plane, forming a flat facet which provides suitable reflection for the waveguides on the chip to from FP cavities with ∼33% reflectivity.

3.5 Laser Characterisation

With three different samples using different epitaxies for each, over 60 FP lasers of varying widths and lengths were cleaved into testable chips. These chips were mounted onto a temperature-controlled gold plated chuck as seen in Fig.3.22. The temperature during measurement was maintained at 25 °C during testing unless otherwise stated. The device under test (DUT) was provided with positive electrical contact via a needle probe. The needle probe

was connected via electrical cabling to a source measurement unit (SMU). The SMU used was a 2-channel Keithley 2600 series SMU. The grounding of the SMU was connected to the gold plated chuck to complete the circuit. This allowed the SMU to pump electrical current through the PIN junction to stimulate continous wave (CW) lasing in the FP devices.

This laser light was collected via lensed fibre coupling. This fibre was connected to a Thorlabs optical power meter which measured the collected power in mW. The collection of the optical power measured from a corresponding applied current to the DUT was automated through the creation of a suitable LabView programme. This program supplied a current to the DUT and recorded both the current supplied, the voltage measured across the device, and the resultant optical power collected from the fibre coupling.

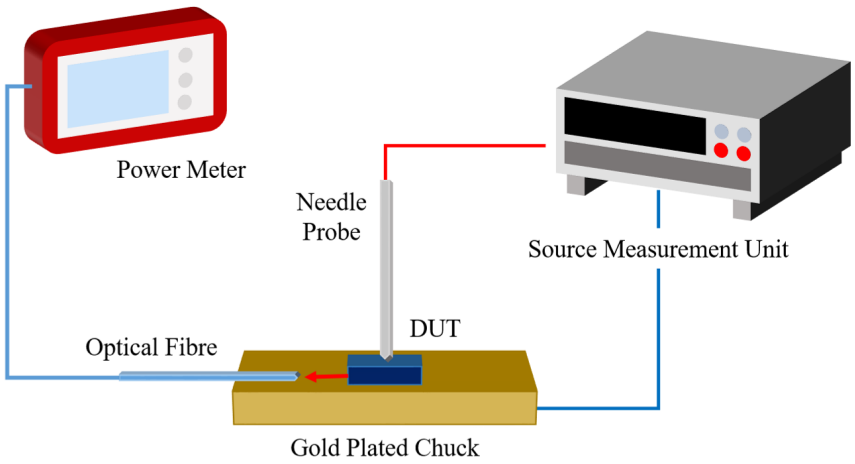

Figure 3.22: Experimental setup used for collecting LIV measurements

The three different epitaxies each produced an array of lasers of different waveguide widths which were cleaved into varying lengths. Shallow-etched waveguide devices were all tested using the setup described above in order to obtain the threshold current (I_{th}) and slope efficiency ($S.E.$). A selection of the results obtained is shown in tables 3.2, 3.3, and 3.4.

In our original simulations shown in Table 3.1, we focused on a $2.5\,\mu\mathrm{m}$ wide $300\,\mu\mathrm{m}$ long FP laser and, as such, the measured experimental threshold currents and slope efficiencies have been used to calculate the threshold current density and the slope efficiency per unit area for each device tested. Thus, by multiplying the measured averages by the width and length of our simulated laser structure ($2.5{\cdot}300\,\mu\mathrm{m}^2$) then we can compare our theoretical and experimental results directly.

Table 3.2: A selection of some of the experimental results obtained when testing FP lasers on 6QW with width $7\,\mathrm{nm}$

Ridge Width (μm)	Device Length (μm)	Ith (mA)	S.E. (W/A)	Jth ($mA/\mu m^2$)	S.E. ($WA^{-1}\mu m^{-2}$)
2.5	500	24	0.171	0.0192	0.000137
2.5	1000	47	0.327	0.0188	0.000131
2.5	1500	72	0.512	0.0192	0.000137
3	500	33	0.185	0.022	0.000123
3	1000	60	0.435	0.02	0.000145
3	1500	95	0.625	0.021111	0.000139
3.5	500	36	0.228	0.020571	0.00013
3.5	1000	73	0.499	0.020857	0.000143
5	500	53	0.366	0.0212	0.000146
5	1000	97	0.682	0.0194	0.000136
AVERAGE				**0.020234**	**0.000137**

Table 3.3: A selection of some of the experimental results obtained when testing FP lasers on 6QW with width $9\,\mathrm{nm}$

Ridge Width (μm)	Device Length (μm)	Ith (mA)	S.E. (W/A)	Jth ($mA/\mu m^2$)	S.E. ($WA^{-1}\mu m^{-2}$)
2.5	500	24	0.208	0.0192	0.000166
2.5	1000	56	0.36	0.0224	0.000144
2.5	1500	84	0.534	0.0224	0.000142
3	500	38	0.219	0.025333	0.000146
3	1000	74	0.436	0.024667	0.000145
3	1500	108	0.622	0.024	0.000138
3.5	500	36	0.249	0.020571	0.000142
3.5	1000	83	0.458	0.023714	0.000131
5	500	64	0.374	0.0256	0.00015
5	1000	117	0.664	0.0234	0.000133
AVERAGE				**0.023129**	**0.000144**

Table 3.4: A selection of some of the experimental results obtained when testing FP lasers on 8QW with width $7\,\mathrm{nm}$

Ridge Width (μm)	Device Length (μm)	Ith (mA)	S.E. (W/A)	Jth ($mA/\mu m^2$)	S.E. ($WA^{-1}\mu m^{-2}$)
2.5	500	40	0.116	0.032	9.28E-05
2.5	1000	69	0.274	0.0276	0.00011
2.5	1500	107	0.392	0.028533	0.000105
3	500	44	0.193	0.029333	0.000129
3	1000	83	0.287	0.027667	9.57E-05
3	1500	124	0.458	0.027556	0.000102
3.5	500	46	0.162	0.026286	9.26E-05
3.5	1000	105	0.424	0.03	0.000121
5	500	77	0.314	0.0308	0.000126
5	1000	148	0.528	0.0296	0.000106
AVERAGE				**0.028937**	**0.000108**

Using the previous tables we can compare the simulated and experimental performance of a $2.5\,\mu\mathrm{m}$ wide, $300\,\mu\mathrm{m}$ long FP laser and check the accuracy of our simulations in Table 3.5. The experimental results show a lower slope efficiency which is to be expected. All of the power of the simulated laser is accounted for in the simulation however the experimental results relied on fibre coupling, thus undergoing coupling loss which explains the discrepancy. Lower power might also be a result of fabrication induced waveguide losses which would not be accounted for in the simulations.

In comparison the threshold current of the lasers measured experimentally is lower than that of the simulated values. This may be due to the fact that the simulated lasers were all measured for $300\,\mu\mathrm{m}$, a length which is difficult to manually cleave, and thus the smallest laser measured was $500\,\mu\mathrm{m}$. The threshold current of a laser is dependent on the length of the laser as the experimental measurements show. Thus, decreasing the length of the laser decreases the overall threshold however this only holds true up until a turning point, L_{min}, below which the threshold current increases rapidly [87]. Below this turning point the amplification of the light struggles to overcome the internal losses, eventually preventing lasing when the cavity becomes short enough. An additional explanation could be simply due a difference between the simulated gain used for the simulation material versus the real gain of the fabricated lasers. These behaviours may serve to explain the quantitative difference between the simulated and experimental values but ultimately, the numerical values are not what we are interested in but rather the trend of the data itself.

Table 3.5: A comparison of $2.5\,\mu\mathrm{m}$ wide, $300\,\mu\mathrm{m}$ long FP lasers based on simulated and experimental data

		Simulated		Experimental	
Number of QW	QW Width (nm)	Threshold Current (mA)	Slope Efficiency (W/A)	Threshold Current (mA)	Slope Efficiency (W/A)
6	7	19.16	0.325	15.18	0.103
6	9	25.24	0.303	17.35	0.108
8	7	23.28	0.312	21.7	0.0808

In the simulation increasing the width of the QWs by $2\,\mathrm{nm}$ resulted in a higher threshold current and lower slope efficiency than adding two additional quantum wells. However the reverse becomes true in our experimental measurements. This tells us that increasing the width of the QWs degrades the overall laser performance less than increasing the number of quantum wells. This behaviour remains true when only comparing the $2.5\,\mu\mathrm{m}$ lasers characterised experimentally. Alone, however, this result cannot be used to make a decision as to the optimal epitaxial structure for a monolithically integrated EML. For the final decision we must analyse the change in absorption versus the change in QW structure.

3.6 Absorption Characterisation

In the same process run which was used to create the FP lasers, vertical photodiode (PD) structures were also produced which could measure the vertical absorption for each material. A Santec tunable laser was connected to a top-down optical fibre to provide incident light on circular PD structures of diameter $800\,\mu\mathrm{m}$ as shown in Fig.3.23. These circular structures had a contact metal annulus with an outer diameter of $760\,\mu\mathrm{m}$ and an inner diameter of $320\,\mu\mathrm{m}$ which exposed the P-I-N semiconductor to incident light. The PD was placed on a gold mounted chuck for grounding. A needle probe connected to a Keithley 2400 series SMU was then placed on the P-metal ring. With this setup in place, the PD could be reverse biased, causing the incident light of the TLS to produce photocurrent in the semiconductor which was recorded by the Keithley SMU.

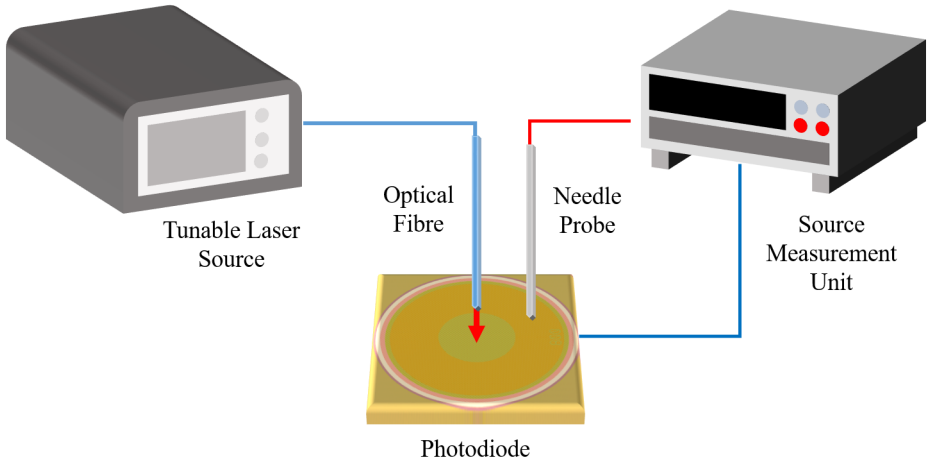

Figure 3.23: Experimental setup used for collecting material absorption measurements

Fig.3.24 shows a closer view of a cross-section of the vertical PD. The Santec laser had a tuning range of $1260\text{-}1360\,\mathrm{nm}$. A Labview code was written in order to sweep the wavelength of the TLS at a set power, while setting the SMU to reverse bias the PD. A photocurrent measurement was collected in $1\,\mathrm{nm}$ steps from $1260\text{-}1360\,\mathrm{nm}$. In addition, the Labview code recorded the dark current of the material by recording the current reading for each reverse bias voltage without the TLS being active. The dark current was then automatically subtracted from the measurement data.

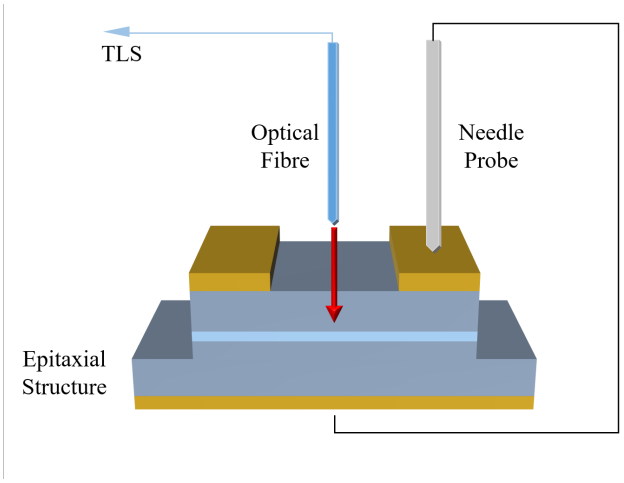

Figure 3.24: Close up view of the photodiode structure used for absorption measurements in Fig.3.23

The results of this test are shown in Fig.3.25 for the three different epitaxies tested. Fig.3.25(d) shows the ER/IL for each of the materials at $1\,\mathrm{V}$.

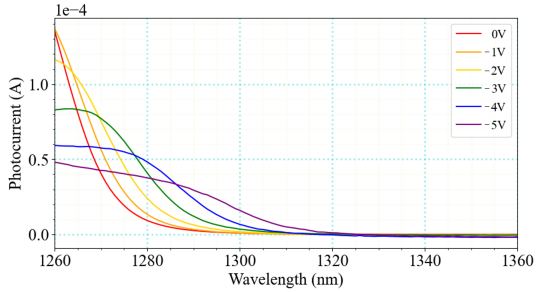

(a) Absorption spectrum for a PD with 6QW of width 7 nm

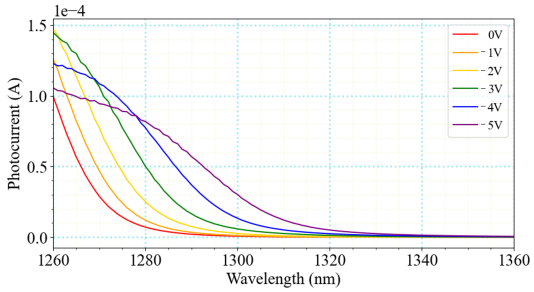

(b) Absorption spectrum for a PD with 6QW of width 9 nm

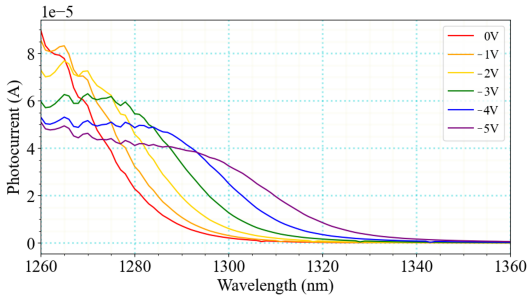

(c) Absorption spectrum for a PD with 8QW of width 7 nm

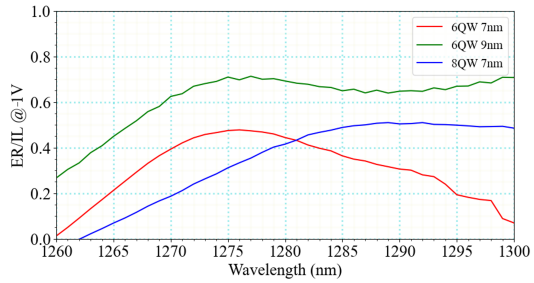

(d) ER/IL for 1 V-0 V for the PDs for different epitaxies

Figure 3.25: Absorption results for PD test measurements

The results of this experiment are consistent with our previous simulations earlier in the chapter. Increasing the number of quantum wells does not increase the value of ER/IL as the increase in absorption caused by an increase in the number of quantum wells will lead to a matching increase in absorption loss. Thus, the maximum value for ER/IL for both 6 QWs and 8 QWs, each with a width of 7 nm, is identical in magnitude. The change in the width of the quantum wells from 7 nm to 9 nm caused over a 50 % increase in our desired figure of merit.

3.7 Epitaxial Verdict

From the characterisation of the various materials we have separate conclusions. In terms of laser threshold current the best performing material was 6 QWs with a width of 7 nm. The material with the greatest slope efficiency had 6 QWs with widths of 9 nm. Finally the material with the best absorption in terms of our figure of merit had 6 QWs with widths of 9 nm.

The conclusion from this chapter is as such. The deterioration in laser

performance per quantum well added is greater than the deterioration in performance per $2\,\mathrm{nm}$ increase in the width of the quantum wells used. Increasing the number of quantum wells increases the absorption of the material but also increases the insertion loss, thus leading to no change in our desired figure of merit; ER/IL. Thus, the increase in our EAM figure of merit due to an increase in the width of the quantum wells used in the material is automatically greater than the change induced from the addition of more quantum wells to the epitaxial structure.

Overall, given the goal of this project is to create an epitaxy used for the monolithic integration of both lasers and EAMs, the material which best satisfies these requirements is that with 6 quantum wells, each with a width of $9\,\mathrm{nm}$. As such, this was the material used for the fabrication of our high-speed electro-absorption modulated lasers.

Finally, with our optimised material we are free to move onto exploring single mode laser designs to be used for our EML. The goal of these designs is to be high power, low threshold and single mode, with the capacity to be redshifted past the absorption peak of the laser.

Chapter 4

Laser Design, Simulation & Characterisation

When designing lasers it is assumed that we are always aiming for low threshold, high slope efficiency and high wall plug efficiency. For the purposes of this project we are also interested in a laser with good single mode performance which is capable of being tuned or redshifted suitably far so as to avoid absorption in our monolithically integrated EAM at $0\,\mathrm{V}$. Given this goal we explored a selection of tunable laser designs, simulating, fabricating and characterising each so that the most suitable design may form the laser portion of our EML.

Spawning from the simple Fabry-Pérot laser which were fabricated in the last chapter we explore the usage of minor reflective perturbations in an FP to form single mode reflectors. The perturbations used for this project were full waveguide etches referred to as "slots" and smaller circular etches into the waveguide referred to as "pits", both of which will be detailed in the sections below.

We explored and analysed the benefits of using these perturbations directly onto our gain sections with single-section slotted Fabry-Pérot lasers (SSFPs) and single-section pitted Fabry-Pérot lasers (SPFPs). After this we moved these perturbations to a separate electrically isolated section to form two section devices with a gain section and a mirror section, wherein the mirror section consisted of an array of slots, forming slotted Fabry-Pérot lasers (SFPs), and pits, forming pitted Fabry-Pérot lasers (PFPs). Subsequently we explored a variation of slot usage by creating a device with two mirror sections we

referred to as a dual-mirror slotted Fabry-Pérot lasers (DSFPs). For the pits we explored using multiple spacings within a single mirror section, first grouping pits together and placing multiple groups within the same mirror section, forming grouped Fabry-Pérot lasers (GPFPs). Subsequently we investigated the inverse scattering method to truly optimise our perturbation positions used within our FP cavities.

Additional time was taken to explore the usage of ring lasers to satisfy the laser requirements of this project. Initially more traditional racetrack ring lasers were investigated before an atypical design of ring laser, a snail laser, was focused on. Though racetrack ring lasers were investigated none were fabricated and characterised. Multiple snail laser designs were fabricated and characterised to inspect the feasibility of their usage in this project.

The lasers in this section of the project were fabricated on a multi-project wafer which used a commercial IQE $1550\,\mathrm{nm}$ emission epitaxial structure as shown in Fig. 4.1. The focus here was to determine optimal design techniques for red-shifting and single mode lasing and then transfer these lessons learned to the less plentiful $1310\,\mathrm{nm}$ epitaxial material.

Layer	Material	Group	Repeat	Mole Fraction (x)	Mole Fraction (y)	Strain (ppm)	PL (nm)	Thickness (um)	Dopant	Type	CV Level (cm -3)
16	GaIn(x)As			0.530		0		0.2000	Zinc	P	> 1.50e19
15	GaIn(x)As(y)P			0.710	0.620	0	1300 +/-50	0.0500	Zinc	P	> 3.00e18
14	InP							0.1000	Zinc	P	> 1.50e18
13	InP							1.5000	Zinc	P	= 1.00e18
12	GaIn(x)As(y)P			0.850	0.330	0	1100 +/-20	0.0200	Zinc	P	= 1.00e18
11	InP							0.0500	Zinc	P	= 7.00e17
10	[Al(x)Ga]In(y)As			0.900	0.530	0		0.0600	Zinc	P	= 4.00e17
9	[Al(x)Ga]In(y)As			0.720 to 0.900	0.530	0		0.0600	Undoped	U/D	
8	[Al(x)Ga]In(y)As			0.440	0.490	-3000	1100 +/-20	0.0100	Undoped	U/D	
7	[Al(x)Ga]In(y)As	1	5	0.240	0.710	12000	1530	0.0060	Undoped	U/D	
6	[Al(x)Ga]In(y)As	1	5	0.440	0.490	-3000	1100 +/-20	0.0100	Undoped	U/D	
5	[Al(x)Ga]In(y)As			0.900 to 0.720	0.530	0		0.0600	Undoped	U/D	
4	[Al(x)Ga]In(y)As			0.900	0.530	0		0.0600	Silicon	N	= 1.00e18
3	[Al(x)Ga]In(y)As			0.860 to 0.900	0.530	0		0.0100	Silicon	N	= 1.00e18
2	InP							0.5000	Silicon	N	= 1.00e18
1	InP							0.3000	Silicon	N	= 3.00e18
SUBSTRATE											

Figure 4.1: The commercially produced IQE epitaxial material designed for $1550\,\mathrm{nm}$ emission.

4.1 Fabry-Pérot Lasers

When simulating lasers it makes sense to begin with the most basic laser structure. The simplest semiconductor laser is the Fabry-Pérot (FP) Laser, which consists of a waveguide surrounded by two facets. When an electric current is supplied to this semiconductor system, light is generated via spontaneous emission. The reflective ends of the cavity maintain this light within the waveguide portion of the semiconductor which leads to stimulated emission amplifying the light. This process continues until the round trip gain is equal to the round trip losses inherent in the material's absorption and the loss of the reflectors. Subsequent to this point, lasing is said to begin.

Stimulated emission can only be achieved within the cavity by wavelengths which are capable of satisfying the standing wave equation;

$$L_{cav} = \frac{N\lambda}{2n_{cav}} \qquad N \in \mathbb{N} \tag{4.1}$$

where L_{cav} is the cavity length, λ is the wavelength in a vacuum, n_{cav} is the cavity's index, and k is the longitudinal mode number. The reflectivity and transmission of a simple cavity can be well described by the scattering matrix method. In a one dimensional setting, the component parts of semiconductor system can be treated as individual 2x2 matrices in order to manage input and output amplitudes in a normalised expression.

These matrices relate the initial and final state of a system undergoing a scattering process and represent the amplitudes of the waves scattering out of the system in terms of the input amplitudes as shown in Fig. 4.2.

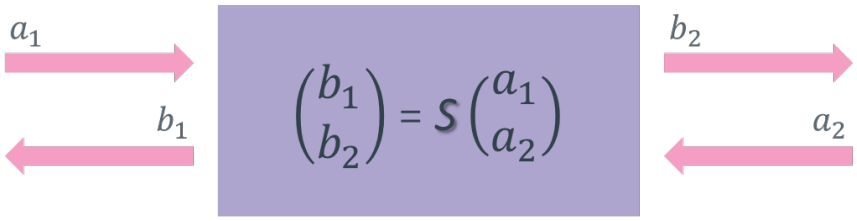

Figure 4.2: Scattering matrices represent the transformation from input to output of a system

In the case of a Fabry-Pérot, there are two distinct components which can be described via scattering matrices; a reflective interface $\mathbf{S}_{RF}$, and a waveguide $\mathbf{S}_{WG}$. A laser structure of length, L, and refractive index, n, can be represented

as a series of reflectors (RF) and waveguides (WG) which can be written as;

$$\mathbf{S}_{RF_{i,j}} = \begin{pmatrix} r_{i,j} & t_{i,j} \\ t_{i,j} & -r_{i,j} \end{pmatrix} \qquad \mathbf{S}_{WG_j} = \begin{pmatrix} 0 & e^{-i\theta_j} \\ e^{-i\theta_j} & 0 \end{pmatrix} \tag{4.2}$$

where θ_j represents the propagation constant of the system where $\theta_j = 2\pi n_j L/\lambda$. $r_{i,j}$ represents the reflection coefficient from port i to j and vice versa, $t_{i,j}$ represents the transmission coefficient from port i to j and vice versa.

$$r_{i,j} = \frac{n_j - n_i}{n_j + n_i} = -r_{j,i} \qquad t_{i,j} = \sqrt{1 - r_{i,j}^2} = t_{j,i} \tag{4.3}$$

Another important matrix that relates the normalised amplitudes is the transmission matrix. The transmission matrix expresses the inputs and outputs at a given port in terms of those at the other port.

$$\begin{pmatrix} a_1 \\ b_1 \end{pmatrix} = \mathbf{T} \begin{pmatrix} a_2 \\ b_2 \end{pmatrix} \tag{4.4}$$

In the case of a two-port network, it is used most often to cascade networks together because simple matrix multiplication can be used as seen in Fig. 4.3. In the case of a simple FP system there are once again two matrix components, a reflective interface T_{RF}, and a waveguide T_{WG}.

$$\mathbf{T}_{RF_{i,j}} = \frac{1}{t_{i,j}} \begin{pmatrix} 1 & r_{i,j} \\ r_{i,j} & r_{i,j}^2 + r_{i,j}^2 \end{pmatrix} \qquad \mathbf{T}_{WG_j} = \begin{pmatrix} e^{i\theta_j} & 0 \\ 0 & e^{-i\theta_j} \end{pmatrix} \tag{4.5}$$

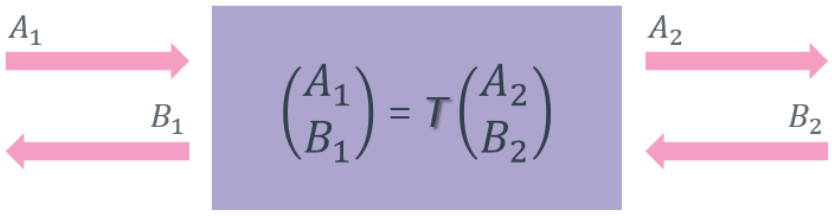

Figure 4.3: Transfer matrices represent the transformation from left to right in a system

Thus an FP etalon with index, n_j, surrounded by facets which interface with an index of n_i, can thereby be represented by transforming the scattering matrices into transfer matrices and multiplying the components of the cavity together;

$$\begin{aligned} \mathbf{T}_{FP} &= \mathbf{T}_{RF_{i,j}}\,\mathbf{T}_{WG_j}\,\mathbf{T}_{RF_{j,i}} \\ &= \frac{1}{t_{i,j}}\begin{pmatrix} 1 & r_{i,j} \\ r_{i,j} & r_{i,j}^2 + t_{i,j}^2 \end{pmatrix}\begin{pmatrix} e^{i\theta_j} & 0 \\ 0 & e^{-i\theta_j} \end{pmatrix}\frac{1}{t_{i,j}}\begin{pmatrix} 1 & -r_{i,j} \\ -r_{i,j} & r_{i,j}^2 + t_{i,j}^2 \end{pmatrix} \end{aligned} \tag{4.6}$$

$\mathbf{T}_{RF_{i,j}}$ and $\mathbf{T}_{RF_{j,i}}$ only differ by the sign of the $\mathbf{T}_{12}$ and $\mathbf{T}_{21}$ elements as such we will now refer to the entrance and exit facets as $\mathbf{T}_{in}$ and $\mathbf{T}_{out}$ respectively. Solving this equation results in a transfer matrix whose elements consist of the reflectivity (R) and transmission (T) of the etalon such that

$$R = \left|\frac{T_{21}}{T_{11}}\right|^2 \qquad T = \left|\frac{1}{T_{11}}\right|^2 \tag{4.7}$$

Fig. 4.4 shows the relationship between reflectivity, transmission, and the available wavelengths in the cavity. Lasing requires that the wavelengths desired be able to make multiple passes through the cavity in order to achieve the necessary gain. The reflective profile shows where the resonant wavelengths of the cavity exist. These resonant wavelengths will become the lasing wavelengths when the cavity is actively biased as these wavelengths are able to reflect back and forth within the cavity, creating stimulated emission. In the FP laser all of the resonant reflective wavelength peaks have the same transmission which leads to many active laser modes. This is why the FP laser does not have good single mode operation.

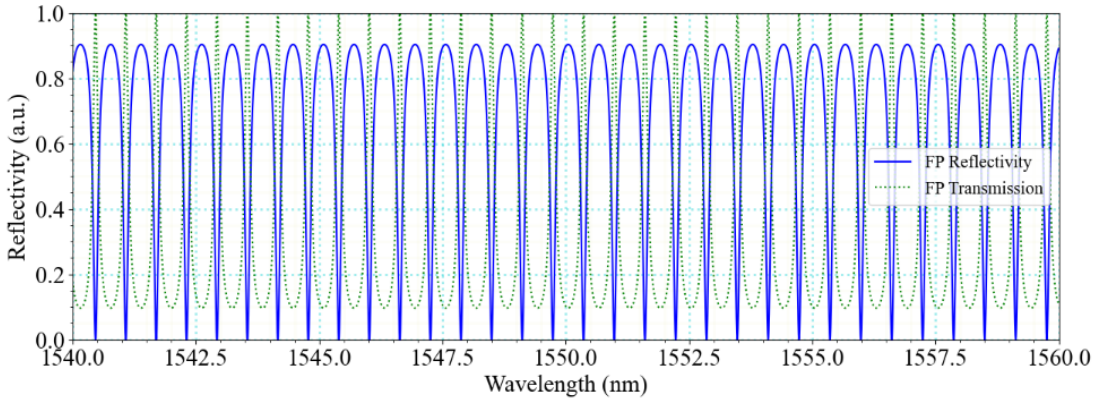

Figure 4.4: The reflectivity versus wavelength for an $600\,\mu m$ Fabry-Pérot etalon.

Cassidy provides a relationship between the resonance, $\Upsilon(\lambda)$ of a cavity and the resultant lasing power, $I_m^{\pm}(\lambda)$ [88]. For an FP cavity the resonant modes of the cavity are the transmission modes.

$$\Upsilon = |\mathbf{S}_{FP_{21}}|^2 = \left| \frac{1}{\mathbf{T}_{FP_{11}}} \right|^2 \tag{4.8}$$

Using this relationship we construct Eqn. (4.9), taking the total amount of spontaneous light which couples into the m mode; $\delta_m = 1$, and using a Gaussian shape for the gain profile; $G(\lambda)$. We transform the result into a an arbitrary decibel format to more closely resemble laser power measurements.

$$I_m^{\pm}(\lambda) = 10 \log_{10} \left(\frac{< |\delta_m|^2 >}{1 - \Upsilon(\lambda) G(\lambda)} \right) \tag{4.9}$$

The result of this equation applied to an FP laser cavity shown in Fig. 4.5 demonstrates the multi-modal behaviour of FP lasers which limits their usefulness in communication systems.

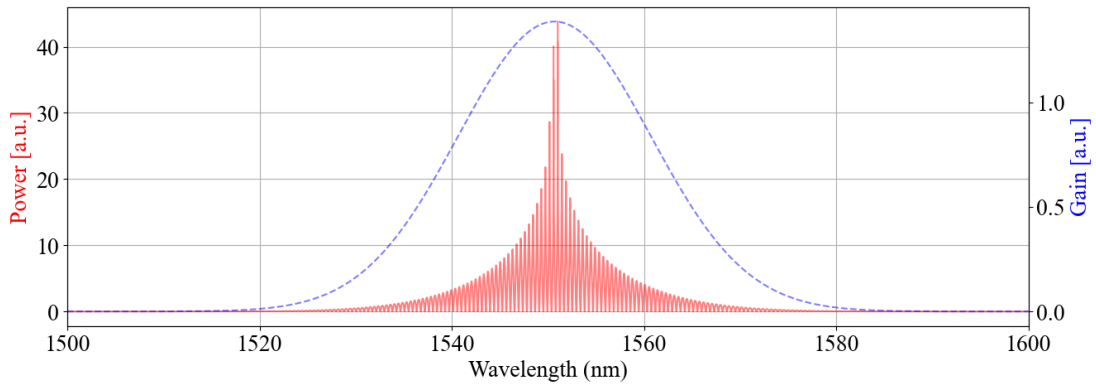

Figure 4.5: The lasing modes for a $600\,\mu\mathrm{m}$ Fabry-Pérot with an arbitrary gain profile centred on $1550\,\mathrm{nm}$

4.2 Slotted Fabry-Pérot Lasers

In distributed feedback lasers (DFBs) and other such grating based laser structures, the index variations induced by altering the core of the material provide sub-cavity reflective feedback for single mode lasing. This method necessitates a costly process involving two or more growth steps. A cost effective alternative to a DFB is provided by the slotted Fabry-Pérot laser (SFP). In an SFP a surface perturbation is etched into the waveguide stopping just above the quantum wells as shown in Fig. 4.6.

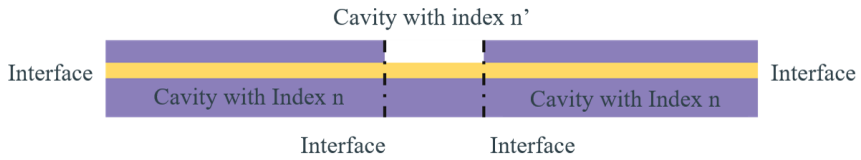

Figure 4.6: Schematic of a waveguide with a single slot

These imperfections induce a local refractive index variation that can be used to select the modes that are maintained in the cavity. By carefully positioning the slot, it is possible to prevent some longitudinal modes from developing in the laser cavity, leading to single-mode lasing. The benefit of this technique is that it can be added to existing lithographic steps used to define the ridge of the laser, requiring no additional fabrication steps. These slots are typically of width 1μm which aligns with standard processing, allowing "slots" to be a more cost effective and less time intensive manner of creating single mode ridge lasers.

A Slotted Fabry-Pérot (SFP) refers to a standard Fabry-Pérot waveguide which has been monolithically integrated with a grating mirror section composed of slots. The slots in an SFP form reflectors within the main cavity by altering the index of refraction in the local area of the perturbation. The SFP can be effectively modelled by the scattering matrix method by considering the slot as a sub-cavity within the main FP etalon. The loss induced by the slot aids in increasing the dominance of a singular longitudinal mode. The slot's loss, reflection and transmission is intrinsically linked to its etch depth as shown in a study completed by Dernaika et. al. [89]. The reflectivity of a slotted laser can thus be calculated by considering the slot as a separate facet-waveguide-facet combination with 3% reflectivity, 15% loss and refractive index n'. Using this technique, a slotted mirror (SM) section with

one slot would have the transfer matrix form of

$$\mathbf{T}_{SM_1} = \mathbf{T}_{in}\,\mathbf{T}_{WG'}\,\mathbf{T}_{in_S}\,\mathbf{T}_{WG_S}\,\mathbf{T}_{out_S}\,\mathbf{T}_{WG''}\,\mathbf{T}_{out} \tag{4.10}$$

where the total length of the etalon, $L = L_{WG'} + L_{WG_S} + L_{WG''}$. $\mathbf{T}_{WG_S}$ is the transfer matrix of the slot waveguide and $\mathbf{T}_{in_S}$ and $\mathbf{T}_{out_S}$ are the facets from and to the regular waveguide to the slot waveguide respectively. The reflective effect of slots can be further compounded with the addition of multiple slots to form an effective single mode reflector. The profile of this reflector can be modelled by isolating the transfer matrix which represents a single slot section $\mathbf{T}_{S_1}$ as,

$$\mathbf{T}_{S_1} = \mathbf{T}_{RF_S}\,\mathbf{T}_{WG_S}\,\mathbf{T}_{RF_S}\,\mathbf{T}_{WG''} \tag{4.11}$$

In Eqn. 4.11, WG'' now represents the unetched waveguide between each consecutive slot which will be prove to be a critical factor in the slot's wavelength selectivity. This allows the transfer matrix of the reflective grating formed by N slots, T_{S_N}, to be expressed as;

$$\mathbf{T}_{S_N} = \left(\mathbf{T}_{RF_S}\,\mathbf{T}_{WG_S}\,\mathbf{T}_{RF_S}\,\mathbf{T}_{WG''}\right)^N \tag{4.12}$$

The reflectivity profile of a slotted mirror (SM) section can be calculated using Eqn. 4.7 and is heavily dependent on the width of the slots, the separation of the slots, the refractive index of the waveguide between slots, and the refractive index of the slot itself.

An SFP, formed from an FP waveguide integrated with a SM section with N slots thus has resonant modes defined by both the transmission modes of the complete length of the FP cavity ($T_{FP}(\lambda)$) modulated by the reflectivity of the slotted mirror section ($R_{S_N}(\lambda)$) with which it is integrated as shown in Fig. 4.7 wherein the output modes of the SFP is thus defined as;

$$\Upsilon(\lambda) \propto T_{FP}(\lambda)\tilde{R}(\lambda) = T_{FP}(\lambda)\,|r_{1,2}\,r_{S_N}(\lambda)| \tag{4.13}$$

Where $\tilde{R}$ is the modulation effect on the transmission modes caused by one side of the FP having a regular non-wavelength selective facet reflectivity $r_{1,2}$ which is not dependent on lambda, while the other side has a wavelength

selective slotted mirror with $r_{S_N}(\lambda)$, which is wavelength dependent. The interaction between the FP etalon and the SM leads to many of the longitudinal modes of the FP section being suppressed.

Fig. 4.7 demonstrates this. This figure shows an etalon with with 6 slots equally distributed across a $1000\,\mu\mathrm{m}$ cavity, each with a widths of $1\,\mu\mathrm{m}$ and a depth sufficient enough to provide 3% reflection. In a standard FP multi-modal behaviour occurs due to all longitudinal modes under the materials gain envelope having equal resonance as shown in blue. The reflectivity of the SM however, shown in red, offers an additional constraint on the allowable modes of the SFP etalon. The resultant resonance spectrum of this interaction, shown in green, demonstrates how the introduction of a SM section leads to few dominant modes preferentially arising within the cavity, leading to single mode lasing.

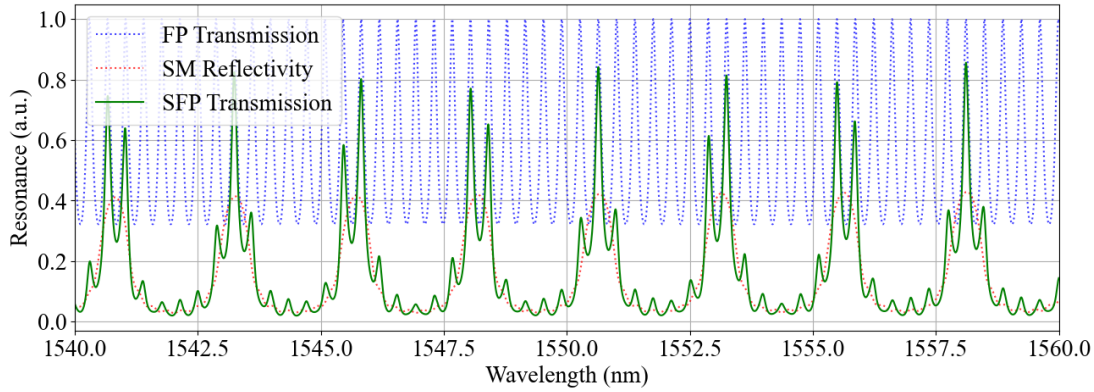

Figure 4.7: Transmission of a $1000\,\mu\mathrm{m}$ cavity (blue), reflectivity of a slotted mirror with a $150\,\mu\mathrm{m}$ separation (red), and the combined resonance (green).

Now by transforming this reflective profile using Eqn. 4.9 we can see in Fig. 4.8 how the SMSR of a multi-modal cavity can be improved.

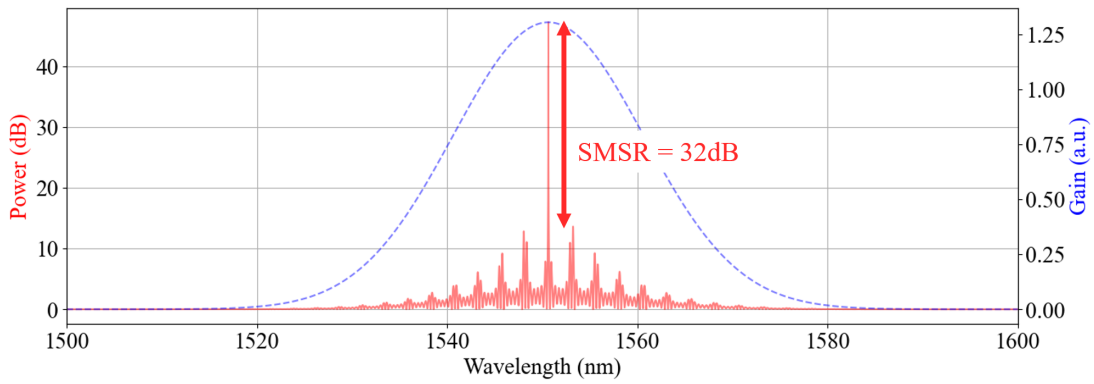

Figure 4.8: The reflectivity of Fig. 4.7 with gain as in Eqn. 4.9

4.2.1 Tuning

The resonant wavelengths in a SFP are dictated as shown in Fig. 4.7 and if the slotted mirror section were to remain unchanged then the wavelengths shown could be tuned between by increasing the current in the gain section of the cavity causing the position of the gain to shift to higher wavelengths and thus overlap with different SFP modes. Monolithically integrated SFPs have their mirror section biased to passivate that section and prevent loss unless a different technique is used to passivate the mirror. Electrically biased waveguides undergo heating unless temperature controlled. Heating effects within the waveguide can change the optical path length of the material. This effect can lead to a change in the reflectivity profile of the etalon.

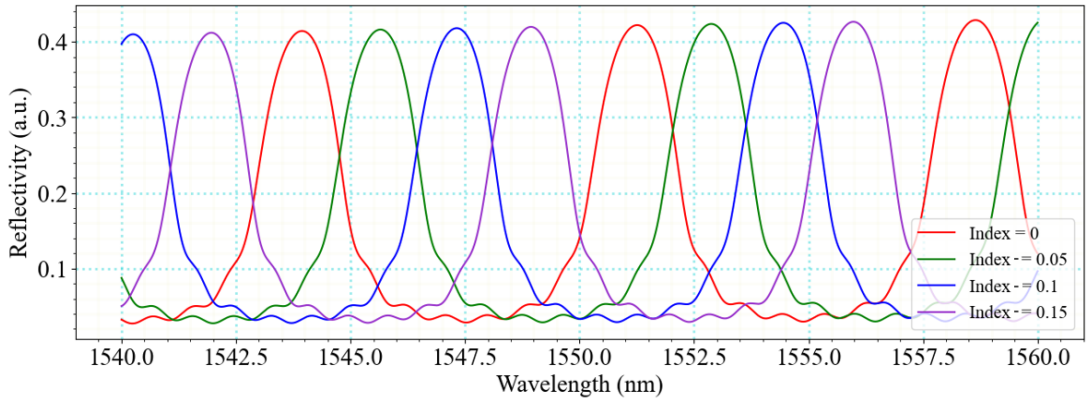

Figure 4.9: The reflectivity versus wavelength for changing refractive index of the waveguide between slots. The number of slots was fixed at 8 and the slot width was $1\mu m$

In simple FP lasers this can often lead to a change in the dominant laser wavelength. By changing the application of a current or voltage we can shift the modal positions of the slotted mirror. We can simulate this by varying the refractive index of the SM section in our simulations, which can be seen in Fig. 4.9.

When designing the SFP the separation between slots in the mirror section can dictate the separation and width of the supermodes created in the slotted mirror section as shown in Fig. 4.10. Smaller slot separations lead to wider supermodes which are farther apart. In theory this could allow for a completely single mode laser for direct wavelength targetting however wider supermodes can fail to suppress neighbouring longitudinal modes of the wavelength of interest.

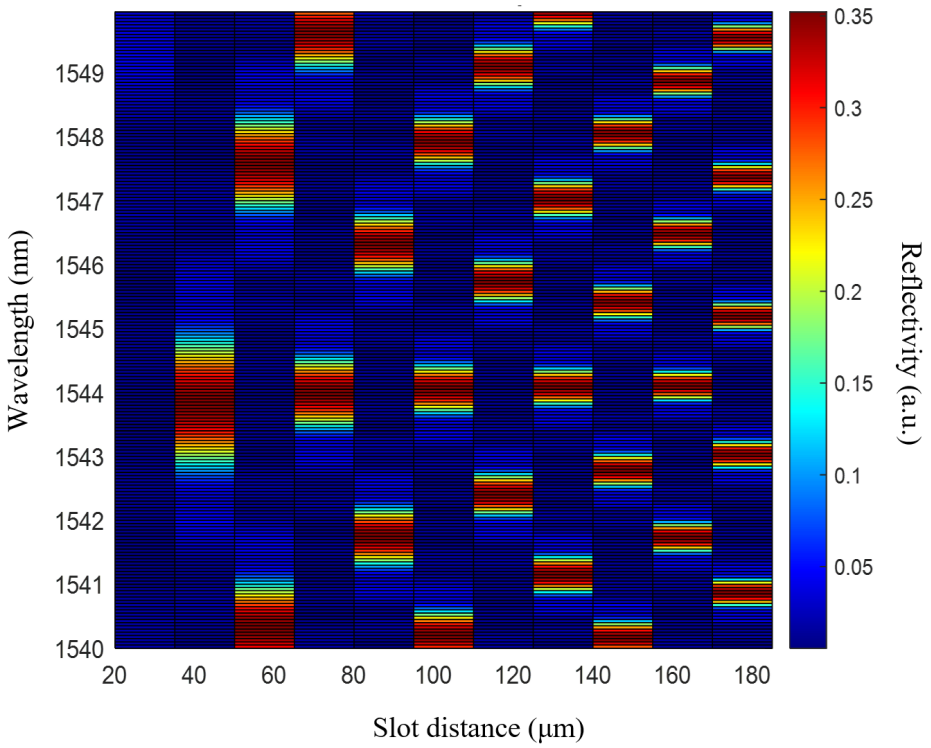

Figure 4.10: The reflectivity versus wavelength for changing slot separations. The number of slots was fixed at 8 and the slot width was $1\mu m$

4.2.2 Single Section Slotted Fabry-Pérot Laser Testing

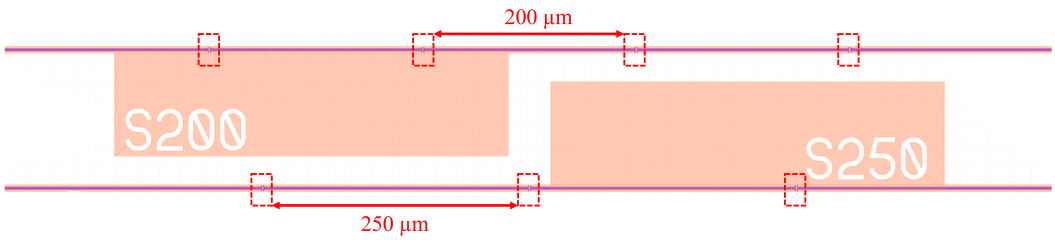

Figure 4.11: A view of the lithographic mask design for the single section SFP. The numbers in the metal layer represent the separation between slots which are highlighted in red. The slot width is $1\,\mu\mathrm{m}$

To experimentally verify this behaviour, a single section laser with slots etched into the gain section was fabricated and characterised. This device consisted of a $1000\,\mu\mathrm{m}$ long cavity enclosed by two cleaved facets. Three slots were equally distributed across the cavity resulting in a slot separation of $250\,\mu\mathrm{m}$. The results of this characterisation are shown in Fig. 4.12.

The device can be seen to perform well with good single mode behaviour at $I = 2I_{th}$ however at $I = 3I_{th}$ the single mode behaviour is lost. Similar behaviour was observed for single section slotted devices where the number of slots was varied from 3-8. Initial single mode behaviour was observed. However, increased current saw the empowerment of neighbouring modes. Thus, single section slotted Fabry-Pérot lasers offer a simple method of turning an FP cavity into a single mode laser but the small range of operable currents and the lack of tunability severely limit the usefulness of this design.

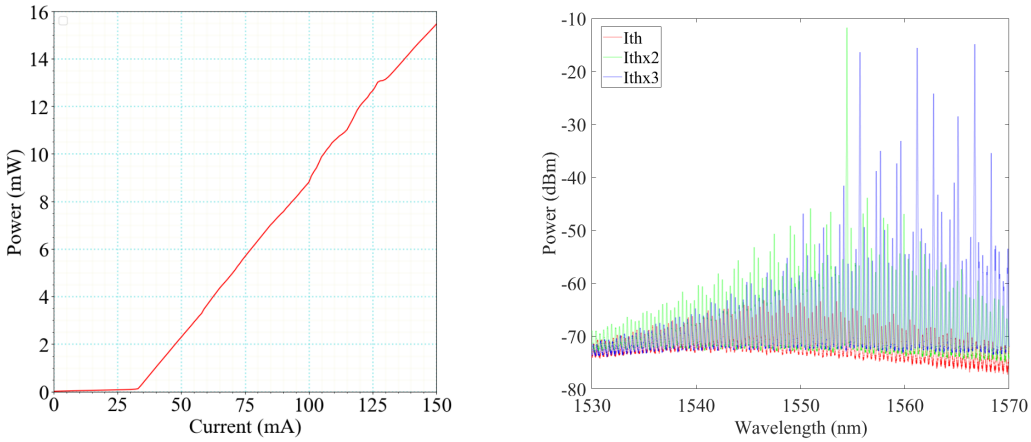

(a) LI curve of a single section SFP with 3 slots $250\,\mu$m apart

(b) Spectra from a single section SFP at various currents

Figure 4.12: Experimental measurements of an FP laser with slots etched into the gain section

The device performance matched well with the simulated single mode operation predicted from simulations as seen in Fig. 4.13.

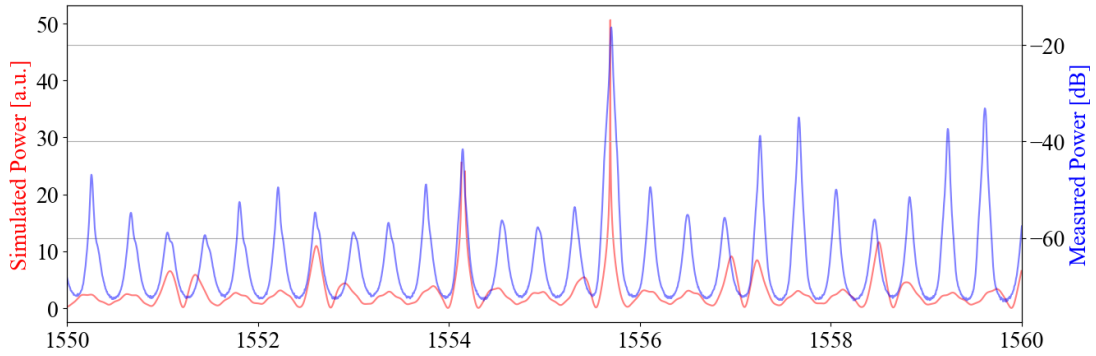

Figure 4.13: A comparison of the experimentally measured spectra of a $1000\,\mu m$ device with 3 slots placed $250\,\mu m$ apart (blue) and the corresponding simulated power output (red) showing a good match for a separation of $250\,\mu m$ with $n = 3.22$.

The number of slots present in a section can also be seen to increase the loss in that section. Fig. 4.14 shows how increasing the number of slots increases the threshold current and reduces the slope efficiency in an FP cavity of length $1000\,\mu\mathrm{m}$.

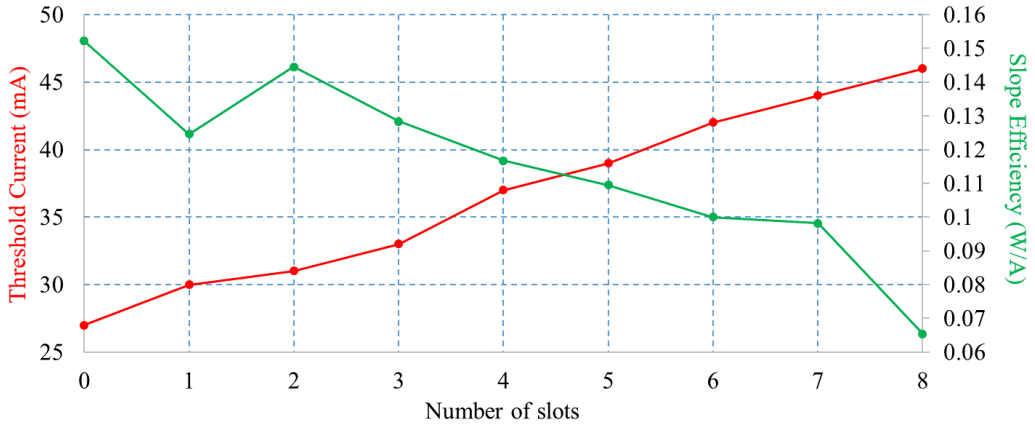

Figure 4.14: The number of slots in a $1000\,\mu\mathrm{m}$ device v.s. the measured threshold current and slope efficiency

4.2.3 Two Section Slotted Fabry-Pérot Laser Testing

Figure 4.15: A view of the lithographic mask design for the two section SFP with six slots spaced $108\,\mu\mathrm{m}$ apart and a gain length of $800\,\mu\mathrm{m}$

Although the wavelength selectivity of a slotted waveguide offers excellent suppression of unwanted modes, its usefulness is limited as increasing the power of this section changes the positioning of the slotted modes and allows additional unsuppressed modes to lase. This limitation can be overcome by combining a slotted waveguide with an additional electrically isolated straight FP etalon as seen in the two section laser. The slotted section acts as a wavelength selective mirror and is given enough power to be optically passive while the section without slots is operated as a gain section, being the main source of the laser's power output. This style of slotted laser is what is normally being referenced when a slotted Fabry-Pérot (SFP) is mentioned, thus moving forward to distinguish between the two slotted lasers mentioned we will refer to a laser made from a single section containing slots as a single section slotted Fabry laser (SSFP).

Fig. 4.16 shows the LI curve obtained from experimental measurements of an SFP with six slots spaced $108\,\mu\mathrm{m}$ apart and a gain length of $800\,\mu\mathrm{m}$. The threshold current and the peak power of the laser can be seen to depend heavily on the current supplied to both sections. A threshold current and maximum power of $50\,\mathrm{mA}$ and $4\,\mathrm{mW}$ is observed when the mirror section is set at $10\,\mathrm{mA}$. The threshold current is reduced to $10\,\mathrm{mA}$ at a mirror section bias of $60\,\mathrm{mA}$ while the maximum output power of the laser increases to $12\,\mathrm{mW}$.

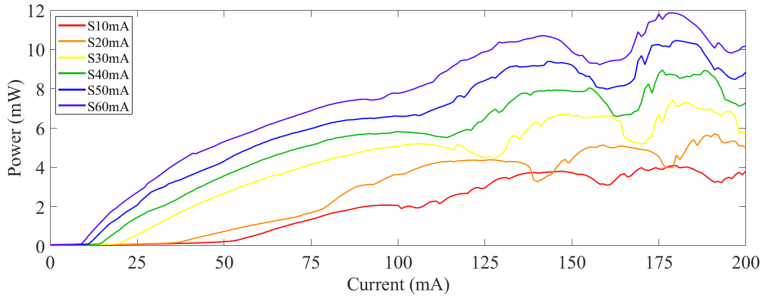

Figure 4.16: An experimentally measured LI of the dual slot Fabry-Pérot Laser with varying left (L) and right (R) mirror currents. Each colour represents a different bias current on the mirror section from $10\,\mathrm{mA}$ (red) to $60\,\mathrm{mA}$ (purple).

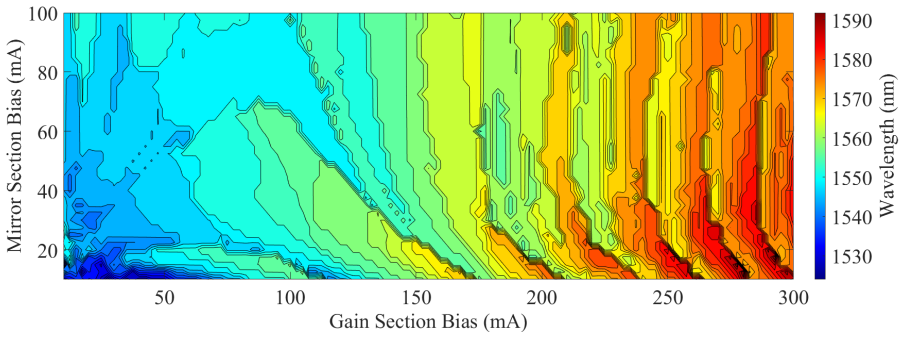

Figure 4.17: An experimental measurement of a two section slotted device comparing section currents and the resultant wavelength.

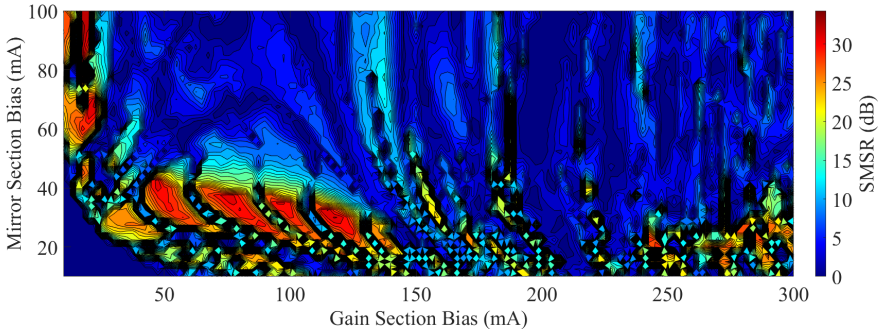

Figure 4.18: An experimental measurement of a two section slotted device comparing section currents and the resultant SMSR.

Fig. 4.17 shows the resultant peak wavelengths obtained by sweeping the currents applied to the gain and mirror section from $20-300\,\mathrm{mA}$ and $10-100\,\mathrm{mA}$ respectively. Using a slotted mirror rather than a slotted gain section leads to an improvement in the SMSR and now allows us to tune between the supermodes present in the slotted mirror, similar to those shown in Fig. 4.7. Fig. 4.18 shows the resultant SMSR corresponding to these wavelengths. Similar to the single section slotted laser, this single mode behaviour fails when the gain section or the mirror section receive higher currents. This limits both the continuity of the output laser spectrum and the extent of the lasers tunability. This also limits the overall power output of the laser as we are only interested in areas of the laser where we can achieve good single mode behaviour. It is interesting to note from the figures we can observe that this also implies that the highest power obtained from the SFP occurs when both sections receive sufficiently high current however our colour maps show that this point of operation does not achieve high SMSR.

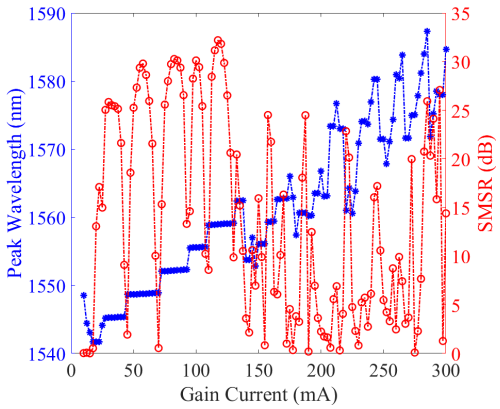

(a) Gain current vs the peak wavelength and corresponding SMSR while the mirror section was fixed at $30\,\mathrm{mA}$

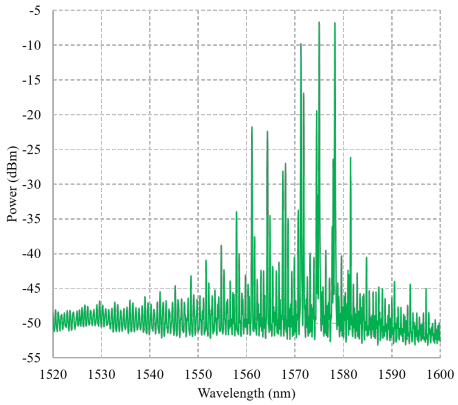

(b) Spectrum of the SFP with the mirror section at $30\,\mathrm{mA}$ and the gain section at $275\,\mathrm{mA}$

Figure 4.19: SFP behaviour while the mirror section was at a fixed 30mA

We can take a closer look at the tuning behaviour of the SFP device by observing how the peak wavelength and SMSR of the device vary with gain current at set mirror currents. Fig. 4.19a shows how the peak wavelength and corresponding SMSR change with current supplied to the gain section while the mirror section is fixed at $30\,\mathrm{mA}$. Here we can see how the wavelength changes somewhat linearly with the current supplied to the gain section but the wavelength output is discontinuous, with minimal change being observed over $10\,\mathrm{mA}$ before the emission wavelength jumps to the next supermode. We

can note that at around $150\,\mathrm{mA}$ this behaviour breaks down and the peak wavelength breaks the previously established trend. The peak wavelength trends towards higher wavelengths but switches unpredictably at increasing currents with much narrower regions of high SMSR.

Fig. 4.19b shows a spectrum obtained from the SFP while the mirror section was set at $30\,\mathrm{mA}$ and the gain section was set at $275\,\mathrm{mA}$ so we can observe what is happening during the breakdown of the high SMSR operation. We can see that as the power of the laser has increased, multiple sidemodes have increased in power relative to the central mode of the laser, $1575\,\mathrm{nm}$, with a nearby wavelength, $1578\,\mathrm{nm}$ achieving near identical power. The limitations of an SFP are similar to the limitations of the single section slotted laser as seen in Fig. 4.12b. When an FP etalon becomes an FP laser, each of these longitudinal modes has the same reflectivity which causes as many of them to lase simultaneously as the material gain of the laser allows. The supermodes present in the mirror section also have an equal reflectivity which means that when the SFP receives sufficient power multiple wavelengths will begin to lase simultaneously. This limits the SFP to discontinuous tuning.

By observing all of the wavelengths that can be obtained from electrically sweeping both the slotted mirror section and the gain section the modal behaviour of the SFP device becomes clearer. Fig. 4.20 shows the spread of wavelengths vs SMSR for the SFP device wherein each point on the graph represents the results of an individual spectrum taken at each bias point of the laser. Here the full tuning spread of the laser becomes clear with a full range of $40\,\mathrm{nm}$ of high SMSR ($>30\,\mathrm{dB}$) wavelengths being available between $1545\,\mathrm{nm}$ and $1585\,\mathrm{nm}$.

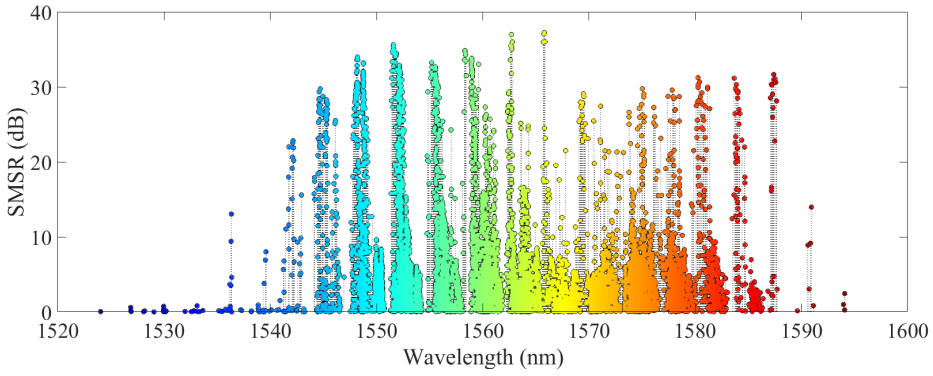

Figure 4.20: Experimentally measured Wavelength vs SMSR for each collected spectrum of the SFP. Each point on the graph represents a a spectrum collected under different bias conditions.

In Fig. 4.20 the supermodes of the device are quite clear as the tuning spread of the SFP is discontinuous across its wavelength range. As seen in Fig. 4.21a, we can map the positioning of these supermodes quite closely by comparing them to our simulated mirror supermodes for a slotted mirror waveguide with a slot separation of $108\,\mu\mathrm{m}$ with an index of $n_{WG} = 3.217$. The etched part of the waveguide was taken to have an index of $n_S = 3.193$.

Not all of the single mode emissions observed from the full sweeping of the device align to the original mirror reflectivity shown in Fig. 4.21a. Some of the high SMSR spectral outputs can be attributed to the supermodes generated by a slotted mirror with altered refractive index due to increased current supply and the resultant bandgap shrinkage. Fig. 4.21b shows the wavelength vs SMSR output of the laser aligned to a slotted mirror with $n = 3.215$. We can see that some of the wavelengths which did not align with a mirror section of index $n = 3.217$ now align to this higher index mirror section. We can note from these observations that the most consistent single mode outputs occur when the mirror has a low bias, enough to be optically passive. An increased current in the mirror section allows for longer wavelengths to be achieved but with less consistent emission than the passive mirror section as evidenced by the scarcity of high SMSR emissions at longer wavelengths.

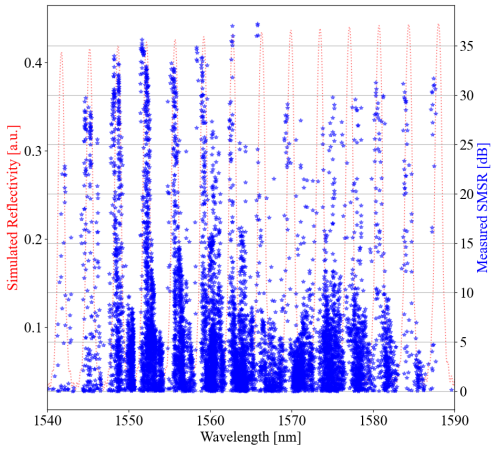

(a) Wavelength vs SMSR for the SFP device (blue) compared to a simulated reflectivity of a slotted mirror with $n = 3.217$ (red)

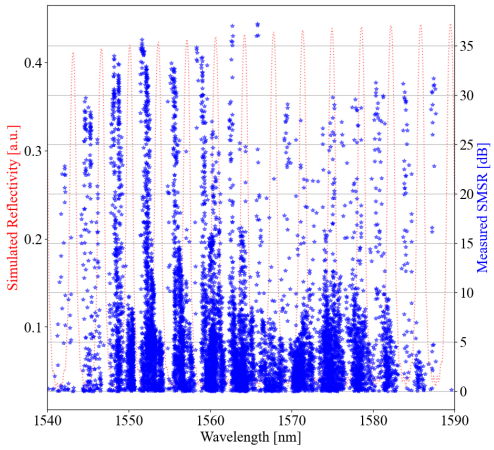

(b) Wavelength vs SMSR for the SFP device (blue) compared to a simulated reflectivity of a slotted mirror with $n = 3.215$ (red)

Figure 4.21: Experimental vs simulated output of a the SFP with a slot separation of $108\ \mu m$

4.3 Dual-mirror Slotted Fabry-Pérot Lasers

When an FP etalon becomes an FP laser, each of these longitudinal modes has the same resonance which causes as many of them to lase simultaneously as the material gain of the laser allows. The supermodes present in the mirror section also have an equal resonance which means that when the SFP receives sufficient power multiple wavelengths will begin to lase simultaneously. This limits the single-mirror SFP to discontinuous tuning between the supermodes as tuning is achieved by changing the current across the gain section of the device. This effect can be overcome by using two SMs at either side of FP etalon to act as overlapping wavelength selective mirrors. By choosing SMs with different spacings, the modal selectivity of two SMs can be aligned to favour a single one of the supermodes leading to the outer supermodes being suppressed. Fig. 4.22 shows an SFP with slot separation of $36\,\mu\mathrm{m}$ for the left mirror, M_1, with the addition of a secondary slotted mirror on the right, M_2, with a slot separation of $74\,\mu\mathrm{m}$. It can be seen that now the supermodes generated by the slotted mirror are imbalanced with one wavelength, $\lambda = 1550.5\,\mathrm{nm}$, having the highest resonance.

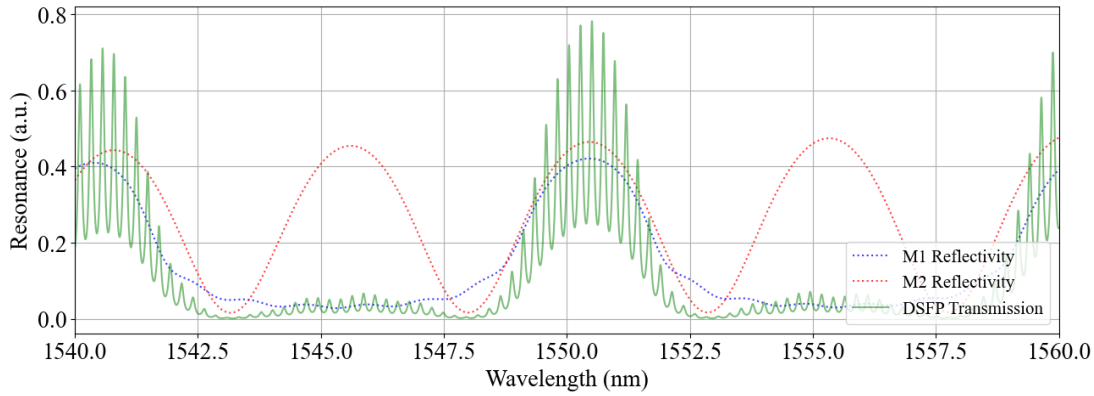

Figure 4.22: A Dual-mirror slotted Fabry-Pérot (DSFP) with overall cavity length $1600\,\mu m$. Mirror 1 has $74\ \mu m$ slot separation (red). Mirror 2 has $36\mu m$ slot separation (blue). The DSFP resonant peaks are shown in green.

Fig. 4.23 shows the resonance of Fig. 4.22 converted into lasing modes using Eqn. 4.9. We can note that previous side-modes present in an SFP as shown in Fig. 4.8 are further suppressed by the usage of two slotted mirrors. This leads to a simulated $8\,\mathrm{dB}$ increase in the SMSR for our device when compared to Fig. 4.8 when using the same gain profile. The additional mirror does increase the overall length of the device which is reflected in the increased number of longitudinal modes.

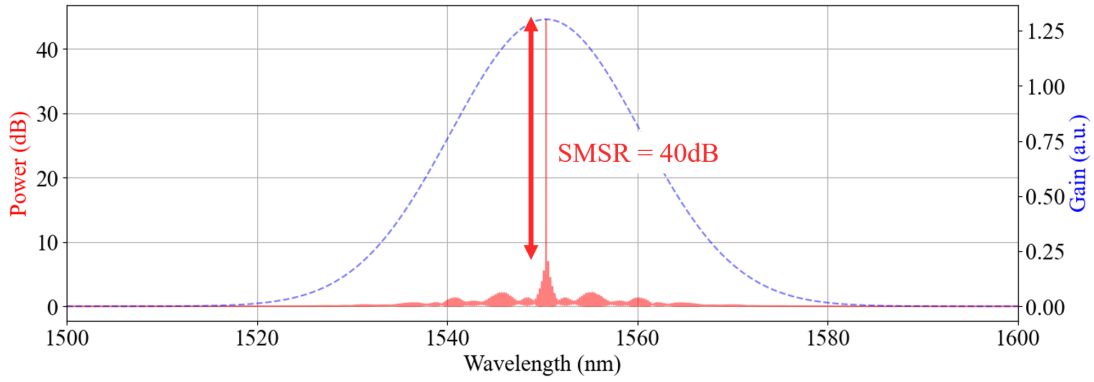

Figure 4.23: Simulated available lasing modes of Fig. 4.22

4.3.1 Dual-mirror Slotted Fabry-Pérot Testing

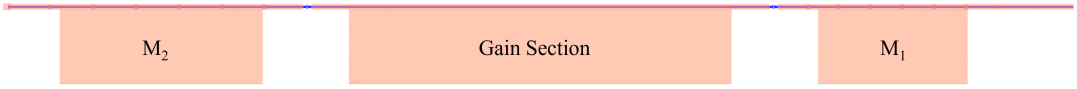

Figure 4.24: A view of the lithographic mask design for the three section SFPs. The gain section had length $800\,\mu\mathrm{m}$. The two surrounding mirror sections have 6 slots each. M1 had a slot separation of $36\,\mu\mathrm{m}$. M2 had a slot separation of $74\,\mu\mathrm{m}$.

Using the device model several suitable combinations of slot separations were designed to facilitate fabrication of an array of three section DSFPs. This device has two slotted mirrors, M_1 and M_2. M_1 had a slot separation of $36\,\mu\mathrm{m}$. M_2 had a slot separation of $74\,\mu\mathrm{m}$ each with 6 slots. The DC characteristics of the device were first examined. The device was mounted on a temperature controlled chuck at $20\,^{\circ}\mathrm{C}$, and a lensed optical fibre was used to couple light from right side of the device. To test the LI output of the laser, the current through the gain section was swept while both surrounding mirror sections (mirror section 1&2) were maintained at a set current. The current sweep on the gain section was repeated for varying mirror section currents. The results are shown in Fig. 4.25. The threshold of the laser can be seen to vary, depending on the current across the three sections with the smallest noted threshold being $12\,\mathrm{mA}$.

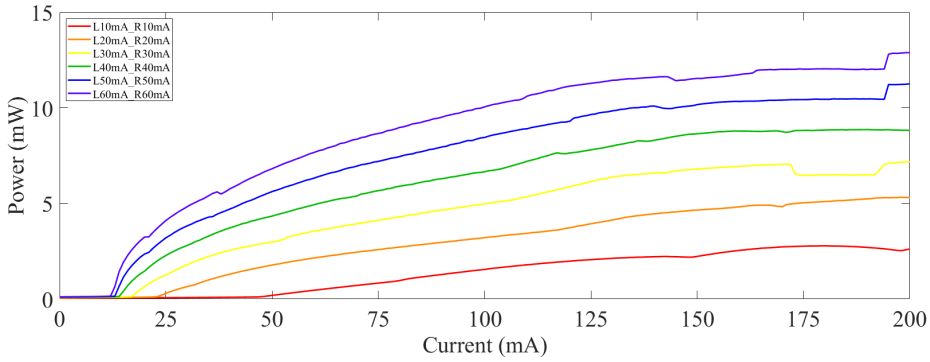

Figure 4.25: An experimentally measured LI of the dual-mirror slotted Fabry-Pérot Laser with varying left (L) and right (R) mirror currents.

The tuning of the DSFP involved varying the current across three different sections, gain, the left mirror; M_1, and the right mirror; M_2. The light was then coupled into a lensed fiber and then into a Yokogawa OSA to measure the resultant spectra. This measurement was collected through a program written in LabVIEW which varied the current on each of these three sections and collected a spectrum at each point of variance. The mirror sections were each independently varied from $20\,\mathrm{mA}$-$200\,\mathrm{mA}$ with a step size of $10\,\mathrm{mA}$. The gain section was varied from $20\,\mathrm{mA}$-$300\,\mathrm{mA}$ with a step size of $10\,\mathrm{mA}$. The total number of spectra obtained was 10469 of which 40.6% had an SMSR $>30\,\mathrm{dB}$, 30.1% had an SMSR between $30\,\mathrm{dB}$ and $20\,\mathrm{dB}$, and 7.3% had an SMSR between $20\,\mathrm{dB}$ and $10\,\mathrm{dB}$. Fig. 4.26 shows a sample of the wavelengths that were able to be obtained from the DSFP ranging from 1530-$1590\,\mathrm{nm}$. Each of these samples is $\sim 5\,\mathrm{nm}$ apart. The full list of wavelengths obtained v.s the corresponding SMSR is shown in Fig. 4.27.

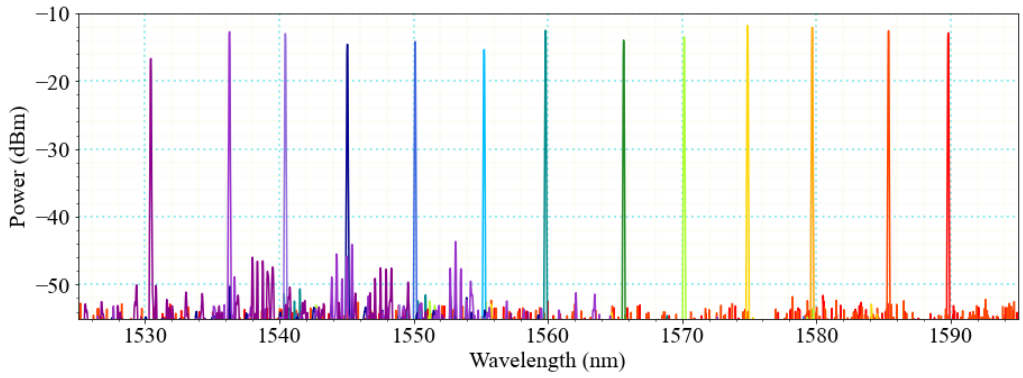

Figure 4.26: A selection of experimentally measured spectra with $\sim 5\,\mathrm{nm}$ gaps showcasing some of the available lasing wavelengths

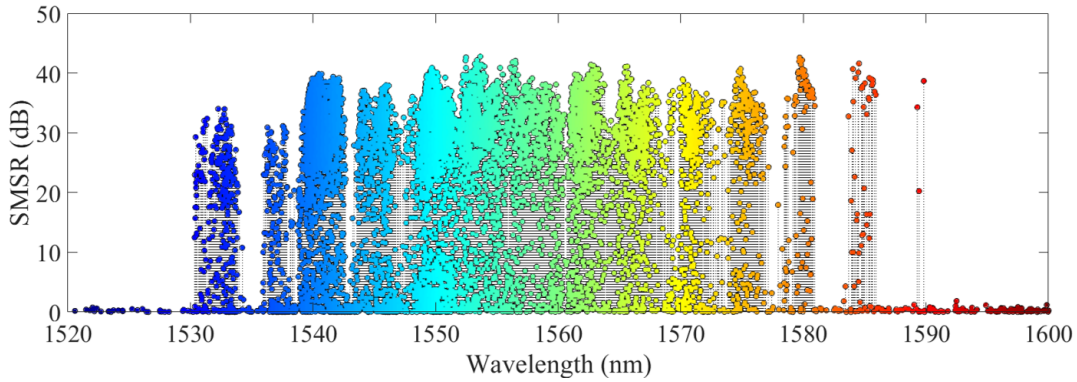

Figure 4.27: Experimentally measured Wavelength vs SMSR for each collected spectrum of the DSFP.

The selection of the wavelengths is determined by the currents of mirror sections; M_1 and M_2. By setting the supermodes using the first mirror we generate a series of possible supermodes within which our main mode is capable of occurring. This behaviour is shown experimentally in Fig. 4.28a where we can see that when the spectra are divided by the current supplied to M_1 distinct grouping patterns become apparent. Using our previous simulation techniques we can see how these groupings correspond to the supermodes generated by M_1.

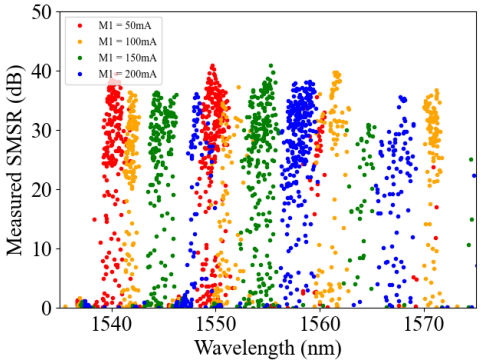

(a) SMSR measured from fixing the current in M_1 and varying the current in M_2 and the gain.

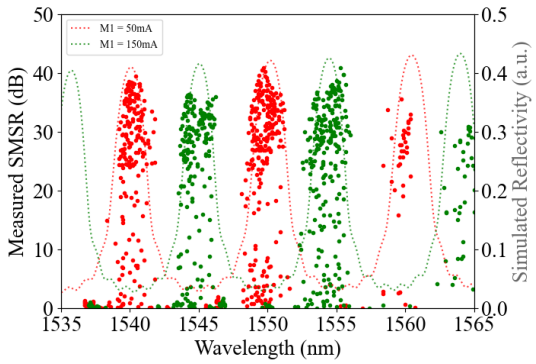

(b) A comparison of SMSR measured with simulated reflectivities for a $36\,\mu\mathrm{m}$ separation with $n = 3.217$ (red) and $n = 3.147$ (green)

Figure 4.28: Experimental measurements of the DSFP device with M_1 at fixed currents. M_2 was varied from $20\,\mathrm{mA}$-$200\,\mathrm{mA}$ with a step size of $10\,\mathrm{mA}$. The gain section was varied from $20\,\mathrm{mA}$-$300\,\mathrm{mA}$ with a step size of $10\,\mathrm{mA}$.

Fig. 4.28b shows a good agreement between the measured values and the reflectivity envelope generated by a slot spacing of $36\,\mu\mathrm{m}$ with $n = 3.217$ for a

M_1 current of $50\,\mathrm{mA}$ (red) and $n = 3.147$ for a M_1 current of $150\,\mathrm{mA}$ (green) as shown. Similarly it can be shown that an M_1 current of $100\,\mathrm{mA}$ and $200\,\mathrm{mA}$ can be obtained using $n = 3.187$ and $n = 3.107$ respectively. Increasing current across the mirror section causing the bandgap in this section to shrink reducing the refractive index of the area in our simulations and shifting the supermode position.

Tuning between these supermodes can be seen in Fig. 4.29a. Increasing current in either section causes a minor change in wavelength until the next supermode becomes available. Fig. 4.29b shows that during the transition between these modes the SMSR of the device is reduced. This is similar to the two section SFP, however the key difference being that due to the additional mirror, both the gain section and the secondary mirror section, M_2, can be pumped to higher currents while still maintaining areas of high SMSR. The ability to vary both sections while maintaining a high SMSR allows the DSFP to lase at a wide variety of wavelengths. Smaller variations in wavelength can be obtained by fixing both mirror sections and varying the current across the gain and larger changes in wavelength can be obtained by keeping one mirror section, such as M_1, fixed and varying the current across both the gain and the other mirror section, in this case M_2.

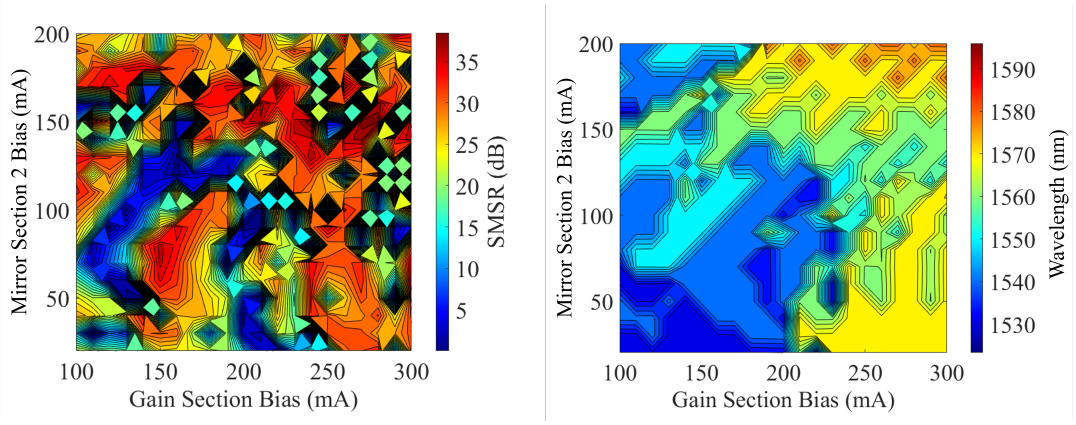

(a) Wavelength versus the current supplied to the gain section and M_2 when M_1 is fixed at $150\,\mathrm{mA}$

(b) SMSR versus the current supplied to the gain section and M_2 when M_1 is fixed at $150\,\mathrm{mA}$

Figure 4.29: Colour plot measurements of the DSFP device with M_1 at fixed currents.

This method of control on its own allows a full wavelength spread of nearly $60\,\mathrm{nm}$ and $> 20\,\mathrm{nm}$ of continuous $50\,\mathrm{GHz}$ channel spacings to be obtained

within this tuning range as shown in Fig. 4.30a. The power level of the spectra in this figure are normalised to compensate for a noted fibre drift which led to a decrease in fibre coupling over the course of the spectra collection. By introducing thermal variance into the system using the temperature controlled chuck at $25\,°\mathrm{C}$ and $30\,°\mathrm{C}$ the gaps present in this spread can be filled to create $> 40\,\mathrm{nm}$ of continuous $50\,\mathrm{GHz}$ channel spacing to an accuracy of $1\,\mathrm{GHz}$ as seen in Fig. 4.30b.

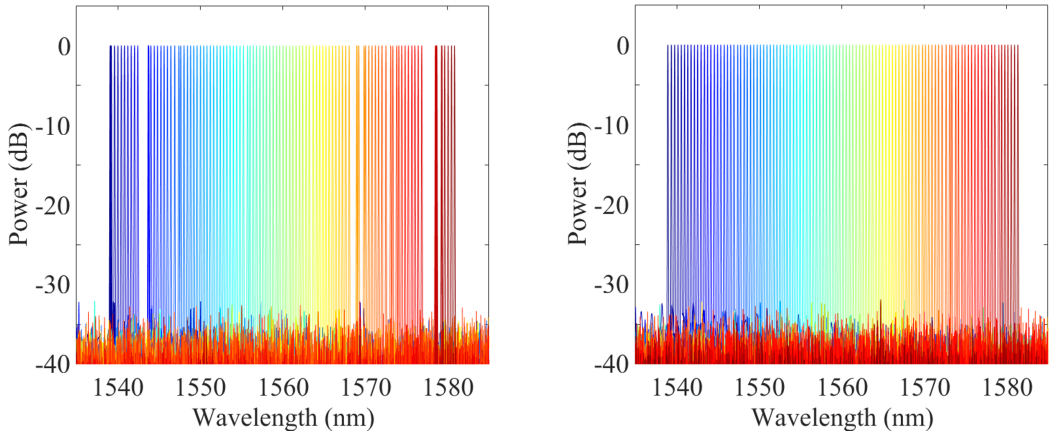

(a) Wavelength spread of the device with $50\,\mathrm{GHz}$ spacing

(b) Wavelength spread of the device with $50\,\mathrm{GHz}$ spacing with additional spectra taken from thermal tuning of the device

Figure 4.30: Wavelength spread of the device showing $> 40\,\mathrm{nm}$ $50\,\mathrm{GHz}$ spacing achieved. Spectra are normalised to $0\,\mathrm{dB}$ to accommodate for variations on power due to optical fibre drift during automated measurements.

4.3.2 Dual-mirror Slotted Fabry-Pérots as Externally Modulated Laser Sources

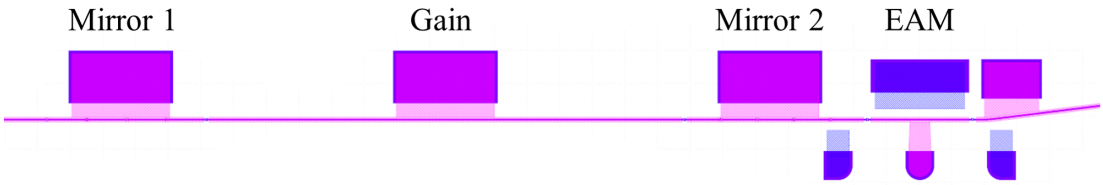

Figure 4.31: A schematic view of the DSFP integrated monolithically with an electro-absorption modulator.

The large tuning range of the DSFP allows it to be monolithically integrated with an electro-absorption modulator (EAM). The DSFP device shown previously was integrated with an EAM as shown in Fig. 4.31. The DSFP was then set to specific wavelengths by tuning the 3 sections; gain, M_1, and M_2, in order to produce high SMSR single mode lasing at these wavelengths. The light from the DSFP was then collected into a fibre through the EAM, whose bias was varied from $1\,\mathrm{V}$ to $-3\,\mathrm{V}$ in steps of $0.25\,\mathrm{V}$

In general, monolithic integration between lasers and EAMs on the same material proves difficult as the primary emission peak of the laser aligns with the absorption peak of the material. Thus, the change in absorption via a change in voltage does not produce a significant change in the measured power outputted from the EML. EAMs operate at $\leq 0\,\mathrm{V}$, and as Fig. 4.32 shows, lower wavelengths such as $1549\,\mathrm{nm}$ are already heavily absorbed at $0\,\mathrm{V}$.

Longer wavelengths avoid this as seen at $1579\,\mathrm{nm}$. The monolithic integration of high speed lumped element EAMs to form EMLs minimises the loss from laser coupling compared to off-chip modulators or regrown modulators. Lumped element EAMs can be made to achieve bandwidths $\geq 70\,\mathrm{GHz}$ [90]. Thus, a monolithically integrated EML when incorporated with techniques such as transfer printing [91] could provide a highly efficient modulated light source for the silicon platform.

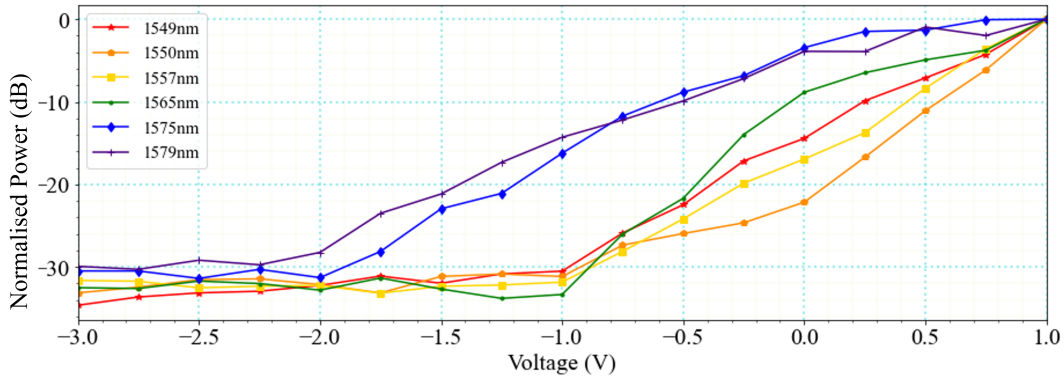

Figure 4.32: With the DSFP set to specific wavelengths the light was injected into a monolithically integrated EAM and the voltage across the EAM was varied. The normalised result of the change in power is presented for various tuned wavelengths set via varying the current across the three DSFP sections.

The design shown in Fig. 4.31 shows the device that we will use for our EML. The material and process used thus far however will not produce the high speed required for this project due to the relatively large parasitic capacitance associated with the n-doped substrate of the material. In the next chapter we will focus on developing a high-speed compatible process using a semi-insulating substrate to optimise the modulation speed of our device. The remainder of this chapter will detail the exploration of alternative laser designs which were investigated in parallel to the DSFP, outlining their design, benefits, and drawbacks.

4.4 Pitted Fabry-Pérot Lasers

Slots offer an innovative manner of introducing index perturbations along the laser cavity without introducing too much loss into the structure. The main downside of slots however is due to their depth sensitivity, which means that their absolute repeatability is poor in a research environment.

Another method of index perturbation can be attained by etching small circular holes in the waveguide down past the quantum wells through to the substrate as seen in Fig. 4.33. These circular holes are referred to as "pits" and operate in much the same way as slots. The main benefit of these pits is that, as the etch goes through the quantum wells entirely, their performance is insensitive to the specific etch depth.

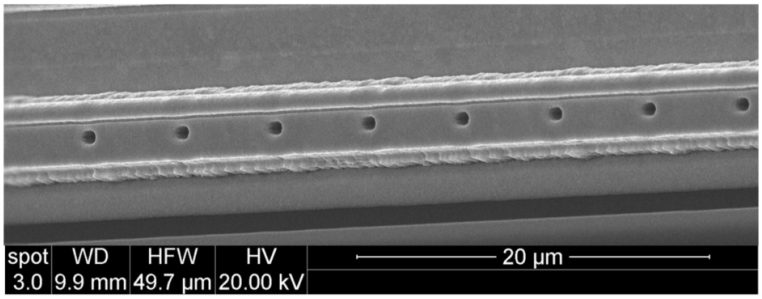

Figure 4.33: A SEM image of a waveguide with multiple pits etched, each with a diameter of $1\,\mu\mathrm{m}$

A pitted mirror (PM) can be modelled similarly to the slotted mirror, the main difference being that while the slot is formed by two interfaces and the shallow etched waveguide in between, the pit can be treated as a single mirror interface. The reflectivity and loss of a single pit are virtually identical to that of a slot, thus we can use $T_P = T_{RF_S}$ [89]. As such, a PM with N pits can be modelled as;

$$T_{PM} \;=\; \left(T_{WG''}\, T_P\right)^N \tag{4.14}$$

Using this we can write the equation for pitted Fabry-Pérot (PFP) as;

$$T_{PFP} \;=\; T_{RF}\, T_{WG}\, T_{PM}\, T_{RF} \tag{4.15}$$

The interaction between the FP etalon and the PM leads to many of the longitudinal modes of the FP section being suppressed. Fig. 4.34 demonstrates

this. In a standard FP, multi-modal behaviour occurs due to all longitudinal modes under the material's gain envelope having equal resonance as shown in blue. The reflectivity of the PM however, shown in red, offers an additional constraint on the allowable modes of the PFP etalon. The resultant reflectivity spectrum of this interaction, shown in green, demonstrates how the introduction of a PM section leads to few dominant modes preferentially arising within the cavity, leading to single mode lasing.

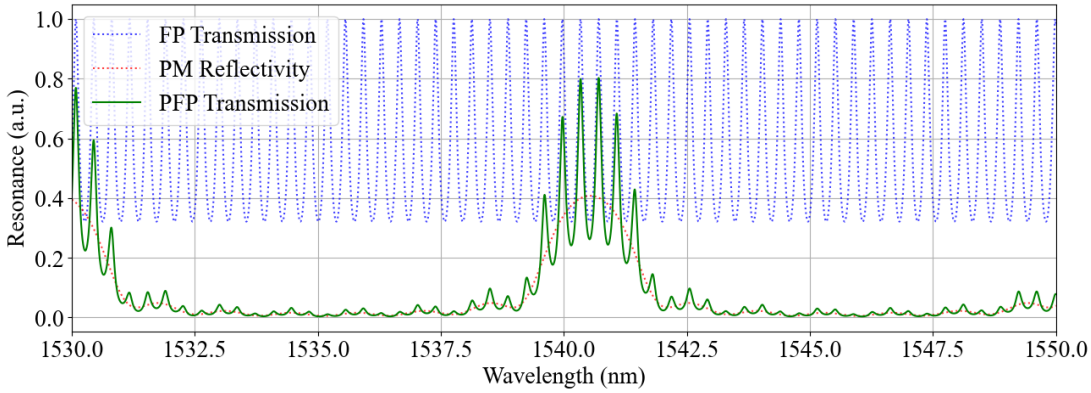

Figure 4.34: Transmission of a $1000\,\mu\mathrm{m}$ cavity (blue), reflectivity of a pitted mirror with a $34\,\mu\mathrm{m}$ separation (red), and the combined resonance (green).

Now by transforming this resonance profile using Eqn. 4.9 we can see in Fig. 4.35 how the SMSR of a multi-modal cavity can be improved.

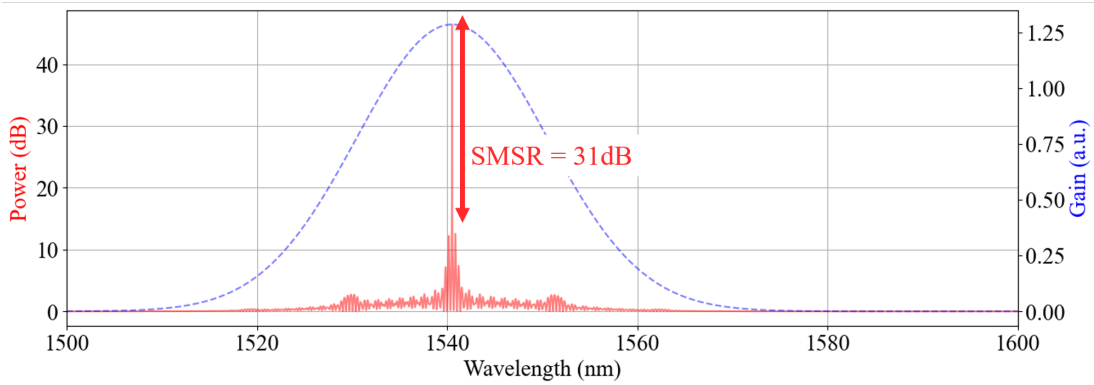

Figure 4.35: The reflectivity of Fig. 4.34 with gain as in Eqn. 4.9

Fig. 4.36 shows how the spacing of the pits changes the supermodes present in the pitted mirror.

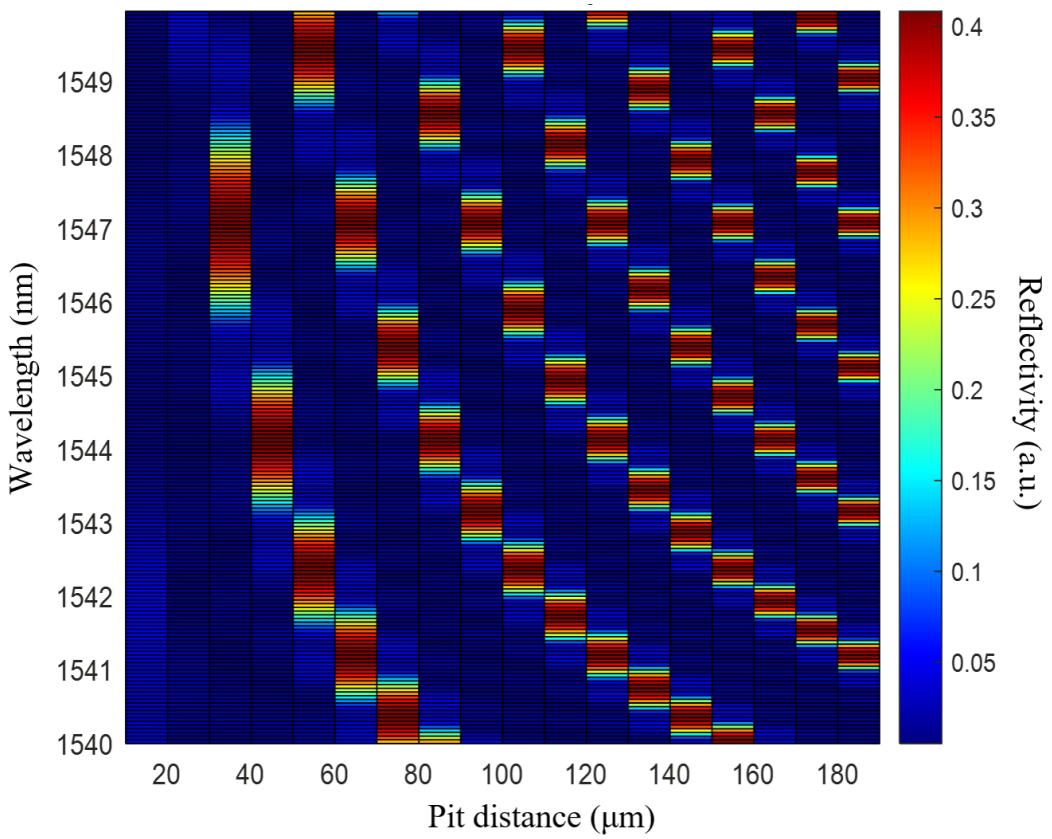

Figure 4.36: The reflectivity versus wavelength for changing pit separations. This simulation used 10 pits each with a diameter of $1\,\mu\mathrm{m}$ to cause a 3% reflection.

4.4.1 Single Section Pitted Fabry-Pérot Laser Testing

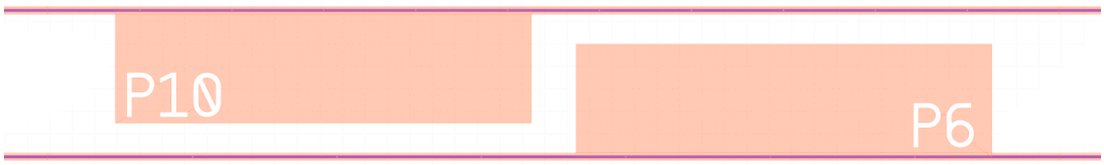

Figure 4.37: A view of the lithographic mask design for the single section PFP. P6 is a device with 6 pits equally dispersed throughout the cavity. P10 is a device with 10 pits equally dispersed throughout the cavity.

To experimentally verify the use of pits to form single mode lasers, a single section laser with pits etched into the gain section was fabricated and characterised. This device consisted of a $1000\,\mu\mathrm{m}$ long cavity enclosed by two cleaved facets. Pits were equally distributed across the cavity. The results of this characterisation for a device with 16 pits are shown in Fig. 4.38.

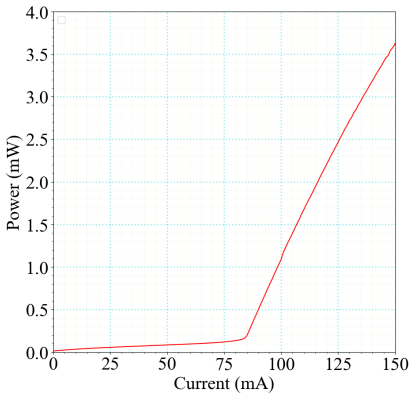

(a) LI curve of a single section PFP with 3 pits $250\,\mu\mathrm{m}$ apart

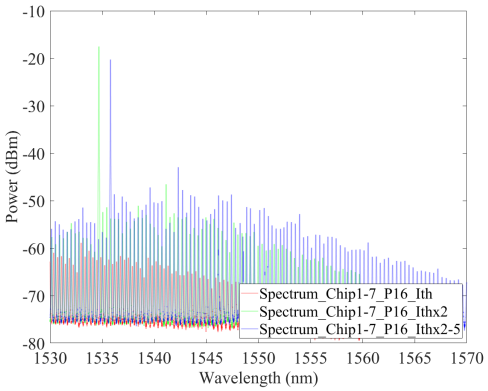

(b) Spectra from a single section PFP at various currents

Figure 4.38: Experimental measurements of an FP laser with pits (PFP) etched into the gain section

The device can be seen to perform well with good single mode behaviour at $I = 2I_{th}$ and $I = 2.5I_{th}$. Single section pitted devices where the number of pits was varied from 4-24 were produced. An interesting point identified through the testing of these devices is that, compared to the same number of slots, more pits were required to attain single mode lasing from the device. Single section pitted Fabry-Pérot lasers offer a simple method of turning an FP cavity into a single mode laser however single mode lasing requires a significant

number of pits which incurs more loss in the device, increasing its threshold current.

The single mode operation of the 16 pit device matches well with predicted simulations as seen in Fig. 4.39.

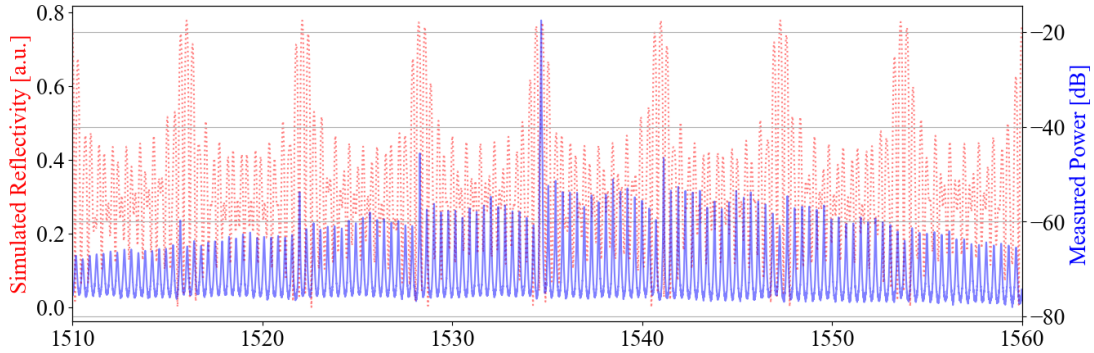

Figure 4.39: A comparison of the experimentally measured spectra of a $1000\ \mu m$ device with 16 pits placed $62.5\ \mu m$ apart (blue) and the corresponding simulated reflectivity values (red) showing a good match for a separation of $62.5\ \mu m$ with $n = 3.22$.

The number of pits present in a section increases the loss in that section. Fig. 4.40 shows how increasing the number of pits increases the threshold current and reduces the slope efficiency in an FP cavity of length $1000\,\mu\mathrm{m}$.

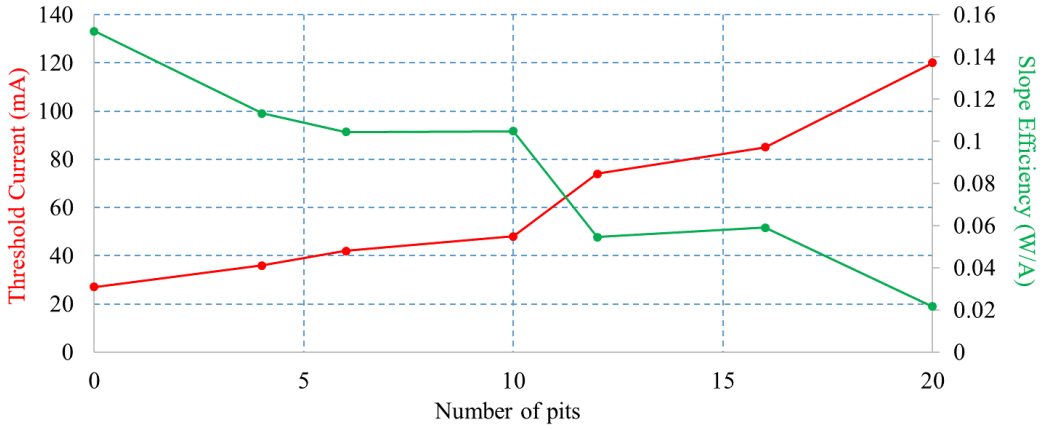

Figure 4.40: The number of pits in a $1000\ \mu m$ device v.s. the measured threshold current and slope efficiency

4.4.2 Two Section Pitted Fabry-Pérot Laser Testing

Figure 4.41: A view of the lithographic mask design for the two section PFP with six pits spaced $34\,\mu\mathrm{m}$ apart and a gain length of $800\,\mu\mathrm{m}$.

A pitted waveguide is a useful tool for suppressing unwanted modes in lasers, but its effectiveness can be limited when the power of the waveguide is increased as with the slotted devices. This is because the positioning of the pitted modes can change, allowing additional unsuppressed modes to lase. However, this limitation can be overcome by combining a pitted waveguide with an electrically isolated straight FP etalon, similar to the SFP. In this configuration, the pitted section acts as a wavelength selective mirror and is given enough power to be optically passive, while the section without pits is operated as a gain section, providing the main source of the laser's power output. This type of laser is called a pitted Fabry-Pérot (PFP) and is capable of achieving excellent wavelength selectivity while avoiding the limitations of the single section pitted waveguide.

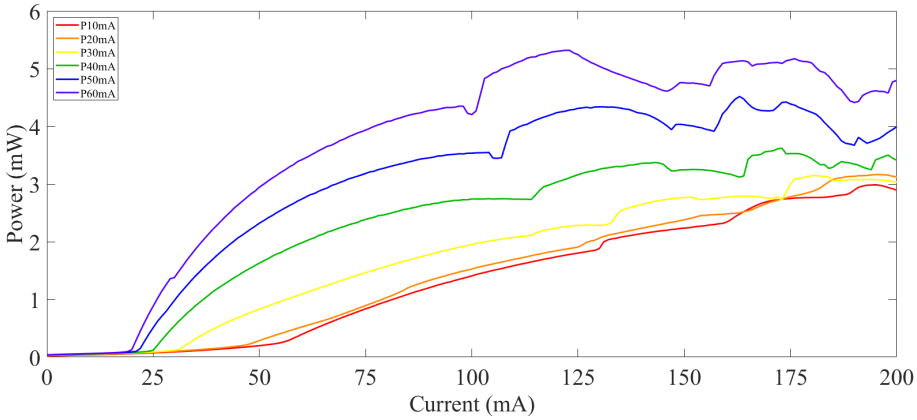

Figure 4.42: An experimentally measured LI of the pitted Fabry-Pérot Laser with varying mirror currents. Each colour represents a different bias current on the mirror section from $10\,\mathrm{mA}$ (red) to $60\,\mathrm{mA}$ (purple).

Fig. 4.42 shows the LI curve obtained from experimental measurements of a PFP with six pits spaced $34\,\mu\mathrm{m}$ apart and a gain length of $800\,\mu\mathrm{m}$. The threshold current and the peak power of the laser can be seen to depend heavily on the current supplied to both sections. A threshold current and

maximum power of $55\,\mathrm{mA}$ and $2.5\,\mathrm{mW}$ is observed when the mirror section is set at $10\,\mathrm{mA}$. The threshold current is reduced to $20\,\mathrm{mA}$ at a mirror section bias of $60\,\mathrm{mA}$ while the maximum output power of the laser increases to $5\,\mathrm{mW}$.

Fig. 4.43 shows the resultant peak wavelengths obtained by sweeping the currents applied to the gain and mirror section from $10{-}200\,\mathrm{mA}$ and $10{-}200\,\mathrm{mA}$ respectively. Using a pitted mirror rather than a pitted gain section leads to an improvement in the SMSR and now allows us to tune between the supermodes present in the pitted mirror, similar to those shown in Fig. 4.34. Fig. 4.44 shows the resultant SMSR corresponding to these wavelengths. Similar to the single section pitted laser, this single mode behaviour degrades when the gain section or the mirror section receive higher currents.

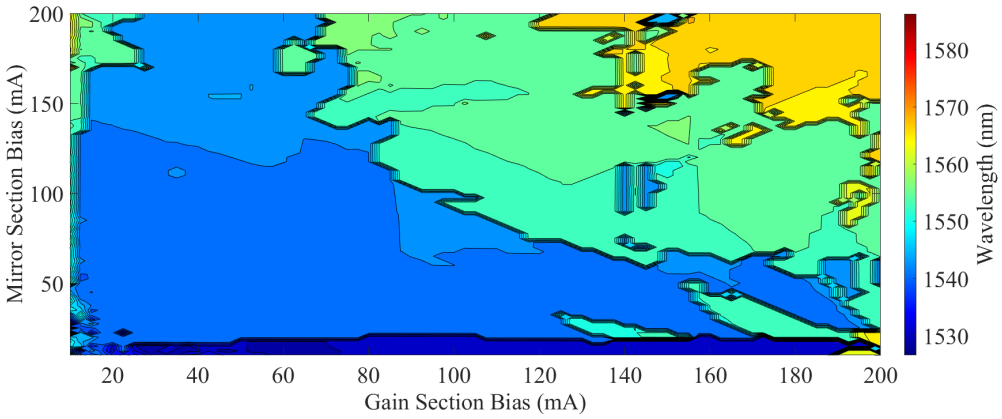

Figure 4.43: An experimental measurement of a PFP with six pits spaced $34\,\mu\mathrm{m}$ apart and a gain length of $800\,\mu\mathrm{m}$ comparing section currents and the resultant wavelength.

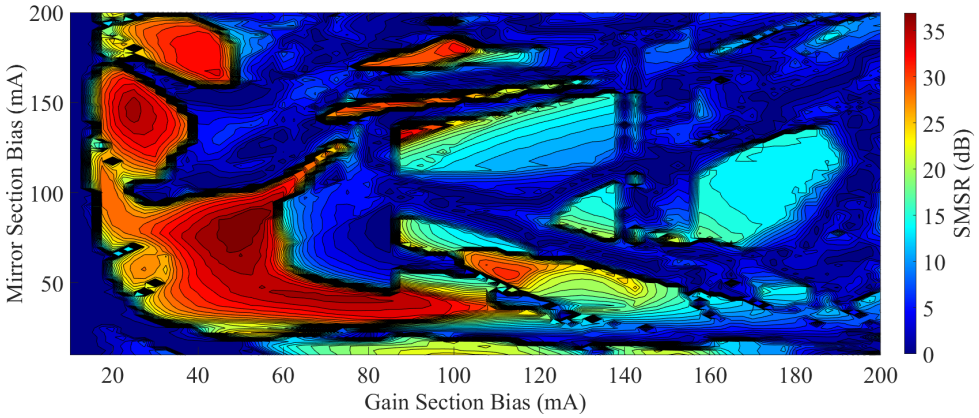

Figure 4.44: An experimental measurement of a two section pitted device comparing section currents and the resultant SMSR.

Comparing Fig. 4.43, which has a perturbation separation of $34\,\mu\mathrm{m}$, and Fig. 4.17, which has a separation of $108\,\mu\mathrm{m}$, we can see how the width and separation of the supermodes changes with the change in perturbation separation. Smaller separations lead to wider supermodes which are further apart and larger separations lead to narrower supermodes which are closer together.

By observing all of the wavelengths that can be obtained from electrically sweeping both the pitted mirror section and the gain section the modal behaviour of the PFP device becomes clearer. Fig. 4.45 shows the spread of wavelengths vs SMSR for the PFP device wherein each point on the graph represents the results of an individual spectrum taken at each bias point of the laser. Here the full tuning spread of the laser becomes clear with a full range of $40\,\mathrm{nm}$ of high SMSR ($>30\,\mathrm{dB}$) wavelengths being available between $1540\,\mathrm{nm}$ and $1580\,\mathrm{nm}$. The full spread of the supermodes can be seen to span from $1530\,\mathrm{nm}$ to $1590\,\mathrm{nm}$. However these supermode areas do not obtain sufficiently high SMSR to be considered single mode emission.

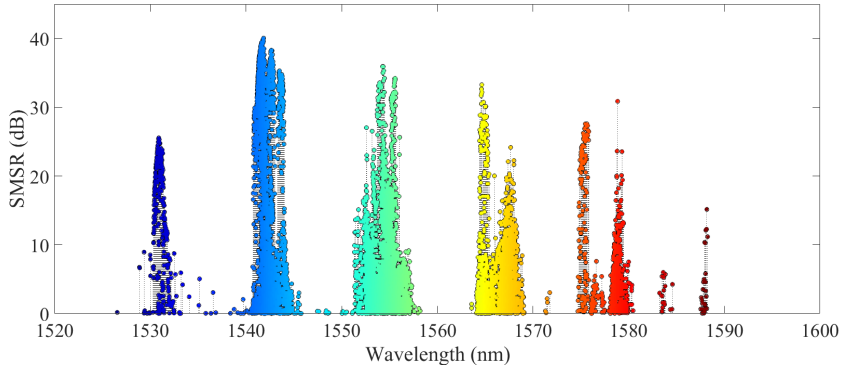

Figure 4.45: Experimentally measured Wavelength vs SMSR for each collected spectrum of the PFP.

In Fig. 4.45 the supermodes of the device are quite clear as the tuning spread of the PFP is discontinuous across it's wavelength range. As seen in Fig. 4.46a, we can map the positioning of these supermodes quite closely by comparing them to our simulated mirror supermodes for a pitted mirror waveguide with a slot separation of $34\,\mu\mathrm{m}$ with an index of $n_{WG} = 3.221$.

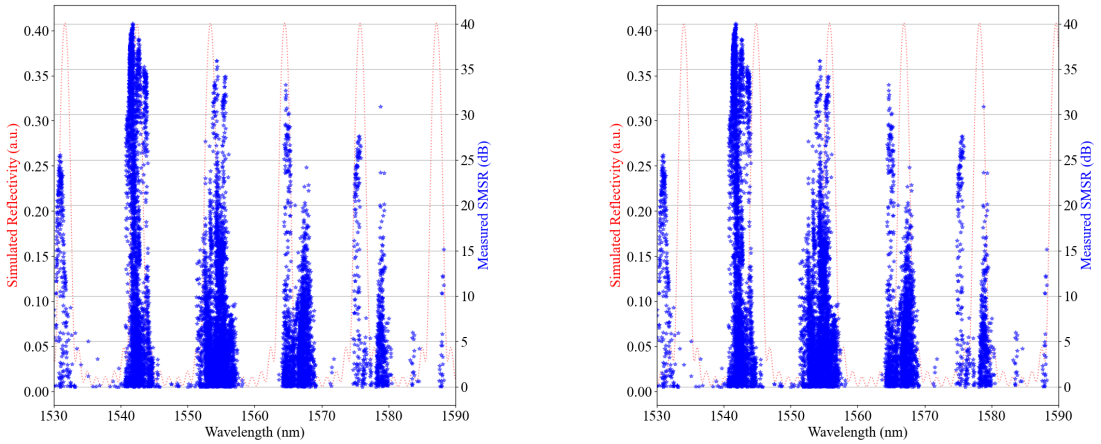

(a) Wavelength vs SMSR for the PFP device (blue) compared to a simulated reflectivity of a pitted mirror with $n = 3.221$ (red)

(b) Wavelength vs SMSR for the PFP device (blue) compared to a simulated reflectivity of a pitted mirror with $n = 3.218$ (red)

Figure 4.46: Experimental vs simulated output of a the PFP with a slot separation of $34\,\mu\mathrm{m}$

Some of the high SMSR spectral outputs can be attributed to the supermodes generated by a pitted mirror with decreased refractive index due to increased current supply. Fig. 4.46b shows the wavelength vs SMSR output of the laser aligned to a pitted mirror with $n = 3.218$.

4.5 Grouped Pitted Fabry-Pérot Lasers

Slots when placed within close proximity quickly degrade the performance of the device they are implemented on as their losses increase when positioned within $20\,\mu\mathrm{m}$. Pits lack this weakness and are capable of being placed within $10\,\mu\mathrm{m}$ of each other while still forming a functional lasing device. Thus the design for a Grouped Pitted Fabry-Pérot (GPFP) laser consists of a single sided mirror unlike the DSFP, with one large spacing ($>80\,\mu\mathrm{m}$) separating smaller groupings of closely packed pits ($<15\,\mu\mathrm{m}$). A schematic view of the device's topology is shown in Fig. 4.49.

In terms of simulation, the formation of a DPFP is similar to that of the DSFP with a lower range of possible spacing options. In a similar manner to how suitable DSFP configurations were calculated and swept via Matlab code with successful targettings being automatically recorded.

The interaction between the FP etalon and the PM leads to many of the

longitudinal modes of the FP section being suppressed. However, by combining two separate mirror spacings onto a single mirror section we can create a mirror where one single mode has higher reflectivity than all others. Fig. 4.47 demonstrates this, showing the highest reflectivity on a mode at $1542.8\,\mathrm{nm}$. This device design should offer an improved SMSR compared to single spaced pitted mirrors while sacrificing tunability.

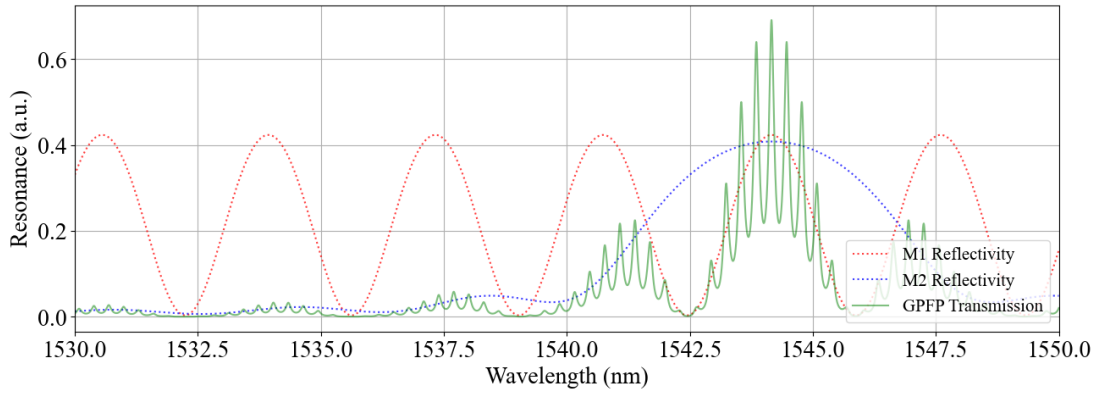

Figure 4.47: Resonance of a $1200\,\mu\mathrm{m}$ cavity with grouped pits with an outer separation of $108\,\mu\mathrm{m}$ (red) and an inner separation $12\,\mu\mathrm{m}$ (blue). The combined resonance is shown in green

Now by transforming this reflective profile using Eqn. 4.9, we can see in Fig. 4.48 how the SMSR of a multi-modal cavity can be improved.

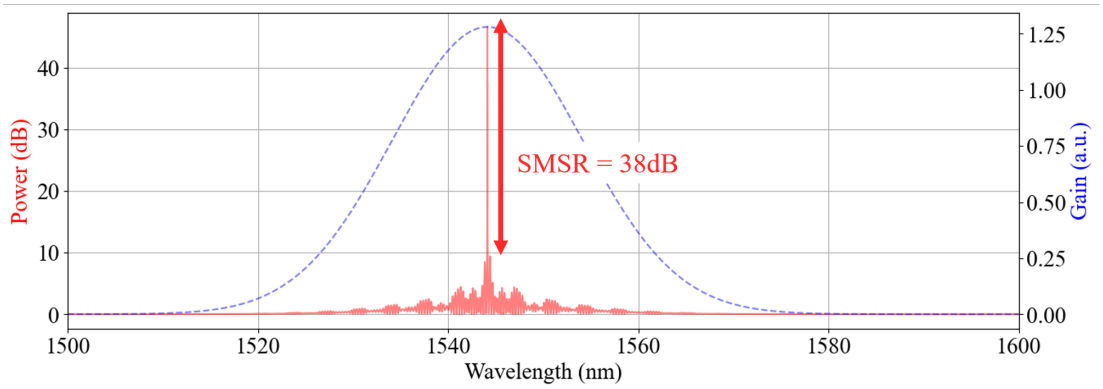

Figure 4.48: The reflectivity of Fig. 4.47 with gain as in Eqn. 4.9

4.5.1 Grouped Pitted Fabry-Pérot Laser Testing

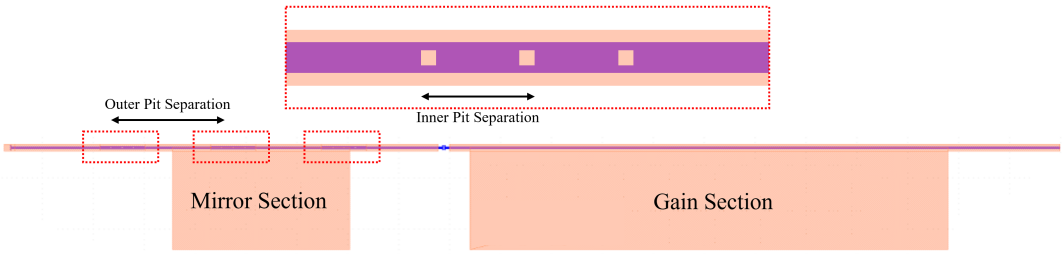

Figure 4.49: A view of the lithographic mask design for the grouped PFP showing a zoomed in view of the inner pit groupings. The outer pit separation was $108\,\mu\mathrm{m}$. The inner pit separation was $12\,\mu\mathrm{m}$.

Fig. 4.50 shows the LI curve obtained from experimental measurements of a GPFP with three groupings of pits spaced $108\,\mu\mathrm{m}$ apart, with the groupings themselves having three pits at a separation of $12\,\mu\mathrm{m}$. The gain section had a length of $800\,\mu\mathrm{m}$.

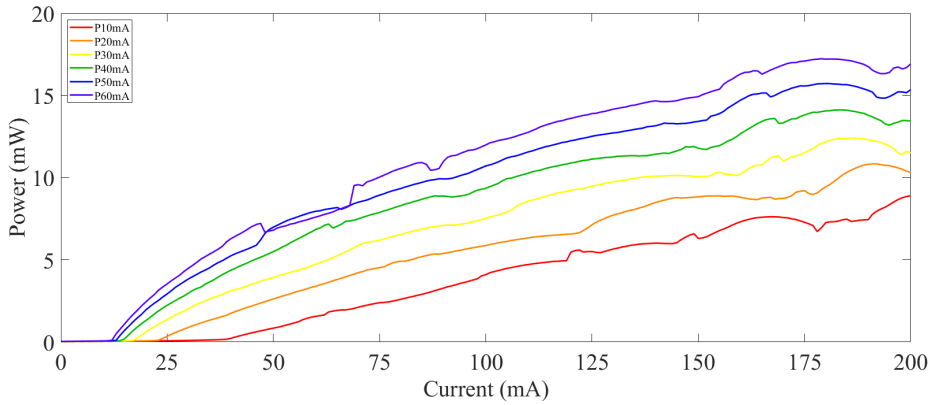

Figure 4.50: An experimentally measured LI of the grouped pitted Fabry-Pérot Laser with varying mirror currents. Each colour represents a different bias current on the mirror section from $10\,\mathrm{mA}$ (red) to $60\,\mathrm{mA}$ (purple).

The threshold current and the peak power of the laser can be seen to depend heavily on the current supplied to both sections. A threshold current and maximum power of $35\,\mathrm{mA}$ and $9\,\mathrm{mW}$ is observed when the mirror section is set at $10\,\mathrm{mA}$. The threshold current is reduced to $12\,\mathrm{mA}$ at a mirror section bias of $60\,\mathrm{mA}$ while the maximum output power of the laser increases to $18\,\mathrm{mW}$.

Figure 4.51 shows the peak wavelengths obtained by varying the currents applied to the gain and mirror sections between 20–$300\,\mathrm{mA}$ and 10–$200\,\mathrm{mA}$,

respectively. Using a pitted mirror instead of a pitted gain section improves the SMSR and allows for tuning between the supermodes present in the mirror, as depicted in Figure 4.52.

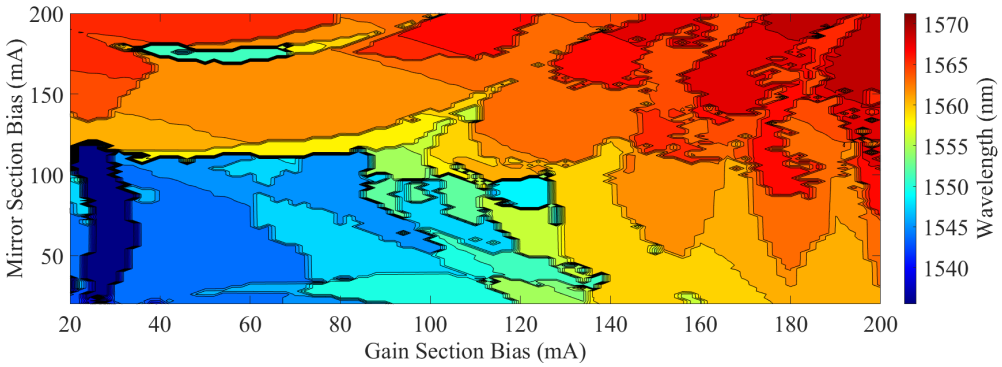

Figure 4.51: An experimental measurement of the grouped pitted device comparing section currents and the resultant wavelength.

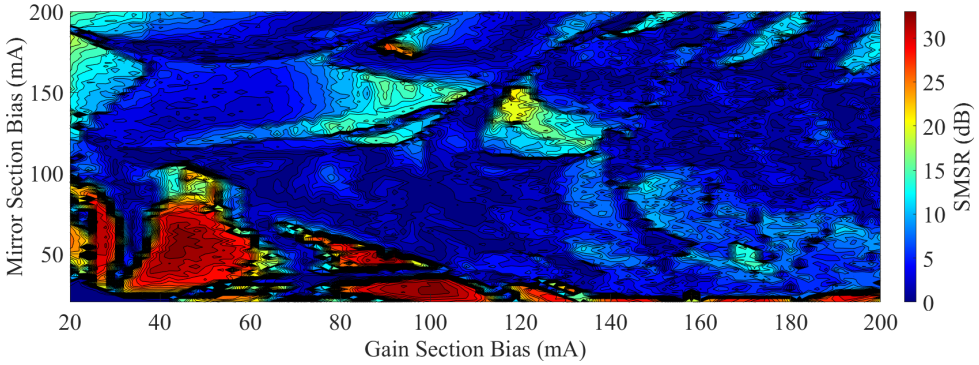

Figure 4.52: An experimental measurement of the grouped pitted device comparing section currents and the resultant SMSR.

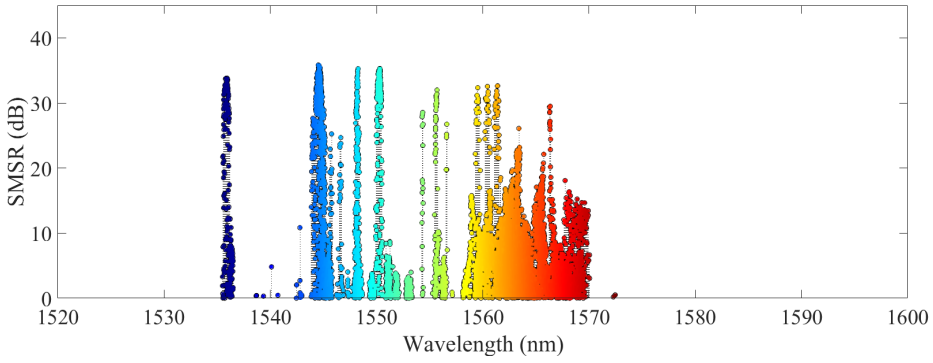

Figure 4.53: Experimentally measured Wavelength vs SMSR for each collected spectrum of the SFP.

The GPFP device exhibits single-mode behaviour at lower current levels similar to the PFP, but this fails when the gain or mirror sections receive higher currents. This is a limitation associated with single mirror section laser structures. To gain a better understanding of the GPFP device's modal behaviour, we analyse all the wavelengths obtained by electrically sweeping both the grouped pitted mirror and gain sections. Fig. 4.53 shows the spread of wavelengths versus SMSR, with each point representing the results of an individual spectrum taken at each bias point of the laser. This graph highlights the full tuning range of the laser, revealing a total range of $26\,\mathrm{nm}$ of high-SMSR ($>30\,\mathrm{dB}$) wavelengths available between $1536\,\mathrm{nm}$ and $1562\,\mathrm{nm}$.

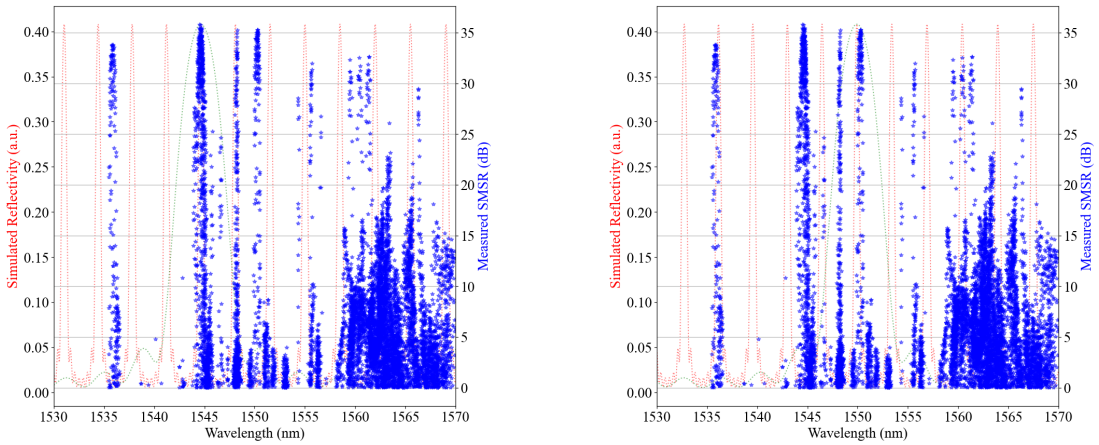

(a) Wavelength vs SMSR for the GPFP device (blue) compared to a simulated reflectivity of a pitted mirror with $n = 3.218$.

(b) Wavelength vs SMSR for the GPFP device (blue) compared to a simulated reflectivity of a pitted mirrors with $n = 3.215$.

Figure 4.54: Experimental vs simulated output of a the GPFP (blue) with an outer pit separation of $108\,\mu\mathrm{m}$ (red) and an inner pit separation of $12\,\mu\mathrm{m}$ (green)

As seen in Fig. 4.54a, we can map the positioning of these supermodes quite closely by comparing them to our simulated mirror supermodes for a pitted mirror waveguide with a grouped pit separation of $108\,\mu\mathrm{m}$ and inner pit separation of $12\,\mu\mathrm{m}$ with an index of $n_{WG} = 3.218$. The simulations here match quite well and we can see that the wavelength which aligns to both the outer pit separation (red) and the inner pit separation (green) is where the majority of the peak wavelengths occur. This confirms that the GPFP improves our wavelength targetting when a specific wavelength is desired however as predicted the tuning range of the device suffered, with only $26\,\mathrm{nm}$ tuning achieved.

Some of the high SMSR spectral outputs can be attributed to the supermodes generated by a a pitted mirror with decreased refractive index due to increased current supply. Fig. 4.54b shows the wavelength vs SMSR output of the laser aligned to a pitted mirror with $n = 3.215$. At higher wavelengths, as the gain section of the laser received increased currents and the laser in turn moves to longer wavelengths we can see that the single mode behaviour becomes notably weaker, with fewer points of high SMSR being achieved. This aligns with the predicted behaviour of the device as these wavelengths likely align to the outer pit separation of $108\,\mu\mathrm{m}$ but not the inner pit separation. This results in a weaker suppression of surrounding longitudinal modes when compared to a regular SFP or PFP.

4.6 The Inverse Scattering Method

So far we have discussed how the introduction of different perturbations into a waveguide system can turn an FP laser into a single mode laser. Subsequently, we determined that by having more than one spacing between these perturbations we can improve our wavelength targeting and our mode stability, at the cost of the laser's tunability.

The next logical step to consider must now be the addition of even more variation in the spacing between our perturbations. There must exist some combination of slot or pit spacing which perfectly targets our desired single mode. However pure computation of such an arrangement would be incredibly intensive if calculated by simply attempting all possible combinations. Thus, we will need more intense mathematics in order to solve this. Cue the inverse scattering method, which we will aim to use to reduce the threshold gain of a target wavelength.

The Inverse Scattering method describes how the positions, j, of our perturbations must be arranged to lower the threshold gain of a specific wavelength while generating a high SMSR. As described in [92] the threshold condition for lasing in a cavity with refractive index, n, containing N perturbations, with each causing an index change, Δn can be denoted up to the first order of Δn as;

$$1 = r_{-}r_{+}e^{2i\sum_{j}^{N}\theta_{j}} + i\frac{\Delta n}{n}\sum_{j=1}^{N}\sin\left(\theta_{2j}\right)\left[r_{-}e^{2i\phi_{j}^{-}} + r_{+}e^{2i\phi_{j}^{=}}\right] \tag{4.16}$$

where r_- and r_+ represent the field reflections to the left and right of the facets respectively. θ_j is the phase change at section j and ϕ_j^+ and ϕ_j^- are the changes in phase when travelling from position j to the left and right respectively.

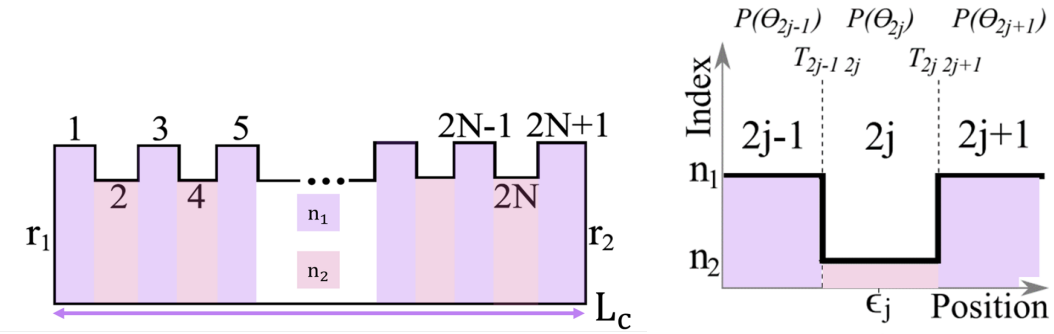

(a) Index Perturbations along a cavity of length L_c. (b) A single perturbation at ϵ_j

Figure 4.55: Index perturbations along a cavity form subcavities, $P(\theta)$ and sub-facets, T. The cavity has varying refractive index regions shown in purple (n_1) with no perturbation, and and pink (n_2) with perturbation.

This threshold condition can be used to calculate the threshold gain of the cavity mode, m, up to the first order as;

$$\gamma_m = \frac{1}{L_c}\ln\frac{1}{|r_- r_+|} + \frac{\Delta n}{n}\frac{1}{L_c\sqrt{r_- r_+}}\sum_{j=1}^{N}\sin\theta_{2j} \quad \cdot$$
$$\cdot\left[r_-\sin\left(2\phi_j^-\right)e^{\epsilon_j\gamma_m^{(0)}L_c} + r_+\sin\left(2\phi_j^+\right)e^{-\epsilon_j\gamma_m^{(0)}L_c}\right] \tag{4.17}$$

where $\gamma_m^{(0)}$ is the threshold gain of the mode m in a cavity with no perturbations. L_c is the length of the cavity and ϵ_j are the fractional positions of the perturbations along the cavity such that $-\frac{1}{2} < \epsilon_j < \frac{1}{2}$. To determine these fractional positions we first choose a function as a basis on which we can model our threshold function such that our desired mode m_0 has a minimal threshold gain when compared to all other modes in the cavity $m \neq m_0$.

In this case we will use $sinc(\Delta m)$ where $\Delta m = m_0 - m$. The position of N perturbations can therefore be calculated by determining solutions to the equation

$$A\sum_{n}\int_{\epsilon_{j_{min}}}^{\epsilon_j}\left[r_-\sin\left(2\phi_j^-\right)e^{x\gamma_m^{(0)}L_c}+r_+\sin\left(2\phi_j^+\right)e^{-x\gamma_m^{(0)}L_c}\right]^{-1}\cdot \cdot\Gamma_n(x)dx=j-\frac{1}{2} \tag{4.18}$$

for $1 \leq j \leq N$. A is a normalisation constant. Γ_n is a series of Gaussians which represent the Fourier transform of our modulation function. The term ϵ_{min} exists to provide a minimum position at which a perturbation can be placed in order to avoid perturbation crowding.

Using Eqn. 4.18, an initial set of suitable positions for the perturbations can be calculated numerically using a purpose written C++ code. This set of values is then reinserted into Eqn.4.16 where the positions of the perturbations can be minorly shifted in order to maximise the value of the $\sin(\theta_{2j})$ term. This is then used to take into account the optical path length changes due to the perturbations introduced.

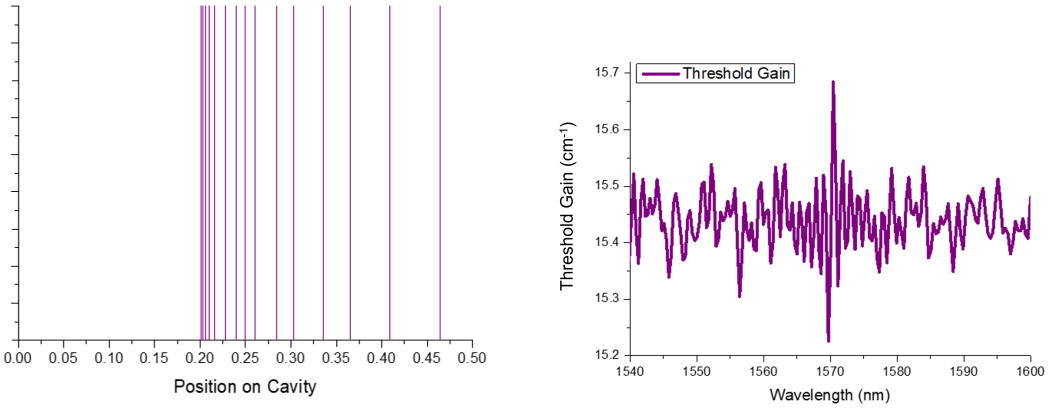

(a) Fractional positions of 15 index perturbations along a cavity of length $1000\,\mu\mathrm{m}$

(b) Threshold gain spectrum of the cavity with perturbations as shown in (a)

Figure 4.56: Distribution of 15 perturbations along a $1000\,\mu\mathrm{m}$ cavity to minimise the threshold gain at $1570\,\mathrm{nm}$. Here, the 0 position of the cavity is taken to be the center. The right facet is at 0.5.

For the lasers produced for this project, pits were used as the perturbation as the reflectivity of a pit is insensitive to etch depth and the precise calculation of the inverse scattering method requires a consistent reflectivity when calculating perturbation positions. The pits used were designed to be $1\,\mu\mathrm{m}$ wide and were noted to cause an index change of $\Delta n = 0.075$ [92].

4.6.1 Inverse Scattering Device Testing

Figure 4.57: A view of the lithographic mask design for the inverse scattering design device. A zoomed in view shows the scattered distribution of the pits.

Inverse scattering devices were fabricated targetting $1550\,\mathrm{nm}$ and $1570\,\mathrm{nm}$ to test the validity of the simulated outputs. Each of these devices used 15 pits to act as perturbations.

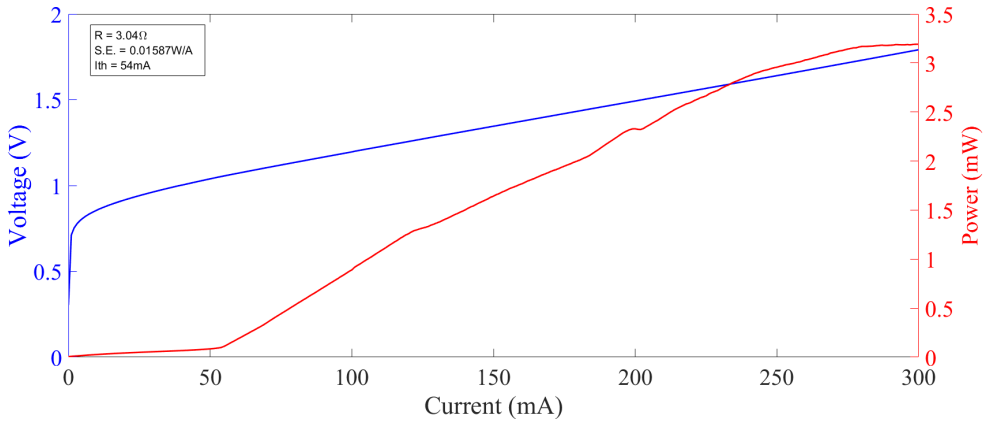

Figure 4.58: LI curve of an inverse scattering device with 15 perturbations targetting $1570\,\mathrm{nm}$.

Fig. 4.58 shows the LIV curve for an IS device designed to target $1570\,\mathrm{nm}$. This device had a length of $1000\,\mu\mathrm{m}$. The device is noted to have a high threshold of $54\,\mathrm{mA}$ and a maximum output power of $3.2\,\mathrm{mW}$.

The wavelength behaviour of the device can be seen in Fig. 4.59, once the lasing output is reached the laser initially begins lasing at $1545\,\mathrm{nm}$. Once the laser current reaches $75\,\mathrm{mA}$, the device quickly reaches single mode operation. However, the emission wavelength is not the target $1570\,\mathrm{nm}$. It is not until the laser current reaches $180\,\mathrm{mA}$ that the laser reaches its target wavelength of $1570\,\mathrm{nm}$, only achieving single mode operation at $200\,\mathrm{mA}$.

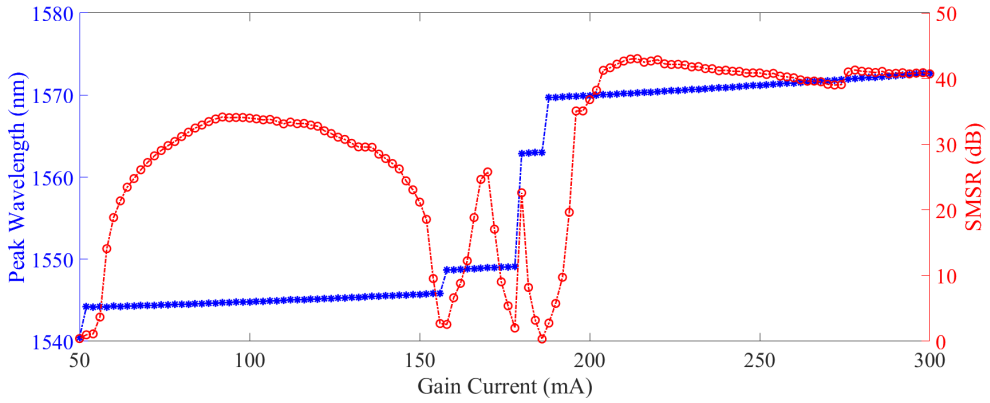

Figure 4.59: Peak wavelength (blue) and SMSR (red) of a $1570\,\mathrm{nm}$ inverse scattering device vs a changing current across the laser.

The cause of this discrepancy between the emitted wavelength and the target wavelength is likely due to the overall FP emission of the cavity. The gain curve of this cavity determines the primary emitted wavelength. The perturbations placed along this cavity attempt to target a single wavelength to create single mode lasing. However if the gain curve does not align to this target point then the target wavelength cannot lase, with the emission wavelength instead matching a permissible mode available within the gain curve. As the current across the laser increases, the gain curve shifts to higher wavelengths which overlap our target mode of $1570\,\mathrm{nm}$, causing it to become the primary emission wavelength.

Across these two primary emission wavelengths achieved, $1545\,\mathrm{nm}$ and $1570\,\mathrm{nm}$, the latter achieves higher SMSR due to the arrangements of the perturbations being designed around this wavelength. We can confirm this behaviour by observing the same wavelength, SMSR, and current relationship for a device which targets $1550\,\mathrm{nm}$, as in Fig. 4.60. Therein we can see how, after the device reaches threshold the emission begins at $1543\,\mathrm{nm}$. However, this emission wavelength does not achieve a sufficiently high SMSR to be considered single mode.

Once the emission reaches the target output of $1550\,\mathrm{nm}$ the device achieves single mode emission. As the current across the device increases we can see the emission wavelength vary slowly due to thermal effects and though the peak wavelength emitted does not change, by $200\,\mathrm{mA}$ the device no longer outputs a high SMSR. This follows the trend seen in the $1570\,\mathrm{nm}$ device. When the gain curve and the target wavelength align, a high SMSR can be achieved. However, once the gain curve moves away from the target wavelength, the

single mode output of the device fails.

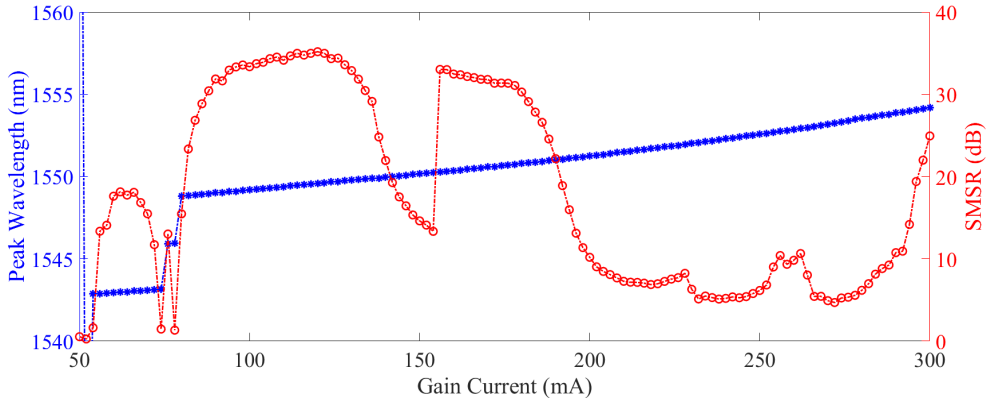

Figure 4.60: Peak wavelength (blue) and SMSR (red) of a 1550 nm inverse scattering device vs a changing current across the laser.

4.7 Ring Lasers

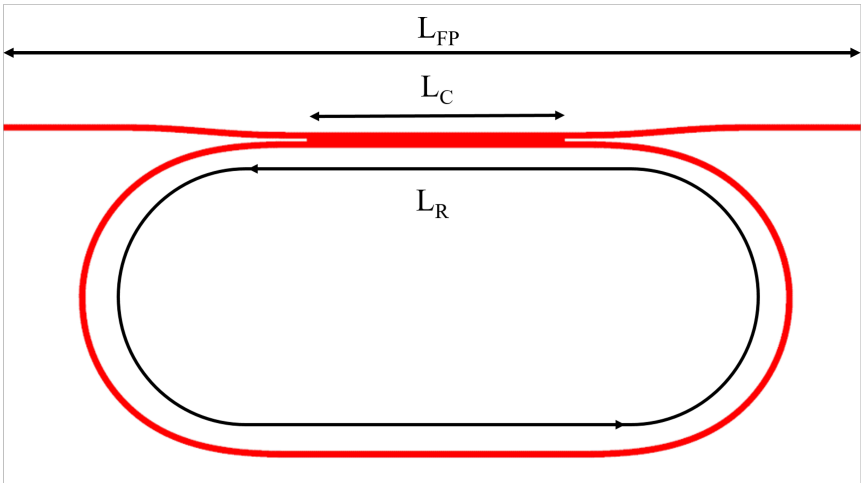

Figure 4.61: A schematic of a ring resonator with a half-wave coupler

Active semiconductor ring lasers (SRLs) are devices of interest in photonics as they do not require cleaved facets or gratings in order to achieve the necessary optical feedback for lasing [93–96]. In Wavelength Division Multiplexing (WDM) and dense WDM systems, ring resonators have been used to de-multiplex closely spaced channels and are frequently used as add-drop filters. Sharp response is necessary for closely spaced channel filtering in order to prevent channel interference and maintain a good SMSR. The filter response therefore requires a high Q-factor of the ring cavities. The cavity loss must be kept to a minimum to achieve a high Q-factor ring. The waveguide

losses and the coupling losses are the two key factors that control the cavity losses in a racetrack ring structure. An example of this is shown in Fig. 4.61.

The disadvantage of ring lasers versus conventional Fabry-Pérot lasers comes from the inherent loss of curved waveguides. Improving the mode mismatch between the straight waveguide and the bent waveguide is one method of lowering the loss of the InP-based waveguide [97]. The mode mismatch develops as a result of the change in mode shape from the straight waveguide to the curved waveguide. The mode of curved waveguides is not centralised in the horizontal; rather the shape of the mode favours the side along which the waveguide is bending. This change in mode shape arises from the inherent behaviour of light to travel in straight lines.

To overcome this challenge, traditional circular bends are replaced with continuous curvature bends wherein the curvature of the waveguide is made to change gradually, thus reducing the loss due to the modal mismatch. This reduction in loss allows for the fabrication of better, tighter bends. Fig. 4.62 shows the threshold current of an array of deeply etched U-bend FP lasers fabricated and characterised as described in the previous chapter. All lasers in the array were the same length, $840\,\mu\mathrm{m}$ before being cleaved.

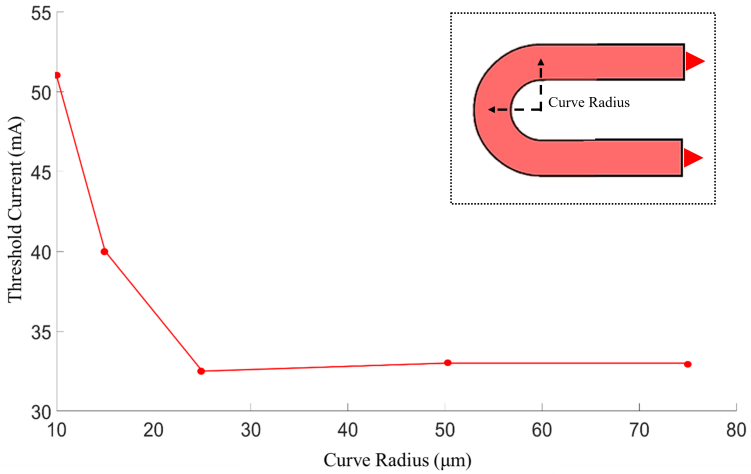

Figure 4.62: U bend FP laser radii vs corresponding threshold current. In the inset is a schematic representation of the U bend FP with curve radius highlighted.

These devices were fabricated on non-custom, commercially available lasing material used to fabricate the single mode lasers in this Chapter. The results show that continuous curvature bends can be made to lase down to a radius of

$10\,\mu\mathrm{m}$. A $5\,\mu\mathrm{m}$ U-bend was also fabricated as part of this run but could not be made to lase, providing a lower limit on the available bend radius.

The spectral behaviour of a ring structure can be modelled using the transfer function of a directionally-coupled ring structure with coupling ratio, c, given in Coldren and Corzine [98] as

$$S_{21} = \frac{ic^2 e^{-i\beta L_C} e^{-i\beta L_R/2}}{1-(1-c^2)e^{-i\beta L_R}} \tag{4.19}$$

where L_C and L_R are the coupling and ring lengths respectively as shown in Fig. 4.61. The transmission of the ring can therefore be calculated as $T(\lambda) = |S_{21}|^2$. An example of the ring transmission is shown in Fig. 4.63 with a ring length of $600\,\mu\mathrm{m}$, a coupling length of $200\,\mu\mathrm{m}$, and a coupling ratio of 0.6.

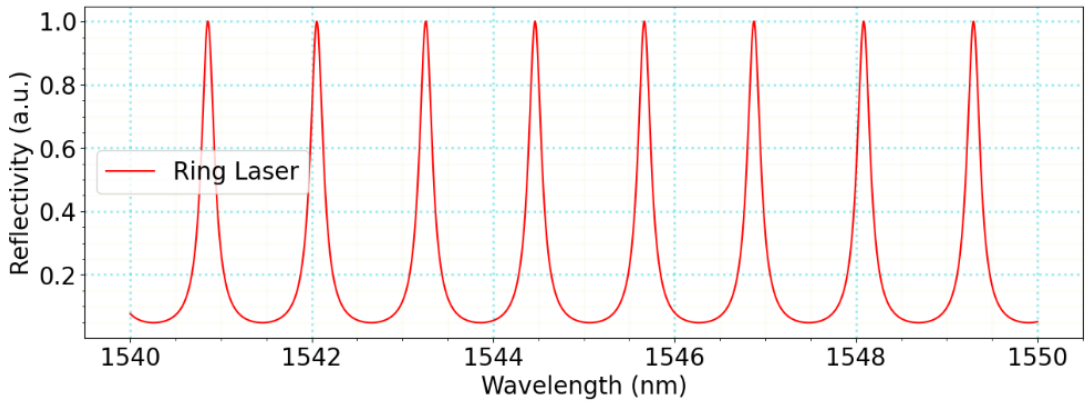

Figure 4.63: A simulated ring transmission spectrum

The figure illustrates how a ring can be used as a filter if injected, as the peak of the modes will be the only wavelengths able to escape the ring, with all others being suppressed. Thus, if two waveguides were coupled to a ring resonator on opposite sides and one of these waveguides was injected with light, the output measured from the waveguide on the opposite side would be spaced similar to Fig. 4.63. SRLs can also be used to create active lasing structures with output spectra similar to that of an FP laser. SRLs are also able to form single mode lasers if the waveguide to which it is coupled also forms an active laser cavity. The resonant conditions of both cavities become restrictions on the available lasing modes which restricts the possible laser modes of both cavities.

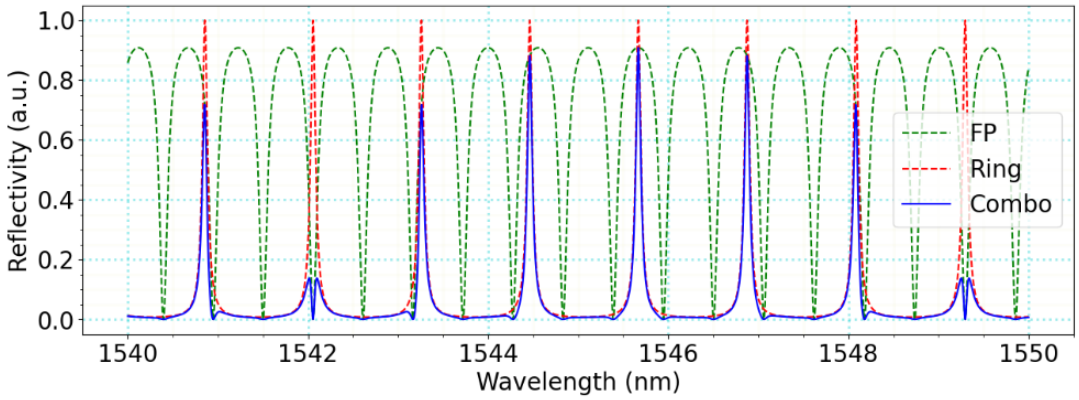

Figure 4.64: A simulated ring transmission spectrum (red), Fabry-Pérot reflectivity spectrum (green), and a combined laser mode spectrum (blue)

Fig. 4.64 shows the previous ring spectrum coupled with an FP waveguide of length $650\,\mu\mathrm{m}$. This can be achieved using a halfwave coupler as in Fig. 4.61. Here we can see how the combined restrictions of both reflectivity spectra has introduced an imbalance into the magnitude of the modes, causing one mode at $1545.5\,\mathrm{nm}$ to have a higher reflectivity compared to all other neighbouring modes, leading to single mode lasing.

Ring lasers were not fabricated on the commercial epitaxy used to make the other single mode laser designs analysed in this chapter and thus no experimental characterisation of these devices is presented. Instead a focus was placed on a variation of a ring laser known as a snail laser.

4.8 Snail Lasers

SRLs are of interest to this project as the future goal of creating a monolithically integrated EML is to form a single chip which can be brought to the silicon platform through means such as micro-transfer printing, which will be detailed later. As such we seek to minimise our use of facets, which makes SRLs of great interest. A notable variation of the classic SRL structure is a snail laser as shown in Fig. 4.65, with a unique geometry which differentiates it from the more classical racetrack ring resonator.

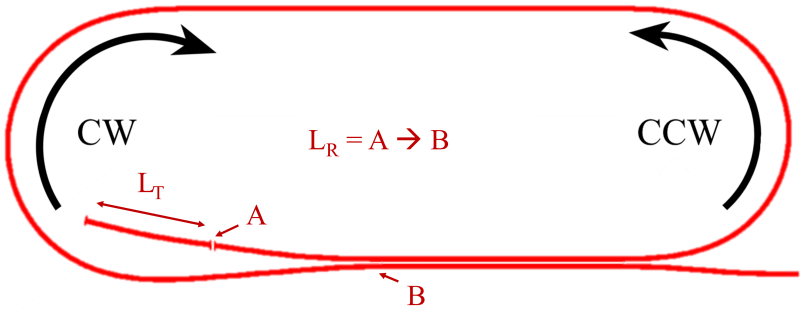

Figure 4.65: A schematic of a snail laser with a directional coupler. L_T is the length of the tail section. L_R is the remainder of the ring until it re-couples back into itself from point A to B.

In SRLs, the lasing cavity is formed by the closed ring waveguide with light extracted using waveguide coupler structures, avoiding the inclusion of facets in the lasing cavity. The snail differs by forming a lasing cavity using the crossed ports of the coupler, leaving uncoupled light to be extracted. The symmetric nature of the SRL can produce bidirectional lasing. The geometry of the snail has an inherent imbalance in the reflectivity of the two facets which couples a large fraction of the clockwise (CW) mode into the counter-clockwise (CCW) mode, creating unidirectional lasing in this direction.

A major benefit of SRLs is their strong single mode behaviour due to the coupled cavity effect. In a standard SRL this single mode behaviour is due to the interaction between the permissible modes in the ring and the straight waveguide to which it couples. In the snail, single mode behaviour is achieved through the interaction between the CW mode and the CCW mode. In the snail, the CW mode travels toward the reflective facet, with an amount of power being reflected back to the CCW direction dependent on the reflectivity of the etched facet used. Thus we have two different path lengths present with

the cavity; the CCW path length which travels the length of the ring $L_{CCW} = L_R$, and the CW which travels to the end of the tail with length L_T and back again, rejoining the ring, $L_{CW} = L_R + 2L_T$. Fig. 4.66 shows the modes of a snail with $L_R = 570\,\mu\mathrm{m}$ and $L_T = 120\,\mu\mathrm{m}$. here we can see how the coupled modes lead to single mode lasing, similar to how the coupled ring laser operates.

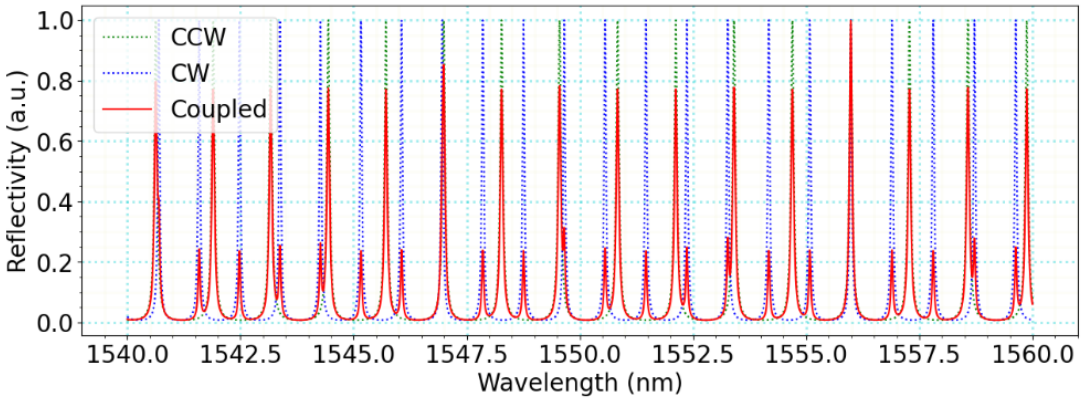

Figure 4.66: CCW and CW modes of a snail laser, as well as their coupled modes

4.8.1 Snail Laser Testing

To experimentally verify the usefulness of snail lasers as single mode facetless laser sources, a variety of different snail lasers were designed and fabricated. The list of the snail lasers designed is shown in Table 4.1. These snails used either a directional/evanescent coupler [99] or a halfwave coupler [100]. The distance between coupled ridges was fixed at $1\,\mu\mathrm{m}$ regardless of coupler type.

Table 4.1: Experimental Measurements of varying snail designs

Device Number	Coupler Type	Coupling Length (μm)	Ring Radius (μm)	Ith (mA)	Slope Effiency (W/A)
1	Halfwave	60	60	45.8	0.0252
2	Halfwave	180	60	45.7	0.0214
3	Halfwave	180	60	52	0.0251
4	Evanescent	100	60	60	0.0223
5	Evanescent	200	60	64	0.0165
6	Evanescent	300	60	74	0.0185
7	Halfwave	180	60	53.1	0.0196
8	Halfwave	180	60	54.6	0.0197
9	Halfwave	180	60	58.4	0.0226

Fig. 4.67 shows an LI curve collected for device 4. Snail devices had a relatively high threshold current and low power output. However, the snail devices were able to achieve suitable SMSR $> 30\,\mathrm{dBm}$ at certain current values

as shown in Fig. 4.68. This was due to the coupling between the clockwise and counter-clockwise mode. This change in single mode is not as predictably spaced as either the slotted or the pitted laser.

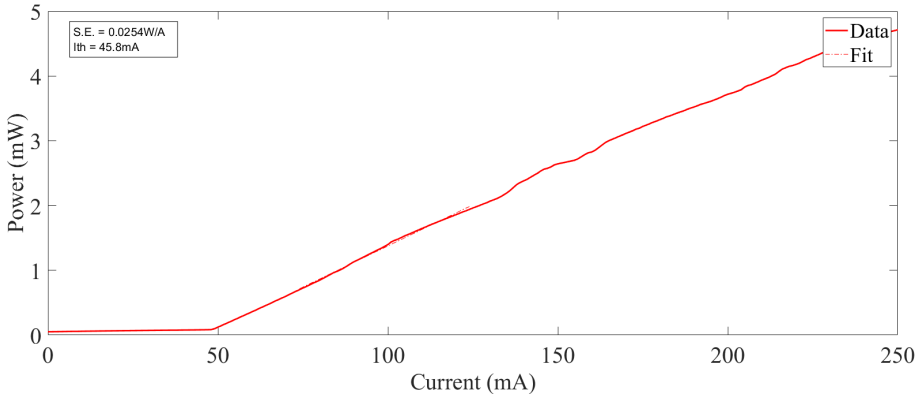

Figure 4.67: LI curve of a snail laser, device 4 from Table 4.1.

Fig. 4.69 shows a spectral output of device 4 at a current of $175\,\mathrm{mA}$ in red. In blue are the beating modes of two cavities with lengths matching the clockwise ($899\,\mu\mathrm{m}$) and counterclockwise ($775\,\mu\mathrm{m}$) modes in blue. The resonances of these cavitities were calculated using the scattering matrix method for equivalently long straight FP cavtities which were then multiplied together. The power imbalance caused by the lower reflectivity of the tail facet (33%) results in the clockwise mode being weaker than the counterclockwise mode when we measure our output from the output facet on the right as seen in Fig. 4.65.

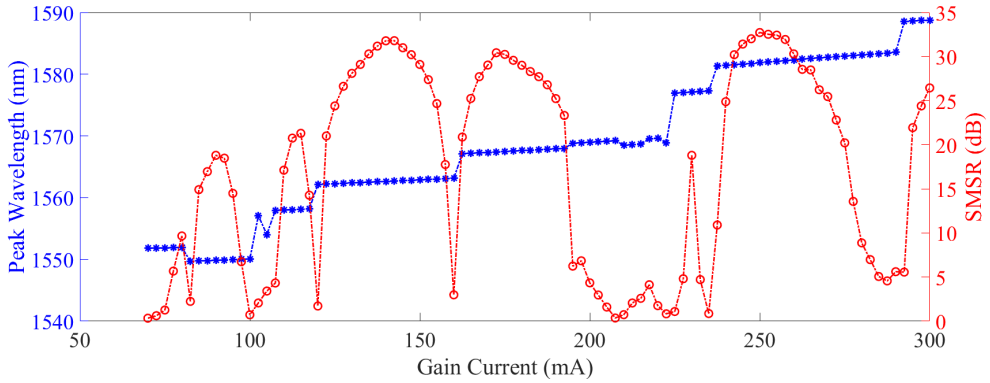

Figure 4.68: Peak wavelength (blue) and SMSR (red) of device 4 vs a changing current across the ring.

The primary mode spacing seen in Fig. 4.69 matches a cavity with a path length of the counterclockwise mode ($775\,\mu\mathrm{m}$). Of those cavity modes, we can

see an increase in resonance at the points where both CCW and CW modes align and beat together. This increases the resonance of that longitudinal mode relative to the others in the cavity which leads to a single mode output.

The separation between the single modes achieved by the snail laser is set by the beat resonance between the two ring cavities. However, as the current increases across the ring section, so too does the index of the ring which can vary where these beat resonances occur. This behaviour can be noted at the $240\,\mathrm{mA}$ point in Fig. 4.68 where the snail undergoes a larger change in emission wavelength.

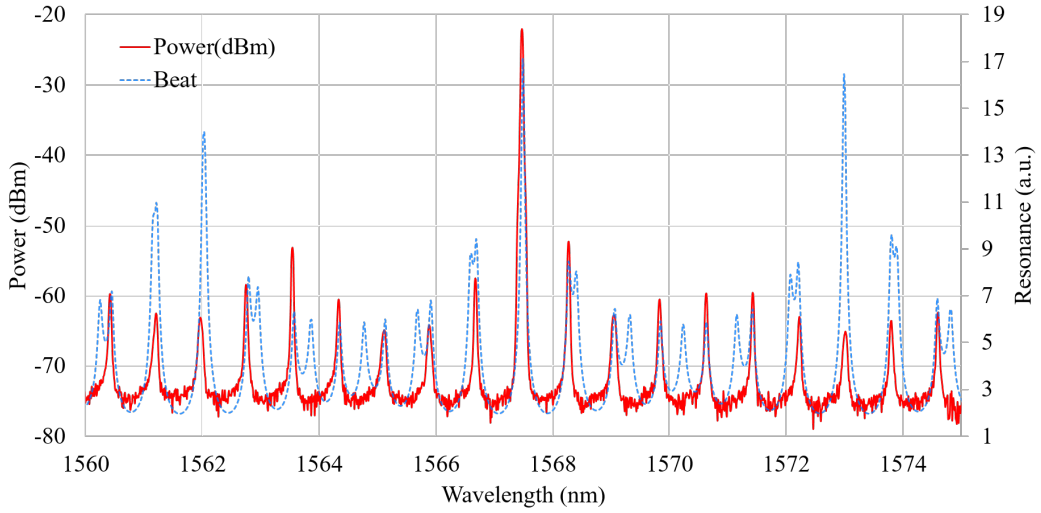

Figure 4.69: Experimentally measured spectra of device 4 at $I = 175mA$ (red) and the beat resonance of two ring cavities of length $775\,\mu\mathrm{m}$ and $899\,\mu\mathrm{m}$.

Overall the snail lasers offered an interesting route for single mode lasing, although their low power output made them an unattractive option for EML integration.

4.9 Laser Verdict

Many lasers were fabricated and characterised for the purposes of determining the optimal source for monolithic EAM integration. For this we require a laser which has high power, low threshold, and good single mode operation. Additionally we required a laser which is capable of emitting this single mode at a longer wavelength than where the initial gain peak of the device would be. We want a laser that can redshift its emission so as to avoid the absorption peak of the material so that the majority of the injected light from our laser to our EAM is not absorbed at $0\,\mathrm{V}$. With these qualities in mind a summary of the performance of each laser structure is shown in Table 4.2. Here we can see which devices satisfy our requirements and thus will be suitable for EAM integration.

Table 4.2: A summary of the characterisation of the various laser designs.

Laser Type	Ith (mA)	Highest Power (mW)	Highest SMSR (dB)	Tunability (nm)
SSFP	27	15	25	0
SFP	10-50	12	36	40
DSFP	12-49	12	45	60
SPFP	80	3.5	25	0
PFP	20-55	5.5	40	40
GPFP	12-35	18	38	30
IS	52	3.2	45	25
Snail	45-74	4	32	30

The ***SSFP*** offers excellent power output and acceptable threshold current but the SMSR is not enough to qualify for single mode behaviour. The ***SFP*** succeeds in all categories and thus warrants consideration for moving to the next round of integration. The ***DSFP*** similarly succeeds in all categories of interest, offering the best tuning range of all devices presented, thus warranting a continuation to the next stage.

The ***SPFP*** offers poor threshold current, power output, and unsatisfactory single mode behaviour. The ***PFP*** offers excellent SMSR and tunability, similar to the SFP. However, it offers lower power in comparison to the SFP laser and thus does not need to be continued. The ***GPFP*** offers excellent power output, threshold, and SMSR. However, its tunability does not compare favourably to other devices. This would not be a problem in the case that the GPFP were able to properly target a single wavelength similar to the inverse scattering

device, as was the intention of the design, but instead the GPFP was tunable where it was not intended to be. This makes the emission spectrum of the GPFP somewhat unpredictable and thus not suitable for continued research for the needs of this project. Pitted features also proved to be somewhat difficult to resolve when compared to slots of a similar size which affects the overall yield of devices, adding another negative to their usage for this project.

The ***IS*** device offered interesting behaviour and high SMSR but high threshold and low power. Its tunability is poor, but was intended to be so. The device offers an interesting case for further study of methods to improve its output power via separating the device into a gain section and an IS mirror section as was done to other pitted and slotted devices. However its performance in this case does not prove it suitable for EAM integration. Similarly the ***Snail*** laser offers an intriguing method for single mode lasing, making minimal use of facets to form a cavity, which is especially suitable for integration with EAMs. However, its low output power and relatively low tunability compared to other devices means it is not the optimal laser design for usage in this project.

In summary, the ***SFP*** and ***DSFP*** proved to be the most reliable methods of obtaining high power, single mode, redshifted emission, which makes them the most suitable candidates for the next stage of integration.

Chapter 5

EAM Design, Fabrication & Characterisation

Each optical data transmission system needs to modulate the optical signal in some way. In photonic integration, optical modulation can be done either directly, by modulating the source itself, or indirectly by modulating the light after it is emitted from the source. The first of these modulation methods is known as direct modulation, the latter is known as external modulation. There are numerous additional manners of modulating an optical signal, including polarisation, frequency, and phase modulation. With the additional capacity to create various combinations of the modulated optical properties, these can also be accommodated for through various forms of of external modulation.

5.1 Direct Modulation

In semiconductor lasers, direct modulation (DM) is accomplished by adjusting the laser's gain to change the output power of the device. Usually, this is accomplished by changing the laser's drive current. Because there is only one device involved, direct modulation of lasers is simpler to develop than external modulation. There are also fewer contacts and a shorter absorption path. Transmission systems capable of 40 Gbps have been demonstrated using DM [101]. Vertical cavity surface emitting lasers (VCSEL) [101, 102], distributed feedback (DFB) [103], distributed Bragg reflector (DBR) [104], and sampled grating distributed Bragg reflector (SGDBR) [105] have all been directly modulated with large electro-optical bandwidths. Single growth

slotted Fabry-Pérot (SFP) lasers have also been shown to function at 10 GHz throughout the course of this investigation [106]. High differential gain, low nonlinear gain saturation, high optical confinement, short and narrow cavities, and high optical confinement are necessary for high speed direct modulation of ridge waveguide lasers in order to shorten photon lifespan. The small signal frequency response is given by [107]

$$H(\omega) = \left(\frac{1}{1 + i\omega\tau_s}\right)\left(\frac{1}{1 + i\omega\tau_{RC}}\right)\left(\frac{A}{\omega_r^2 - \omega^2 + i\omega\gamma}\right) \tag{5.1}$$

where A is an amplitude factor and ω_r is the angular relaxation resonance frequency. τ_{RC} is a measure of how quickly the voltage across the capacitor in the RC circuit changes in response to an input signal. The damping factor γ is given by

$$\gamma = \omega_r^2 \tau_p + \tau_c^{-1} \tag{5.2}$$

where τ_p is the photon lifetime and τ_c is the differential carrier lifetime.

The carrier transit time, τ_s, is the initial limiting term, and it greatly depends on the design of the device. By building the cavity for speed rather than gain, this can be decreased in a number of ways [108]. The second limiting term, τ_{RC}, depends on the chip's RC parasitics because lasers are typically lumped element devices. Ridge waveguide lasers have a rather high capacitance due to their potential for being quite long ($> 300\,\mu\mathrm{m}$). For a laser with a differential gain, a, a differential internal efficiency, η_i, an optical confinement factor, Γ, a group velocity, ν_g, and an active area that produces gain, V_a, it can be demonstrated that the angular resonance frequency, ω_r, has the solution [109]

$$\omega_r = 2\pi f_r = \sqrt{\frac{\Gamma \eta_i \nu_g a}{q V_a}}\sqrt{I - I_{th}} \tag{5.3}$$

where q is the electron charge. As $\omega_r \sim \sqrt{I}$, we can see that increasing the current across our cavity shifts the resonance to a higher frequency. The difficulty in direct modulation can be explained via the Kramer Kronig relations [110, 111], by modulating the gain of the device i.e. the imaginary part of the refractive index (n_i), the real part of the refractive index (n_r) is also being modulated. This modulation can cause a few problems. First, the

frequency changes can lead to "chirping," where the output frequency of the laser fluctuates rapidly. This can make it difficult to use the laser for high-speed data transmission. Second, changes in the refractive index can cause nonlinear distortion in the output signal, leading to errors in data transmission. Finally, the modulation bandwidth of a directly modulated laser is limited by the relaxation oscillation frequency, which is determined by the laser cavity and damping. This limited modulation bandwidth can make directly modulated lasers less suitable for some applications where high-speed and stable data transmission is required.

Chromatic dispersion is a significant problem in long-haul communications because it limits the achievable data rate and transmission distance of optical fiber systems. Chromatic dispersion refers to the phenomenon where different wavelengths of light travel at different speeds through an optical fiber, causing the pulses of light to spread and overlap with neighbouring pulses over long distances. This dispersion arises due to the dependence of the refractive index of the fibre material on the wavelength of light.

The impact of chromatic dispersion becomes more severe as the transmission distance and data rate increase. At higher data rates, the pulses become narrower and closer together, making them more susceptible to dispersion effects. Additionally, over long distances, the cumulative dispersion can cause significant degradation in the signal quality, limiting the achievable transmission distance. The dispersion penalty, δ_c, is related to the chirp via [107].

$$\delta_c = 5\log_{10}\left[(1+8\alpha_c DB^2L)^2 + (8DB^2L)^2\right] \tag{5.4}$$

where α_c is the chirp parameter, D is the group velocity dispersion parameter, B is the bit rate, and L is the fibre length.

Direct laser modulation can be simpler and less expensive compared to external modulation setups since it eliminates the need for additional modulators and associated drive electronics. It can be suitable for applications where the modulation requirements are relatively simple and cost considerations are important. However, if higher performance or flexibility is required, the added complexity and cost of external modulation may be justified.

5.2 External Modulation

External modulation (EM) has major benefits in increasing bit rate and reducing chirp. Due to their high speed operation, high extinction ratio, low driving voltage, and compact size, multiple quantum well (MQW) electro-absorption modulators (EAMs) based on the quantum confined Stark effect (QCSE) are used for external modulation and are a crucial part of PICs [110]. EAMs are active devices and have a band edge near to that of a single mode laser. EAMs are one of the simplest devices to monolithically integrate with single mode lasers. They can be comparatively short devices, as low as $50\,\mu\mathrm{m}$, because they are dependent on a voltage-induced absorption shift that can be significant near the band edge.

High-speed phase modulators typically require long waveguides which results in a large device footprint, often being on the order of millimetres [112, 113]. These longer waveguides therefore require travelling-wave contacts which are demanding to design and fabricate. This is especially true in InP, where the RF and optical velocities are very different [114]. By contrast, lumped element EAMs do not share these issues. The electro-absorption effect in InP is strong, especially the quantum-confined Stark effect [115], and consequently an EAM can be as short as $50\,\mu\mathrm{m}$. Lumped element EAMs are also more easily fabricated, consisting of reverse biased p-i-n waveguides whose electrical contacts do not require overly-specific design restrictions. Lumped element EAMs enable the realisation of highly efficient, small footprint, high modulation efficiency and low drive voltage modulators.

5.3 Lumped Element EAMs

In comparison to other modulators, the design of a lumped element EAM is relatively simple, consisting of waveguide, similar to a laser, but rather than being forward biased, the EAM is reverse biased to facilitate absorption. This reverse bias signal can be modulated electrically using an applied RF signal to create a modulated light output. The microwave signal is applied to the top of the waveguide in a lumped element system as seen in Fig. 5.1. We can then model this device as a differential resistance R_j, and a capacitance C_j. This capacitance is a junction capacitance. The device performs as a lumped element with response time given by $\tau_{RC} = R_j C_j$, though it is often the driving circuit resistor which acts as a limiting factor for an EAM circuit as seen in

Fig. 5.1. Thus τ_{RC} may be more accurately written as $\tau_{RC} = R_l C_j$, where R_l is a load resistor placed in parallel. This response time determines the bandwidth. In a deeply etched ridge waveguide, the junction capacitance can be seen to operate like a parallel plate capacitor with the area being determined by the ridge width and length. The separation between the capacitive areas is the thickness of the depletion region, d_i. The length of the device thus operates as a limiting factor for both the speed of the device and the extinction ratio of the device for a given bandwidth. Longer devices will be slower but absorb more for a higher extinction ratio and vice versa.

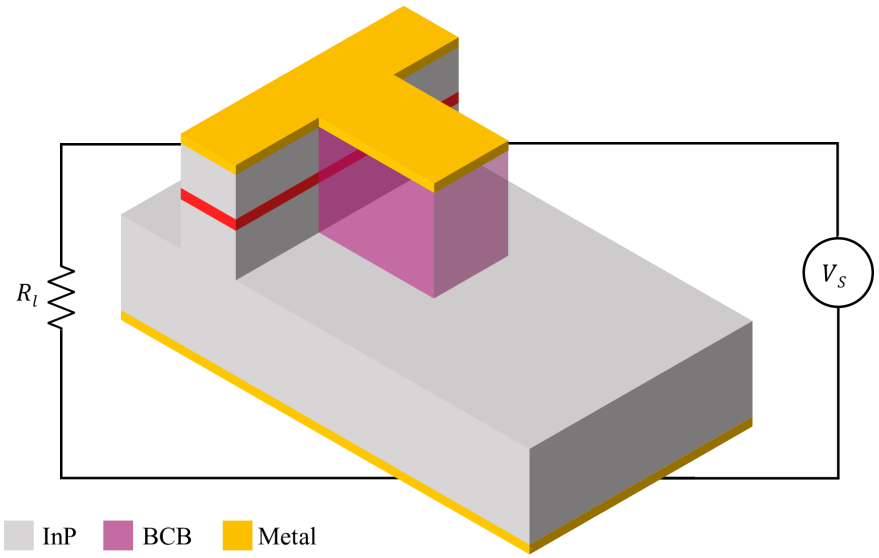

Figure 5.1: Electronic schematic diagram of lumped element EAM with A load resistor (R_l) in parallel terminating the electrical signal.

The driving voltage will decide how much power the EAM uses. This element becomes more significant as the number of integrated devices on a single PIC rises. In order to compare EAM performance with other integrated modulators we must define certain equivalent terminologies. The intensity of a forward propagating waveguide mode as it travels a distance z was previously defined by Eqn. 2.27.

$$P(z) = P_0 e^{-\Gamma(\alpha_0+\alpha)z} = P_0 e^{-\Gamma\alpha_{eff}} \tag{5.5}$$

where α denotes the absorption due to the QCSE. The light passing through the waveguide undergoes scattering and diffraction, which we will denote as propagation losses. The effective absorption α_{eff} collates the absorption from

three different regimes:

$$\alpha_{eff}(F,\lambda) = \alpha_0 + \Delta\alpha_{bias}(F_{bias},\lambda) + \Delta\alpha_{RF}(F_{C_j,RF}cos(\omega t)) \tag{5.6}$$

α_{eff} is the effective attenuation constant of the mode's intensity within the waveguide. P_0 is the input optical power at $z = 0$. Γ is defined in Eqn. 2.28. The DC component of the electric field is denoted as F_{bias}. The RF component across the junction, C_j, is denoted as $F_{C_j,RF}cos(\omega t)$.

The attenuation coefficient of the waveguide mode at $V_{bias} = V_{RF} = 0$ is given by α_0. This attenuation combines the exciton absorption of λ with zero applied field with other previously mentioned loss effects, scattering and diffraction.

$\Delta\alpha_{bias}$ is the change in the absorption factor caused by the application of a DC bias and is calculated via

$$\Delta\alpha_{bias}(F_{bias},\lambda) = \alpha_{bias}(F_{bias},\lambda) - \alpha_0 \tag{5.7}$$

The contribution from $\Delta\alpha_{RF}$ is due to the RF electric field across the diode, denoted here as $F_{C_j,RF}cos(\omega t)$. Using the represented attenuation, the fractional transmission, T, along a distance L, with a fibre coupling efficiency η_{ff}, representing the combined fractional coupling into and out of the EAM waveguide, can therefore be denoted as

$$T = \frac{P(z=L)}{P_0} = \eta_{ff}e^{-\Gamma\alpha_0 L}e^{-\Gamma\Delta\alpha_{bias}L}e^{-\Gamma\Delta\alpha_{RF}L} \tag{5.8}$$

where, as in Eqn. 2.30, the the insertion loss attributed to the waveguide and material, η_{ins};

$$\eta_{ff}e^{-\Gamma\alpha_0 L} = \eta_{ins} = \frac{P_{on}}{P_0} \tag{5.9}$$

5.3.1 Bandwidth and equivalent circuit

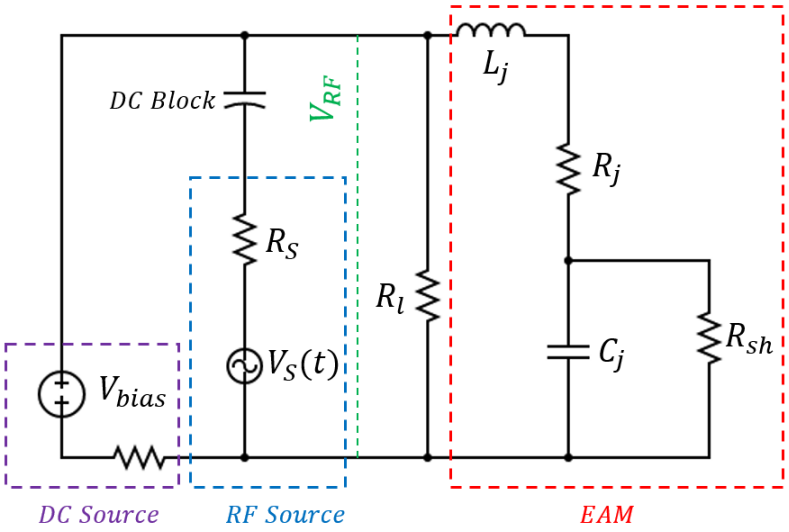

Figure 5.2: An equivalent circuit diagram of an EAM driven by a biased RF source

Fig. 5.2 demonstrates a simple equivalent circuit for an EAM, driven by an RF source which is powered by a DC voltage source. The EAM is dependent on the electric field across the quantum wells to cause the QCSE. Given that the shunt resistance R_{sh} is large, $R_{sh} >> R_j$, and the inductance L_j is small, we can treat the total voltage across the intrinsic region as

$$V_{C_j} \approx V_{bias} + V_{C_j,RF} cos(\omega t) \tag{5.10}$$

When reverse biased, the EAM's resistance is large, and thus a load resistor, R_l, is placed in parallel to terminate the RF signal at the device and minimise electrical reflections back to the source [116]. With perfect termination and a small photocurrent, the RF voltage transfer from the RF source to the EAM junction can be calculated using [109].

$$\left| \frac{V_{C_j,RF}}{V_s} \right| = \frac{1/\omega C_j}{\sqrt{(R_l + 2R_j)^2 + (2/\omega C_j)^2}} \tag{5.11}$$

The bandwidth, as mentioned previously, is the frequency at which the voltage transfer drops by $3\,\mathrm{dB}$, or when the voltage drops to $\frac{1}{\sqrt{2}}$ of its original value

$$f_{3dB} = \frac{1}{\pi C_j (R_l + 2R_j)} \tag{5.12}$$

The model can also be adjusted to include the induced photocurrent [117]. In Fig. 5.3 we can see how the capacitance of the device affects the bandwidth and how even slight reductions in capacitance can cause a larger increase in bandwidth.

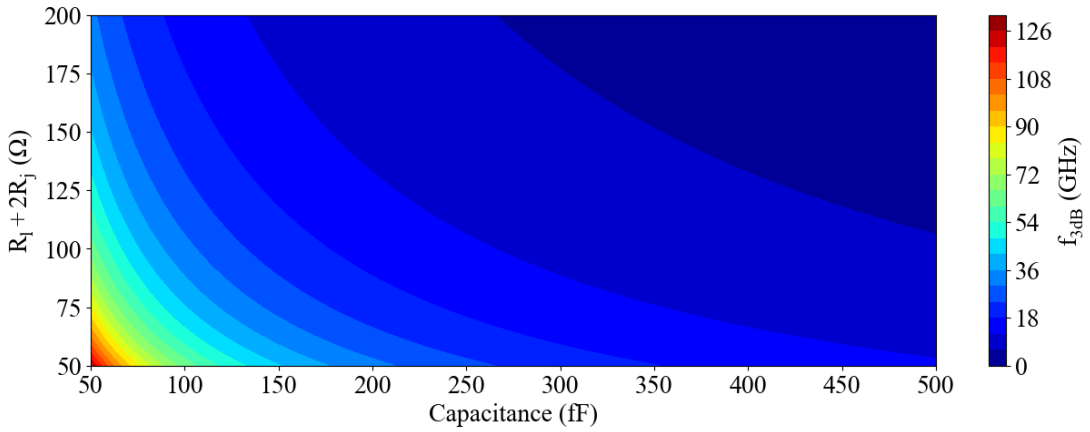

Figure 5.3: How f_{3dB} is affected by changing capacitance and $R_l + 2R_j$

5.3.2 Parasitic impedances

The modulation bandwidth of a lumped element EAM depends on the capacitance of the device, which consists of the waveguide and the electrical contacts used to reverse bias it to facilitate absorption. The equivalent circuit voltage transfer function given in Eqn. 5.11 is based on the assumption that all the resistances and capacitance of the device stem from the EAM itself. For lumped p-i-n type structures a parasitic impedance is always associated with the contact scheme used to deliver the RF signal. Thus, we seek to minimise this parasitic capacitance in order to maximise the speed of our devices. The minimisation of parasitic capacitance in lumped element Electro-Absorption Modulators (EAMs) is a critical aspect in the design of high-performance optical transmitters.

The contact pads for the lumped element device in question are the areas of metal placed near the waveguide to carry the electrical signal to the device. The ridge waveguides commonly used for lasers in our previous processes are on the order of $2.5\,\mu\mathrm{m}$ wide. This makes the possibility of direct probing or wire bonding to the device unfeasible. The DC laser process places metal

contacts on a layer of passivating dielectric such as $300\,\mathrm{nm}$ thick SiO_2 next to the waveguide. This dielectric sits atop the n-doped area of the semiconductor. The metal is evaporated onto the sidewalls of the waveguide to make contact with the waveguide's contact at the top of the ridge. These pads are designed to have a large area to facilitate needle probing for electrical testing and are robust. The large area of the pads also makes it easier to wire bond when packaging devices.

However this large metal contact on top of the passivation essentially forms a parallel plate capacitor with the n-doped substrate beneath the passivation, creating an additional capacitor in parallel with the EAM with a separation equal to the thickness of the passivation. This could have a parasitic capacitance on the order of $1\,\mathrm{nF}$, severely limiting the bandwidth of the device. These parasitics must be included when analysing the whole device and when determining the correct driving circuit to package the device with [116].

5.3.3 Traditional RF Contacts

Traditionally, lumped element EAMs make use of two methods to minimise the parasitic capacitance caused by the RF contact scheme. The first is to place the RF contact on the semi-insulating substrate and using topside n contacts. This reduces the transit time for the electrical signal but creates a height mismatch between the upper waveguide and lower contacts [118]. This approach requires either a thick dielectric, or an air bridge [119], to connect the contact on the SI substrate to the metal contact atop the waveguide. The area that runs over the n-doped layers needs to be minimised as metal placed in proximity to the n-doped layers will form additional parasitic capacitors. To this end, the passivation must be sufficiently thick due to the metal on the sidewall and on the n-doped layers contribution to the contact scheme capacitance.

The second approach is to planarise the entire structure using a dielectric such as benzocyclobutene (BCB) or polyimide and then place the ground contacts on the n-doped layers and the signal contact on this planarised layer [120]. These lower n contacts can then be connected with additional metal climbing the BCB to become planar with the signal contact. The contacts can alternatively be placed on a planarised dielectric, with contact being made through etched vias to the required layers. However, both approaches suffer from delamination which is common when placing the contacts on dielectrics such as SiO_2 and BCB. Additionally, contacts placed directly on BCB are less

robust than those placed on dielectric or semiconductor making cure bonding difficult.

5.3.4 Contact Pillar Isolation

In the fabrication of DC devices ($< 10\,\mathrm{GHz}$ operation), an n-doped substrate is often used as shown on the left in in Fig. 5.4. This is unsuitable for high-speed performance as the signal contact pillar's parasitic capacitance is large which limits the devices overall speed. The contact pillars are formed from the same p-i-n structure as the EAM waveguide, wherein the p-doped layers of the semiconductor and the n-doped layers may act as parallel plate capacitors with capacitance $> 400\,\mathrm{fF}$.

The isolated contact pillar shown in Fig. 5.4 addresses some of the issues with the contact configurations mentioned in the previous section. In this version, the GSG contacts are planar with the ridge waveguide, and are placed directly on semiconductor pillars formed in the same step as the ridge waveguide. The ground contact is formed through an angled n-metal evaporation, shorting the ground pillars to the n-doped layers. The signal contact pad is isolated from the rest of the device through a deep etch into the semi-insulating substrate similar to [121]. By isolating the signal contact through the semi-insulating etch no charge can build up below the signal contact, eliminating the capacitance between the signal contact and the n-doped layers. This method also places the probe metal in contact with the semiconductor rather than a dielectric.

The signal contact is connected to the device using a metal bridge on planarised BCB. The BCB could also be eliminated to form an air bridge. This sufficiently minimises parasitics for high speed operation by keeping a relatively large distance between the bridge metal and n-doped layers. This configuration is suitable for devices that require the contacts to be placed to the side of the waveguide, generally perpendicular to the waveguide. This is the case for an EAM or a laser where there is a facet or entry and exit point at either side of the device. This configuration provides an excellent platform for flip-chip packaging due to the planarisation of the contacts and the ridge [122]. Flip-chip packaging is favourable when packaging high-density PICs, as doing so minimises the use of bond wires and the inductance associated with them.

The planarisation of the contacts also makes testing with RF probes easier, as the probes no longer have to be bent in order to make contact. This occurs when the signal contact is at a different height relative to the ground contacts. These advantages make the isolated pedestal contact suitable for high density PICs.

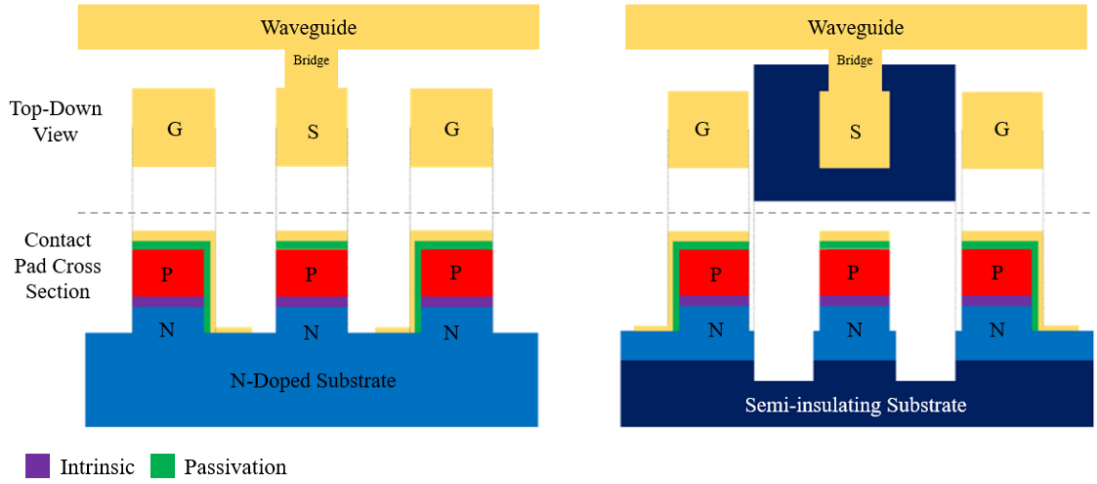

Figure 5.4: On the left is a DC device with GSG contacts planar to the waveguide on an n-doped substrate. On the right is a modified contact scheme designed to minimise the influence of the signal pad's capacitance.

5.4 Device Design

Fig. 5.5 shows a schematic of the lumped element EAM device design used for this research. The design consists of a p-i-n InP waveguide and three p-i-n InP pillars upon which the ground-signal-ground contacts sit in order to be planar with the EAM waveguide. The signal pillar and the waveguide are connected by a metal bridge which sits atop patterned benzocyclobutene (BCB). The EAM is formed from a central electrically isolated section of the main waveguide as can be seen in the SEM image on the right of Fig.5.5. This divides the waveguide into three sections. From left to right these sections are a passive section for input, the EAM waveguide, and a passive section for output. The passivation of these sections is achieved through forward bias. This design minimises the difficulty in manually scribing and cleaving EAMs as short as $50\,\mu\mathrm{m}$ by ensuring the overall chip size is $\geq 400\,\mu\mathrm{m}$.

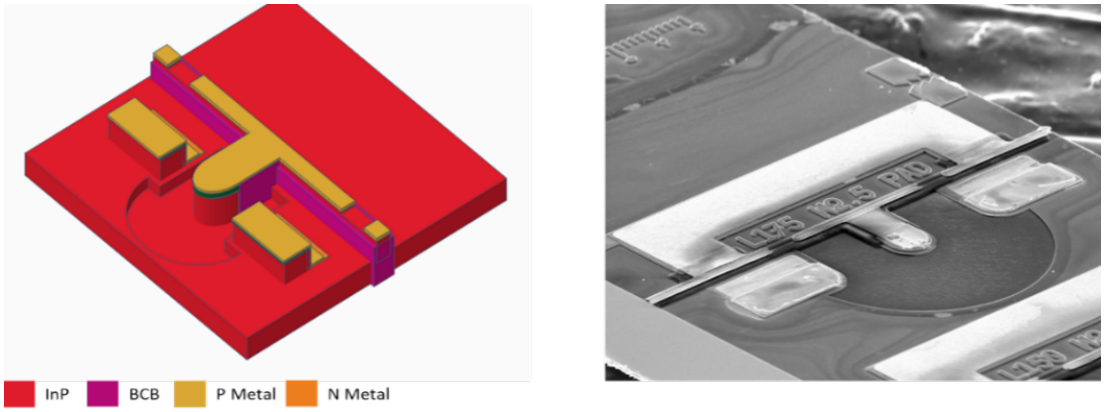

Figure 5.5: On the left is a 3D model of the EAM device showing the main EAM waveguide connected to the signal contact and two accompanying ground contacts suitable for a GSG probe. On the right is a SEM image of the fabricated device. The fabricated device has an additional metal contact to allow for forward biasing of the waveguide surrounding the EAM.

The lumped element EAM device was fabricated on two different in-house grown InP based materials on a semi-insulating substrate. These materials were designed to modulate wavelengths around $1310\,\mathrm{nm}$. The first material consisted of six compressively strained quantum wells, which is denoted as 6QW. The second consisted of twelve compressively strained quantum wells, which is denoted as 12QW. Standard lithographic techniques were used to define the ridge, with a ridge width of $2.5\,\mu\mathrm{m}$, and height of $1.7\,\mu\mathrm{m}$. The modulating section of the EAM is electrically isolated from surrounding pseudo-passive sections by etching away the contact layers resulting in a measured isolation resistance of $> 10\,\mathrm{k}\Omega$. A separate etch through the quantum wells was performed so as to provide access to the n region to form a ground-signal-ground (GSG) contact.

5.5 High-Speed Processing

5.5.1 Ridge-etch Lithography

The fabrication of electro-absorption modulators capable of operating at a higher speed than $10\,\mathrm{GHz}$ requires that we make use of material with semi-insulating substrate rather than n doped substrate, so as to minimise the transit time needed for an electron to traverse the p-i-n junction. This requires that we now make use of topside n-metal contacts in the form of both ground-signal (GS) and ground-signal-ground (GSG) contacts.

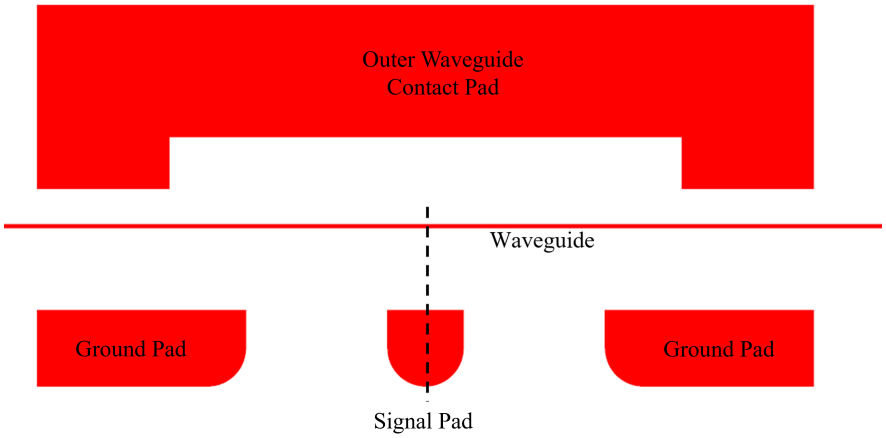

Figure 5.6: A view of the ridge definitions for the high speed fabrication process shown in red. Here we define the waveguide and the planar contact pillars.

These GS and GSG contacts need to be of the same pitch in order to be contacted by a GS or GSG probe. To accomplish this we make use of pillars to support our contact pads and keep them planar with the waveguide which we will define at the same time as our ridge waveguides as shown in Fig. 5.6. Here we have defined our waveguide, as in the DC process, and additionally we have defined several pad pillars which will support our electrical contact pads for the EAM and the surrounding waveguide we hope to electrically passivate.

For the EAM processing we use deep-etched waveguides and a metal-first process. We begin by evaporating a thick metal coating of $25{:}500{:}25\,\mathrm{nm}$ of Ti:Au:Ti as shown in Fig 5.7(a). Next a $900\,\mu\mathrm{m}$ layer of SiO_2, is deposited via PECVD as a hard mask, a covering which will protect the area of semiconductor which we do not wish to etch as shown in Fig 5.7(b).

Next S1800 Microposit photoresist (PR) was used as a soft mask, which defines the areas we do not want to etch from our hard mask. HMDS was used as an adhesion promoter. Once developed, the exposed resist is removed using MF319. Following this step a plasma etch is used to etch away the areas of SiO_2 which are not protected by PR. Now, in Fig 5.7(c) we use reactive ion etching with Cl_2, CH_4, and Ar gasses to etch away our metal covering. Finally we begin our semiconductor etch down below the quantum wells, to the n-doped material in our epitaxy as shown in Fig 5.7(d). In this step we must avoid etching down into the substrate to preserve our n contacts.

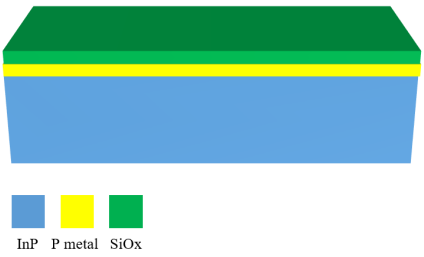

(a) A layer of Ti:Au:Ti and passivation, SiO_2, is deposited

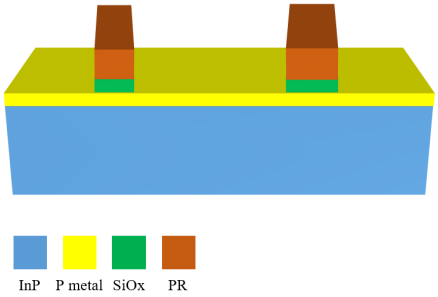

(b) PR is used to define the waveguides and plasma etching is used to remove the SiO_2 from the area to be deep etched

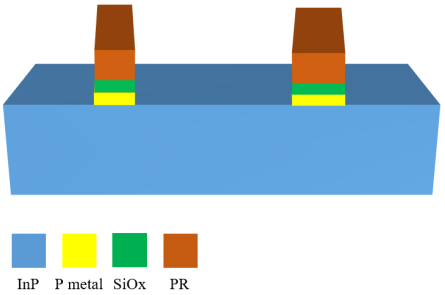

(c) Plasma etching is used to remove the metal where required using a recipe with Cl_2, CH_4, and Ar.

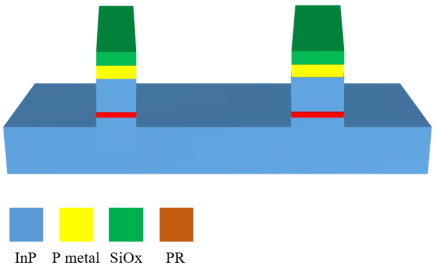

(d) The area of the semiconductor to be deeply etched is dry etched using Cl_2, CH_4, and H_2.

Figure 5.7: Process flow for the first lithographic step at the cross section shown in the dashed line in Fig. 5.6.

5.5.2 Substrate Isolation-etch Lithography

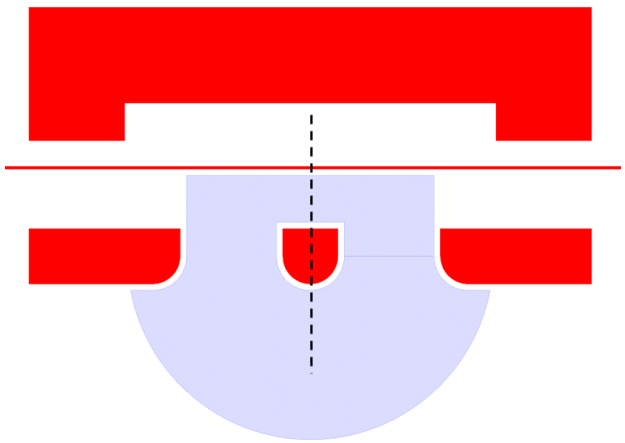

Figure 5.8: A view of the isolation etch definitions for the high speed fabrication process shown in blue.

The isolation etch is a secondary semiconductor etch completed after the etch to define the ridge waveguides. In this step the quality of the sidewalls is unimportant as the isolation etch is purely for electrical isolation and serves no purpose optically. For this stage we replace the old layer of SiO_2 with a new layer with thickness $300\,\mathrm{nm}$ and use photolithography to pattern the areas we want to etch as in Fig. 5.8 and Fig. 5.9(a). Next we use plasma etching to etch away the SiO_2 hard mask to expose the semiconductor as in Fig. 5.9(b). The soft mask is then removed and the semiconductor is etched down into the substrate to electrically isolate the signal pad pillar as in Fig. 5.9(c). After this the semiconductor is wet etched with HCl:H_3P to remove any conductive contaminants deposited by the plasma etch.

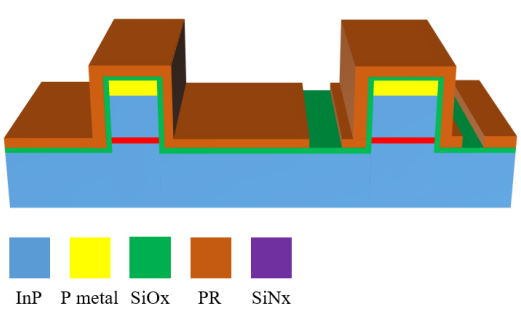

(a) Old SiO_2 is replaced with a fresh layer and PR is patterned to expose areas to be etched.

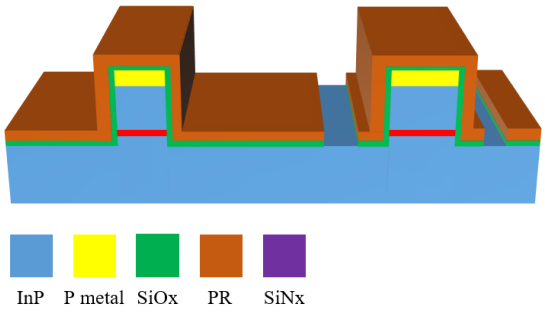

(b) SiO_2 is etched to expose the semiconductor area to be etched.

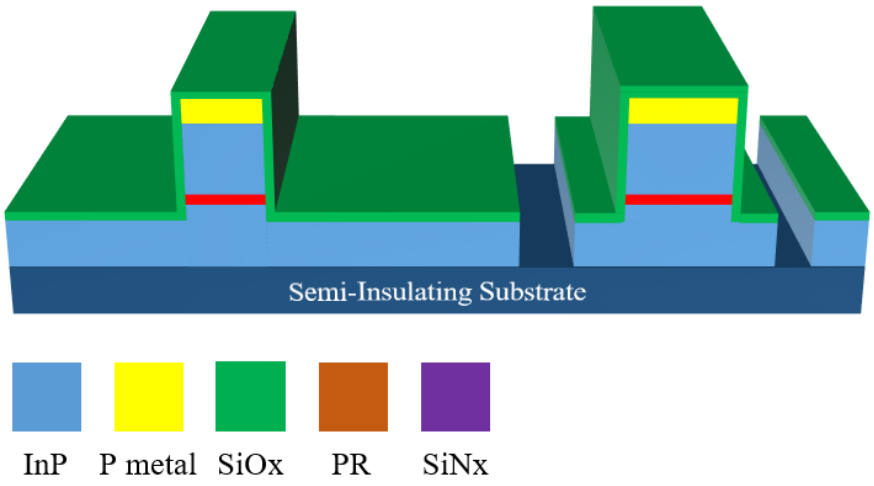

(c) PR is removed and the semiconductor is etched through to the substrate.

Figure 5.9: Process flow for the second lithographic step at the cross section shown in the dashed line in Fig. 5.8

5.5.3 Lower N-Metal Lithography and BCB Planarisation

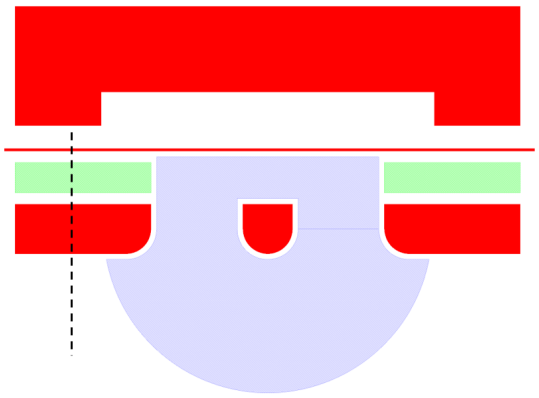

Figure 5.10: A view of the n-metal definitions for the high speed fabrication process shown in light green.

For the next step we need to open our passivation on top to expose the n doped semiconductor so that we can complete the n-contact on the topside of the device as shown in light green in Fig. 5.10. This step is also a combined metal deposition step, to deposit n contact metal; nickel, gold and germanium. We deposit LOR and S1800 PR and use photolithography to open up the area of interest as shown in Fig. 5.11(a) and remove the passivation SiO_2 as in Fig. 5.11(b). This leaves our n-doped semiconductor exposed and ready for metal deposition as in Fig. 5.11(c). Metal is deposited using an electron beam evaporator. Evaporation is done under a high vacuum in a bell jar chamber and is achieved by heating the desired metal source with an electron beam. As the source material evaporates, it forms a thin film on the samples. Metal liftoff is done in MF319 as in Fig. 5.11(d).

As this is n metal we also anneal it in a furnace at $420\,^{\circ}\mathrm{C}$ for 10 minutes to improve the contact resistivity. We are able to do TLM measurements to measure the initial contact n metal resistance, which confirms that before annealing the contact resistance is on the order of $10^{-4}\ \Omega cm^2$. After annealing the n metal can be noted to change from a golden hue to a pink tint and the contact resistance improves to $\sim 10^{-7}\ \Omega cm^2$.

The next step is the introduction of the polymer benzocyclobutene used to support the metal bridges used to connect the signal pillar pad to the EAM waveguide for electrical contact. Initially the surface of the wafer is placed on a hot plate at $120\,^{\circ}\mathrm{C}$ to ensure the surface is dehydrated. Next, adhesion promoter AP3000 is used to prepare the surface. AP3000 is based on

organosilane primer chemistry and are supplied as dilute solutions of the organosilane compounds in 1-methoxy-2-propanol. After this BCB is spun on and cured overnight in a curing furnace. With this step the surface appears as in Fig. 5.11(e).

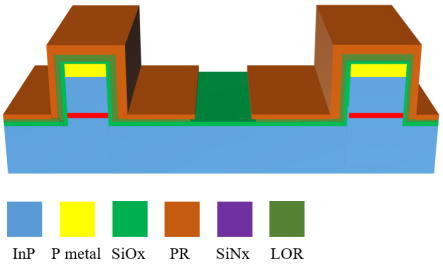

(a) LOR and PR are spun onto the surface. Lithography is used to expose areas of n-doped material.

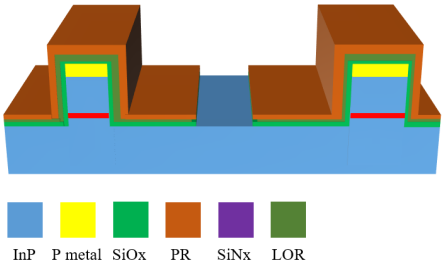

(b) SiO_2 covering the n-doped semiconductor region is etched.

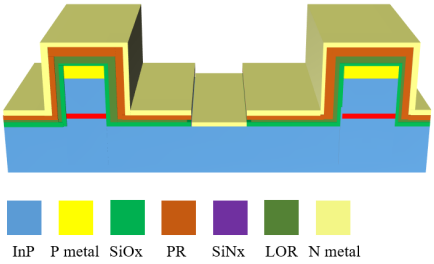

(c) N metal is deposited on the sample.

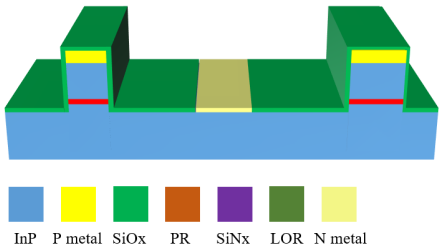

(d) Metal liftoff is completed and the n metal is annealed.

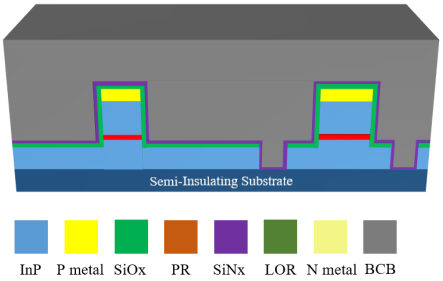

(e) Adhesion promoter and polymer are spun onto the sample and cured.

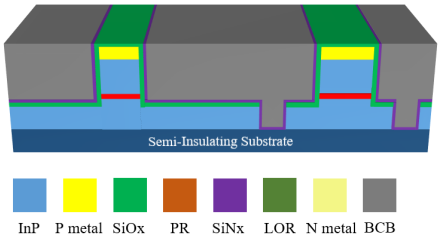

(f) The BCB is etched back to become planar with the ridge waveguide.

Figure 5.11: Process flow for the third lithographic step

In an attempt to aid better planarisation, additional layers of PR are spun on top of the BCB. Following this a plasma etch with sulphur hexafluoride (SF_6) chemistry is used to etch the PR and the BCB. The selectivity of the etch recipe of PR and BCB is equivalent. Endpoint monitoring is used over P TLM pillars to determine the stop point of the etch to leave the oxide at the top of the

ridges exposed. This point of the step is why a thick metal first process is used, so that there is a $500\,\mu\mathrm{m}$ tolerance in the exposure of the waveguide through the BCB. The final result of this process is shown in Fig. 5.11(f).

5.5.4 BCB Patterning Lithography

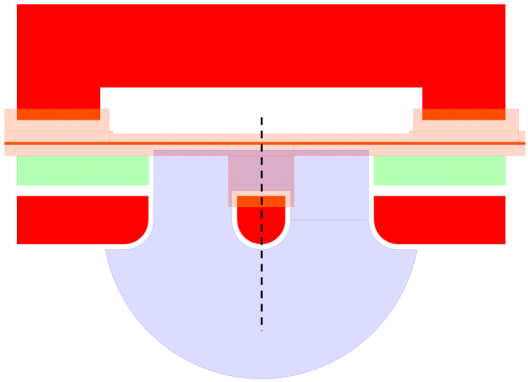

Figure 5.12: A view of the BCB patterning definitions for the high speed fabrication process show in orange.

The next part of the process involves removing BCB from unintended areas. BCB is used around the waveguides for a low tolerance oxide opening later in the process and as a bridge to connect the EAM to the signal pillar pad as shown in Fig. 5.12. Removing the BCB requires using SPR220 PR as a softmask instead of S1800 resist to achieve a high selectivity in the BCB etch, as shown in Fig. 5.13(a). The SPR220 requires a longer wait time of at least 40 minutes after exposure before development to allow the lithography to complete. After this the BCB is etched using the same recipe used in the previous step, resulting in Fig. 5.13(b). Following this the PR is removed and the piece is cleaned using O_2 plasma and 1165 solution in preparation for the next step.

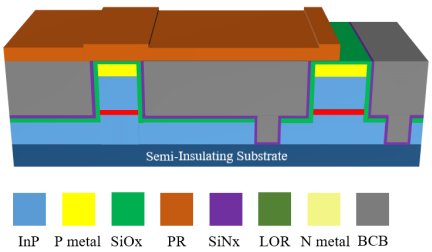

(a) Lithography is used to define the areas where BCB is to be removed.

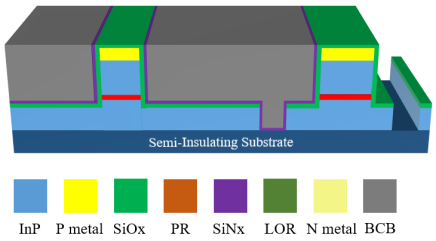

(b) BCB is etched away in exposed areas.

Figure 5.13: Process flow for the fourth lithographic step

5.5.5 P-metal Window-Opening Lithography

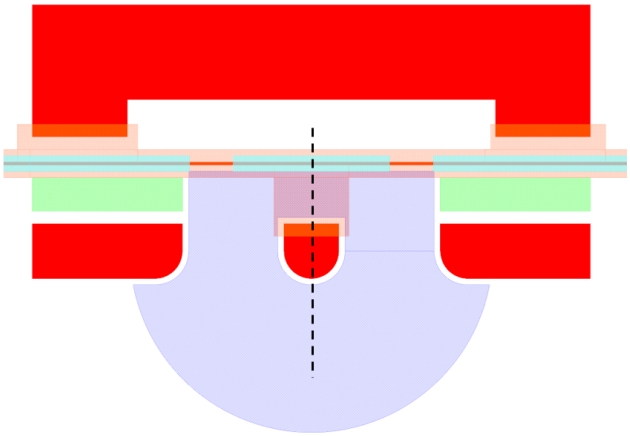

Figure 5.14: A view of the oxide opening patterning definitions for the high speed fabrication process shown in cyan. Dielectric is removed here to provide an opening for metal contacts to the waveguide.

The next step involves opening up the passivation on the waveguides. In the window open lithography in the DC fabrication process the oxide opening was $1.5\,\mu\mathrm{m}$ which was $1\,\mu\mathrm{m}$ smaller than the waveguide. This alignment in the high speed process has a higher tolerance with a width of $7.5\,\mu\mathrm{m}$ which is $5\,\mu\mathrm{m}$ larger than the waveguide. For this alignment we are relying on the accuracy of our BCB planarisation to expose only the thick metal atop our waveguide without exposing the lower intrinsic part of our p-i-n semiconductor. This allows our oxide opening to be larger as we are not concerned with the sidewall's passivation coverage being removed in the oxide etch thanks to the BCB covering most of the waveguide. The view of the larger oxide opening is shown in Fig.5.14.

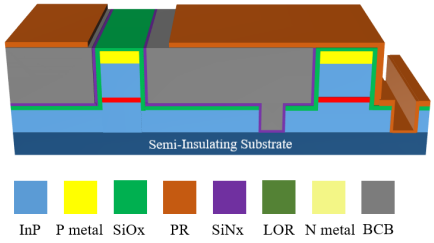

(a) Lithography is used to expose areas of the waveguide where metal contact is required.

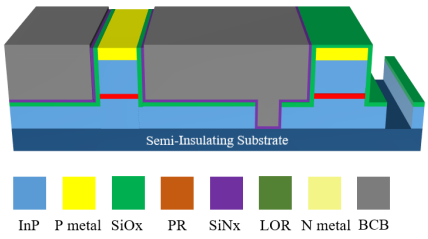

(b) A buffered oxide etch is used to remove SiO_2 from the required areas.

Figure 5.15: Process flow for the fifth lithographic step

Fig. 5.15 shows the processing used for this step. First S1800 series PR is spun on to coat the sample. Next lithography is used to expose the areas of the waveguide where electrical contact will be required. The exposed SiO_2 is removed by dipping the sample into a buffered-oxide etchant, a mixture of nitric acid (HNO_3) and hydrofluoric acid (HF). With the passivation removed from the area of interest, O_2 plasma and 1165 solvent remover are used to remove PR from the piece in preparation for the next step.

5.5.6 P-metal Deposition Lithography

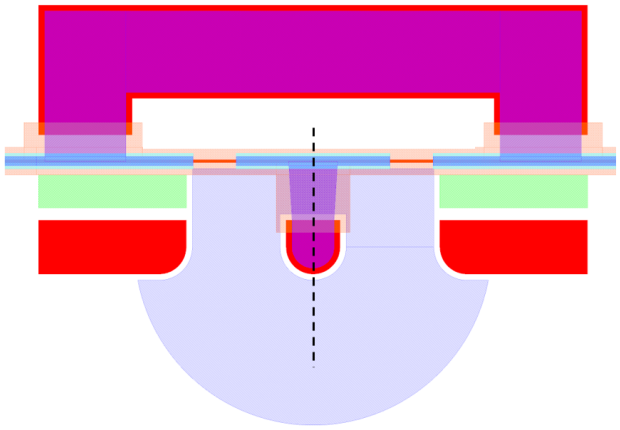

Figure 5.16: A view of the P metal deposition definitions for the high speed fabrication process shown in purple.

The next lithographic stage of the process is used to define the areas of the mask where a p-contact metal is to be deposited as shown in Fig.5.16. In this step we use a thick metal consisting of $25\,\mathrm{nm}$ of titanium which provides excellent adhesion, and $500\,\mathrm{nm}$ of gold. The metal covers the oxide opening to link the signal contact pad to the EAM waveguide to allow the EAM section of the waveguide to be biased. The p metal coating also links the outer areas of the waveguide to a larger contact pad.

The placement of the metal divides the waveguide into two sections; the EAM to be reverse biased, and the remaining sections of waveguides which will be forward biased to prevent them from being absorptive. These two sections will be electrically isolated in the final stage of the fabrication process. Isolating the EAM in this way allows EAMs as small as $50\,\mu\mathrm{m}$ in length to be easier to cleave by increasing the length of the overall device, as mentioned earlier. Secondly this allows for several EAMs of varying lengths to be placed on the

same bar which can be convenient for optimising device placement and quantity across a wafer.

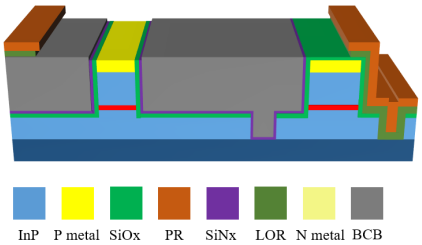

(a) LOR and S1800 series PR is used for this lithography to expose areas where metal is to be deposited.

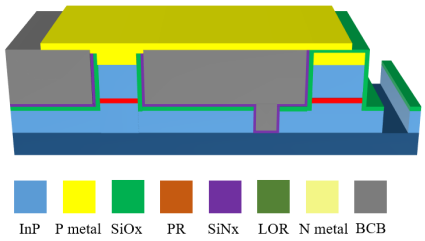

(b) Metal is evaporated onto the sample, connecting waveguides to be biased and contact pad pillars.

Figure 5.17: Process flow for the sixth lithographic step

The definition of the metal contact lithography requires two separate photoresist polymers in addition to the regular adhesion promoter HMDS. The first is LOR and the second is S1800 series PR. The sample is exposed for approximately $22\,\mathrm{s}$, in order to create an undercut in the two resists used to facilitate the lift-off of the unwanted metal. The undercut can be visually inspected using a microscope to confirm the piece is suitable for metal deposition. This process is shown in Fig. 5.17.

5.5.7 Full N-metal Deposition Lithography

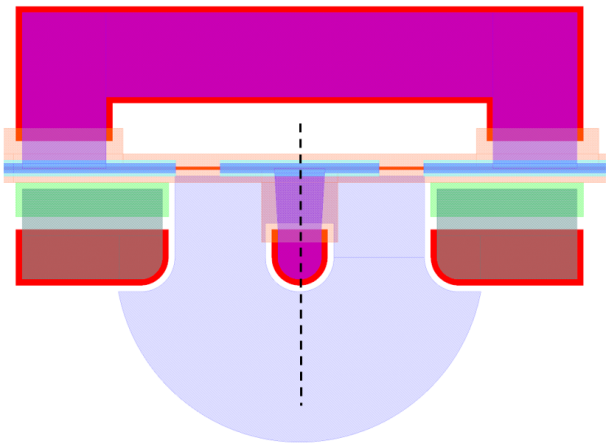

Figure 5.18: A view of the n metal deposition definitions for the high speed fabrication process shown in grey.

In order to have the RF contacts for the GSG pads be planar with each other, we have created three pillars for the probe to be placed upon. The next step of the fabrication process, as shown in Fig. 5.18, connects the top of the pillars to the n-metal we deposited earlier onto the exposed n-doped semiconductor.

The definition of the metal contact lithography is identical to the previous p-metal deposition. Metal is deposited using an electron beam evaporator. Afterwards the sample is placed in 1165 solution to lift off the metal in areas unexposed by the lithography. This process is shown in Fig. 5.19. A thicker layer of titanium is used in this deposition step to aid in sidewall metal coverage connecting the lower n-metal to the upper contact pillar.

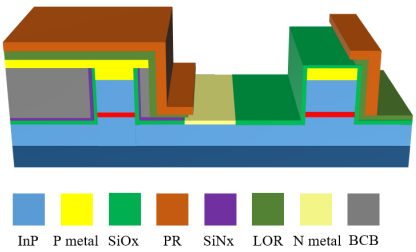

(a) LOR and S1800 series PR is used for this lithography to expose areas where metal is to be deposited.

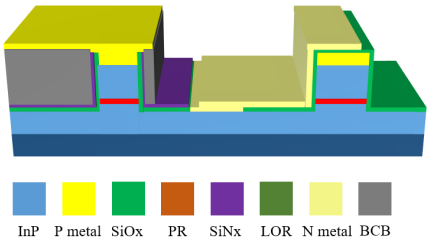

(b) Metal is evaporated onto the sample, connecting the lower n-metal and the contact pad pillars.

Figure 5.19: Process flow for the seventh lithographic step

5.5.8 Contact Layer Etch Lithography

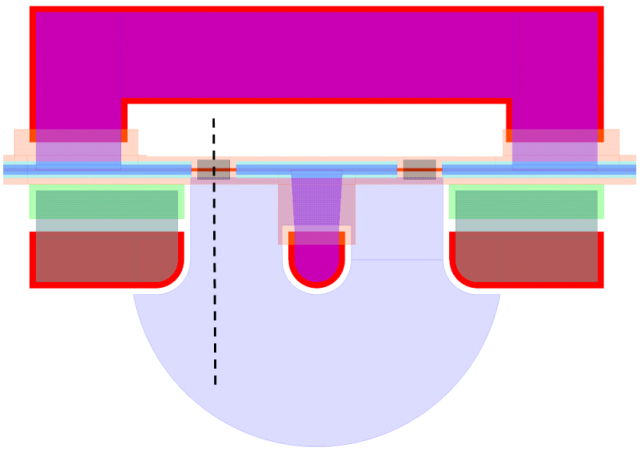

Figure 5.20: A view of the contact layer etch definitions for the high speed fabrication process

The EAM device shown in Fig. 5.20 is intended to consist of two distinct electrical sections, the central EAM itself connected to the signal pad, and the outer waveguides connected to a large pad. The EAM is intended to be reverse biased to increase absorption in that section when required. The outer waveguides are intended to be forward biased to create passive sections. Thus, these sections are required to be electrically isolated to allow them to fulfil their purposes.

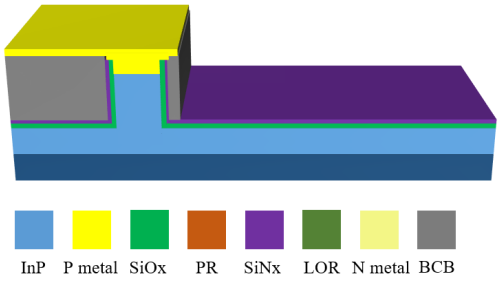

(a) Lithography exposes the area where the contact layer is to be removed.

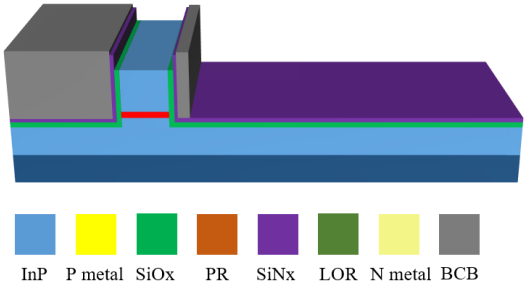

(b) Gold is removed from the waveguide using $KI : I_2$. Titanium is removed using BOE.

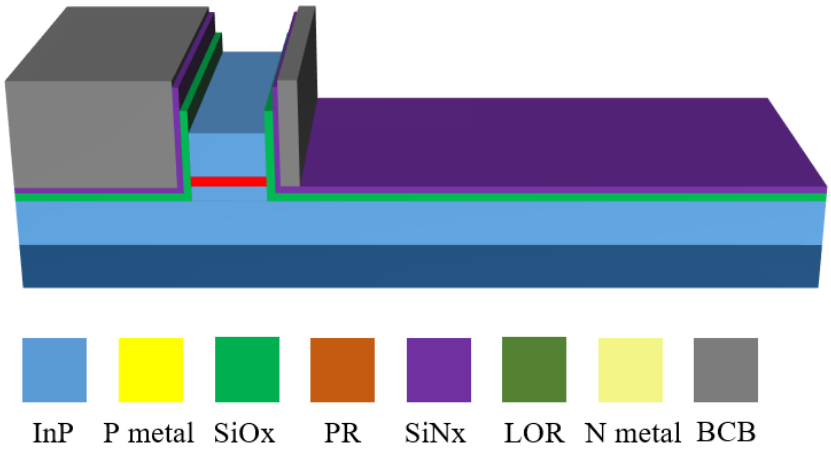

(c) The contact layer is removed via wet etching.

Figure 5.21: Process flow for the eighth lithographic step

The electrical isolation technique used for the EAM process removes the contact layer of the epitaxial structure between the two sections of the device shown in Fig. 5.20. To accomplish this, first lithography is used to expose the areas of the waveguide where the contact layer is to be removed. Next the metal covering the waveguide needs to be removed to expose the semiconductor beneath. The gold layer is removed via wet etching using a

solution of $KI : I_2$. The titanium beneath is then etched using BOE. The exposed InGaAs and InGaAsP is then wet etched using a solution of H_2S0_4, H_20_2, and de-ionised water. A portion of the InP beneath is then etched away using a solution of HCl and H_3PO_4. A view of this process is shown in Fig. 5.21. The sample is subsequently thinned in a manner identical to the DC process. In this process, due to the semi-insulating substrate, no n-metal is deposited on the backside of the sample. Once thinned the sample is cleaved into devices ready to be tested.

5.6 Equivalent Circuit Modelling

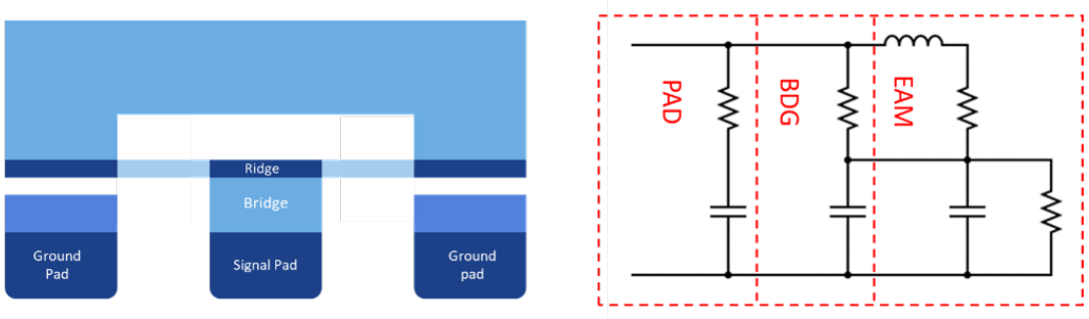

Figure 5.22: Electrically, the EAM device can be broken down into 3 distinct sections; the contact pad, the metal bridge connecting the contact pad to the EAM, and the EAM itself.

As seen in Fig. 5.22, the EAM can be separated into three distinct electrical sections; the GSG contacts, the metal bridge suspended on a polymer connecting the signal contact to the EAM, and the EAM itself. The contact pads and the bridge are part of the electrical contact scheme to deliver the RF signal to the EAM. The bandwidth of the EAM, f_{3dB} is inversely related to the impedance of the entire circuit, thus minimising these parasitic impedances maximises the EAM's speed.

In order to model the device we calculate the impedance of each section of our circuit, resistors, Z_R, inductors, Z_L, and capacitors, Z_C, from an equivalent Thevenin circuit of the entire structure. This is done by adding the impedance in series and parallel until only one remains, Z_T. For radio frequency (RF) signals we have

$$Z_R = R \qquad Z_L = \frac{1}{i\omega L} \qquad Z_C = \frac{1}{i\omega C} \tag{5.13}$$

Using complex variables, the mathematics proceeds as if these quantities were simple resistors. Thus, by finding the frequency dependent equivalent impedance circuit for the EAM we can find the reflection coefficient, $S_{11}(\omega)$.

$$S_{11}(\omega) = \frac{Z_T(\omega) - Z_0}{Z_T(\omega) + Z_0} \tag{5.14}$$

Here Z_0 is our impedance match. With a method of calculating $S_{11}(\omega)$ based on our equivalent circuit we can now recursively solve the equation to match the simulated $S_{11}(\omega)$ to an experimental $S_{11}(\omega)$ measurement. This allows us to solve for the parasitic capacitance present in each of our components by creating individual test structures which can isolate the constituent components of our EAM; the contact pads, the metal bridge, and finally the EAM itself.

5.7 Contact Pad Optimisation

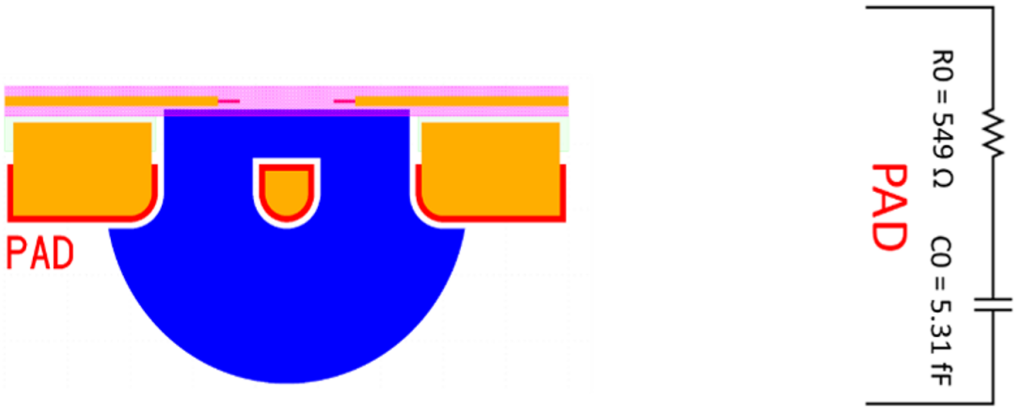

Figure 5.23: On the left is the test structure fabricated to perform a measurement of the capacitance of the pads. On the right is a fitted model of the experimental data.

A test structure based on Fig. 5.23 was fabricated and characterised by measuring the S_{11} scattering matrix from 0-40GHz using an Anritsu vector network analyser (VNA). The measured complex impedance values were then fitted to an inductor-resistor-capacitor (LRC) circuit as described in the previous section with the extracted capacitance being $\sim$ 5fF for the device.

Fig. 5.24a shows the S_{11} measurements from the test structure as a Smith chart and Fig. 5.24b shows the magnitude vs. frequency for the test structure

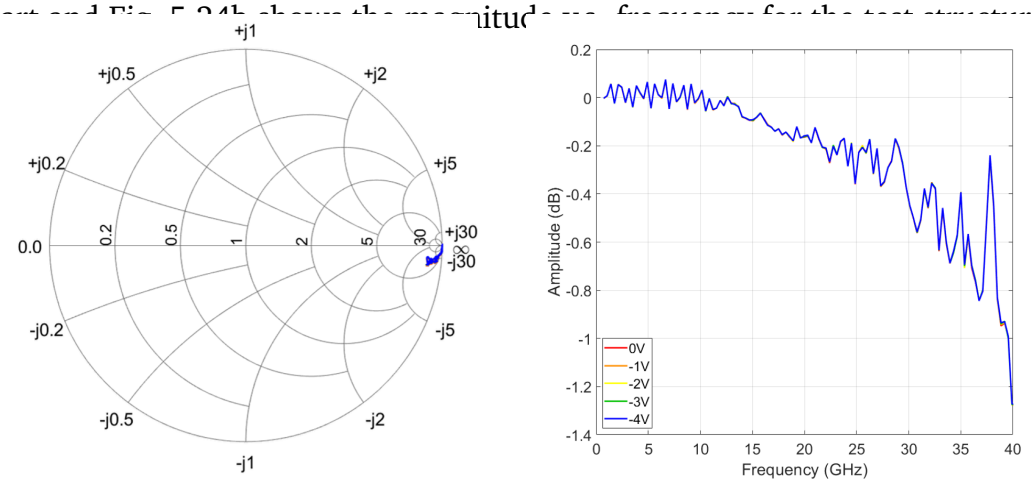

(a) Smith chart for the S_{11} data from the pad test structure shown in Fig. 5.23.

(b) Magnitude vs frequency for the S_{11} data from the pad test structure shown in Fig. 5.23.

Figure 5.24: Experimental measurements from the pad test device.

Additional test structures were fabricated which varied the width of the deep etch isolation as shown on the left of Fig. 5.25. The numeric value of the isolation separation was taken to be the width of the isolation between the signal contact pillar and the area occupied by the waveguide. These devices were measured using an Anritsu VNA and the capacitance was extracted. Overall, not much variation was found due to the decrease in isolation width. The results on the right of Fig. 5.25 show that $10\,\mu\mathrm{m}$ of isolation is sufficient to reduce the parasitic capacitance to acceptable levels.

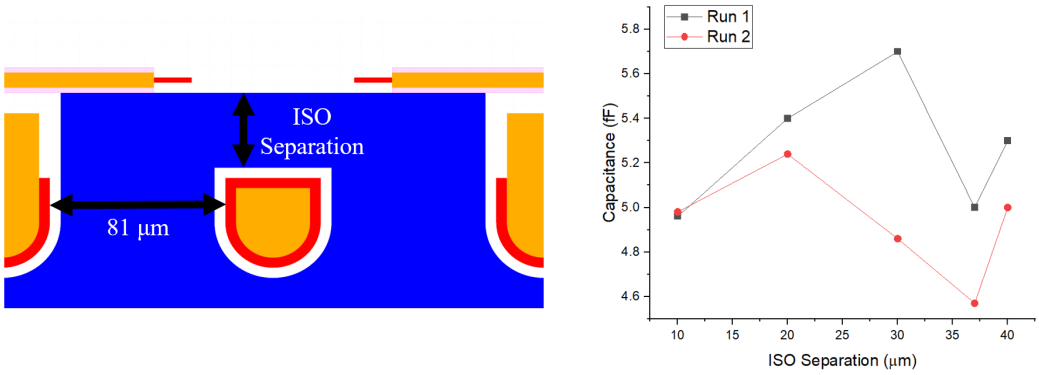

Figure 5.25: On the left is a closer look at the test structure used to measure the pad capacitance. The isolation separation is highlighted. On the right is the collated result of the pad's capacitance with varying isolation separation.

This test was repeated using full EAM test structures to obtain a full view of the effect of bringing the contact pillars close to the waveguide. For this test, EAMs of length $150\,\mu\mathrm{m}$ were fabricated using the design shown on the left of Fig. 5.26. The S_{11}s of these devices were measured and the parasitic capacitances were extracted. Minimal variation was observed between isolation separations $\geq 20\,\mu\mathrm{m}$ however a large increase in capacitance was noted at an isolation separation of $10\,\mu\mathrm{m}$.

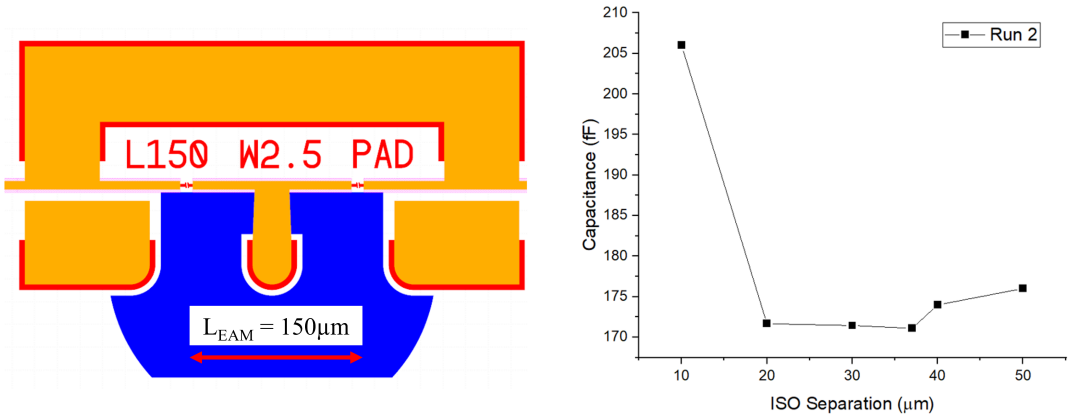

Figure 5.26: On the left is an EAM test structure. The centre waveguide acts as the EAM and receives it's biasing from the GSG contacts. The outer waveguides serve to lengthen the device length to $500\,\mu\mathrm{m}$ to make manual scribing and cleaving easier. An array of EAMs with varying isolation separation were fabricated and tested. On the right is the collated result of the EAM's capacitance with varying isolation separation.

5.8 Metal Bridge Optimisation

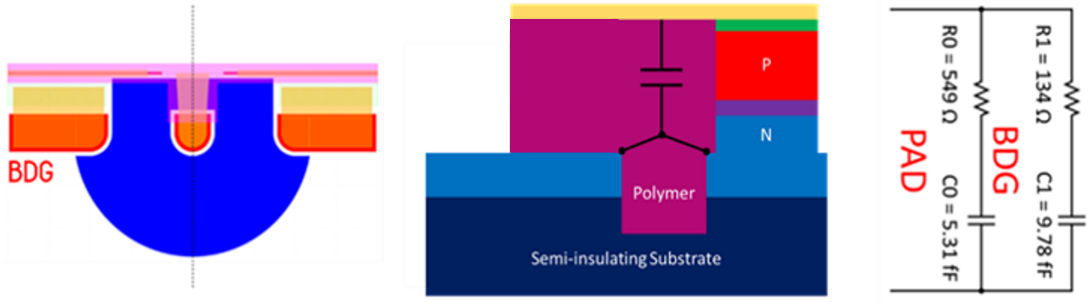

Figure 5.27: On the left is the test structure used to determine the metal bridge's contribution to the EAM's parasitic capacitance. In the centre is a cross section schematic of the source of the bridge's capacitance. On the right is the fitted model of the experimental data measured.

The impedance of the pillars to the ridge waveguide was quantified using a test structure as shown in Fig. 5.27. Using the equivalent circuit model fitted to the already measured data of the contact pads shown previously, measurements of this test structure were able to isolate the parasitic capacitance exclusive to the metal bridge. The metal bridge forms a pair of capacitor plates with the lower n region remaining following the deep isolation etch as shown in the figure below. Fig. 5.28a shows the S_{11} measurements from the test structure as a Smith chart and Fig. 5.28b shows the magnitude v.s. frequency for the test structure. The parasitic capacitance of the bridge was experimentally verified from S_{11} analysis to be $\sim$10 fF.

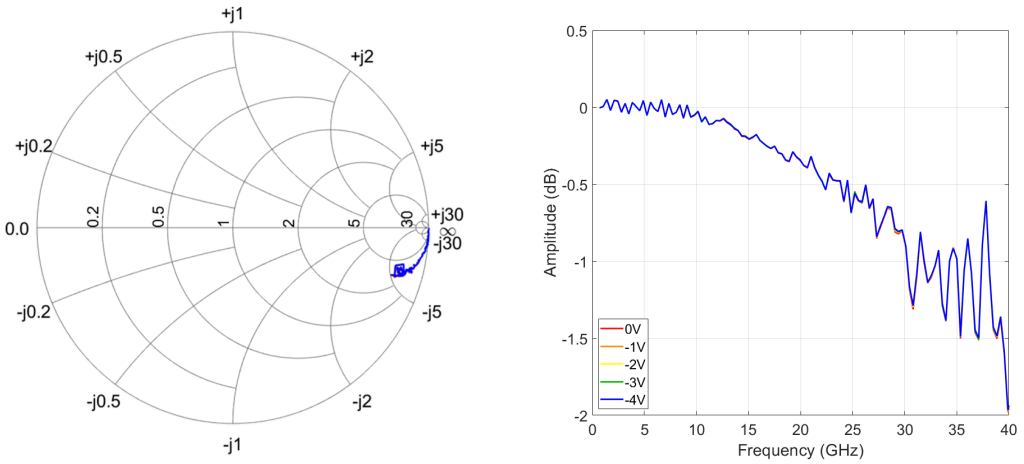

(a) Smith chart for the S_{11} data from the pad test structure shown in Fig. 5.27.

(b) Magnitude vs frequency for the S_{11} data from the pad test structure shown in Fig. 5.27.

Figure 5.28: Experimental measurements from the bridge test device.

These measurements offered a chance to further improve the bridge contribution to the parasitic capacitance of the overall device.

Recognising that the capacitance of the metal air bridge depends on the surface area of the bridge as $C \propto A$, decreasing the area of the bridge overlapping with the remaining n-doped semiconductor linearly reduces the bridge's parasitic capacitance. To measure this effect test structures were fabricated which varied the width of the metal bridge as shown on the left of Fig. 5.29. These test structures were measured and characterised in order to isolate the capacitance of each bridge width, with the results being shown on the right of Fig. 5.29.

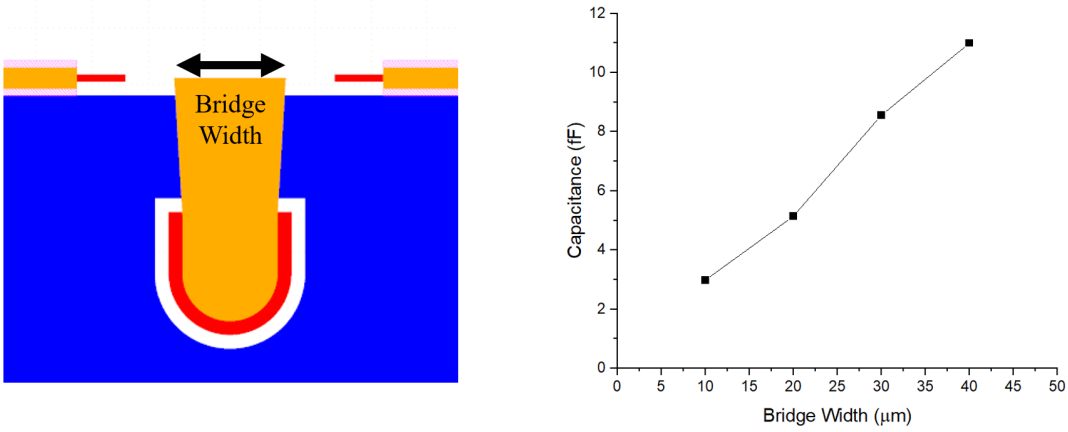

Figure 5.29: On the left is a closer look at the test structure used to measure the bridge capacitance. The bridge width is highlighted. On the right is the collated result of the bridge's capacitance with varying bridge width.

These results show a bridge with $\sim 3\,\mathrm{fF}$, which brings the total parasitic capacitance of the contact scheme down to below $10\,\mathrm{fF}$. The inductance of the bridge test structure does not notably increase with changing bridge size as shown in Fig. 5.30, which plots the fitted inductance from the S_{11} measurements. This figure also shows data collected for full EAM structures with length $150\,\mu\mathrm{m}$ and width $2.5\,\mu\mathrm{m}$ fabricated with varying bridge sizes. The resistance was measured through a GSG probe connected to the $150\,\mu\mathrm{m}$ EAM. $1\,\mathrm{V}$ was applied to the GSG pad of the EAMs with varying bridge width using a Keithly SMU which also measured the resultant resistance. The results demonstrate that the resistance of the full EAM is not heavily impacted by the reduction of bridge size.

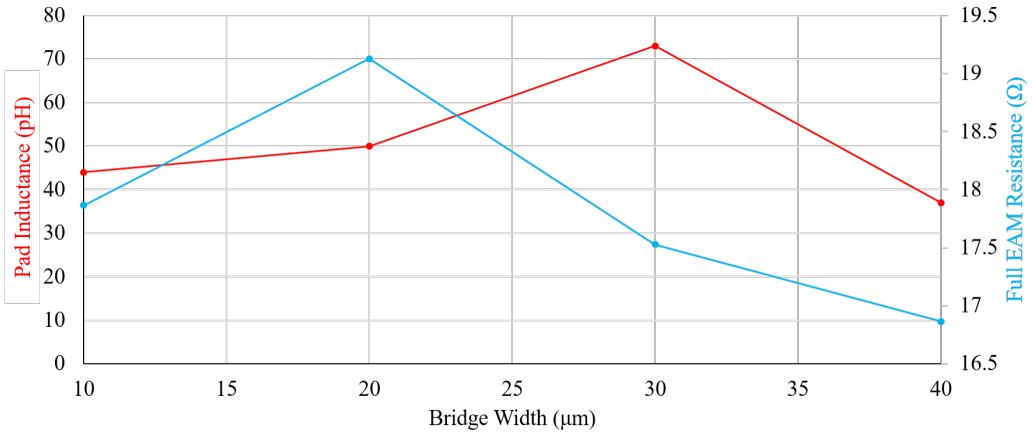

Figure 5.30: In red, the change in the impedance of the bridge test structure with varying bridge width. In blue, the change in resistance due to bridge width in a full EAM structure with length $150\,\mu\mathrm{m}$.

5.9 EAM Measurements

Full EAM structures were fabricated using the contact scheme proposed in the previous sections. S_{11} measurements were taken of these devices. This data was then inserted into the equivalent circuit model shown in Fig. 5.22. With the values of the contact pad and bridge elements of the circuit already measured using the aforementioned test structures, the full equivalent circuit of the EAM alone was able to be isolated through fitting the measured data as described in Section 5.6. This process was applied to EAMs of lengths varying from 50 to $175\,\mu\mathrm{m}$. With the equivalent circuit of the contact pads, the bridge and the EAMs, a simulated S_{21} of the proposed EAM device could be calculated.

This is done by calculating an equivalent impedance for the entire structure. We then form a simplified circuit with an idealised voltage source with a series impedance of Z_0, which is connected to the circuit with a total impedance of Z. In this case the voltage across the circuit is

$$V_{temp} = \frac{V_{source} Z}{Z + Z_0} \tag{5.15}$$

Taking $V_{source} = 1$ for an idealised case and using Ohm's law we can then write

$$I = \frac{V_{source}}{Z + Z_0} \qquad \rightarrow \qquad V_{temp} = IZ = \frac{V_{source} Z}{Z + Z_0} \tag{5.16}$$

With our branch being made up of the inductor, Z_L, plus the remainder, Z_m then the voltage on the other side of the inductor will be

$$V_{branch} = \frac{V_{temp}}{Z} \left(Z - Z_L\right) \tag{5.17}$$

which is the value of the voltage at the first stage to the right of the inductor. Calculating this value for each stage will eventually yield

$$V_{final} = S_{21} = \frac{V_{branch}}{Z_m} \left(Z_m - R\right) \tag{5.18}$$

With no shunt resistance, R_{sh} or $R_{sh} \rightarrow \infty$

$$Z_m - R = Z_C = \frac{1}{i\omega C} \tag{5.19}$$

If the shunt resistance exists and does not approach infinity;

$$\frac{1}{Z_m - R} = \frac{1}{R_{sh}} + i\omega C = \frac{1 + i\omega R_{sh} C}{R_{sh}} \rightarrow Z_m - R = \frac{R_{sh}}{1 + i\omega R_{sh} C} \tag{5.20}$$

Thus,

$$V_{final} = S_{21} = \frac{V_{branch}}{Z_m} \left(\frac{R_s}{1 + i\omega R_s C} \right) \tag{5.21}$$

EAMs were fabricated with various lengths on two different materials, one with twelve quantum wells, and one with six quantum wells and a widened separate confinement hetero-structure layer. S_{11} measurements were then made on these devices. Using the test structures present in the previous sections the parasitic capacitance of the EAM device was able to be isolated from the capacitance of the EAM itself.

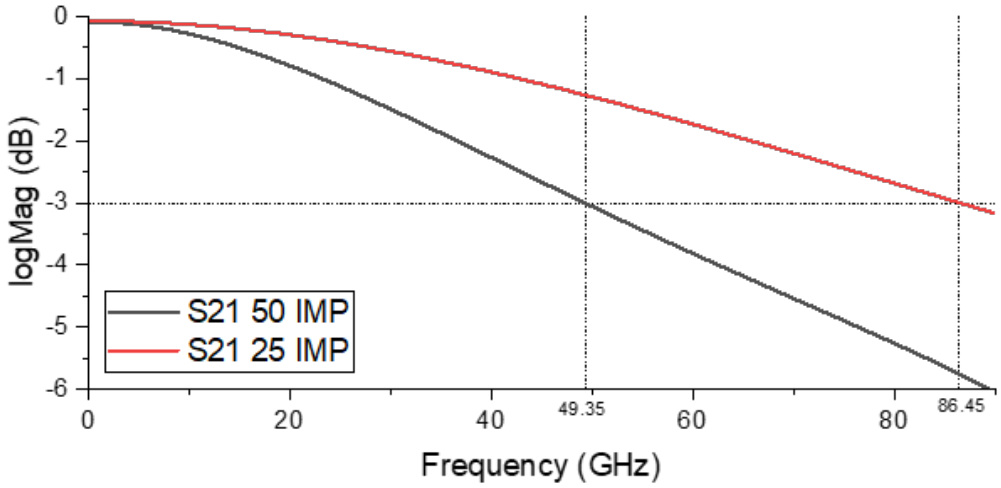

Figure 5.31: A simulated magnitude of a single S_{21} measurement based off experimental S_{11} data taken from an EAM with length of $50\,\mu\mathrm{m}$. The simulation is made for an impedance match of $50\,\Omega$ (black) and $25\,\Omega$ (red).

Using Eqn. 5.21, S_{21} values were calculated with inputs from over sixty different S_{11} EAM measurements for devices of varied lengths for both materials. Fig. 5.31 shows the best result obtained from one of these simulated S_{21} values calculated using data from an EAM made from the material with six quantum wells. This EAM had a length of $50\,\mu\mathrm{m}$ and a width of $2.5\,\mu\mathrm{m}$.
Fig. 5.32 shows the averaged result from the characterisation of all devices

fabricated which predicts a a f_{3dB} bandwidth of near $80\,\mathrm{GHz}$ for a $25\,\Omega$ impedance matched EAM of length $50\,\mu\mathrm{m}$.

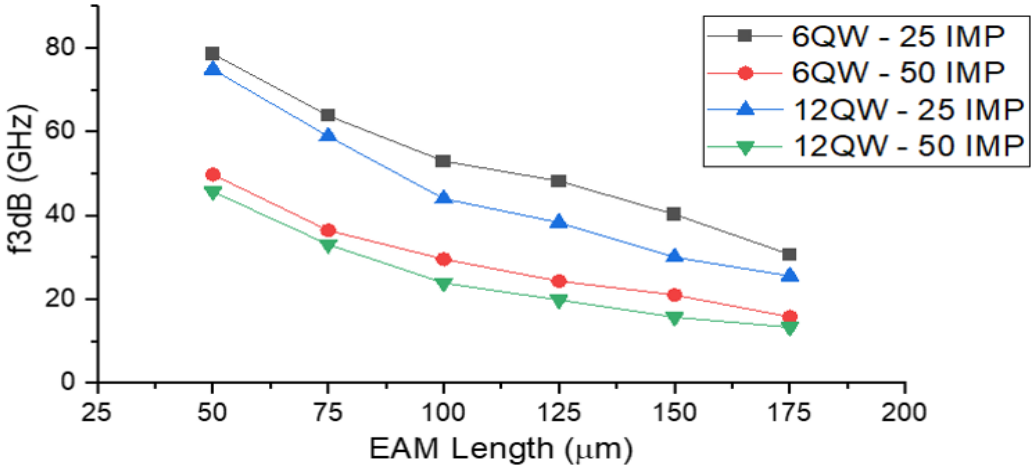

Figure 5.32: Over 60 devices were experimentally characterised. By isolating the parasitic capacitance measured before, simulated S_{21} values were generated and f_{3dB} values were extracted for devices of varying length. The average value for each material is presented above for impedances of $25\,\Omega$ and $50\,\Omega$.

The epitaxial materials used in Fig. 5.32 have the same intrinsic region thickness ($386\,\mathrm{nm}$ as in Fig. 3.1) but differ in the number of quantum wells within this intrinsic region, which would imply that the capacitive performance of both structures would be nearly identical. The 6QW material slightly outperforms the 12QW however, for which two possible explanations exist. The first possibility is due to the different number of quantum wells themselves. The total width of the intrinsic region for both materials is equal however the 12QW material has more AlInGaAs wells and barriers while the 6QW material has a thicker InGaAsP region to replace the decreased number of wells while keeping the intrinsic thickness equal. The change in structure could lead to a change in the average permittivity of the region, ϵ, and as $C \propto \epsilon$ this change would be reflected in the bandwidth of the device. For AlInGaAs, $\epsilon \approxeq 10$ at $\lambda = 1.3\,\mu\mathrm{m}$, whereas for InGaAsP, $\epsilon \approxeq 12$. Capacitors in series add like resistors in parallel thus a capacitor with N layers of materials i between "plates" of area, A, would have capacitance

$$\frac{1}{C} = \sum_{i=1}^{N} \frac{d_i}{\epsilon_i A} \tag{5.22}$$

This would lead to the 6QW material having a slightly lower capacitance and thus a slightly higher f_{3dB} as seen in FIg.5.32.

The second possibility is that, though the materials were processed in parallel, variations in fabrication could occur which would change the overall performances of the devices measured. A third explanation could be a variation in actual intrinsic thickness between two samples due to variations during the material growth phase.

Overall, the measurements confirm that the 6QW is electrically comparable to the 12QW material in terms of bandwidth and through the minimisation of the parasitic capacitance we are able to optimise our EAM performance to reach the theoretical limits of lumped EAM operation.

Chapter 6

EML Design, Fabrication & Characterisation

Externally modulated lasers (EMLs) are a type of laser in which the modulation of the optical signal is performed outside of the laser cavity. In other words, instead of modulating the laser directly, the modulation is applied to an external device such as an electro-optic amplitude modulator or phase modulator, which is then coupled to the laser cavity which allows for greater control over the modulation process and can result in higher modulation speeds and improved signal quality. A key advantage of EMLs is their ability to achieve higher modulation speeds compared to directly modulated lasers. This is because the modulation bandwidth of the laser is limited by its intrinsic properties, such as the carrier lifetime and the linewidth while under modulation. By performing modulation externally, the modulation bandwidth is no longer limited by these factors, but instead by the characteristics of the modulator, which can be designed for much higher speeds.

Another advantage of externally modulated lasers is their ability to maintain stable operation over a wide range of operating conditions. This is because the modulation process is decoupled from the laser cavity, which means that changes in temperature, wavelength, or other factors that may affect the laser cavity do not affect the modulation process. As a result, externally modulated lasers are often used in applications where high stability and reliability are critical, such as in fibre optic communications, where they are commonly used to transmit high-speed data over long distances.

Three commonly used types of externally modulated lasers are

electro-absorption modulated lasers (EAMLs), Mach-Zehnder modulated lasers (MZMLs), and electro-optic modulated lasers (EOMLs). MZMLs use a Mach-Zehnder interferometer to modulate the optical signal. The interferometer splits the light into two arms, which are then recombined with a relative phase shift that is modulated by an external electrical signal. One benefit of MZMLs is their ability to achieve high modulation speeds, which makes them suitable for use in high-speed communication systems. However, they can be more expensive and complex to manufacture than other types of externally modulated lasers.

EOMLs use an electro-optic crystal to change the refractive index of the laser material, which modulates the phase of the optical signal. This allows for high-speed modulation of the laser output. One benefit of EOMLs is their high modulation bandwidth, which makes them suitable for use in high-speed communication systems. However, their power consumption is typically higher than other types of externally modulated lasers, which can limit their usefulness in certain applications.

In EAMLs, the EAM is integrated into the laser cavity and modulates the output of the laser by changing its absorption properties. This allows for the modulation of the optical signal at high speeds while consuming low power. EAMLs have been used in a variety of applications, including fiber-optic communication systems, optical networks, and optical sensors.

EAMLs have a simple structure and are easy to manufacture in comparison to other EMLs, which can lead to lower manufacturing costs. Additionally, EAMLs have a relatively low noise figure [123], which makes them suitable for high-sensitivity applications. However, one of the limitations of EMLs is their chirp-induced distortion, which can affect the quality of the modulated signal. This distortion becomes problematic because it can cause inter-symbol interference (ISI), which occurs when the distorted optical pulses overlap in time and interfere with each other, making it difficult to accurately detect the transmitted data.

The main cause of chirp-induced distortion in EMLs is the relaxation oscillation phenomenon. When the bias current of the laser diode is modulated, it affects the carrier density and the optical frequency of the laser output. This variation in the optical frequency results in chirp, a variation in the instantaneous frequency of the optical signal.

6.1 EML Device Design

For the purposes of this project we have chosen to focus on the usage of slotted Fabry-Pérot lasers with a single mirror section (SFPs) and two mirror sections (DSFPs) as these devices have shown good output power, high SMSR, and the capability of being redshifted past the initial gain peak of the material on which they are fabricated.

The laser fabrication process highlighted in the previous chapters made use of shallow waveguides due to their improved threshold and reduced loss when compared to lasers with deep-etched waveguides. In addition the laser designs chosen for integration make use of shallow etched slots in order to facilitate single-mode operation. Thus, the integration of these lasers into the high-speed process requires the modification of the previous ridge waveguide lithographic definitions to accommodate the same two-depth process used for the DC process.

Additionally during the EAM testing process, issues were noted with the throughput power of the EAMs. Further investigation revealed that the optical loss was caused by the contact layer etches. Given that shallow etched slots were already set to be included in a new high-speed fabrication process for EMLs, a new test mask was designed to optimise the electrical and optical isolation structures by comparing slots and contact layer etches.

6.2 EML Processing

6.2.1 Electrical Isolation Techniques

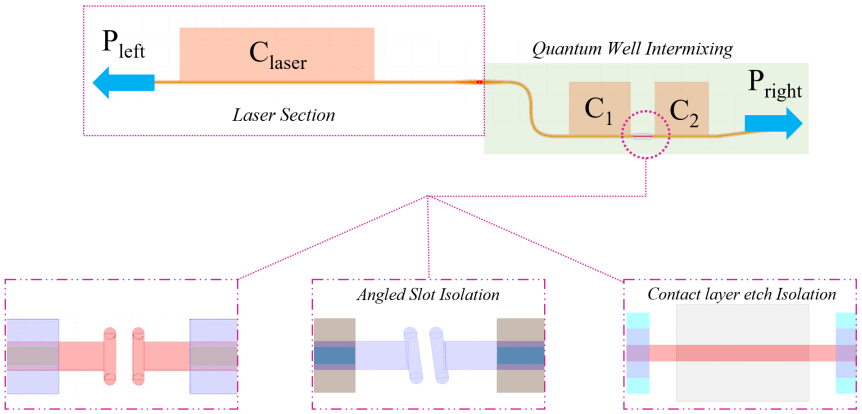

Figure 6.1: A schematic of the test structure used for electrical isolation measurement and optical loss measurements.

This photolithography mask designed to improve the electrical isolation and optical throughput focused on testing several different isolation methods

- Contact layer etches
- Shallow straight slots
- Shallow angled slots
- Deep straight slots
- Deep angled slots

These isolation methods are highlighted in Fig. 6.1 along with the test structure used to characterise their performance. To measure the electrical isolation a p-contact was placed on C_1 and the ground contact was placed on C_2 with the resistance being measured using a Keithley current source at $2.5\,\mathrm{V}$. The results of this test for deep slots, straight slots, and contact layer etches are shown in Fig. 6.2. Angled and straight slots showed no variation in electric isolation. It is noted that a $10\,\mu\mathrm{m}$ contact layer etch is comparable to a $1\,\mu\mathrm{m}$ shallow slot in terms of electrical isolation. A deep slot with width $1\,\mu\mathrm{m}$ is equivalent to a contact layer etch with width $40\,\mu\mathrm{m}$.

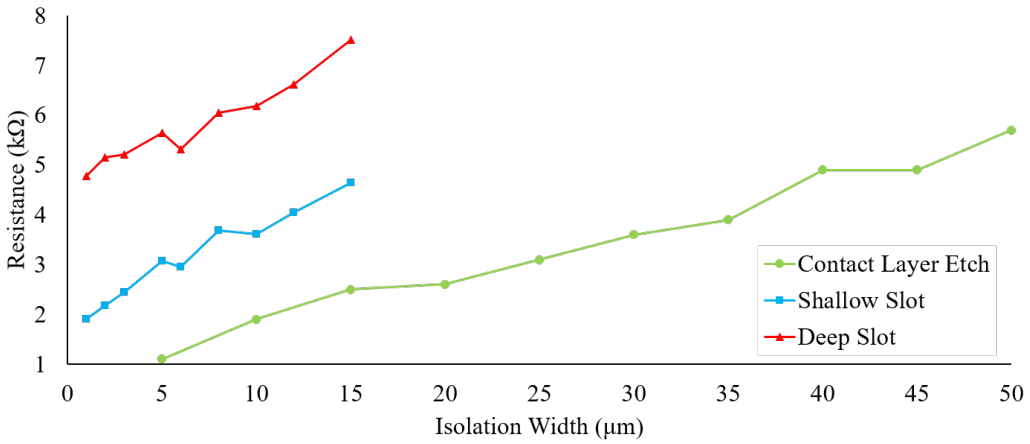

Figure 6.2: The resistance vs isolation width for various isolation styles.

The absolute value of the optical loss could be calculated as $P_{right} - P_{left}$, as seen in Fig. 6.1. However, the absolute value of loss can not be entirely attributed to the isolation elements we are aiming to inspect. This value of loss could be influenced by the varying performance of the lasers used in each laser section. In addition this would assume that the power outputted from the left of the laser is equal to that of the right, which is untrue due the differing facets, the left being a cleaved facet and the right being a tapered etched facet. To create a fair comparison between isolation optical losses a ratio is instead presented as

$$T = \frac{P_{right}}{P_{left}} \tag{6.1}$$

This ratio accounts for the variations between laser performances and results in the fraction of the power which has transmitted through the isolation element. We also make use of a structure where there is no isolation element present in the intermixed area. This gives us a baseline for the fraction of transmitted power which would be expected in a waveguide with no perturbing element, T_{base}. Therefore we can calculate the relative optical loss, L, of each isolation element as

$$L_i = 1 - \frac{T_i}{T_{base}} \tag{6.2}$$

The results of this calculation for a straight shallow slot and a contact layer etch is shown in Fig. 6.3. The straight slot loss is seen to increase quickly

before reaching a maximal loss value of approximately 0.62. This is likely due to the weakened waveguiding as the shallow slot lacks the effective index guiding normally used in shallow waveguides. The contact layer etch meanwhile increases linearly and slowly, which would imply that the light is still being guided.

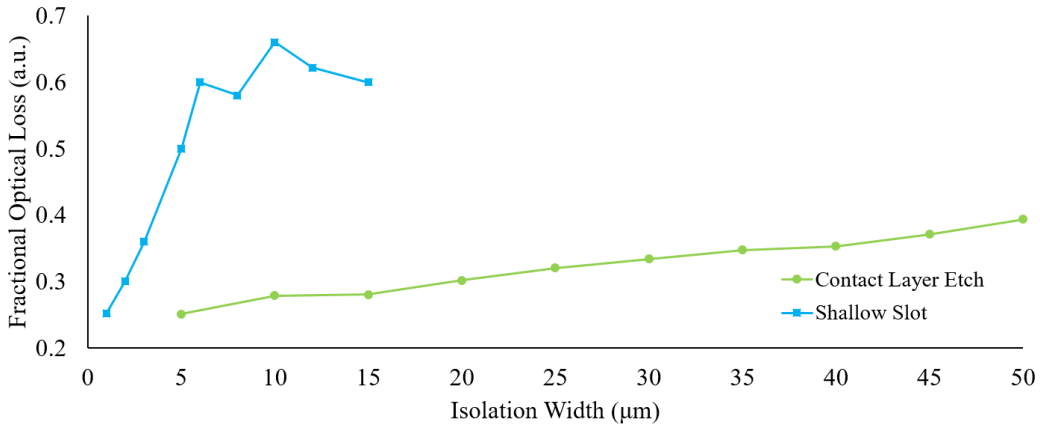

Figure 6.3: The fractional optical loss versus isolation width for various isolation styles.

The linear loss of the contact layer etch likely arises due to the fabrication process involved in creating the contact layer etch. The contact layer etch is a wet etch of the topside semiconductor material which can often lead to a roughness and aberration in the top of the waveguide. For this etch, dielectric is intended to protect the waveguide sidewalls. However, if the sidewall coating was unintentionally damaged as part of the process then the sidewall could also be partially roughened during the contact layer etch. Both or either of these possibilities may be the cause of the loss noted here.

These calculations were also completed for slots of width $1\,\mu\mathrm{m}$ which were a variety of shallow and deep etched and straight and angled. The results of these calculations is presented in Table 6.1. Here we can see by angling the slots we can reduce the loss significantly regardless of whether the slot is deep or shallow-etched. It is also possible that the angle for the deep etched slot can be further optimised to further reduce the loss. Both angled slots and the shallow straight slot have a lower loss than the $15\,\mu\mathrm{m}$ contact layer etch. In conclusion a deeply etched angled slot can offer improved electrical isolation and optical loss in comparison to the previously used contact layer etching, as such the EAM sections of the new EML process design will make use of this technique. Shallow etched slots will be used for the electrical isolation

between sections of the laser as the single mode designs chosen in earlier sections already make use of shallow etched slots for reflection purposes.

Table 6.1: The fractional optical loss of different slot styles with widths $1\,\mu\mathrm{m}$.

	Straight	**Angled**
Shallow	0.252	0.018
Deep	0.52	0.152

6.2.2 Ridge-etch Lithography

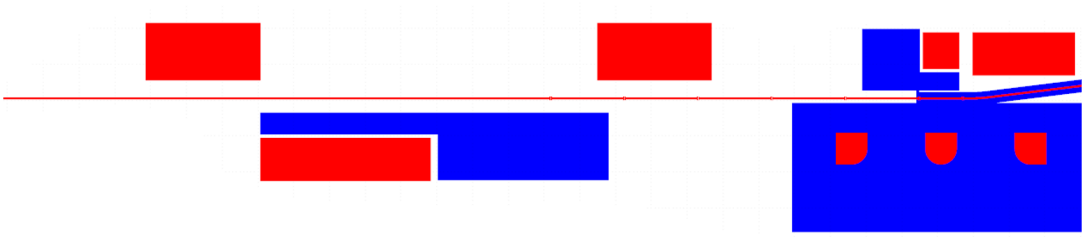

Figure 6.4: A view of the ridge definitions for the EML process shown in red and the deep etch shown in blue.

The optimal combination of laser and EAM process designs requires the use of two different waveguide depths: shallow for the laser and deep for the EAM. To facilitate this the lithography used to define the deep ridge in the previous high speed process is split into two lithographic steps as seen in Fig. 6.4.

The process begins as in the EAM process. A thick coating of Ti:Au:Ti $25:500:25$ is deposited onto a clean semiconductor surface with a metal evaporator. Following this, a thicker coating of silicon dioxide is deposited via plasma enhanced chemical vapour deposition. A thickness of $900\,\mathrm{nm}$ is used to account for the multiple depths used in this process. This step is shown in Fig. 6.5(a).

Following this, an adhesion promoter, HMDS, and photoresist, S1805, is deposited into the sample surface. A thinner photoresist is used to optimise the resolution of the slots used due to their small size ($1\,\mu\mathrm{m}$). The PR is then baked at $115°$ for three minutes. The piece to be exposed is secured in the mask aligner via a vacuum contact and a lithographic mask is used to block exposure to the areas of the mask which will define our waveguides. The piece is then developed in MF319, a developer containing tetramethyl ammonium hydroxide. This step is shown in Fig. 6.5(b).

An inductively coupled plasma etcher is then used to remove the SiO_2 in areas uncovered by the PR soft mask. With the oxide removed, the remaining PR is then removed. The backside of the piece is cleaned, removing any oil used to regulate the temperature during etching and the backside is then coated with metal to protect it from contamination during the semiconductor etch process, and to ensure the high resistance of the semi-insualting substrate. With the oxide now acting as a hard mask, the piece is then etched in an ICP etcher using a room temperature chlorine etch to remove the unwanted metal. This step is shown in Fig. 6.5(c).

Next, a layer of silicon nitride is deposited onto the sample. This is shown in Fig. 6.5(d). A layer of HMDS and PR S1828 is then spun onto the sample and baked on the sample. Hard contact lithography is then used to define the areas of the mask where the sample is to be deep etched. With PR as a soft mask the exposed nitride is etched using an ICP, exposing the semiconductor in the areas to be deep etched. The PR is then removed. Now, with the nitride as a hard mask protecting areas not to be deep etched, and the oxide protecting the waveguides in the deep etched area, the exposed semiconductor is etched using the ICP etcher. This etch is stopped above the quantum wells. This step is shown in Fig. 6.5(e).

Now with the etch part way through, the hard mask of nitride is removed via ICP etching, exposing all areas of the semiconductor that will not be used as waveguides. The semiconductor etch is then continued with the remaining oxide being used as a hard mask to protect the waveguides. The etch is stopped when the shallow etch is just above the quantum wells and the deep etch has entered the n doped area of the epitaxy, below the quantum wells but above the semi-insulating substrate. This step is shown in Fig. 6.5(f).

With the waveguides defined, the remaining oxide hard mask is removed. This process also defines the shallow and deep slots used for reflective feedback and electrical isolation. The remainder of the process continues as with the high speed process defined earlier, with the final lithographic step used to define the contact layer etch being removed. This resulted in a process with eight lithographic steps.

(a) A layer of Ti:Au:Ti and passivation, SiO_2, is deposited

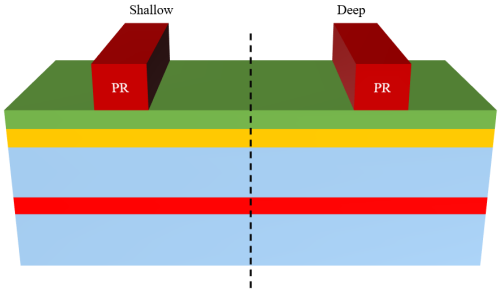

(b) PR is used to define the waveguides in the shallow and deep regions.

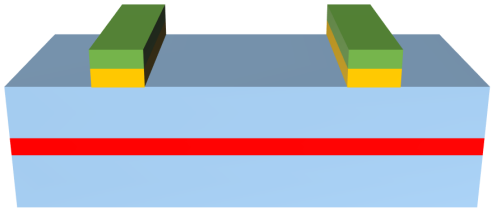

(c) Plasma etching is used to remove the SiO_2 and metal where required

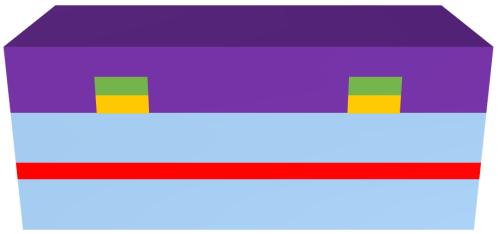

(d) A layer of SiN is deposited.

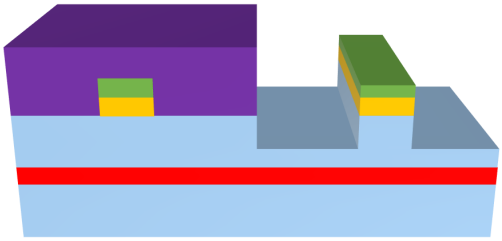

(e) The deep-etched waveguide area is opened via lithography, the SiN is removed and the semiconductor is etched to above the quantum wells.

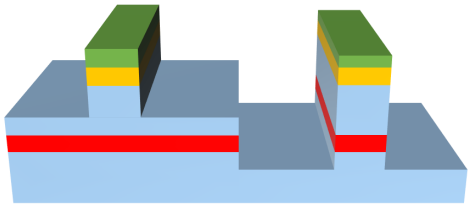

(f) The remaining SiN is removed and the semiconductor is etched to define the shallow and deep waveguides.

Figure 6.5: Process flow for the shallow and deep waveguide definitions

6.3 Device Outputs

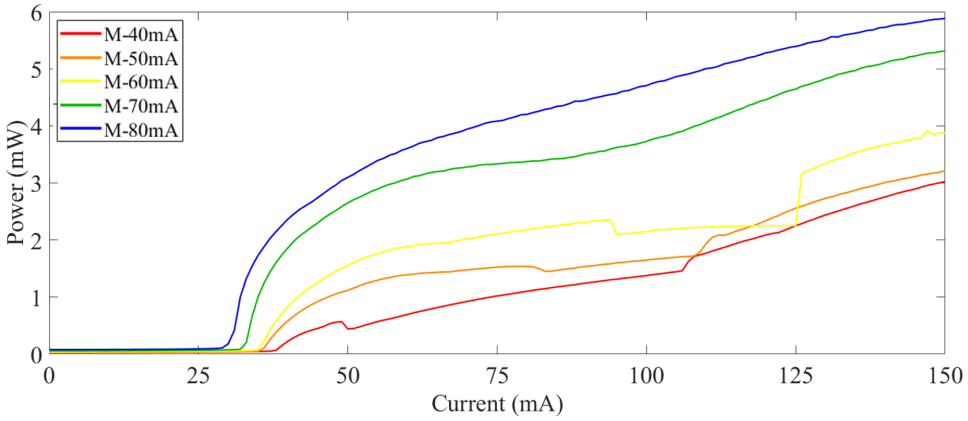

Figure 6.6: The LI curve for the SFP laser at varying mirror currents.

Despite setbacks encountered in the fabrication, results were still able to be obtained for the lasers present in the high-speed EML run. Fig. 6.6 shows the LI curve obtained using an integrating sphere for an SFP with gain length $800\,\mu\mathrm{m}$ and a mirror section consisting of six slots with a slot separation of $60\,\mu\mathrm{m}$.

As was noted in previous SFP devices measured, the threshold current and output power vary with the current supplied to both sections, with the lowest mirror current of $40\,\mathrm{mA}$ providing a threshold and maximum power of $39\,\mathrm{mA}$ and $3\,\mathrm{mW}$ respectively. The highest mirror current of $80\,\mathrm{mA}$ provided a threshold and maximum power of $28\,\mathrm{mA}$ and $6\,\mathrm{mW}$ respectively.

The values noted here show a degradation in laser performance when compared to previous SFP measurements. However, it should be noted that the previous lasers used a commercial epitaxy optimised for laser performance while the devices measured here use an in-house epitaxy designed to accommodate both the EAM's performance in addition to the laser's. Additional variations can be attributed to the device fabrication wherein differences in waveguide definition may lead to lossier structures with smaller power output and higher threshold. Variance in cleaving will also lead to lasers with different facet reflectivities and thus dissimilar laser performance.

Fig. 6.7(a) shows a spectrum obtained for the SFP device when the mirror section was at $65\,\mathrm{mA}$ and the gain section was at $95\,\mathrm{mA}$ (blue) which shows the device achieved good SMSR. The corresponding simulated output power calculated using the simulation methods outlined in earlier chapters is then

shown in (red) for a laser with a gain section of length $800\,\mu\mathrm{m}$ and a mirror section consisting of six slots with a slot separation of $60\,\mu\mathrm{m}$. An index of $n = 3.417$ was used for the shallow etched waveguides and an index of $n_{slot} = 3.39043$ was used for the slots i.e. the area of the guide where the semiconductor was etched down to just above the quantum wells. The single mode wavelength and the mode spacing are well matched to the device and it is noted that the longitudinal modes match a cavity whose length consists of both the gain and mirror section lengths.

Fig. 6.7(b) shows the spread of SMSR versus wavelength obtained from recording a spectrum at each point of an electrical sweep across the gain and mirror sections, sweeping the gain section from $10\,\mathrm{mA}$ to $150\,\mathrm{mA}$ and the mirror section from $10\,\mathrm{mA}$ to $100\,\mathrm{mA}$. Each blue point on the graph represents an individual spectrum obtained at each point of variance. The red line represents the reflectivity of a slotted mirror with six slots at a separation of $60\,\mu\mathrm{m}$ which shows a good match to most of the single mode emissions. Emissions outside these points likely originate from a shift in the reflectivity caused by a change in mirror index due to increased current in the mirror section. The spread of the wavelengths obtained shows single mode behaviour $>30\,\mathrm{dB}$ across a tuning range of $\sim 30\,\mathrm{nm}$ which is a suitable tuning range for EML integration.

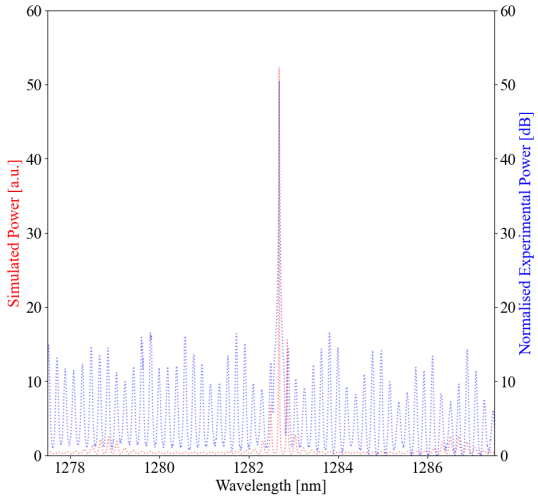

(a) A spectrum obtained for the SFP device when the mirror section was at $65\,\mathrm{mA}$ and the gain section was at $95\,\mathrm{mA}$ (blue). The corresponding simulated output power (red).

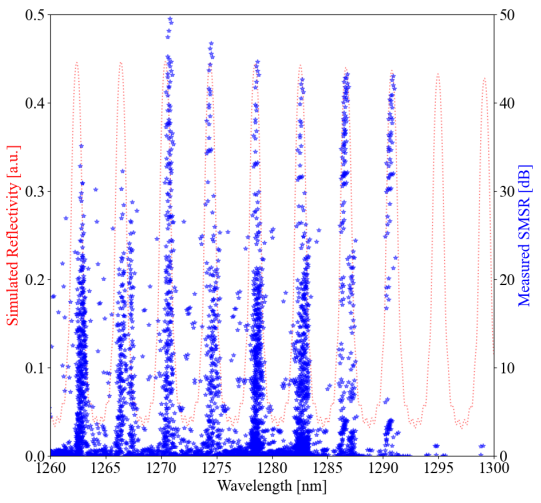

(b) The measured SMSR vs wavelength for the SFP (blue) where each dot represents a spectrum taken. The reflectivity of the mirror section slots (red).

Figure 6.7: Experimental data versus simulated outputs for the SFP laser.

6.4 Fabrication Issues

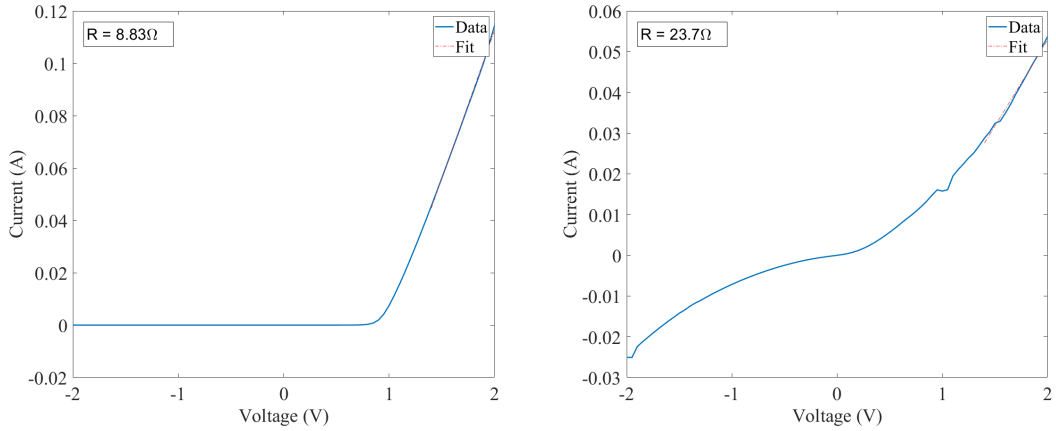

(a) The IV for a laser fabricated in the EML run.

(b) The IV for an EAM fabricated in the EML run.

Figure 6.8: The IV curves for different devices fabricated in the high speed EML process.

In the testing of the devices produced using the modified EML high speed fabrication process it was noticed that the leakage currents measured from the deep etched EAM structures was far larger than the leakage currents measured in the shallow-etched laser structures. The IV measurement for a laser is shown in Fig. 6.8(a). The IV measurement for an EAM is shown in Fig. 6.8(b). This creates a serious issue in the operation of the EAMs as they need to be properly reverse biased in order to absorb the emitted light from the laser. This issue prevented the collection of modulation data for the EAM and EML devices.

This issue was not present in the EAM high speed process An explanation for this behaviour is shown in Fig. 6.9. In the original process, the lithographic step used to open up the SiO_2 to allow for metal contact to the waveguides is larger than the ridge itself. This is feasible because the BCB is planarised in such a way that only the top of the waveguide is uncovered by BCB as shown in Fig. 6.9(a). Thus when the oxide opening lithography is complete and the passivation covering the top of the waveguide is etched away, the sidewall passivation remains intact.

The modifications made to the high speed fabrication were to add an additional etch depth to the process for the facilitation of shallow etched lasers. Originally the process used a deep etch into the n region for the EAM

waveguide definition, the n-contact etch and the isolation etch into the substrate to electrically isolate the EAMs. Now we have an additional etch depth to just above the quantum wells for the laser waveguide. Even with attempts to planarise the BCB, deformations will exist around these different levels. The thick metal deposition allows a tolerance to the height of these deformations as seen in Fig. 6.9(a). The left side of the BCB, the side placed over the etch into the n region, is higher than the right, the side etched into the substrate, but this difference in BCB height is less than or equal to the thickness of the metal atop the waveguide, and thus poor leakage is avoided.

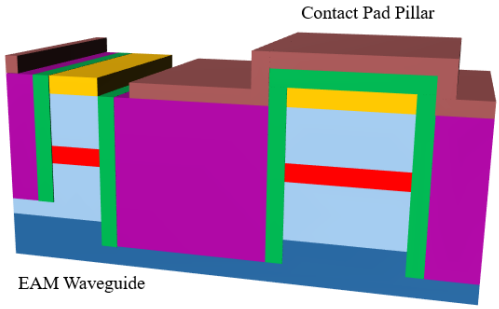

(a) On the left is a deep etched EAM waveguide connected to an electrically isolated contact pillar.

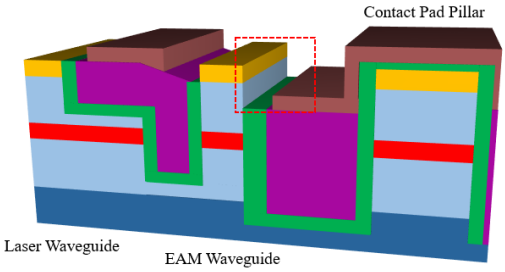

(b) On the left is a shallow etched laser waveguide. In the center is a deep etched EAM waveguide. on the right is an isolated contact pillar.

Figure 6.9: Changes in BCB planarisation for different fabrications processes. Light blue is semiconductor. Dark blue is semi-insulating substrate. Red is the quantum wells. Gold is metal. Brown is photoresist

In the EML process however there are now three different levels of deformation in the BCB, with a $\sim 1.5\,\mu\mathrm{m}$ difference between the shallow etch depth and the isolation etch depth. This depth difference is minimised but not entirely eliminated through planarisation of the BCB. Fig. 6.9(b) shows a possible view of how the BCB etchback process might expose the waveguides in the EML process. If each etch depth now creates a small difference in the BCB height relative to the top of the waveguide, then ensuring that the laser waveguide is exposed in etchback causes the side of the EAM which is etched into the substrate to be etched too far, exposing the upper p region. When the oxide opening lithography is complete the sidewall passivation for the upper p region of the EAM waveguide is removed, leading to a high leakage current when the metal contacts are deposited.

6.5 Proposed Fabrication Modifications

Multiple possibilities exist to fix this issue. The laser designs could be modified to accommodate the use of deep etched waveguides through the reduction in the number of slots used in the mirror sections. However, this change comes with its own drawbacks. Namely, deep etched waveguides degrading the performance of lasers, whose performance we have already degraded by adjusting the epitaxial structure to facilitate the integration of our EAMs.

Fig. 6.10 shows a not-to-scale alternative which aims to eliminate the problem caused by the variance in BCB heights. In this version of the fabrication process BCB is no longer used to facilitate the wide oxide opening shown in magenta in the figure, instead being replaced by an oxide opening smaller than the ridge shown in blue, similar to the DC process used in previous laser fabrications. Because the BCB is no longer required to prevent the sidewalls from being opened then the BCB, shown in orange, is removed from everywhere across the sample, only being used to form the bridge from the isolated contact pillar to the EAM itself. This change simplifies the planarisation of the BCB as it now stands on only a single depth of semiconductor, existing only within the pit etched down to the substrate.

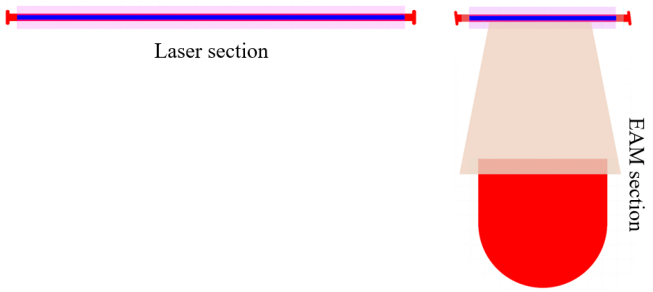

Figure 6.10: The current oxide opening lithography shown in pink and the proposed new oxide opening shown in dark blue. The waveguides are shown in red. BCB (Orange) is removed everywhere except where needed for the bridge.

With the leakage current at an acceptable level for both the laser and the EAM, a high speed, regrowth-free monolithically integrated EML can be achieved using the techniques and designs optimised in previous chapters.

Chapter 7

Conclusions & Future Work

The purpose of this project was to work toward single-growth monolithically integrated electro-absorption modulated lasers and throughout this process multiple important findings have been made

In Chapter 2 I explored the design of quantum well structures and their relation to the performance of active photonic circuit components; lasers and EAMs. I determined that the epitaxy of a lumped element EAM can be limited by the imbalance in carrier mobilities in the materials, and thus to give the material the highest possible bandwidth in a lumped element configuration an imbalance must be introduced in the position of the quantum wells to optimise the transit times of the electrons and holes in the semiconductor, minimising the impact the carrier times have in the f_{3dB} bandwidth of the modulator.

In Chapter 3 I furthered this exploration to look at complete epitaxial structures, simulating their effect on lasers and EAMs. I determined that, within the purview of lasers, there exists an optimal combination of quantum well width and number which results in peak laser performance. Using the simulation tools and verifying these simulations through the fabrication of lasers on these materials I was able to determine an optimal material which balanced the performance of the laser and the EAM to create the optimal platform for EML fabrication.

In Chapter 4 I explored several different laser designs, from slotted Fabry Pérots to snails, with a focus on designing a redshifted single mode laser. Each of these lasers offered unique behaviour and possible benefits toward EML integration. For each laser design presented, I constructed a simulation model which could be used to predict the laser's reflectivity and the full spectrum of the laser. I was then able to use these models to create real laser designs which

I turned into photolithographic masks via PICDraw, and then fabricated. I tested these lasers using test setups I semi-automated to improve the ease of data-acquisition. I was then able to match these experimental outputs to the simulation models, verifying the effectiveness of the models created. Finally, I critically evaluated all the designs to determine the optimal laser for the integrated EML.

In Chapter 5 I created a new high-speed process for the fabrication of high-speed EAMs, designing eight lithographic mask layers. In these high-speed runs I broke the EAM down into its component parts so I could properly optimise them to facilitate the highest possible bandwidth for the overall devices. I electrically isolated the contact pad, reducing the parasitic capacitance it would contribute to the EAM device from $>300\,\mathrm{fF}$ to $5\,\mathrm{fF}$. I additionally isolated the connective metal bridge, for the first time recording its individual contribution to the capacitance of the EAM and finding it to be twice as large as that of the signal pad. Through this analysis I was able to analyse the source of the metal bridge's capacitance and reduce it to $3\,\mathrm{fF}$ reducing the entire parasitic capacitance of the device down to $<10\,\mathrm{fF}$. With these test structures measured, I was able to perform S_{11} measurements on the full EAM structures which predict a near $80\,\mathrm{GHz}$ bandwidth for the $50\,\mu\mathrm{m}$ EAMs at a source impedance match of $25\,\Omega$.

In Chapter 6 I made use of what I had learned from the simulation, fabrication, and characterisation of both the lasers and the EAMs, creating a new high-speed process for EMLs designed to once again favour both the laser and the EAM. With what I learned in previous chapters I designed lasers suitable for the o-band and EAMs which made use of the design principles I determined were optimal. From this fabrication I obtained single mode lasers in the o-band, which I was able to match to the simulated models I used to design them. I was also able to analyse the results of the processing and determine feasible avenues of improvement which could be implemented into the EML process to improve yield in future fabrication runs.

In summary, this thesis presents a journey from material design to device outputs which intends to offer the knowledge and tools necessary for the reader to replicate and hopefully improve upon the creation of single-growth monolithically integrated electro-absorption modulated lasers.

7.1 Future Work

The work done for this project creates a basis for the fabrication of high speed monolithically integrated EMLs. Because these devices are monolithically integrated, they are suitable as modulated light sources for silicon photonics, were the device transferred to the silicon platform. Micro-transfer-printing (MTP) is one method of facilitating that.

7.1.1 Micro-Transfer Printing

Through flip-chip bonding (FCB), many different state-of-the-art III–V-on-Si lasers have been demonstrated based on die-to-wafer bonding techniques. The problem of material wastage is still a concern, which is related to the millimetre-scale minimum die size for handling purposes. This introduces a limit on the density of possible device integration. One possible solution under investigation in recent years is Micro-transfer-printing (MTP) [124, 125]. MTP presents itself as an alternative to FCB as an effective way to integrate III–V opto-electronic components onto a silicon photonic integrated circuit [126, 127].

In MTP, optical components are densely produced on their native III–V substrate which allows the minimisation of waste of III–V material, providing cost savings to the process. The III–V epitaxial structure is grown with a thin sacrificial release layer which can be etched away at the completion of the III–V processing steps, allowing the manipulation of micron-sized thin film devices on coupon structures, such that they can be printed in a massively parallel way to the designated target substrate such as Silicon and patterned Silicon on Insulator (SOI). The sacrificial release layer used in the case of InP-based epitaxy can be either InGaAs or InAlAs [128].

Devices or material coupons are patterned on the III–V source wafer and are covered with a photoresist encapsulation, with local openings to access the release layer. The release layer can then be selectively etched. This selective etching agent uses $FeCl_3$:H_2O for InP-based epitaxy [126]. Small polymer tether-like structures remain after the release etch to prevent immediate disconnection of the coupons from their native substrate. Using a polydimethylsiloxane (PDMS) stamp these coupons can then be individually or massively parallel lifted from the native substrate. Manipulation of the stamp's impact parameters allows it to pick up the coupons and break the tethers

holding the coupon to the substrate. These coupons can be subsequently "printed" on a Silicon target wafer with high alignment accuracy ($\pm 1.5\,\mu\mathrm{m}\sigma$ [129]) again through manipulation of the PDMS stamp. MTP has demonstrated successful lasers on Silicon [130, 131]. The main process flow for micro-transfer printing is shown in Figure 7.1 [132].

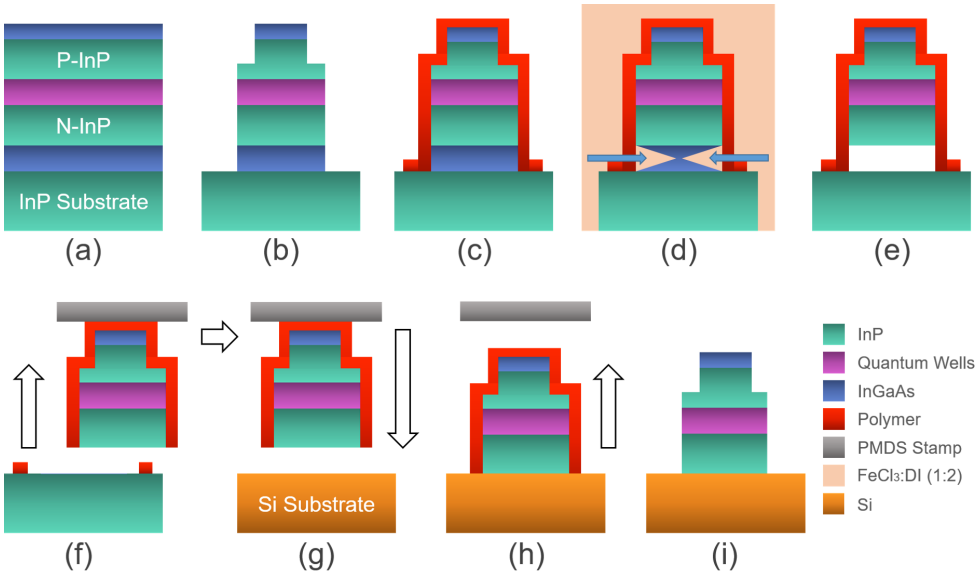

Figure 7.1: Devices are fabricated on an InP wafer including an InGaAs release layer at the bottom of the epitaxial structure (**a**,**b**). An anchor system made of polymer (resist) keeps the devices in place (**c**) during the undercut while allowing the etchant to penetrate underneath the mesas through some openings (**d**,**e**). Finally, the devices are picked up (**f**) and transfer-printed onto the new substrate using a Polydimethylsiloxane (PDMS) stamp (**g**–**i**).

Transfer printing offers a convenient method of integrating laser gain material on silicon. The usefulness of transfer printing does not end there however. Vanackere et al. demonstrates the successful transfer printing of a lithium niobate Mach-Zehnder Interferometer achieving a modulation efficiency of $V_\pi L = 5.5$ V·cm [133].

With the growing improvements in micro-transfer printing (MTP) technology, the options for Silicon compatible III–V modulators grow. The work we have done thus far provides a suitable MTP-compatible III–V EML for use in Silicon photonics. The benefit to transfer printing an EML compared to its individual components is the reduction in coupling losses due to the misalignment of separate components. MTP offers an interesting manner of connecting the wealth of research completed on active III-V components to the silicon platform. However, certain additional considerations must be made to make

the high-speed processes developed in this project MTP-compatible. In an MTP process we lose the high resistance substrate we used for the minimisation of parasitic capacitance in the EAMs (and by extension EMLs) and thus we must find a new method of creating a high resistance epitaxial layer.

7.1.2 Iron Doping

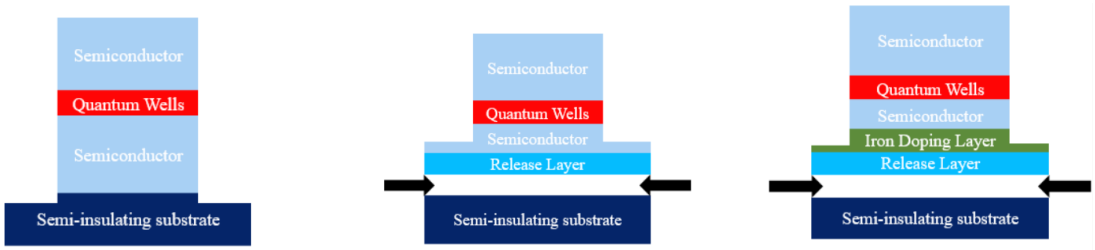

(a) The isolated contact pillar in the original high-speed process. High resistance is required to reduce the parasitic capacitance.

(b) In an MTP process, the coupon is separated from the substrate, which prevents the contact pillar from being isolated electrically.

(c) An iron doping layer is used to recreate the electrical isolation by creating a thinner layer with high resistance to replicate the semi-insulating layer.

Figure 7.2: Contact pillar electrical isolation regimes.

The current high-speed fabrication process uses an etch into a semi-insulating substrate to electrically isolate the contact pad pillar to prevent its parasitic capacitance from negatively impacting the capacitance of the EAM itself. This design is shown in Fig. 7.2(a). This prevents the EAM's bandwidth from being reduced by unnecessary RC impacts. As mentioned in the previous section however, there exists a heavy interest in the integration of III-V PICs on silicon and a notable method of doing so involves the micro-transfer printing of III-V coupons onto a silicon platform.

Creating these coupons requires that a release layer be added between the main epitaxial structure and the substrate so that, once processing of the coupon PIC is complete, the release layer can be wet-etched away to release the coupon for printing, as shown in Fig. 7.2(b). This is a point of incompatibility between the high-speed process we have developed thus far as we are reliant on the large resistance of the semi-insulating substrate for the electrical isolation of the pillars to maintain the low parasitic capacitance of the lumped element EAM devices.

To accommodate the lack of a semi-insulating substrate, it is necessary to form

a thinner layer with comparable resistance to the semi-insulating substrate we have used previously. For this purpose we make use of iron doping, a technique that is used to create high resistance layers. The basic principle behind this technique is that the presence of iron atoms in the lattice of the semiconductor material leads to the creation of defect states in the bandgap, which can trap charge carriers and increase the resistance of the material. Iron doping can be achieved by introducing a small amount of iron atoms into the semiconductor lattice during the epitaxial growth process. The concentration of iron atoms can be controlled by adjusting the growth conditions, such as the temperature and the flux of the iron source. As the concentration of iron atoms increases, the resistance of the material also increases due to the creation of defect states in the bandgap.

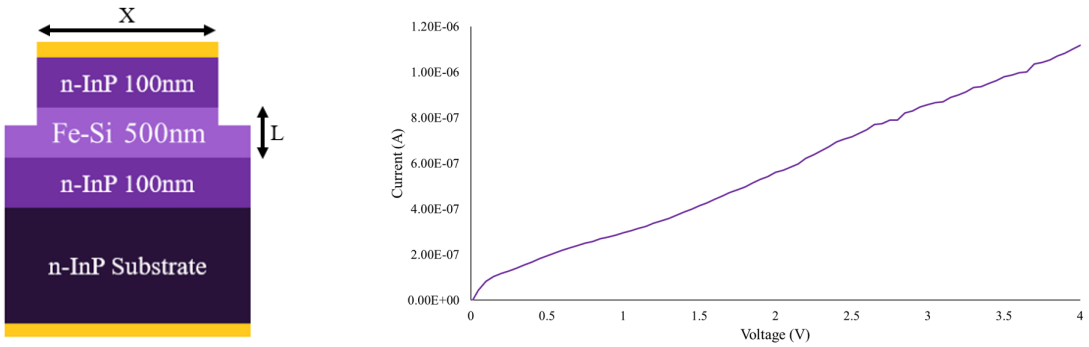

(a) The epitaxial test structure used for testing the resistivity of iron doping layers.

(b) An IV from an iron doping test structure showing a resistance of $33.6\,\mathrm{M\Omega}$.

Figure 7.3: Iron doping test structure and IV.

To test this possible method of electrical isolation, an epitaxial structure was grown with a central iron doping layer as shown in Fig. 7.3(a) with thickness, $L = 500\,\mathrm{nm}$. This epitaxy was used to create test structures used to measure the resistance of rectangular metal contacts of known area, A with width, X, and length, Y. Resistance values were collected for these structures by placing a metal contact on top of the sample and with the bottom of the sample being grounded and connect to the SMU. Sweeping the voltage and reading the corresponding current using a Keithley 2600 series power meter, resulting in an IV curve as shown in Fig. 7.3(b). Using the formula for resistivity

$$\rho = \frac{RA}{L} \tag{7.1}$$

values for the resistivity of the electrically traversed epitaxy could be calculated, with the assumption that the majority of the sample's resistance could be attributed to the iron-doped layer. This test was repeated across the surface of the test quarter with the results being shown in Table 7.1.

Table 7.1: Iron doping test structure results.

R (Ω)	L (cm)	X (cm)	Y (cm)	A (cm^2)	ρ (Ω.cm)
3.36E+07	5.00E-05	0.01	0.038	0.00038	2.55E+08
3.29E+07	5.00E-05	0.01	0.038	0.00038	2.50E+08
3.33E+07	5.00E-05	0.01	0.038	0.00038	2.53E+08
3.35E+07	5.00E-05	0.01	0.038	0.00038	2.54E+08
3.26E+07	5.00E-05	0.01	0.038	0.00038	2.48E+08
3.10E+07	5.00E-05	0.01	0.038	0.00038	2.35E+08
3.14E+07	5.00E-05	0.01	0.038	0.00038	2.39E+08
3.03E+07	5.00E-05	0.01	0.038	0.00038	2.30E+08
2.99E+07	5.00E-05	0.01	0.038	0.00038	2.27E+08
2.39E+07	5.00E-05	0.01	0.038	0.00038	1.82E+08
2.68E+07	5.00E-05	0.01	0.038	0.00038	2.04E+08
2.66E+07	5.00E-05	0.01	0.038	0.00038	2.02E+08

The results of these tests provide confidence that a thin iron doped layer would be sufficient to provide electrical isolation for the contact pad pillars to prevent their parasitic capacitance from interfering with a transfer printable EAM design. This provides a future possible method for the growth of a new epitaxy which is both compatible with the current high-speed process design developed in this project and future MTP modifications.

7.1.3 Quantum Well Intermixed EAMs

Quantum well intermixing (QWI) is a technique used to modify the properties of semiconductor materials by selectively intermixing different layers in a quantum well structure. QWI involves the use of a thermal annealing process to diffuse the layers of the quantum well structure, thereby altering its electronic and optical properties. During the annealing process, the semiconductor material is heated to a high temperature, which causes the atoms in the material to diffuse and mix with adjacent layers. The diffusion process can be selectively controlled by using a suitable mask or by using a laser beam to locally heat the material.

By intermixing different layers in quantum well structures, it is possible to modify the bandgap of the material, which affects its electronic and, more importantly, optical properties. Fig. 7.4 shows the effect QWI has when used on a FP laser, causing a $\sim 30\,\mathrm{nm}$ blueshift in the central emission wavelength of the laser. This offers some interesting future prospects for the monolithic integration of lasers and EAMs as the performance of an electro-absorption modulated laser depends heavily on the wavelength modulated. Wavelengths close to the emission peak of the EAM experience heavy absorption at $0\,\mathrm{V}$, and thus reverse biasing cannot create a larger difference in output power, i.e. extinction ratio, through the EAM. Redshifted wavelengths, however, avoid the majority of the EAM's absorption at $0\,\mathrm{V}$, thus allowing for improved extinction ratios when reverse biased.

For the purposes of this project we aimed at creating laser designs which could be redshifted to avoid the absorption peak of the EAM at $0\,\mathrm{V}$. QWI could reduce the need for tuning by blueshifting the absorption peak of the EAM, making it easier for non-QWI monolithically integrated lasers to avoid the absorption peak at $0\,\mathrm{V}$. QWI also open up different opportunities such as adding an optically passive section between the EAM and the laser to further improve electrical isolation between both sections. Overall, in the aim of single growth monolithic integration, the capability of manipulating laser outputs and EAM absorption peaks is a powerful tool.

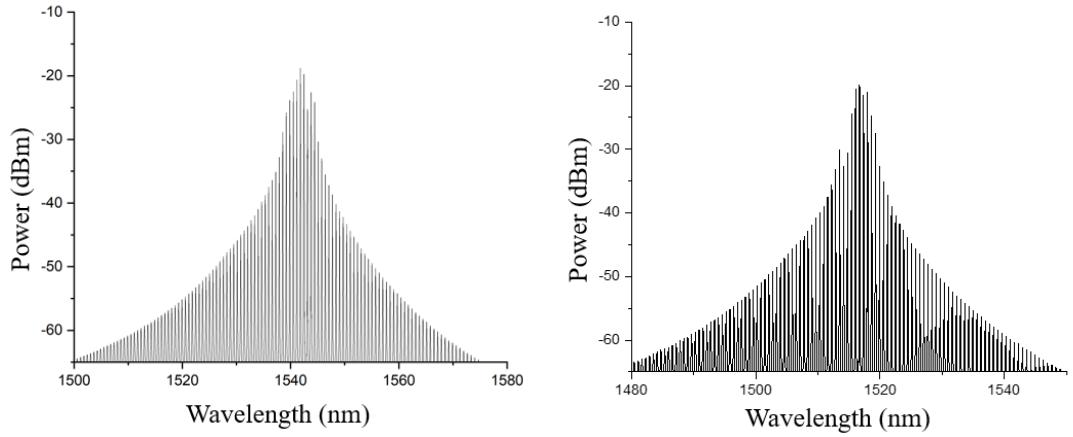

(a) A spectrum obtained for an FP laser with no QWI.

(b) A spectrum obtained for an FP laser with QWI.

Figure 7.4: FP emission spectra for non QWI and QWI FP lasers. The QWI laser underwent rapid thermal annealing to $675\,^{\circ}\mathrm{C}$ for 2 minutes.

References

[1] T. G. Polanyi, *Physics of Surgery with Lasers*, Clinics in Chest Medicine **6**, 179–202 (1985).

[2] E. Schena, P. Saccomandi, and Y. Fong, *Laser Ablation for cancer: Past, present and future*, Journal of Functional Biomaterials **8**, 19 (2017).

[3] A. Chralyvy. *Plenary paper: The coming capacity crunch*. In *2009 35th European Conference on Optical Communication*, pages 1–1, (2009).

[4] A. Einstein, *On the quantum theory of radiation*, Physikalische Zeitschrift **18**, 121–128,.

[5] S. Bose, *Planck's Gesetz und Lichtquantenhypothese, Zs*, Physik **26**, 178–181,.

[6] U. l. Aigrain, P. In *at the International Conference on Solid State Physics in Electronics and Telecommunications*, Brussels.

[7] P. Aigrain. *Masers a semi-conducteurs*. In P. Grivet and N. Bloembergen, editors, *Quantum Electronics, Proceedings of the Third International Congress*, New York. Columbia University Press.

[8] N. Basov, B. Vul, and Y. Popov. *Unpublished paper registered with the Committee on Discoveries and Inventions of the Council of Ministers of the U.S.S.R.*

[9] N. Basov, B. Vul, and Y. Popov, *Quantum-mechanical semiconductor generators and amplifiers of electromagnetic oscillations, Zh*, Eskp. Theo. Fiz **37**, 587–588,.

[10] W. Boyle, D. Thomas, and U. Optical Maser. Reissued as patent RE. 25,632 on August 18,.

[11] D. Thomas and J. Hopfield, *Fluorescence in CdS and its possible use for an optical maser*, J. Appl. Phys **33**, 3243–3249,.

[12] J. Pankove, IEEE J. Quantum Electron **QE-4**, 109–110,.

[13] B. Lax. *Cyclotron resonance and impurity levels in semiconductors*. In C. H. Townes, editor, *1st International Conference on Quantum Electronics, 1959; published in Quantum Electronics*, pages 428–449,, New York. Columbia University Press.

[14] W. Dumke, *Interband transitions and maser action*, Phys. Rev **127**, 1559–1563,.

[15] N. Basov. *Inverted populations in semi-conductors*. In P. Grivet and N. Bloembergen, editors, *Quantum Electronics, Proceedings of the Third International Congress*, New York. Columbia University Press.

[16] J. Gordon, H. Zeiger, and C. Townes, *Molecular microwave oscillator and new hyperfine structure in the microwave spectrum of NH3*, Phys. Rev **95**, 282,.

[17] J. Gordon, H. Zeiger, and C. Townes, *The maser: New type of microwave amplifier, frequency standard, and spectrometer*, Phys. Rev **99**, 1264,.

[18] J. Neumann, *Notes on the photon-disequilibrium-amplification scheme (JvN*, IEEE J. Quantum Electron **QE-23**, 659–673,.

[19] A. Schawlow and C. Townes, *Infrared and optical masers*, Phys. Rev **112**, 1940–1949,.

[20] A. Javan, W. R. Bennett, and D. R. Herriott, *Population Inversion and Continuous Optical Maser Oscillation in a Gas Discharge Containing a He-Ne Mixture*, Phys. Rev. Lett. **6**, 106–110 (1961).

[21] T. Maiman, *Stimulated optical radiation in ruby*, Nature **187**, 493–494,.

[22] M. Bernard and G. Duraffourg, *Laser conditions in semiconductors*, Phys. Stat. Sol **1**, 699–703,.

[23] R. Hall, G. Fenner, J. Kingsley, T. Soltys, and R. Carlson, *Coherent light emission from GaAs junctions*, Phys. Rev. Lett **9**, 366–368,.

[24] N. Holonyak, Jr. and S. Bevacqua, *Coherent (visible) light emission from Ga(AsP) junctions*, Appl. Phys. Lett **1**, 82–83,.

[25] M. I. Nathan, W. P. Dumke, G. Burns, F. H. Dill, and G. Lasher, *STIMULATED EMISSION OF RADIATION FROM GaAs p-n JUNCTIONS*, Applied Physics Letters **1**, 62–64 (1962).

[26] T. Quist, R. Rediker, R. Keyes, W. Krag, B. Lax, A. McWhorter, and H. Zeiger, *Semiconductor maser of GaAs*, Appl. Phys. Lett **1**, 91–92,.

[27] H. Kroemer, *A proposed class of heterojunction injection lasers, Proc*, IEEE **51**, 1782–1783,.

[28] Z. Alferov and R. Kazarinov, *Semiconductor laser with electric pumping (in Russian*, Inventor's Certificate .

[29] Z. Alferov, V. Andreev, E. Portnoi, and M. Trukan, *AlAs–GaAs heterojunction injection lasers with a low room-temperature threshold, Fiz*, Tekh. Poluprov **3**, 1328–1332,.

[30] I. Hayashi, P. Panish, P. Foy, and S. Sumski, *Junction lasers which operate continuously at room temperature*, Appl. Phys. Lett **17**, 109–111,.

[31] L. Esaki and R. Tsu, *Superlattice and negative differential conductivity in semiconductors*, IBM J. Res. Develop **14**, 61–65,.

[32] R. Kazarinov and R. Suris, *Possibility of the amplification of electromagnetic waves in a semiconductor with a superlattice, Fiz*, Tekh. Poluprov **5**, 797–800,.

[33] R. Dingle, W. Wiegmann, and C. Henry, *Quantum states of confined carriers in very thin AlGaAs–GaAs–Al GaAs heterostructures*, Phys. Rev. Lett **33**, 827–830,.

[34] L. Chang, L. Esaki, and R. Tsu, *Resonant tunneling in semiconductor double barriers*, Appl. Phys. Lett **24**, 593–595,.

[35] R. Dingle and C. Henry, *Quantum effects in heterostructure lasers, U.S*, Patent **3 982 207**.

[36] J. Ziel, R. Dingle, R. Miller, W. Wiegmann, and W. Nordland, Jr, *Laser oscillation from quantum states in very thin GaAs–AlGaAs multilayer structures*, Appl. Phys. Lett **26**, 463–465,.

[37] R. D. Dupuis, P. D. Dapkus, R. Chin, N. Holonyak, and S. W. Kirchoefer, *Continuous $300K$ laser operation of single-quantum-well*

$Al_xGa_{1-x}As - GaAs$ *heterostructure diodes grown by metalorganic chemical vapor deposition*, Applied Physics Letters **34**, 265–267 (1979).

[38] K. Iga, *Laboratory Notebook of P& I Laboratory 1977 Issue*, Tokyo Institute of Technology, Tokyo.

[39] J. Jewell, J. Harbison, A. Scherer, Y. Lee, and L. Florez, *Vertical-cavity surface-emitting lasers: Design, growth, fabrication, characterization*, IEEE J. Quantum Electron **27**, 1332–1346,.

[40] R. Geels, S. Corzine, J. Scott, D. Young, and L. Coldren, *Low threshold planarized vertical-cavity surface-emitting lasers*, IEEE Photon. Technol. Lett **2**, 234–236,.

[41] C. Chang-Hasnain, J. Harbison, C. Zah, M. Maeda, L. Florez, N. Stoffel, and T. Lee, *Multiplewavelength tunable surface emitting laser arrays*, IEEE J. Quantum Electron **27**, 1368–1376,.

[42] Y. Arakawa and H. Sakaki, *Multidimensional quantum well laser and temperature dependence of its threshold current*, Appl. Phys. Lett **40**, 77–78,.

[43] N. Kirstaedter, N. Ledentsov, M. Grundmann, D. Bimberg, V. Ustinov, S. Ruvimov, and M. Maximov, *Low threshold, large T0 injection laser emission from (InGa)As quantum dots*, Electron. Lett **30**, 1416–1417,.

[44] J. Faist, F. Capasso, D. Sivco, C. Sirtori, A. Hutchinson, and A. Cho, Quantum cascade laser, Science **264**, 553–556,.

[45] H. Amano, T. Asahi, and I. Akasaki, *Stimulated emission near ultraviolet at room temperature from a GaN film grown on sapphire by MOVPE using an AlN buffer layer*, Jpn. J. Appl. Phys **29**, 205,.

[46] S. Nakamura, M. Senoh, S. Nagahama, N. Iwasa, T. Yamada, T. Matsushita, H. Kiyoku, and Y. Sugimoto, *InGaN-based multi-quantumwell-structure laser diodes*, Jpn. J. Appl. Phys. B **35**, 74–76,.

[47] P. Bhattacharya, J. Singh, H. Yoon, X. Zhang, A. Gutierrez-Aitken, and Y. Lam, *Tunneling injection lasers: A new class of lasers with reduced hot carrier effects*, IEEE J. Quantum Electron **32**, 1620–1629,.

[48] R. KOhler, A. Tredicucci, F. Beltram, H. Beere, E. Linfield, A. Davies, D. Ritchie, R. Iotti, and F. Rossi, *Terahertz semiconductor-heterostructure laser*, Nature **417**, 156–159,.

[49] A. Evans, J. Yu, J. David, L. Doris, K. Mi, S. Slivken, and M. Razeghi, *High-temperature, high power, continuous-wave operation of buried heterostructure quantum cascade lasers*, Appl. Phys. Lett **84**, 314–316,.

[50] G. Walter, M. N. Holonyak, Jr., and R. Chan, *Laser operation of a heterojunction bipolar light-emitting transistor*, Appl. Phys. Lett **85**, 4768–4770,.

[51] H. Rong, R. Jones, A. Liu, O. Cohen, D. Hak, A. Fang, and M. Paniccia, *A continuous wave Raman laser: An all-silicon Raman laser*, Nature **433**, 725–728,.

[52] J. Liu, X. Sun, R. Camacho-Aguilera, L. Kimerling, and J. Michel, *Ge-on-Si laser operating at room temperature*, Optics Lett **35**, 679–681,.

[53] R. Camacho-Aguilera, Y. Cai, N. Patel, J. Bessette, M. Romagnoli, L. Kimerling, and J. Michell, *An electrically pumped germanium laser*, Opt. Express **20**, 11316–11320,.

[54] F. Chang, *Datacenter Connectivity Technologies: Principles and practice*, River Publishers (2022).

[55] Cisco. *Cisco Annual Internet Report (2018–2023) White Paper*, (2023).

[56] Y. Cheng, J. Pan, F. Zhou, W. Feng, B. Wang, H. Zhu, L. Zhao, and W. Wang, *A novel butt-joint scheme for the preparation of Electro-Absorptive Lasers*, Journal of Physics D: Applied Physics **41**, 035108 (2008).

[57] P. Studenkov, M. Gokhale, and S. Forrest, *Efficient coupling in integrated twin-waveguide lasers using waveguide tapers*, IEEE Photonics Technology Letters **11**, 1096–1098 (1999).

[58] A. Tauke-Pedretti, M. Sysak, J. Barton, J. Raring, M. Dummer, and L. Coldren, *Monolithic dual-quantum-well 10 GB/S mach-zehnder transmitter*, 2005 IEEE LEOS Annual Meeting Conference Proceedings (2005).

[59] C. Sun, B. Xiong, J. Wang, P. Cai, J. Xu, J. Huang, H. Yuan, Q. Zhou, and Y. Luo, *Fabrication and packaging of 40-GB/S algainas*

multiple-quantum-well electroabsorption modulated lasers based on identical epitaxial layer scheme, Journal of Lightwave Technology **26**, 1464–1471 (2008).

[60] M. Aoki, M. Suzuki, M. Takahashi, H. Sano, T. Ido, T. Kawano, and A. Takai, *High-speed (10 gbit/s) and low-drive-voltage (1 v peak to peak) InGaAs/ingaasp MQW electroabsorption-modulator integrated DFB laser with semi-insulating buried heterostructure*, Electronics Letters **28**, 1157 (1992).

[61] A. Ramdane, A. Ougazzaden, F. Delorme, J. Landreau, F. Devaux, and M. Schneider, *Very simple approach for high performance DFB laser-electroabsorption modulator monolithic integration*, Electronics Letters **30**, 1980–1981 (1994).

[62] B. Mason, G. Fish, J. Barton, L. Coldren, and S. DenBaars, *Characteristics of sampled grating DBR lasers with integrated semiconductor optical amplifiers*, Optical Fiber Communication Conference. Technical Digest Postconference Edition. Trends in Optics and Photonics Vol.37 (IEEE Cat. No. 00CH37079) .

[63] D. Byrne, Q. Lu, W. H. Guo, J. F. Donegan, B. Corbett, B. Roycroft, P. Lambkin, J.-P. Engelstaedter, and F. Peters, *A facetless laser suitable for monolithic integration*, 2008 Conference on Lasers and Electro-Optics (2008).

[64] V. Tolstikhin, *Distributed feedback lasers for regrowth-free multi-guide Vertical Integration in INP*, 2010 IEEE Photinic Society's 23rd Annual Meeting (2010).

[65] T. Tsuchiya, J. Shimizu, M. Shirai, and M. Aoki, *InGaAlAs selective-area growth on an INP substrate by metalorganic vapor-phase epitaxy*, Journal of Crystal Growth **276**, 439–445 (2005).

[66] V. Sabnis, H. Demir, O. Fidaner, J.-F. Zheng, J. Harris, D. Miller, N. Li, T.-C. Wu, H.-T. Chen, Y.-M. Houng, and et al., *Intimate monolithic integration of chip-scale photonic circuits*, IEEE Journal of Selected Topics in Quantum Electronics **11**, 1255–1265 (2005).

[67] D. Sengupta, V. Jandhyala, S. Kim, W. Fang, J. Malin, P. Apostolakis, K.-C. Hseih, Y.-C. Chang, S. L. Chuang, S. Bandara, and et al., *Redshifting and broadening of quantum-well infrared photodetector's*

response via impurity-free vacancy disordering, IEEE Journal of Selected Topics in Quantum Electronics **4**, 746–757 (1998).

[68] B. Qiu, *Monolithic integration in InGaAs/ingaasp multiple quantum well structures using laser and plasma processing*, IEE Colloquium on Optoelectronic Integration and Switching (1997).

[69] *A quantum-well-intermixing process for wavelength-agile photonic integrated circuits*.

[70] M. Paquette, J. Beauvais, J. Beerens, P. J. Poole, S. Charbonneau, C. J. Miner, and C. Blaauw, *Blueshifting of ingaasp/INP laser diodes by low-energy ion implantation*, Applied Physics Letters **71**, 3749–3751 (1997).

[71] S. K. Si, D. H. Yeo, H. H. Yoon, and S. J. Kim, *Area selectivity of ingaasp-INP multiquantum-well intermixing by impurity-free vacancy diffusion*, IEEE Journal of Selected Topics in Quantum Electronics **4**, 619–623 (1998).

[72] S. C. Du, L. Fu, H. H. Tan, and C. Jagadish, *Investigations of impurity-free vacancy disordering in (AL)InGaAs(p)/InGaAs Quantum Wells*, Semiconductor Science and Technology **25**, 055014 (2010).

[73] H. Susanto Djie, Y. Wang, Y.-H. Ding, D.-N. Wang, J. C. Hwang, X.-M. Fang, Y. Wu, J. M. Fastenau, A. W. Liu, G. T. Dang, and et al., *Quantum Dash Intermixing*, IEEE Journal of Selected Topics in Quantum Electronics **14**, 1239–1249 (2008).

[74] K.-H. Lee, J. O'Callaghan, B. Roycroft, C. L. Daunt, H. Yang, J. H. Song, F. H. Peters, and B. Corbett, *Quantum well intermixing in alingaas MQW structures through impurity-free vacancy method*, SPIE Proceedings (2010).

[75] K.-H. Lee, B. Roycroft, J. O'Callaghan, C. L. Daunt, H. Yang, J. H. Song, F. H. Peters, and B. Corbett, *Integration of AlInGaAs-MQW Fabry–Pérot lasers with emission at two wavelength ranges via quantum-well intermixing*, IEEE Photonics Technology Letters **23**, 27–29 (2011).

[76] Z. Jia, H. Yang, A. H. Perrott, H. Wang, and F. H. Peters, *Study on the proximity of QWI in InP-based AlGaInAs MQWs using the IFVD method and its application in single frequency teardrop laser diodes*, Opt. Express **28**, 31904–31913 (2020).

[77] B. Zhao, T. Chen, and A. Yariv, *The gain and carrier density in semiconductor lasers under steady-state and transient conditions*, IEEE Journal of Quantum Electronics **28**, 1479–1486 (1992).

[78] N. Pikhtin, S. Slipchenko, Z. Sokolova, and I. Tarasov, *Analysis of threshold current density and optical gain in InGaAsP quantum well lasers*, Semiconductors **36**, 344–353 (2002).

[79] Y.-Z. Huang, Z. Pan, and R. Wu, *Analysis of the optical confinement factor in semiconductor lasers*, Journal of Applied Physics **79**, 3827 – 3830 (1996).

[80] L. A. Coldren and S. W. Corzine. *2.6 THRESHOLD CURRENT AND POWER OUT VERSUS CURRENT*, page 60–70. Wiley-Blackwell, (2012).

[81] Z. A. Weinberg, *On tunneling in metal-oxide-silicon structures*, Journal of Applied Physics **53**, 5052–5056 (1982).

[82] I. Merkulov and V. Perel', *Effects of electron-hole interaction on electro absorption in semiconductors*, Physics Letters A (2002).

[83] G. Parry, M. Whitehead, P. Stevens, A. Rivers, P. Barnes, D. Atkinson, J. S. Roberts, C. Button, K. Woodbridge, and C. Roberts, *The design and application of III-V multiquantum well optical modulators*, Physica Scripta **T35**, 210–214 (1991).

[84] K. W. Böer, H. J. Hänsch, and U. Kümmel, *Anwendung elektro-optischer Effekte zur Analyse des elektrischen Leitungsvorganges in CdS-Einkristallen*, Zeitschrift für Physik **155**, 170–183 (1959).

[85] S. L. Chuang, *Physics of optoelectronic devices*, J. Wiley (1995).

[86] G. Zhou and P. Runge, *Modeling of multiple-quantum-well P-i-N photodiodes*, IEEE Journal of Quantum Electronics **50**, 220–227 (2014).

[87] V. Z. B. V. *Chapter 4: p-n Diodes*. Prentice Hall, (2010).

[88] D. Cassidy, *Analytic description of a homogeneously broadened injection laser*, IEEE Journal of Quantum Electronics **20**, 913–918 (1984).

[89] M. Dernaika, L. Caro, N. P. Kelly, and F. H. Peters, *Single facet semiconductor laser with deep etched V-notch reflectors integrated with an active multimode interference reflector*, Journal of Modern Optics **64**, 1941–1946 (2017).

[90] J. Mulcahy, F. H. Peters, and X. Dai, *Modulators in Silicon Photonics—Heterogenous Integration & and beyond*, Photonics **9**, 40 (2022).

[91] R. Loi, J. O'Callaghan, B. Roycroft, C. Robert, A. Fecioru, A. J. Trindade, A. Gocalinska, E. Pelucchi, C. A. Bower, B. Corbett, and et al., *Transfer printing of algainas/INP etched facet lasers to SI substrates*, IEEE Photonics Journal **8**, 1–10 (2016).

[92] K. Shortiss, M. Dernaika, L. Caro, M. Seifikar, and F. H. Peters, *Inverse scattering method design of regrowth-free single-mode semiconductor lasers using pit perturbations for monolithic integration*, IEEE Photonics Journal **10**, 1–10 (2018).

[93] D. Rabus, M. Hamacher, U. Troppenz, and H. Heidrich, *Optical filters based on ring resonators with Integrated Semiconductor Optical Amplifiers in GAINASP-INP*, IEEE Journal of Selected Topics in Quantum Electronics **8**, 1405–1411 (2002).

[94] S. Xie, J. Guo, K. Guan, L. Mao, W. Guo, L. Qi, and X. Li, *Design and realization of INP/Algainas multiple quantum well ring laser*, Transactions of Tianjin University **20**, 402–406 (2014).

[95] M. Hamacher, U. Troppenz, H. Heidrich, and D. G. Rabus, *Active ring resonators based on Gainasp/INP*, SPIE Proceedings (2003).

[96] R. Grover, T. A. Ibrahim, L.-C. Kuo, T. N. Ding, S. Kanakaraju, L. C. Calhoun, and P.-T. Ho, *Ultracompact Single-Mode Gainasp-INP microracetrack resonators*, Integrated Photonics Research (2003).

[97] P. Bienstman, E. Six, A. Roelens, M. Vanwolleghem, and R. Baets, *Calculation of bending losses in dielectric waveguides using eigenmode expansion and perfectly matched layers*, IEEE Photonics Technology Letters **14**, 164–166 (2002).

[98] L. A. Coldren, S. W. Corzine, and M. M. L. *8.2 TUNABLE, WIDELY TUNABLE, AND EXTERNALLY MODULATED LASERS*, page 458–470. Wiley, (2012).

[99] H. Chandrahalim, S. C. Rand, and X. Fan, *Evanescent coupling between refillable ring resonators and laser-inscribed optical waveguides*, Appl. Opt. **56**, 4750–4756 (2017).

[100] Q. Chen, Z. Wang, J. Zhao, J. Meng, and J.-J. He, *Improved Half-Wave Coupled V-Cavity Laser Using Aggregating-Image Multimode Interference Coupler*, IEEE Photonics Journal **14**, 1–7 (2022).

[101] A. Larsson, *Advances in VCSELs for communication and sensing*, IEEE Journal of Selected Topics in Quantum Electronics **17**, 1552–1567,.

[102] F. Peters and M. MacDougal, *High-speed high-temperature operation of vertical-cavity surface-emitting lasers*, IEEE Photonics Technology Letters **13**, 645–647,.

[103] T. Chen, P. Chen, C. Gee, and N. Bar-Chaim, *A high-speed InGaAsP/InP DFB laser with an air-bridge contact configuration*, IEEE Photonics Technology Letters **5**, 1–3,.

[104] R. Schatz, O. Kjebon, and M. Akram. *Design and evaluation of high speed DBR lasers for analog and digital transmission*. In *Proc. 5th Int. Workshop Laser and Fiber-Optical Networks Modeling LFNM 2003*, pages 32–37,. IEEE.

[105] J. Klamkin, J. Hutchinson, J. Getty, L. Johansson, E. Skogen, and L. Coldren, *High efficiency widely tunable SGDBR lasers for improved direct modulation performance*, IEEE Journal of Selected Topics in Quantum Electronics **11**, 931–938,.

[106] J. Song, M. Rensing, C. Daunt, P. O'Brien, and F. Peters, *Directly modulated laser diode module exceeding 10 Gb/s transmission*, IEEE Transactions on Components, Packaging and Manufacturing Technology **1**, 975–980,.

[107] J. Barton. *The integration of Mach-Zehnder Modulators with Sampled Grating DBR*.

[108] P. Westbergh, J. Gustavsson, B. Kogel, A. Haglund, A. Larsson, A. Mutig, A. Nadtochiy, D. Bimberg, and A. Joel, *40 gbit/s error-free operation of oxide-confined 850 nm vcsel*, IEEE Electronics Letters **14**, 1014–1016,.

[109] W. Chuang, *RF Photonic Technology in Optical Fiber Links*, Cambridge University Press.

[110] S. Chuang, *Physics of Optoelectronic Devices*, John Wiley and Sons. Inc.

[111] C. Warwick. *Understanding the Kramers-Kronig relation using a pictorial proof*.

[112] R. Griffin, R. Johnstone, R. Walker, S. Wadsworth, A. Carter, and M. Wale, *Integrated DQPSK transmitter for dispersion-tolerant and dispersion-managed DWDM transmission*, OFC 2003 Optical Fiber Communications Conference, 2003. (2003).

[113] H. Klein, H. Chen, D. Hoffmann, S. Staroske, A. Steffan, and K.-O. Velthaus, $1.55\,\mu\mathrm{m}$ *Mach-Zehnder modulators on INP for optical 40/80 Gbit/s transmission networks*, 2006 International Conference on Indium Phosphide and Related Materials Conference Proceedings (2006).

[114] R. Walker, *High-speed III-V semiconductor intensity modulators*, IEEE Journal of Quantum Electronics **27**, 654–667 (1991).

[115] H. Kawanishi, Y. Yamauchi, N. Mineo, Y. Shibuya, H. Mural, K. Yamada, and H. Wada, *EAM-integrated DFB laser modules with more than 40-GHz bandwidth*, IEEE Photonics Technology Letters **13**, 954–956 (2001).

[116] W. Han, C. Daunt, H. Yang, M. Rensing, X. Wang, P. O'Brien, and F. Peters. *Development of a broadband matching network for electro-absorption modulators*. In *Proc. 11th Int Numerical Simulation of Optoelectronic Devices (NUSOD) Conf*, pages 81–82,. IEEE.

[117] G. Li, W. Chen, P. Yu, C. Sun, and S. Pappert. *The effects of photocurrent on microwave properties of electroabsorption modulators*. In *Proc. IEEE MTT-S Int. Microwave Symp. Digest*, volume 3, pages 1003–1006,. IEEE.

[118] Y.-G. Wey, K. Giboney, J. Bowers, M. Rodwell, P. Silvestre, P. Thiagarajan, and G. Robinson, *GHz GaInAs/InP double heterostructure p-i-n photodetectors*, Journal of Lightwave Technology **13**, 1490–1499,.

[119] G. Robinson, *Multi-layer photoresist air bridge fabrication method*, United States of America Patent **5219713**.

[120] U. Westergren, Y. Yu, P. Janes, P. Holmstrom, and L. Thyten. *Efficient and Compact Light-Intensity Modulators for High Frequencies and High Bitrates*. In *Proc. Int Transparent Optical Networks Conf*, volume 2, pages 142–145,. IEEE.

[121] F. Peters and J. Geske, *Low-capacitance bond pads for high speed devices*, United States of America Patent **6465811**.

[122] R. Sheehan, M. Guina, J. Viheriälä, R. Isoaho, M. Harjanne, F. Azarello, M. Yang, A. Malacarne, T. Aalto, and F. Peters, *Data transmission at*

1300 nm using optical interposer comprising hybrid integrated silicon waveguide and dilute nitride electroabsorption modulator, Optics Express **26**, 34336 (2018).

[123] L. Johansson, J. Getty, Y. Akulova, G. Fish, and L. Coldren, *Sampled-grating DBR laser-based analog optical transmitters*, Journal of Lightwave Technology **21**, 2968–2976 (2003).

[124] J. Zhang, B. Haq, J. O'Callaghan, A. Gocalinska, E. Pelucchi, A. Trindade, B. Corbett, G. Morthier, and G. Roelkens, *Transfer-printing-based integration of a III–V-on-silicon distributed feedback laser*, Opt. Express , 8821–8830.

[125] A. Groote, P. Cardile, A. Subramanian, A. Fecioru, C. Bower, D. Delbeke, R. Baets, and G. Roelkens, *Transfer-printing-based integration of single-mode waveguide-coupled III–V-on-silicon broadband light emitters*, Opt. Express , 13754–13762.

[126] J. Zhang, A. Groote, A. Abbasi, R. Loi, J. O'Callaghan, B. Corbett, A. Trindade, C. Bower, and G. Roelkens, *Sili-con photonics fiber-to-the-home transceiver array based on transfer-printing-based integration of III–V photodetectors*, Opt. Express , 14290–14299.

[127] J. O'Callaghan, R. Loi, E. Mura, B. Roycroft, A. Trindade, K. Thomas, A. Gocalinska, E. Pelucchi, J. Zhang, and R. Roelkens, *Comparison of InGaAs and InAlAs sacrificial layers for release of InP-based de-vices*, Opt. Express , 4408–4414.

[128] J. Han, F. Boeuf, J. Fujikata, S. Takahashi, S. Takagi, and M. Takenaka, *Efficient low-loss InGaAsP/Si hybrid MOS optical modulator*, Nat. Photonics , 486–490.

[129] T. Hiraki, T. Aihara, K. Hasebe, K. Takeda, T. Fujii, T. Kakitsuka, T. Tsuchizawa, H. Fukuda, and S. Matsuo, *Heterogeneously integrated III–V/Si MOS capacitor Mach–Zehnder modulator*, Nat. Photonics , 482–485.

[130] R. Soref and B. Bennett, *Electrooptical effects in silicon*, IEEE J. Quantum Electron **23**, 123–129.

[131] B. Haq, J. Rahimi Vaskasi, J. Zhang, A. Gocalinska, E. Pelucchi, B. Corbett, and G. Roelkens, *Mi-cro-transfer-printed III–V-on-silicon C-band distributed feedback lasers*, Opt. Express , 32793.

[132] R. Loi, J. O'Callaghan, B. Roycroft, C. Robert, A. Fecioru, A. Trindade, A. Gocalinska, E. Pelucchi, C. Bower, and B. Corbett, *Transfer Printing of AlGaInAs/InP Etched Facet Lasers to Si Substrates*, IEEE Photonics J. , 1–10.

[133] T. Vanackere, M. Billet, C. Beeck, S. Poelman, G. Roelkens, S. Clemmen, and B. Kuyken. *Micro-Transfer Printing of Lithium Niobate on Silicon Nitride*. In *Proceedings of the 2020 European Conference on Optical Communications (ECOC*, Brussels, Belgium.